

2-24-2026 1:30 PM

Recycling Silicon Photovoltaic Cells into Silicon Anodes for Li-ion Batteries Using 3D Printing and an Open Source Toolchain

Maryam Mottaghi

Supervisor: Pearce, Joshua M., *The University of Western Ontario*

A thesis submitted in partial fulfillment of the requirements for the Doctor of Philosophy degree in Mechanical and Materials Engineering

© Maryam Mottaghi 2026



This work is licensed under a [Creative Commons Attribution 4.0 License](https://creativecommons.org/licenses/by/4.0/).

Abstract

With the increasing adoption of solar energy, the disposal of end-of-life photovoltaic (PV) modules has become a growing environmental concern. The crystalline silicon embedded in these modules offers significant potential as a high-capacity anode material for lithium-ion batteries. This thesis addresses the central research question of how waste silicon solar cells can be upcycled into anodes for lithium-ion batteries using an open-source, low-cost, and scalable manufacturing toolchain. The aim is to develop a sustainable pathway that integrates Open-source hardware and additive manufacturing to create battery anodes from discarded materials. To investigate this question, an Open-source toolchain was designed and validated, including an AC/off-grid photovoltaic-powered ball mill, an Open-source scientific bottle roller, and an Open-source inert-gas glove box. Silicon recovered from waste PV cells was incorporated into photocurable resin formulations and 3D printed into electrode geometries using stereolithography (SLA) technology. The printed structures were pyrolyzed to convert the polymer matrix into conductive carbon, and form silicon-carbon composite anodes. An investigation was conducted across four pyrolysis temperatures including 800, 1100, 1200, and 1400 °C, to determine their influence on structural evolution, carbon formation, and electrochemical behaviour. Among these, 1200 °C provided the optimal balance between suppressing electrochemically inactive SiC formation, enhancing carbon conductivity, and maintaining mechanical integrity. The corresponding anodes delivered 771 mAh g⁻¹ with 61% capacity retention over 120 cycles. To further improve conductivity and mitigate silicon volume changes, carbon nanotubes (CNTs) synthesized from post-consumer plastic-waste pyrolysis were incorporated into the resin. The CNT-reinforced anodes showed enhanced electrochemical behavior and exhibited an initial discharge capacity of 862 mAh g⁻¹ with 98.88% initial Coulombic efficiency, which increased to 1,044 mAh g⁻¹ upon cycling due to improved silicon activation and electronic pathways. This thesis demonstrates that waste silicon PV cells can be transformed into functional Li-ion battery anodes through an accessible, open-source, and sustainable manufacturing approach. The results provide a proof of concept for decentralized battery fabrication, advance circular-economy strategies for PV and plastic waste and expand the role of additive manufacturing in energy-storage materials research.

Keywords: 3D printing; Additive manufacturing; Batteries; Recycling; Sustainability; Solar cells; Stereolithography; Silicon; Photovoltaic; Open-source; Open-source hardware

Summary for Lay Audience

With the rapid expansion of solar energy, the hidden environmental challenge of managing a huge amount of discarded photovoltaic modules becomes a concern. These end-of-life panels contain valuable materials, including crystalline silicon that holds significant potential for improving lithium-ion batteries as anode material. This thesis addresses this opportunity by developing a method to upcycle waste silicon solar cells into battery anodes using an affordable, Open-source manufacturing process. To achieve this, Open-source low-cost tools, including a ball mill to grind solar cells, bottle roller to mix the ground solar cell with other materials, and a glove box to prepare the materials in an inert gas environment, were designed and built. The research involved recovering silicon from discarded panels, mixing it with a liquid resin, and 3D printing it into precise electrode structures. These printed parts were then pyrolyzed (heated at extreme temperatures), to convert the resin into a conductive carbon framework that covers the silicon. Different pyrolysis temperatures were used, and the anode structural, electrical, and electrochemical properties were tested. The study identified that processing at 1200°C created the optimal balance for battery performance. Also, for improving the battery performance carbon derived from plastic waste was included to the structure which helped reinforce the material against the physical stress of charging. This work demonstrates a viable circular economy pathway and proves that accessible, decentralized technology can successfully transform solar and plastic waste into energy storage solutions.

Co-Authorship Statement

This thesis includes several manuscripts that were co-authored with collaborators. I (Maryam Mottaghi) was the primary contributor to all papers, with major roles in conceptualization, experimental design, data collection, analysis, and manuscript preparation. Co-authors provided guidance, supervision, technical assistance, and manuscript revisions appropriate to their roles and expertise. A summary of contributions for each publication is provided below.

Chapter 2: A Review of 3D Printing Batteries

This chapter is based on the published paper “A Review of 3D Printing Batteries” in *Batteries* (MDPI) and the in-press book chapter “3D Printing of Batteries,” in *Next-Generation Energy Storage Systems: From Advanced Lithium to Beyond-Lithium Batteries*, Wiley-VCH GmbH. All conceptualization, methodology development, formal analysis, investigation, data curation, and the preparation of the original draft were undertaken by M. Mottaghi under the supervision of Dr. J. M. Pearce. Visualization and the initial manuscript drafting were conducted by M. Mottaghi under the supervision of Dr. J. M. Pearce. Review, editing, supervision, project administration, and funding acquisition were provided by Dr. J. M. Pearce.

Citation: M. Mottaghi and J. M. Pearce, “A Review of 3D Printing Batteries,” *Batteries*, vol. 10, no. 3, Art. no. 3, Mar. 2024. doi: <https://doi.org/10.3390/batteries10030110>

Chapter 3, Section 3.1: AC/Off-Grid Photovoltaic Powered Open-Source Ball Mill

This section is based on the published paper “AC/off-grid photovoltaic powered open-source ball mill” in *HardwareX* (Elsevier). The methodology, validation, formal analysis, investigation, data curation, original drafting, visualization, and manuscript review and editing were undertaken by M. Mottaghi under the supervision of Dr. J. M. Pearce. Methodology development, validation, analysis, visualization, and manuscript review were contributed by M. Rahman. Dr. A. Kulkarni contributed to methodology, validation, analysis, visualization, and review and editing. Conceptualization, methodology, analysis, data curation, drafting, reviewing and editing, resources, supervision, and funding acquisition were provided by Dr. J. M. Pearce.

Citation: M. Mottaghi, M. Rahman, A. Kulkarni, and J. M. Pearce, “AC/off-grid photovoltaic powered open-source ball mill,” *HardwareX*, vol. 14, p. e00423, June 2023, doi: 10.1016/j.ohx.2023.e00423.

OSF: <https://osf.io/xa4ws/overview>

Chapter 3, Section 3.2: Open-Source Scientific Bottle Roller

This section is based on the published paper “Open-source scientific bottle roller” in *HardwareX* (Elsevier). Methodology, validation, analysis, investigation, data curation, original drafting, visualization, and manuscript review and editing were undertaken by M. Mottaghi under the supervision of Dr. J. M. Pearce. Y. Bai contributed to methodology, validation, analysis, visualization, and manuscript review. Dr. A. Kulkarni contributed to methodology, validation, analysis, visualization, and review and editing. Conceptualization, methodology, analysis, resources, data curation, drafting, reviewing and editing, supervision, and funding acquisition were provided by Dr. J. M. Pearce.

Citation: M. Mottaghi, Y. Bai, A. Kulkarni, and J. M. Pearce, “Open-source scientific bottle roller,” *HardwareX*, vol. 15, p. e00445, Sept. 2023, doi: 10.1016/j.ohx.2023.e00445.

OSF: <https://osf.io/ps57u/overview>

Chapter 3, Section 3.3: Open-Source Inert-Gas Glove Box

This section is based on the published paper “Open-source Inert Gas Glove Box,” in *HardwareX* (Elsevier). Methodology, validation, analysis, investigation, data curation, original drafting, visualization, and manuscript review and editing were undertaken by M. Mottaghi under the supervision of Dr. J. M. Pearce. Conceptualization, methodology, analysis, resources, data curation, drafting, review and editing, supervision, and funding acquisition were provided by Dr. J. M. Pearce.

Citation: M. Mottaghi and J. M. Pearce, “Open-source Inert Gas Glove Box,” 2024, SSRN. doi: 10.2139/ssrn.5015252.

OSF: <https://osf.io/xnqk3/overview>

Chapter 4: Recycling Silicon Photovoltaic Cells into Silicon Anodes for Li-ion Batteries Using 3D Printing

This chapter is based on the published paper “Recycling silicon photovoltaic cells into silicon anodes for Li-ion batteries using 3D printing” in RSC *Sustainability*. Conceptualization, methodology, software development, investigation, formal analysis, data curation, validation, visualization, original draft preparation, and manuscript review and editing were undertaken by M. Mottaghi under the supervision of Dr. J. M. Pearce. Dr. A. Kulkarni contributed to investigation, resources, methodology, and manuscript review and editing. Conceptualization, methodology, analysis, resources, data curation, writing (original draft, review and editing), supervision, project administration, and funding acquisition were provided by Dr. J. M. Pearce.

Citation: M. Mottaghi, A. Kulkarni, and J. M. Pearce, “Recycling silicon photovoltaic cells into silicon anodes for Li-ion batteries using 3D printing,” RSC Sustain., Feb. 2025, doi: 10.1039/D4SU00808A.

Chapter 5: Effect of Pyrolysis Temperature on the Performance of 3D-Printed Silicon–Carbon Anodes

This chapter is based on the submitted paper “Effect of Pyrolysis Temperature on the Performance of 3D-Printed Silicon–Carbon Anodes Derived from Recycled Photovoltaic Silicon.” Conceptualization, methodology, software development, investigation, formal analysis, data curation, validation, visualization, original draft preparation, and manuscript review and editing were undertaken by M. Mottaghi under the supervision of Dr. J. M. Pearce. Dr. A. Kulkarni contributed to conceptualization, investigation, resources, analysis, methodology, and manuscript review and editing. Conceptualization, methodology, analysis, resources, writing (original draft, review and editing), supervision, project administration, and funding acquisition were provided by Dr. J. M. Pearce.

Citation: “Effect of Pyrolysis Temperature on the Performance of 3D-Printed Silicon–Carbon Anodes Derived from Recycled Photovoltaic Silicon by Maryam Mottaghi, Apoorv Kulkarni, Joshua M. Pearce :: SSRN.” Accessed Nov. 27, 2025. Available at: https://papers.ssrn.com/sol3/papers.cfm?abstract_id=5812933

Chapter 6: Upcycling Post-Consumer Plastic and Waste Silicon PV Cells into Carbon-Enhanced Silicon Anodes

This chapter is based on the submitted paper “Upcycling Post-Consumer Plastic and Waste Silicon PV Cells into Carbon-Enhanced Silicon Anodes.” Conceptualization, methodology, materials preparation, software development, investigation, analysis, data curation, visualization, and manuscript drafting and editing were undertaken by M. Mottaghi under the supervision of Dr. J. M. Pearce. Dr. A. Kulkarni contributed to methodology, investigation, analysis, and manuscript review. R. Ghode, R. Z. Cao, M. S. H. Boutilier, and C. L. Briens contributed to materials preparation and writing (review and editing). Conceptualization, methodology, analysis, writing (review and editing), supervision, project administration, and funding acquisition were provided by Dr. J. M. Pearce.

Acknowledgments

I would like to express my deepest gratitude to my advisor, Professor Joshua M. Pearce, whose guidance, mentorship, and unwavering support have shaped every stage of my research and academic development. His encouragement, patience, and commitment have profoundly influenced both this thesis and my growth as a researcher.

I owe heartfelt thanks to my mother, who has been my greatest supporter throughout my life. Her love, resilience, and sacrifices have made my achievements possible. I would also like to acknowledge my father, whose memory continues to inspire and guide me. I am deeply grateful to my boyfriend, Dr. Mohammadtaghi Badakhshan, whose love and support carried me through this entire journey. He stood by me during the hardest moments, rearranged his life to help me move forward, and supported me in countless ways.

My sincere thanks go to Dr. Apoorv Kulkarni, whose collaboration, technical expertise, and thoughtful discussions contributed to multiple stages of my work.

I would like to sincerely thank and acknowledge Dr. Yolanda Hedberg and Narges Hajighasemi for their support in facilitating my receipt of the Corrosion Research and Training Experience (CRTE) Award, offered through the CREATE–CORRECT program (Excellence in Canadian Corrosion Education through Internationalization, Equity, and Interdisciplinarity).

I gratefully acknowledge the many colleagues and collaborators who contributed their expertise, equipment access, and thoughtful discussions throughout this work, including Dr. C. Kingston, Dr. M. Jakubinek, Dr. B. Ashrafi, Dr. H. Sarvestani, A. Bassi, A. Kalbasi, A. Zali, Y. Zhao, P. Pirayesh, H. Shi, R. Noroozi, D. Pjontek, L. Gaburici, T. Lacelle, and O. Kodra. Their technical assistance and scientific insights played an important role in the progress of this research. I also thank Jacomex for providing access to equipment and for their helpful feedback during the development of the Open-source glove box system. This research was financially supported by the Natural Sciences and Engineering Research Council of Canada (NSERC), the Thompson Endowment, the Ontario Research Fund (ORF) Small Infrastructure Fund, the Canada Foundation for Innovation (CFI) John R. Evans Leaders Fund (Project No. 39702), and the Strategic Priority Fund at Western University. Support from Carbon Solutions for CNT synthesis development is also gratefully acknowledged.

List of Abbreviations

Abbreviation	Definition	Abbreviation	Definition
AC	Alternating Current	LCA	Life Cycle Assessment
AM	Additive Manufacturing	LIB	Lithium-Ion Battery
CAD	Computer-Aided Design	OSF	Open Science Framework
CNT	Carbon Nanotube	PA	Polyacrylate
c-Si	Crystalline Silicon	PLA	Polylactic Acid
CV	Cyclic Voltammetry	PMMA	Poly(methyl methacrylate)
DIW	Direct Ink Writing	PV	Photovoltaic
DTA	Differential Thermal Analysis	SEI	Solid Electrolyte Interphase
EDS (EDX)	Energy-Dispersive X-ray Spectroscopy	SEM	Scanning Electron Microscopy
EIS	Electrochemical Impedance Spectroscopy	SiC	Silicon Carbide
EV	Electric Vehicle	SLA	Stereolithography
FFF	Fused Filament Fabrication	TGA	Thermogravimetric Analysis
FDM	Fused Deposition Modeling	UV-Vis	Ultraviolet–Visible Spectroscopy
IJP	Inkjet Printing		

Table of Contents

Abstract.....	ii
Summary for Lay Audience.....	iv
Co-Authorship Statement.....	v
Acknowledgments.....	ix
Table of Contents.....	xi
List of Tables.....	xv
List of Figures.....	xvi
Preface.....	xx
Chapter 1.....	1
1 Introduction.....	1
1.1 Background.....	1
1.2 Research Objectives.....	2
1.3 Thesis Outline.....	4
1.3.1 Chapter 2 - Literature Review: 3D Printing Batteries.....	4
1.3.2 Chapter 3 - Open-Source Hardware for Sustainable Battery Fabrication... ..	4
1.3.3 Chapter 4 - Recycling Silicon Photovoltaic Cells into Silicon Anodes for Li-ion Batteries Using 3D Printing.....	4
1.3.4 Chapter 5 - Effect of Pyrolysis Temperature on Silicon–Carbon Composite Anodes.....	5
1.3.5 Chapter 6 - Upcycling Post-Consumer Plastic and Waste Silicon Photovoltaic Cells into Carbon-Enhanced Silicon Anodes for Li-ion Batteries Using 3D Printing.....	5
1.3.6 Chapter 7 - Limitations, Future Directions, and Conclusions.....	5
1.4 Contribution of the Thesis.....	5
Chapter 2.....	7
2 Literature review.....	7

2.1	Introduction.....	7
2.2	Background.....	9
2.2.1	Basic Geometries	9
2.2.2	Impact of 3D Printing on Battery Performance	10
2.2.3	Goals of Geometric Design for Batteries.....	12
2.3	Review	13
2.3.1	Direct Ink Writing.....	13
2.3.2	Fused Filament Fabrication.....	24
2.3.3	Hybrid energy storage system design for mobile	34
2.3.4	Stereolithography	41
2.4	Conclusions.....	50
	Chapter 3.....	52
3	Open-Source Hardware for Battery Fabrication	52
3.1	AC/off-grid photovoltaic powered open-source ball mill.....	53
3.1.1	Hardware in context.....	53
3.1.2	Hardware description	56
3.1.3	Validation and characterization	57
3.1.4	Conclusions.....	61
3.2	Open-source scientific bottle roller.....	62
3.2.1	Hardware in context.....	62
3.2.2	Hardware description	64
3.2.3	Validation and characterization	64
3.2.4	Future work.....	66
3.3	Open-source Inert Gas Glove Box	68
3.3.1	Hardware in context.....	68
3.3.2	Hardware description	73

3.3.3	Validation and characterization	74
Chapter 4	78
4	Recycling Silicon Photovoltaic Cells into Silicon Anodes for Li-ion Batteries Using 3D Printing.....	78
4.1	Introduction.....	78
4.2	Experimental Section	81
4.2.1	Materials	82
4.2.2	Resin fabrication	82
4.2.3	3D printing of customized resin.....	82
4.2.4	Pyrolysis.....	84
4.2.5	Material tests	84
4.2.6	Electrochemical tests	85
4.3	Results and discussion	86
4.3.1	UV-Vis spectrometry	86
4.3.2	DTA and TGA	87
4.3.3	Raman spectra and XRD.....	87
4.3.4	Optical Microscopy and Visual Inspection.....	89
4.3.5	SEM and EDX	90
4.3.6	Cyclic Voltammetry (CV).....	93
4.3.7	Galvanostatic Cycling.....	93
4.3.8	Electrochemical Impedance Spectroscopy (EIS).....	94
4.4	Discussion	95
Chapter 5	100
5	Effect of Pyrolysis Temperature on the Performance of 3D Printed Silicon–Carbon Anodes Derived from Recycled Photovoltaic Silicon	100
5.1	Experimental Section	100

5.2 Results.....	102
5.2.1 Pre-cycling	102
5.2.2 Electrochemical results	107
5.2.3 Post cycling.....	111
5.3 Discussion.....	114
5.4 Conclusions.....	116
Chapter 6.....	117
6 Upcycling Post-Consumer Plastic and Waste Silicon Photovoltaic Cells into Carbon-Enhanced Silicon Anodes for Li-ion Batteries Using 3D Printing	117
6.1 Experimental section.....	117
6.1.1 Materials and Method	117
6.1.2 Material tests	119
6.1.3 Electrochemical tests	120
6.2 Results.....	120
6.2.1 XRD	120
6.2.2 Raman	121
6.2.3 SEM and EDS	122
6.2.4 Galvanostatic Cycling.....	123
6.2.5 Cyclic Voltammetry (CV).....	124
6.2.6 Electrochemical Impedance Spectroscopy (EIS).....	125
6.3 Discussion	126
6.4 Conclusions.....	128
Chapter 7.....	129
7 Conclusions, Limitations, and Future Works.....	129
8 References	133
9 Appendices.....	172

List of Tables

Table 2-1. Summary and comparison of electrochemical performance of DIW of batteries.	21
Table 2-2. Key parameters for the DIW process.	22
Table 2-3. Summary and comparison of electrochemical performance for FFF of batteries.	31
Table 2-4. Key Parameters for FFF Process	32
Table 2-5. Summary and comparison of electrochemical performance for IJP of batteries...	39
Table 2-6. Key Parameters for IJP Process.....	40
Table 2-7. Summary and comparison of electrochemical performance for SLA of batteries.	46
Table 2-8. Key Parameters for SLA Process	47
Table 2-9. Advantages and disadvantages of DIW, FFF, IJP, and SLA.....	48
Table 3-1. Commercial ball mill costs in CAD	54
Table 3-2. Proprietary commercial bottle roller costs and specifications.....	63
Table 3-3. Representative selection of commercial glove boxes specifications.....	71
Table 3-4. DIY glove boxes.....	71
Table 6-1. Comparison of CNT-reinforced Si/C anodes in the literature and this work	127

List of Figures

Figure 1-1. Graphical abstract.....	3
Figure 2-1. Illustrations of (a) DIW, (b) FFF, (c) IJP, and (d) SLA.....	14
Figure 2-2. (a) Illustration of DIW of aligned BN in electrolyte film. Reprinted/adapted with permission from Ref [121] ; published by ACS, 2022, (b) Capacity retention of the cells fabricated using DIW.....	24
Figure 2-3. (a) “one shot” FFF of battery [144], (b) required modifications for printing customized PEO/LiTFSI filament [148], (c) illustration of FFF of TPU-based electrodes. Reproduced from Hu et al. (2023) with permission from Wiley [147], (d) Capacity retention of the cells fabricated by FFF.	34
Figure 2-4. (a) Illustration of the IJP process for fabricating a graphene thin-film electrode [157], (b) Capacity retention of the cells fabricated by IJP.	38
Figure 2-5. (a) SLA printed electrodes before and after pyrolysis. Reproduced from Katsuyama et al. (2022) with permission from Wiley [172], (b) Capacity retention of the cells fabricated by SLA.....	48
Figure 3-1. Assembly of the open-source ball mill: (a) individual components, including the PVC pipe, 3D-printed drum, and magnets; (b) assembled drum; (c) end view showing insertion of the front bearing; (d) mounting of the drum onto the drive shaft; (e) fully mounted drum secured on the support frame; and (f) complete ball mill system.	57
Figure 3-2. a) Micro-CT image of silicon particles after 18 hours ball milling, and b) Particle size distribution after 18 hours ball milling.	58
Figure 3-3. Smart phone pictures of silicon particles: a) before ball milling, b) after 6 hours ball milling, c) after 12 hours ball milling, and d) after 18 hours ball milling.	59
Figure 3-4. 3D printable adapter for microcentrifuge tube.....	67

Figure 3-5. a) Oxygen reduction in the glove box vs time, b) Moisture level reduction in the glove box vs time	74
Figure 4-1. Processing steps for recycling silicon solar cells into batteries.	81
Figure 4-2. Photorheology results of the plain resin, showing the storage modulus as a function of step time.....	84
Figure 4-3. UV–Vis spectra of (a) resin formulations containing solid load and (b) pure acrylate resins, showing absorbance as a function of wavelength.	86
Figure 4-4. A) DTA, and B) TGA results from different acrylate resins.	87
Figure 4-5. A) Raman spectra of transparent red resin before and after pyrolysis, showing Raman intensity as a function of Raman shift, and B) XRD pattern of samples pyrolyzed at 1400 °C, showing diffraction intensity as a function of 2θ	89
Figure 4-6. A) CAD model of the designed anode (I) Isometric view, (II) front view (diameter), and (III) side view (thickness), B) pictures of the (I) as-printed sample, and (II) pyrolyzed sample, C) the measured thickness of the as-printed sample, and D) the measured thickness of the pyrolyzed sample.	90
Figure 4-7. SEM images of (A, B) as-ball-milled solar cell powder and (C, D) acid-washed solar cell powder after ball milling	91
Figure 4-8. A) Optical microscopy image of printed sample using Openflexure microscope, B) SEM, and C) EDS elemental analysis of the pyrolyzed samples at 1400°C.	92
Figure 4-9. A) CV curves of printed silicon–carbon composite anodes, showing current as a function of voltage, B) Specific capacity comparison between printed anodes and a commercial graphite anode, showing specific capacity versus cycle number, and C) EIS Nyquist plots comparing printed anodes and a commercial graphite anode, showing Z' versus $-Z''$	95

Figure 5-1. XRD patterns of silicon–carbon composite anodes pyrolyzed at 800 °C, 1100 °C, and 1200 °C, showing diffraction intensity as a function of 2θ	102
Figure 5-2. Raman spectra of silicon–carbon composite anodes pyrolyzed at 800 °C, 1100 °C, and 1200 °C, showing Raman intensity as a function of Raman shift.....	104
Figure 5-3. Electrical conductivity of silicon–carbon composite anodes pyrolyzed at 800 °C, 1100 °C, and 1200 °C, measured by four-point probe, showing conductivity as a function of pyrolysis temperature.....	105
Figure 5-4. EDS elemental mapping of acid-washed solar cell powder showing the spatial distribution of constituent elements.....	106
Figure 5-5. SEM images of an SLA-printed solar-cell-derived silicon sample showing surface morphology and microstructural features.	106
Figure 5-6. EDS elemental mapping of silicon–carbon composite anodes pyrolyzed at (a–d) 800 °C, (e–h) 1100 °C, and (i–l) 1200 °C.....	107
Figure 5-7. a) Galvanostatic charge–discharge voltage profiles of anodes pyrolyzed at 800–1200 °C, showing voltage versus specific capacity, b) Long-term cycling performance of the anode pyrolyzed at 1200 °C, showing specific capacity versus cycle number, c) Voltage versus specific capacity profiles of the anode pyrolyzed at 1200 °C, d) Rate performance showing specific capacity as a function of current density.	109
Figure 5-8. CV curves of the silicon–carbon composite anode pyrolyzed at 1200 °C, showing current as a function of voltage.....	110
Figure 5-9. EIS Nyquist plots of silicon–carbon composite anodes pyrolyzed at 800 °C, 1100 °C, and 1200 °C, showing Z' versus $-Z''$	111
Figure 5-10. XPS spectra of the silicon–carbon composite anode showing (a–c) the sample pyrolyzed at 1200 °C and (d–i) the post-cycled sample.	112

Figure 5-11. Raman spectra of the silicon–carbon composite anode pyrolyzed at 1200 °C before and after electrochemical cycling, showing Raman intensity as a function of Raman shift.	113
Figure 6-1. XRD patterns of silicon–carbon composite anodes containing carbon nanotubes, showing diffraction intensity as a function of 2θ	121
Figure 6-2. Raman spectra of silicon–carbon composite anodes containing carbon nanotubes, showing Raman intensity as a function of Raman shift.....	122
Figure 6-3. EDS analysis of the silicon–carbon composite anode containing carbon nanotubes: (a) SEM micrograph of the selected region, (b) overlaid EDS elemental map, (c) carbon elemental map, (d) oxygen elemental map, and (e) silicon elemental map.....	123
Figure 6-4. Galvanostatic charge–discharge voltage profiles of the silicon–carbon composite anode containing carbon nanotubes, showing voltage as a function of specific capacity. ...	124
Figure 6-5. CV curves of the silicon–carbon composite anode containing carbon nanotubes, showing current as a function of voltage.	125
Figure 6-6. EIS Nyquist plot of the silicon–carbon composite anode containing carbon nanotubes, showing Z' versus $-Z''$	126

Preface

This thesis is the culmination of several years of study, experimentation, and personal growth. My journey in materials science began with a fascination for how sustainable energy technologies intersect with the physical properties of materials, and a determination to address global challenges through engineering innovation. Over the course of this research, I have focused on developing and refining strategies for resource-efficient materials and devices. I hope that these explorations, including both the recovery of valuable components from end-of-life silicon solar cells and the potential of open-source hardware for accessible battery research, will contribute meaningfully to a more circular, resilient energy future.

The process of producing this thesis demanded equal measures of scientific rigour and persistence. It involved countless hours designing experiments, analysing data, troubleshooting unexpected results, and engaging with diverse research communities and collaborators. Through these experiences, I deepened my understanding of interdisciplinary methods and sharpened my ability to communicate complex ideas clearly. The lessons learned extend beyond the pages of this document, which influence how I approach problem-solving and collaboration in both academic and professional contexts.

I hope that the insights presented here will not only advance academic discussions in materials science and sustainable energy but also offer practical guidance for researchers and engineers who seek to develop greener technologies. By sharing the successes and challenges encountered along the way, I aim to encourage others to pursue innovative solutions that balance technical excellence with environmental stewardship.

Chapter 1

1 Introduction

1.1 Background

The rapid growth of portable electronics, electric vehicles, and renewable energy systems has intensified the demand for high-performance and cost-effective energy storage technologies. Among these, lithium-ion batteries (LIBs) remain the dominant solution due to their high energy density, stability, and broad applicability [1,2]. Conventional battery electrode production relies heavily on expensive industrial processes which increase manufacturing costs and limit flexibilities. LIBs are composed of three main components: an anode, a cathode, and an electrolyte. Graphite and other carbon-based materials are commonly used as anodes because of their low cost and reliable electrochemical behaviour, but their theoretical capacity is limited to 372 mAh g^{-1} [3].

Silicon has emerged as a promising alternative to graphite, which offers natural abundance and a high theoretical capacity of $\sim 3579 \text{ mAh g}^{-1}$ [4]. Despite these advantages, large-scale implementation of silicon anodes is constrained by its low intrinsic conductivity and severe volume expansion during cycling. These challenges necessitate innovative composite architectures that can stabilize silicon, enhance conductivity, and withstand repeated lithiation–delithiation.

Simultaneously, the rapid increase in end-of-life photovoltaic (PV) modules presents an opportunity for sustainable material sourcing. Crystalline silicon (c-Si) PV panels dominate global production and contain high-purity silicon that has already undergone energy-intensive purification. Upcycling this silicon into battery anodes aligns with circular-economy principles, reduces dependence on virgin materials, and lowers both environmental and economic burdens associated with battery manufacturing.

Additive manufacturing, particularly stereolithography (SLA), creates new possibilities for engineering advanced silicon–carbon architectures. SLA enables precise control over geometry and material distribution. This overcomes many limitations of conventional

slurry-based methods. Since SLA resins are electrically insulating, a subsequent pyrolysis step should be employed to convert the printed structures into conductive, polymer-derived ceramic composites.

To further reduce cost and improve accessibility, this thesis incorporates a fully open-source hardware toolchain, including an open-source ball mill, bottle roller, and inert-gas glove box, to process recycled PV silicon and prepare printable resins. Open-source tools dramatically lower equipment costs, democratize battery research, and enable sustainable, decentralized manufacturing.

By integrating recycled silicon, SLA 3D printing, and open-source toolchain, this thesis establishes a sustainable and economically viable pathway for producing high-performance silicon–carbon anodes. Studies of pyrolysis temperature and functional carbon additives, including carbon derived from post-consumer plastic waste, advance both the scientific understanding and practical implementation of circular-economy battery materials.

1.2 Research Objectives

The main objective of this research is to develop, characterize, and optimize a sustainable manufacturing platform for silicon–carbon anodes using recycled photovoltaic silicon, SLA 3D printing, and open-source hardware. The steps are illustrated in Figure 1-1.

The research aims to:

- Develop open-source hardware to process and prepare PV-derived silicon and resin formulations in a low-cost and accessible way
- Formulate printable resin formulations by incorporating silicon extracted from broken photovoltaic cells
- Investigate the electrochemical performance of the printed anodes.
- Investigate the influence of pyrolysis temperature on carbon structure, electrical conductivity, and electrochemical performance

- Evaluate carbon enhancement strategies, including CNTs synthesized from plastic-waste-derived hydrocarbons, to improve conductivity, mechanical integrity, and cycling stability.

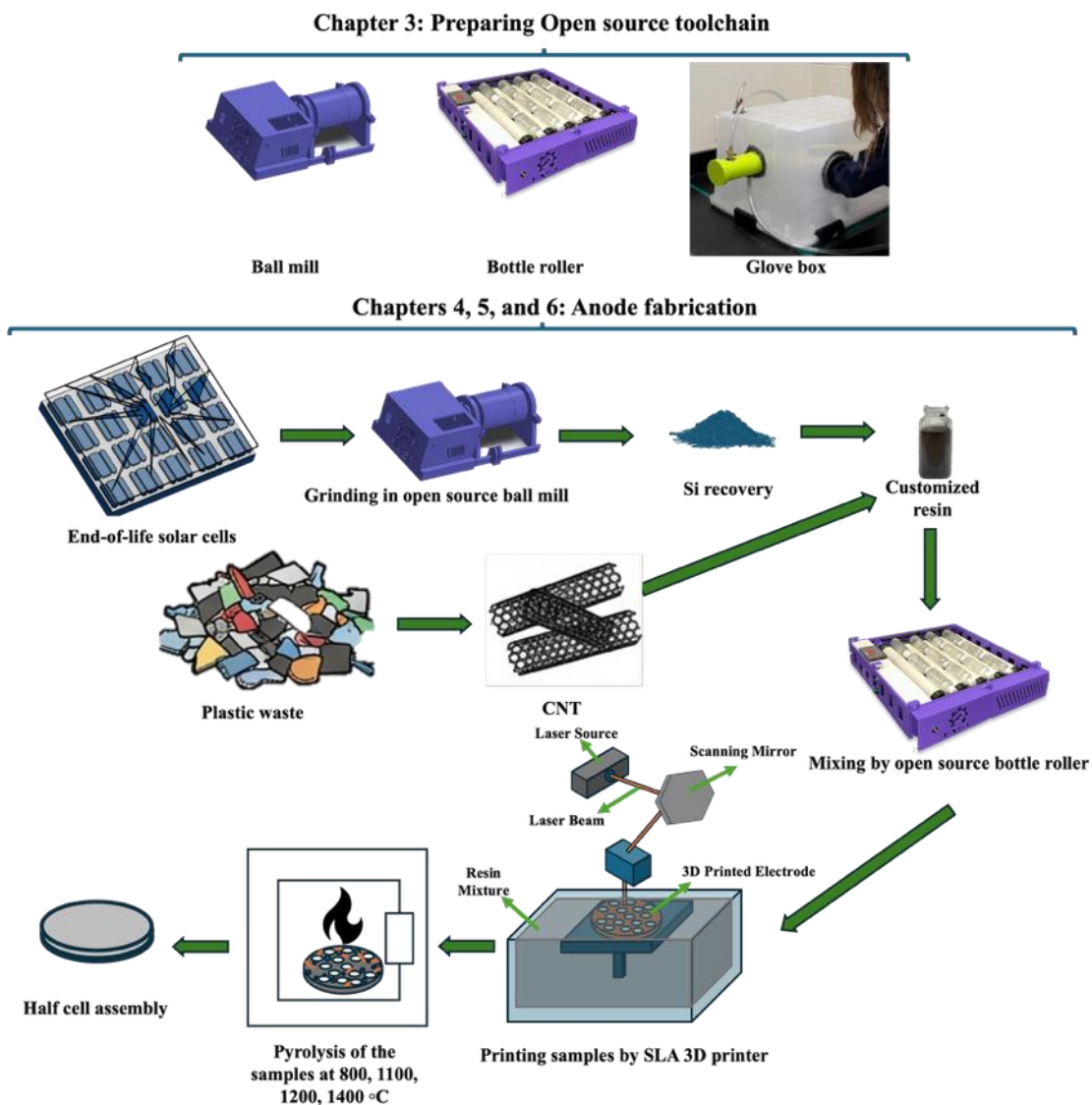


Figure 1-1. Graphical abstract

1.3 Thesis Outline

This thesis is organized into six research Chapters (Chapters 2–7). Each Chapter builds on the previous, to establish a comprehensive understanding of sustainable SLA-printed silicon–carbon anodes derived from recycled materials.

1.3.1 Chapter 2 - Literature Review: 3D Printing Batteries

Chapter 2 provides a comprehensive review of additive manufacturing for batteries. This Chapter establishes the technical and conceptual foundation for developing 3D-printed batteries.

1.3.2 Chapter 3 - Open-Source Hardware for Sustainable Battery Fabrication

Chapter 3 introduces the open-source toolchain developed and validated in this research, including a solar-powered ball mill, scientific bottle roller, and inert-gas glove box. Each tool is designed for low-cost material processing and safe handling of PV-derived silicon and resin formulations. The contribution lies in enabling scalable, accessible, and reproducible material fabrication outside traditional high-cost laboratories.

1.3.3 Chapter 4 - Recycling Silicon Photovoltaic Cells into Silicon Anodes for Li-ion Batteries Using 3D Printing

Chapter 4 presents the first integration of recycled PV silicon into SLA-printable resins and demonstrates the successful fabrication and electrochemical testing of 3D-printed silicon–carbon anodes. This work establishes the baseline performance of recycled-silicon anodes.

1.3.4 Chapter 5 - Effect of Pyrolysis Temperature on Silicon–Carbon Composite Anodes

Chapter 5 systematically investigates the impact of pyrolysis temperature (800–1200 °C) on the phase evolution, carbon structure, electrical conductivity, and cycling stability of printed anodes. It identifies the temperature-dependent trade-offs between carbon ordering, silicon retention, SiC formation, and electrochemical behaviour.

1.3.5 Chapter 6 - Upcycling Post-Consumer Plastic and Waste Silicon Photovoltaic Cells into Carbon-Enhanced Silicon Anodes for Li-ion Batteries Using 3D Printing

Chapter 6 expands the sustainability framework by incorporating CNTs synthesized from plastic-waste-derived hydrocarbons. The Chapter evaluates their impact on electrical conductivity, mechanical stability, activation behaviour, and cycling performance. It demonstrates how PV silicon and plastic-derived CNTs waste upcycling can produce anodes through a simple, low-cost, additive-manufacturing-based process.

1.3.6 Chapter 7 - Limitations, Future Directions, and Conclusions

Chapter 7 merges findings across all studies and outlines main limitations and future research pathways.

1.4 Contribution of the Thesis

This thesis makes the following key contributions to sustainable energy-storage research:

- Development of the first open-source toolchain for low-cost, decentralized processing of recycled photovoltaic silicon and resin-based battery materials (including milling, mixing, glove-box for materials processing)
- Demonstration of the first SLA-printable photocurable resin formulation containing PV-silicon and CNTs as solid load

- First demonstration and proof of concept of SLA-printed silicon–carbon anodes fabricated from recycled photovoltaic silicon.
- Investigation of the effect of pyrolysis temperature (800–1200 °C) on electrical conductivity, phase evolution, SiC suppression, and battery performance.
- Integration of CNTs synthesized from plastic-waste-derived hydrocarbons, and providing the first dual-upcycling pathway (PV silicon + plastic waste) that improves electrochemical performance.

Together, these contributions bridge materials science, additive manufacturing, sustainability, and open-source engineering and provides a practical and environmentally responsible pathway for advancing lithium-ion battery technology.

Chapter 2

2 Literature review

To stabilize the climate, large-scale transition is needed to non-carbon-emitting renewable energy technologies like wind and solar energy. Although these renewable energy sources are now lower cost than fossil fuels, their inherent intermittency makes them unable to supply a constant load without storage. To address these challenges, rechargeable electric batteries are currently the most promising option; however, their high capital costs limit current deployment velocities. To both reduce the cost as well as improve performance, 3D printing technology has emerged as a promising solution. This literature review provides state-of-the-art enhancements of battery properties with 3D printing, including efficiency, mechanical stability, energy and power density, customizability and sizing, production process efficiency, material conservation, and environmental sustainability as well as the progress in solid-state batteries. The principles, advantages, limitations, and recent advancements associated with the most common types of 3D printing are reviewed focusing on their contributions to the battery field. 3D printing battery components as well as full batteries offer design flexibility, geometric freedom, and material flexibility, reduce pack weight, minimize material waste, increase the range of applications, and have the potential to reduce costs. As 3D printing technologies become more accessible, the prospect of cost-effective production for customized batteries is extremely promising.

2.1 Introduction

Global climate change, caused by greenhouse gas emissions from conventional power generation from coal, natural gas, and oil, contributing 18%, 40%, and 1% to global electricity production in 2022, poses a concern [5]. This increases negative impacts on human health [6–8], reduces agricultural productivity [9], and has economic [10–12] consequences. One approach to eliminating the need for fossil fuel electric generation is to replace it with renewable sources to address these challenges [13]. Among the array of renewable energy (RE) options, wind, and solar energy are among the most important due to their widespread availability and abundance [14]. Although these RE sources

contributed approximately 11.88% to global energy production in 2022, predictions indicate they could supply up to 50% of the world's electricity demand by 2050 [15,16]. Nonetheless, the inherent intermittency and variability of wind and solar resources make them unable to supply a constant load without storage [17–23]. To address these challenges, various energy storage solutions have been explored, with rechargeable electric batteries emerging as a highly promising option [24]. In addition, with the record growth in electric vehicles (EVs), there is a potential for EV charging to add to stability with a high penetration level RE grid [25]. One of the drawbacks of rechargeable electric batteries is their high cost, and a crucial factor influencing battery production costs is the manufacturing process [26]. In this context, 3D printing technology has emerged as a promising solution to address cost concerns associated with battery production, offering a layer-by-layer approach, which has already been shown to reduce costs for a wide array of products including those used to conduct battery research such as an open-source ball mill [27], open-source bottle roller [28], sample shaker [29], sample stirrer [30], and numerous additional broader applications [31–33]. Utilizing 3D printing in battery fabrication enhances performance, increases design flexibility, reduces pack weight, minimizes material waste, and shortens production time, ultimately leading to cost reductions [31]. Recognizing the enormous potential significance of 3D printing in battery production, this section provides a detailed review of the most promising 3D printing methods employed in this context. First, to provide background, the types and geometries of batteries (See Appendix A.2) will be summarized. Then, the literature review will focus on enhancing battery properties with 3D printing, including efficiency, mechanical stability, energy and power density, customizability and sizing, production process efficiency, material conservation and environmental sustainability, and solid-state batteries (See Appendix A.1). Finally, the principles, advantages, limitations, and recent advancements associated with the most common types of 3D printing (direct ink writing (DIW), fused filament fabrication (FFF), inkjet printing (IJP), and stereolithography (SLA)) will be reviewed, focusing on their contributions to the field of energy storage. This work will be synthesized and discussed, and conclusions will be drawn on the impact of 3D printing on the electric battery technologies able to back up intermittent renewable energy for the future of a sustainable electric system.

2.2 Background

2.2.1 Basic Geometries

Conventional production techniques such as coating operations [33] and screen printing [34] have been extensively employed in the industry to fabricate batteries. These methods offer scalability and reliability but often lack flexibility in design and customization. In contrast, the emerging technologies of 3D printing offer design freedom [31], which leads to customization for specific applications [35,36] and the fabrication of novel and complex structures [37] that were not possible to manufacture through conventional methods and improve the overall performance and efficiency of the batteries. Furthermore, while conventional techniques may excel in terms of established processes and large-scale production capabilities [38], 3D printing offers advantages in rapid prototyping [39] and on-demand manufacturing [40,41].

The geometry of battery electrodes plays a key role in determining both battery application and performance [31,42]. The two fundamental figures of merit for batteries are energy density and power density. Increasing the energy density, however, can negatively impact power density. This occurs due to the longer transport distance for ions within the battery structure, ultimately impeding the rate of energy delivery [43]. Consequently, the manipulation of battery geometry can create a balance between power density and energy density. Battery geometries are shaped by their component architecture, including designs such as thin film [44], 3D porous structure [45], and fiber designs [46]. As these component architectures come together, they result in various battery cell configurations such as sandwich, in-plane, concentric tube, and fiber arrangements. Among these, thin film structures and porous frameworks (grids) stand out as the most common and important forms [31].

2.2.1.1 Thin Film

The thin film structure is one of the most widely recognized configurations that is readily available in the market and can be fabricated through conventional methods [47]. It is made of rectangular electrodes stacked on top of each other; this can improve the performance

through surface area [48]. This structure offers a notable advantage through reduced resistance and a shorter Li⁺ diffusion length, contributing to an increase in power density [49]. In contrast, the energy density within this configuration is comparatively lower than in other structures. This arises from the limited active content that can be accommodated in a thin film and further modifications are required to enhance the overall energy density [50].

2.2.1.2 3D Porous Structure

The porous structure represents an innovative geometry that can be effectively fabricated using techniques such as 3D printing, in contrast to traditional methods, which often struggle to control intricate geometric structures. Creating pores in various scales in the structure and increasing electrode thickness facilitate ion transport within the structure, which is beneficial to balancing energy and power density. An additional advantage of this design lies in its capacity for electrolyte penetration, enhancing the involvement of ions in electrochemical reactions and improving the battery performance [51–60].

2.2.2 Impact of 3D Printing on Battery Performance

The advantages that 3D printing provides for battery fabrication include the ability to achieve high-resolution designs [61], ensuring mechanical stability [62], optimizing energy density and power density [62], customizing battery structures for specific applications [63], accommodating a wide range of battery sizes [64], having the fabrication processes with fewer steps and shorter production times [62], enabling rapid fabrication [65], the ability to create all-solid-state batteries [66], and the ability to fabricate and prototype the batteries with novel materials [61]. Moreover, 3D printing in the context of batteries minimizes material wastage, which is beneficial for environmental sustainability [67].

2.2.2.1 High resolution and mechanical stability

The advent of 3D printing technology has revolutionized the precision and resolution of battery designs, which directly affects the energy and power density and the overall battery performance [68–73]. Furthermore, the ability to fabricate high-resolution geometries through 3D printing results in enhanced mechanical stability [71]. Engineering designs at

the microscopic scale make it possible to control the battery structure precisely, ensuring enhanced mechanical performance. Battery properties, particularly during electrochemical reactions when components undergo changes that can impact structural integrity, benefit from mechanical stability [74]. With 3D printing advantages of high resolution, the risk of electrode breakage and battery failure due to structural instability is eliminated, increasing the overall reliability of the battery [75].

2.2.2.2 Energy density and power density

3D printing with the ability to control the design makes it possible to increase active material loading inside the structure with less volume, which results in higher energy density [76–78]. On the other hand, 3D printing's ability to finely control the geometry of battery components plays a critical role in elevating the energy transfer rate within the structure, ultimately resulting in higher power density [79–81].

2.2.2.3 Customizability and size

One of the advantages of 3D printing is the design control, which leads to the customizability of the structure. Furthermore, depending on the method and the device resolution, the size can be controlled and the part can be fabricated in a wide range of scales for the production of miniaturized batteries [35,36].

2.2.2.4 Efficient production process

In contrast to the conventional method, which consists of multiple steps including slurry preparation, tape casting, material drying, calendaring, material cutting, assembly, electrolyte filling, and final packaging, 3D printing offers notable efficiency. In the 3D printing process, the steps include material preparation, part geometry design, 3D printing, assembly, and optional electrolyte filling, depending on the chosen 3D printing method [82–85]. One of the advantages of 3D printing in battery production is the potential reduction in fabrication time, which is attributed to the straightforward process with fewer steps. Nevertheless, it is crucial to note that the overall fabrication time depends on the specific method employed and any post-treatment requirements [32].

2.2.2.5 Minimized material wastage and environmental sustainability

The computer-driven design and fabrication of batteries using 3D printing minimizes material wastage [86], thus lowering production costs [87] and promoting environmental sustainability [31].

2.2.2.6 Ability to fabricate all-solid-state batteries

Solid-state batteries, utilizing solid electrolytes instead of liquid counterparts, offer high dimensional integrity, excellent mechanical properties, and enhanced safety [88]. 3D printing, with its precision and design control, facilitates the engineering and fabrication of solid-state electrolytes compatible with electrode configurations, which results in all-solid-state batteries through which all the components can be printed on top of each other. This approach eliminates the need for glove boxes, making production more cost-efficient and environmentally friendly [89–92].

2.2.2.7 Ability to fabricate batteries with novel materials

One of the key advantages of 3D printing is its ability to fabricate battery components using novel materials [93]. For instance, the performance of the metal–organic frameworks (MOFs) with carboxyl functionalized channels, which have been proven as extraordinary bi-functional materials usable in both lithium and zinc batteries [94], can be improved further using 3D printing by controlling the design and structure (e.g., 3D printing provides geometric design freedom) [95]. This unique ability enables researchers to explore cutting-edge materials in battery architectures with high precision which not only facilitates rapid prototyping but also opens up possibilities for developing next-generation energy storage solutions that take advantage of the innovative materials [61].

2.2.3 Goals of Geometric Design for Batteries

Specific designs in batteries can solve many scientific or engineering issues and provide the battery with the opportunity to improve the overall performance in specific applications. The main purpose of controlling the design of batteries is to improve the most important properties, including energy density, power density, cycle life, and safety.

2.2.3.1 Energy density and power density

The design helps the user to fabricate the battery component based on the mechanical configuration of the device which makes it possible to customize the shape and size of the battery. With design freedom, batteries can be fabricated with complicated integration and controlled distance between the components to receive the best properties of the battery. The 3D-printed electrodes facilitate ion transfer, which results in high energy density and high power density [31,96,97].

2.2.3.2 Cycle life and safety

The arrangement of electrodes and the distribution of active materials impact uniform charge and discharge cycles, thus affecting cycle life [98]. Additionally, the geometry can improve thermal management, preventing overheating and enhancing safety [99]. Moreover, proper separator and electrolyte design, as well as internal pressure management mechanisms, contribute to safety and longevity [77,100].

2.3 Review

In recent years, 3D printing technology has emerged as a groundbreaking approach for the fabrication of batteries, offering advantages in terms of design flexibility, customization, and rapid prototyping. Various 3D printing methods with their unique characteristics and potential applications have been explored for battery manufacturing. This literature review aims to introduce four of the most promising 3D printing methods for battery fabrication: direct ink writing (DIW), fused filament fabrication (FFF), inkjet printing (IJP), and stereolithography (SLA) (Figure 2-1). First, the principles, advantages, and limitations will be examined and then recent advancements associated with these techniques will be discussed, revealing their contributions to the field of energy storage.

2.3.1 Direct Ink Writing

DIW is a 3D printing technique employed in battery fabrication, relying on the precise extrusion of inks or pastes through a nozzle to create an integrated three-dimensional structure. In DIW for battery manufacturing, the ink typically comprises active materials,

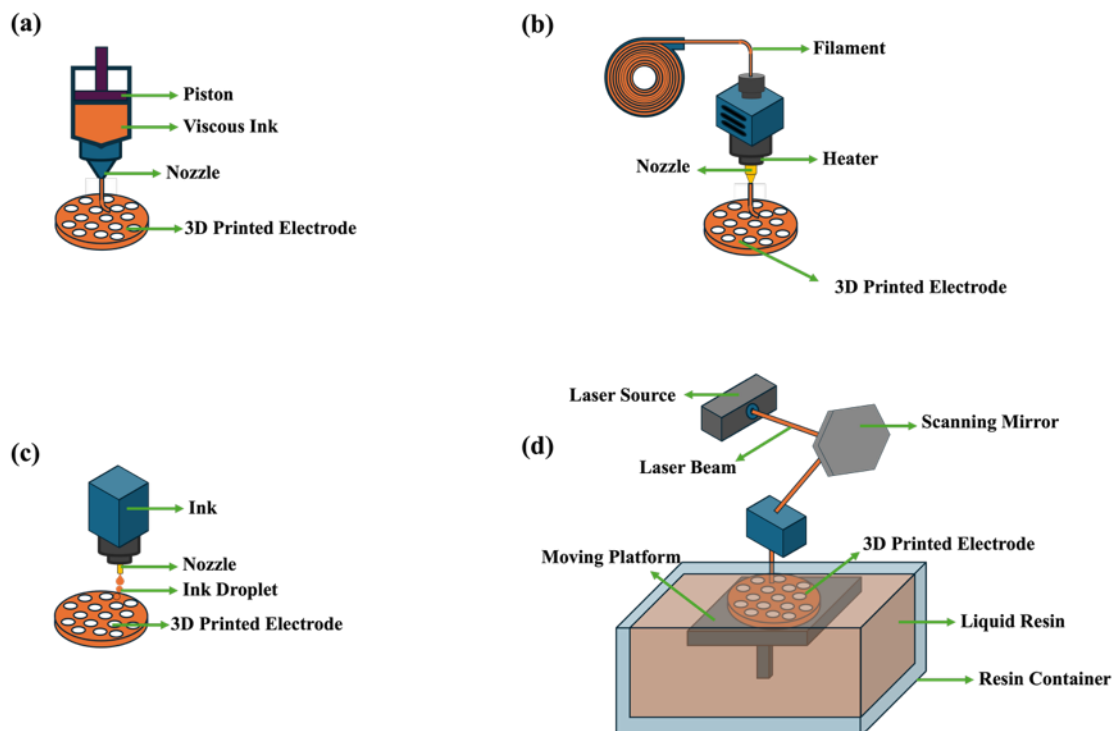


Figure 2-1. Illustrations of (a) DIW, (b) FFF, (c) IJP, and (d) SLA

conductive materials, binders, and solvents. The extrusion process is characterized by high controllability governed by parameters such as pressure, speed, and nozzle size, allowing for the precise positioning of materials [101–103].

One of its features is the resolution it offers over the creation of complex structures and well-aligned lattice designs, which are advantageous for achieving high porosity and facilitating ion transport in energy storage devices with the least material wastage. The resolution of 3D structures printed using DIW is determined by factors such as nozzle diameter, applied pressure, and ink characteristics, typically ranging from 1 to 250 μm [101,103–105]. Furthermore, compared to other 3D printing methods, DIW can be a more affordable choice, making it accessible to a broader range of applications. Moreover, this method is known for its ease of fabrication and typically requires minimal or no post-production treatment [106]. Another key advantage of DIW is the flexibility in material selection, allowing for the use of a wide range of printing feedstocks including metals, ceramics, polymers, and composites, which empowers the users to select materials that align with the specific applications [103,107]. Moreover, this method has the advantage of

printing multi-material structures through the use of multi-nozzle printers or by employing a print–pause–print strategy and swapping syringes containing different materials [108–112].

One of the challenges of DIW is the need for specific techniques to prepare desirable ink formulations. The ink must exhibit viscoelastic and shear-thinning properties to resist gravity-induced deformation and capillary forces during the printing process. The selection of materials and their rheological properties directly influence the quality of the final printed components, contributing to the time-consuming nature of the method [113]. Another limitation lies in the mechanical properties of DIW-fabricated structures. While DIW has precision and customization, the resulting printed components may exhibit poor mechanical properties compared to conventionally manufactured batteries [114].

2.3.1.1 Some examples of DIW of batteries

The study by He et al. focused on the multi-layer biscuit structure feature in the development of a 3D graphite at graphite/silicon oxide (Gt@GS) electrode with high loading using direct ink writing technology. They achieved a remarkable reversible capacity of 3.52 mAh cm^{-2} at 3.6 mA cm^{-2} after 120 cycles. Comparisons between Gt@GS and GS electrodes revealed improved cycling performance and reversible capacity for Gt@GS, with a discharge capacity of 9.28 mAh cm^{-2} after 50 cycles. Cycling performance analysis further demonstrated remarkable reversible capacities for Gt@GS even after 120 cycles, attributed to the dampening effect of Gt layers on Si volume expansion. EIS analysis of 3D Gt@GS electrodes indicated reduced charge transfer resistance, which indicates enhanced ion diffusion facilitated by the 3D structure. Additionally, optical microscopy results highlighted significant thickness changes and cracks in grids of 3D GS electrodes after the first discharge, whereas 3D Gt@GS electrodes exhibited minimal thickness changes and deformation [115].

Li et al. used the advantages of DIW to develop a highly conductive reduced graphene oxide (rGO) with Super-P (rGO-P) aerogel composite anode with a high resolution and complex hierarchically porous structure. The optimized rGO-P aerogel electrode demonstrated a superior initial discharge capacity of 848.4 mA h at 80 mA cm^{-2} , a 14.9%

improvement over traditional graphite electrodes with 61.8% capacity retention over 100 cycles. Additionally, the Coulombic efficiency was higher than 95% over 100 cycles. The rGO structure after 3D printing exhibited integrated macroscale and microscale porous structures with wrinkled sheets, which shows the precise control and design flexibility of the parts made using 3D printing. These structures provide active sites for electrochemical reactions. Furthermore, the rGO-P, with decreased oxygen content, left abundant defect sites that can provide paths for vanadium ion transformation. Moreover, the rGO-P composite has a significantly larger specific surface area which offers ample sites for vanadium ions. Charge–discharge tests showed the superior performance of rGO-P compared to conventional ones, which is attributed to enhanced conductivity, increased reaction sites, and improved mass transfer facilitated by the porous structure [116].

In another study, Zhu et al. fabricated high-resolution metallic 3D Zn electrode structures using DIW. These designs with submillimeter sizes exhibited low electrical resistivity and high mechanical stability. Mechanical testing revealed that the strengths of 3D-printed Zn lattices are comparable to those of Zn foams produced using conventional methods. The results showed that the cell operated over 50 cycles at high discharge rates of 25 mA cm^{-2} and achieved an average specific capacity of $214.85 \text{ mAh g}^{-1}$, which was the highest amount achieved compared to similar electrodes fabricated using other methods. Moreover, capacity retention over 50 cycles was 108% and an average Coulombic efficiency of approximately 87% was achieved. Furthermore, with a cumulative capacity of 7.8 Ah cm^{-2} achieved at a high rate of 25 mA cm^{-2} , this 3D Zn anode offers superior performance compared to the conventional Ni–Zn anodes, which validates the practicality of metallic 3D Zn electrode for high-density alkaline cells [117].

Liu et al. developed $\text{Li}_{1.3}\text{Al}_{0.3}\text{Ti}_{1.7}(\text{PO}_4)_3$ (LATP) electrolyte for solid-state electrolytes in lithium batteries using DIW with post-heat treatment to enhance ceramic density, completing the formation of the final LATP solid-state electrolyte structures. They shaped these materials into various forms. Microcracks were observed between layers in the 3D-printed parts; this has a positive impact on ionic conductivity. Moreover, the sintering temperatures influenced the grain size and densification of the samples. In this regard, $1050 \text{ }^\circ\text{C}$ resulted in a glass state due to lithium volatilization, which affects ionic conductivity.

The final parts maintained a high ionic conductivity of $4.24 \times 10^{-4} \text{ S cm}^{-1}$, which is higher than the ones prepared using other methods ($2.05 \times 10^{-4} \text{ S cm}^{-1}$). Through this process, the solid-state battery exhibited a high discharge capacity of 150 mAh g^{-1} at 0.5 C , along with 84% capacity retention with an average Coulombic efficiency of approximately 100% over 100 cycles [118].

Tao et al. employed DIW to fabricate high-capacity 3D-printed $\text{LiNi}_{0.8}\text{Mn}_{0.1}\text{Co}_{0.1}\text{O}_2$ (NMC) cathodes. Through 3D printing, a crack-free network of NMC particles embedded in conductive carbon black, which was homogeneously distributed within the electrodes, was created. This alleviates binder migration issues and ensures improved electrochemical kinetics and long-term cyclability in high-loading electrodes. The results also showed the reduction in Warburg diffusion impedance which indicates enhanced Li^+ diffusion that was facilitated by the shortened diffusion pathway. The specific discharge capacities for the 1st and 800th cycles were measured at 178.6 and 107.5 mAh g^{-1} , respectively, showing capacity retention of 60.2% over the entire 800 cycles with an average Coulombic efficiency of approximately 99.9% at a current density of 1 C . These results were superior compared to those achieved using conventional methods, which were equal to 162.3 mAh g^{-1} in the 1st cycle and 88.3 mAh g^{-1} , which showed a capacity retention of 54.4%, in the 800th cycle. Notably, the free space in the electrodes that were created through 3D printing has the ability to buffer mechanical stress for long-term cyclability. As the results showed, this innovative approach increased the contact area, shortened diffusion paths, and reduced stress, leading to improvement in battery efficiency compared to conventional full cells [119].

Li et al. used DIW to fabricate a square grid electrode structure for lithium-ion batteries. The ink was prepared by combining LiFePO_4 (LFP), multi-walled carbon nanotubes (MWCNTs), and Polyvinylidene fluoride (PVDF) powder, forming a homogenized paste with *n*-methyl-2-pyrrolidone (NMP) as a solvent. Through 3D printing, a cross-linked network structure, which promoted the efficient transmission of electrons and ions, was formed. This structure also contributed to the uniform formation of the solid electrolyte interface (SEI) film and ensured good contact between the electrode and electrolyte. Conversely, the samples prepared through coating lacked this network structure, which

hindered particle connectivity. The electrochemical results demonstrated an initial discharge capacity of $143.2 \text{ mA h g}^{-1}$ at 0.5 C , aligning with the theoretical specific capacity of 170 mA h g^{-1} . Moreover, the specific charge and discharge capacities remained stable, remaining at approximately 150 mA h g^{-1} even after 100 cycles at 0.5 C , showing capacity retention of 105%. Furthermore, the Coulombic efficiency was around 99.9% over 500 cycles at 5 C [120].

Rasul et al. utilized DIW to embed highly aligned boron nitride (BN) nanosheets into PVdF polymer composite electrolytes (CPEs) with complex structures (Figure 2-2a). The achieved ionic conductivity was $6.74 \times 10^{-4} \text{ S cm}^{-1}$. The initial charge capacity of the cells prepared with CPE-BN was 156 mAh g^{-1} , which was comparable to the theoretical capacity of 165 mAh g^{-1} . The cell exhibited a consistent discharge capacity of 132 mAh g^{-1} over 130 cycles at a 1 C rate (140 mA g^{-1}) and a capacity retention of 90% after 250 cycles. These results are attributed to enhanced dendritic lithium suppression, which is facilitated by aligned BN nanosheets. Additionally, another advantage of the aligned BN is minimizing hotspot formation, resulting in the thermal safety of the battery. The symmetric redox peaks indicated reversible Li^+ ions intercalation and deintercalation which validated successful Li^+ ion transport through the electrolytes. From a materials perspective, CPE-BN inks were synthesized using 0.5 wt% silane-functionalized BN nanosheets that enhanced mechanical, thermal, and electrochemical properties. The silane coupling agent improved the polymer–BN interface, which led to superior thermal conductivity and optimum ionic conductivity. Furthermore, the chain entanglement and molecular interactions between BN nanosheets and the PVdF matrix improved the mechanical properties of the electrolyte while maintaining ductility [121].

Liu et al. utilized DIW for fabricating a comb-like structure of $\text{SiO}@C/\text{graphite}$ anode and LFP cathode for lithium-ion batteries. The anode ink consisted of $\text{SiO}/\text{graphite}$, CNT, and a binder with a weight ratio of 70:20:10 and a solid content of 40% to optimize viscosity. The addition of CNT improved battery efficiency by enhancing the conductive network. Notably, the printed parts exhibited wider line widths and thicknesses than intended due to material expansion during printing. Viscosity analysis revealed shear-thinning behavior, with the 40% solid content ink deemed optimal. The porosity was 60%, facilitating

electrolyte infiltration. Results showed that smaller nozzle tips and increased mass loading resulted in higher areal capacity. Additionally, cyclic voltammetry indicated lithium reacting with SiO to form lithium silicate and Li₂O, acting as a volume buffer. The conventional electrodes initially boast a capacity of 517 mAh g⁻¹, whereas the 3D printed counterparts exhibit a slightly lower initial capacity of 485 mAh g⁻¹. SEM analysis suggests that some Si particles within the structure do not actively engage in the reaction; these are referred to as dead Li. Despite exhibiting lower initial capacity compared to conventional electrodes, the 3D printed electrodes demonstrated a capacity retention of 68.2% after 80 cycles, with the initial Coulombic efficiency improving from 70% to 100% after the first few cycles [122].

Rocha et al. 3D-printed reduced carbon-modified graphene (rCMG) as a self-standing binder-free anode onto a 3D-printed copper current collector using Pluronic F127 polymer. Pluronic F127, known for its thermoresponsive properties, forms a hydrogel when mixed with water, which facilitates the incorporation of active components. The viscosity of the ink can be controlled by temperature. The results demonstrated that rCMG-Pluronic F127 samples exhibited comparable elastic-brittle behavior and electrical conductivity ($90 \pm 20 \text{ S m}^{-1}$) to those produced with other rCMG-derived aerogels. Additionally, these samples showed lower total impedance, indicating improved contact between the rCMG electrode and the copper current collector, as well as enhanced electrolyte diffusion and penetration into the electrode pores, which were facilitated by printing both components together. Moreover, the electrochemical results showed that the device retained 80% capacitance after 10,000 cycles at 15 A g⁻¹. They showed the potential of multi-material printing in energy applications, including lithium-ion batteries and supercapacitors [123].

Table 2-1 provides a summary and comparison of the electrochemical performance achieved through the direct ink writing method for batteries. As evident from the results in Table 2-1, this technique is versatile, which proves its applicability to enhancing battery efficiency in the fabrication of different battery components, including anode, cathode, and solid electrolytes. In Table 2-2, the fundamental materials employed for ink preparation, alongside the viscosity range observed across various shear rates, are shown. As can be seen, a conventional post-printing drying process is necessary to eliminate residual

solvents. In some cases, such as [117], additional heat treatments are applied to the printed component for further structural modifications. Figure 2-2b illustrates the capacity retention of these cells. As can be seen, high-capacity retentions, even exceeding 100%, can be achieved through the fabrication of battery components using this method. This is promising for fabricating high-performance battery cells with a long cycle life.

Table 2-1. Summary and comparison of electrochemical performance of DIW of batteries.

Printed Component	Electrochemical System	Discharge Capacity	Coulombic Efficiency	Cycle Numbers	Application	Ref.
Anode: rGO/Super-P aerogel	Anolyte: $1.6 \text{ mol L}^{-1} \text{V}^{3+} + 4 \text{ mol L}^{-1} \text{H}_2\text{SO}_4$ Catholyte: $1.6 \text{ mol L}^{-1} \text{VO}^{2+} + 4 \text{ mol L}^{-1} \text{H}_2\text{SO}_4$ Membrane: Nafion 117	848.4 mA h at 80 mA cm^{-2}	More than 95%	100	Vanadium redox flow battery	[116]
Anode: metallic Zn	Cathode: NiOOH Electrolyte (gel): Alkaline polyacrylate Separator: Celgard 5150	$214.85 \text{ mAh g}^{-1}$ at 25 mA cm^{-2}	87%	650	Rechargeable alkaline batteries	[117]
Electrolyte: LATP	Li/3D printed LATP CSSE/Li symmetric cell	150 mAh g^{-1} at 0.5 C	100%	100	All-solid-state lithium batteries	[118]
Cathode: NMC	Counter electrode: Lithium foil Electrolyte: LFP in ethylene carbonate:ethylmethyl carbonate (EC:EMC) (3:7 wt%) (Gen II) Separator: Celgard 2325	107.5 mAh g^{-1} at a current density of 1 C	99.9%	800	Lithium-ion batteries	[119]
Cathode: LFP	Counter electrode: Metal Li Separator: Glass fiber Electrolyte: 1 M LFP dissolved in a mixture of EC and dimethyl carbonate (DMC)	150 mA h g^{-1} at 0.5 C	99.9%	100–500	Lithium-ion batteries	[120]
Electrolyte: BN-PVDF	Cathode: LFP Anode: Li metal	132 mAh g^{-1} at 1C rate	N/A	130	Lithium-Metal Batteries	[121]
Anode: SiO@C/graphite Cathode: LFP	Electrolyte 1 M LFP dissolved in a mixture of EC and DMC plus a 2% solution of fluoroethylene carbonate (FEC)	75 mAh g^{-1} at 0.3 C	100%	40	Lithium-ion batteries	[122]
Anode: rCMG/Pluronic F127 Current collector: Copper/Pluronic F127	Counter electrode: silver wire Reference electrode: Ag/AgCl (3 M NaCl) Electrolyte: 1-ethyl-3-methylimidazolium bis(trifluoromethylsulfonyl)imide	N/A	N/A	10,000	Lithium-ion batteries, Supercapacitors	[123]

Table 2-2. Key parameters for the DIW process.

Ink Formulation	Printing Parameters	Fabrication Steps	Design	Ref.
<p>Active material: GO aerogel, Super-P</p> <p>Crosslinking agent: CaCl₂ solution</p> <p>Ink viscosity: 10⁷–10⁴ Pa·s viscosity at 10⁻¹–10² s⁻¹ shear rates</p>	<p>Printing height: 1.4 mm</p> <p>Printing speed: 5 mm/s</p> <p>External diameter: 1.79 mm</p> <p>Inner diameter: 1.24 mm</p>	<p>Ink preparation, 3D printing, freeze-drying at -20 °C for 40 h, drying at 60 °C for 12 h</p>	<p>Layer-by-layer serpentine path</p>	[116]
<p>Active material: Zn powder</p> <p>Binder: Poly(methyl methacrylate)-poly(acrylate)-poly(methyl methacrylate) (PMMA-PA-PMMA) pellets</p> <p>Solvent: Tetrahydrofuran (THF) (2-butoxyethanol) and EGBE</p> <p>Ink viscosity: 10³–10⁰ (30% of Zn), 10⁴–10¹ (55% of Zn) and 10⁵–10² (70% of Zn) Pa·s viscosity at 10⁻²–10² s⁻¹ shear rates</p>	N/A	<p>Ink preparation, 3D printing, drying at 80 °C for 2 h, annealing at 600 °C for 20 min</p>	Honeycomb structure	[117]
<p>Active material: LATP powder</p> <p>Solvent: DI water and IPA</p> <p>Ink viscosity: 5 × 10⁵–5 × 10⁴ Pa·s viscosity at 5–10² s⁻¹ shear rates</p>	<p>Nozzle inner diameter: ~330 μm</p> <p>Printing layers: 3–6 layers</p>	<p>Ink preparation, 3D printing, freeze-drying for 12 h at -50 °C, sintering from 650 to 1050 °C</p>	Random designs	[118]
<p>Active material: NMC, conductive carbon black</p> <p>Binder: Polyvinylidene fluoride</p> <p>Solvent: NMP</p> <p>Ink viscosity: 5 × 10² Pa·s viscosity at 10⁻¹ s⁻¹ shear rates</p>	<p>Needle size: 210 μm</p> <p>Printer bed material: aluminum foil</p> <p>Layer height: 20 μm</p> <p>Printing layers: 20 layers</p> <p>Printing temperature: 60 °C</p>	<p>Ink preparation, 3D printing, drying at 100 °C</p>	<p>Layer-by-layer serpentine path</p>	[119]
<p>Active material: LFP, MWCNT</p> <p>Binder: PVDF powder</p> <p>Solvent: NMP</p>	<p>Ink volume: 3 mL</p> <p>Nozzle inner diameter: 330 μm</p> <p>Extrusion pressure: 2.5–5 MPa</p>	<p>Ink preparation, 3D printing, freeze-drying for 12 h</p>	<p>Layer-by-layer serpentine path</p>	[120]

	Printing speed: 400 $\mu\text{m s}^{-1}$ Layer height: 0.15–0.25 mm			
Active material: BN nanosheet, lithium bis(trifluoromethanesulfonyl)imide (LiTFSI), and N-Propyl-N-methylpyrrolidinium bis(trifluoromethanesulfonyl)imide (Pyr13TFSI) Binder: PVDF powder Solvent: NMP Ink viscosity: 10^3 – 10 Pa·s viscosity at 10^{-1} – 10^2 s^{-1} shear rates	Printer bed material: stainless Steel or cathode substrates Ink storage temperature: 120 $^{\circ}\text{C}$ Nozzle pressure: 7 psi Printing speed: 6 mm s^{-1} Printing temperature: 120 $^{\circ}\text{C}$ Ink thickness: ~ 250 μm Printing temperature: 120 $^{\circ}\text{C}$	Ink preparation, 3D printing	Disc shapes	[121]
Active material: SiO@C/graphite and MWCNTs Binder: styrene-butadiene rubber (SBR), carboxymethyl cellulose (CMC) Solvent: 1,4 dioxane and deionized water Ink viscosity: 10^7 – 10^4 Pa·s viscosity at 10^{-1} – 10^2 s^{-1} shear rates	Nozzle inner diameter 260~610 μm Printing temperature: below -20 $^{\circ}\text{C}$	Ink preparation, 3D printing, vacuum freeze-drying for 12 h	Comb-like designs	[122]
Active material ink 1: Copper Active material ink 2: CMG Solvent: pluronic F127 Ink 1 viscosity: 10^3 Pa·s at 10 s^{-1} shear rate Ink 2 viscosity: 10^2 Pa·s at 10 s^{-1} shear rate	N/A	Ink preparation, 3D printing, freeze-drying for 48 h, heat treatment at 900 $^{\circ}\text{C}$ for 1 h	Layer-by-layer serpentine path for battery, One-leg and two-leg components for supercapacitor	[123]

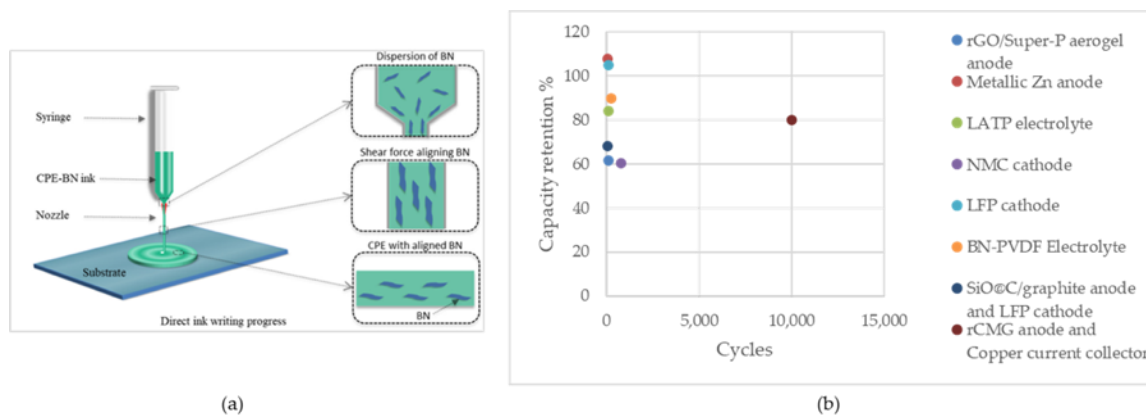


Figure 2-2. (a) Illustration of DIW of aligned BN in electrolyte film. Reprinted/adapted with permission from Ref [121] ; published by ACS, 2022, (b) Capacity retention of the cells fabricated using DIW.

2.3.2 Fused Filament Fabrication

FFF is a widely adopted 3D printing technique, including in the field of battery manufacturing. It is used widely by various manufacturers and open-source 3D printing communities, representing the broader category of 3D printing technologies utilizing melted filament deposition. On the other hand, fused filament modeling (FDM), trademarked by Stratasys, is a proprietary 3D printing technology using FFF associated only with Stratasys machines [124]. This process operates by melting a thermoplastic filament in a heated nozzle. FFF was radically reduced in price and improved performance due to the Open-source self-replicating rapid prototype (RepRap) project and is now the most popular form of 3D printing [125–127]. Within the context of 3D-printed batteries, FFF is employed to produce essential battery components including electrodes, solid state electrolyte, and current collector. For this purpose, FFF offers the capability to integrate conductive materials into the filament, creating conductive pathways within the battery structure [128,129]. FFF is a widely adopted 3D printing technique, including in the field of battery manufacturing. This process operates by melting a thermoplastic filament in a heated nozzle. One of the advantage of FFF 3D printing is that unlike DIW that requires specialized inks, it eliminates the need for ink preparation which simplifies the printing process [36]. Furthermore, its ability to create complex battery designs with the resolution of 50 to 200 μm is a feature that enables the fabrication of battery components that may be challenging to produce using conventional methods [36,130].

FFF generates minimal waste during the printing process which is in alignment with sustainable manufacturing practices [130] and is a mature distributed recycling technology [131–134]. Additionally, the accessibility of FFF along with the user-friendly interface and ease of operation, make it an economical choice for battery production [129,135]. In addition to the low cost, FFF printers are capable of high production rates, suitable for both prototyping and large-scale manufacturing of battery components [136]. Furthermore, FFF is capable of printing multi-material, which enables its ability to print various battery components on top of each other [137,138].

Despite the advantages, FFF of batteries presents its own drawbacks. One of the most important challenges of FFF 3D printing is the material selection to formulate a suitable filament which often leads to difficulties in filament fabrication [31]. The integration of active and conductive particles, necessary to enhance electrochemical performance, can diminish the overall printability of the filament which makes the production process more complex [139]. Moreover, this incorporation can increase the viscosity of the filament which results in the risk of nozzle clogging during the printing operation [140]. Beyond these material-related issues, the printed part has weak mechanical properties in the z-direction due to challenges in ensuring proper layer adhesion [32] and the inherent anisotropy of the process [141]. Furthermore, the printing process can result in components with lower surface quality [32,142].

2.3.2.1 Some examples of FFF of batteries

Beydagh et al. utilized FFF to create 3D printed Si-based electrodes for Li-ion batteries. They fabricated the PLA filament as the polymeric matrix along with carbon-based conductive additives, and Si nanoparticles. The results showed that the Coulombic efficiency progressively increased from 90% in the first cycle to 96% after 10 cycles which remained stable up to 350 cycles. At the 350th cycle, the electrode exhibited a specific capacity of 327 mA h g⁻¹, coupled with capacity retention of 95% at the current density of 20 mA g⁻¹. The cycle stability is due to the flexible structure that preserves mechanical integrity during Si lithiation/de-lithiation. Moreover, carbon-based additives flakes contribute to a conductive porous framework which creates voids that aid electrolyte access and accommodate volumetric expansion during lithiation and maintain electrical

connections during de-lithiation. The resistance results showed that the reduction of the PLA reduces the resistance and enhances electron/ion transport which emphasize the importance of optimizing the ratio of the PLA and active/conductive components [143].

Maurel et al. developed a 3D printable graphite/PLA filament through optimizing the graphite content of the filament along with the plasticizer for lithium-ion battery electrodes. The solvent selection as well as the ratio of the active material, plasticizer and PLA ensure the homogeneous integration of the composite and provide a balance between mechanical properties and printability. Among compositions, the one with the highest amount of conductive additives achieved the initial capacity of 93 mAh g⁻¹ which reached the highest specific capacity of 200 mAh g⁻¹ (215% capacity retention) at the current density of 18.6 mA g⁻¹ (C/20) over 6 cycles. These results were comparable with the theoretical capacity of the active materials. Additionally, 3D printing facilitated the fabrication of a 250 μm-thick anode with remarkable reversible capacity which emphasizes the scalability and adaptability of this approach in battery fabrication [130].

In another work, Maurel et al. produced PLA/LFP as positive electrode and PLA/SiO₂ as the separator for Li-ion batteries (Figure 2-3a). The results showed that the melting temperature of the PLA reduces by adding the active material which affects the printing temperature. Notably, the amount of plasticizer has a positive effect on the solid load as the results showed that the solid load should not exceed 50 vol% with PEGDME500 as a plasticizer and 30% without the plasticizer. The results when PLA/Graphite was used as the negative electrode showed that the composition made of the 10% of the conductive material had the highest specific capacity of 165 mAh g⁻¹ at C/20 over 30 cycles (97% capacity retention) close the theoretical capacity. Furthermore, the infill pattern in 3D printing was set to 70% to enhance the liquid electrode uptake and prevent short circuits caused by lithium dendrite propagation under adverse cycling conditions. Another remarkable finding was that FFF of the entire battery in "one shot" was possible with this technique, which can be further improved by employing a multi-nozzle 3D printing method [144].

Gao et al. improved Aqueous Rechargeable Zinc-Ion Batteries by designing hierarchical core-shell cathodes by integrating the FDM and atomic layer deposition (ALD). In their work, the FFF printed porous carbon network provided an electron-conductive core and ion diffusion channels, while V_2O_5 deposited through the ALD served as an active shell. The results showed that the porous structure of carbon frameworks facilitated the ion diffusion while the amorphous V_2O_5 offers isotropic diffusion pathways and abundant active sites. The high diffusion coefficient in the electrode was further studied through galvanostatic intermittent titration technique (GITT), which exhibited high values, indicating facilitated Zn^{2+} diffusion comparable to conventional pairs. These characteristics resulted in enhanced battery performance, with a specific capacity of 425 mAh g^{-1} at 0.3 A g^{-1} , and 233 mAh g^{-1} at 3 A g^{-1} current density. The capacity at 3 A g^{-1} current density reduces to 183 mAh g^{-1} after 200 cycles and 133 mAh g^{-1} after 800 cycles showing 78.5% and 57.1% capacity retention, respectively. Additionally, the Coulombic efficiency was around 99.9%. The results demonstrate that this method enables the fabrication of binder-free and conductive-additive-free electrodes [145].

Foster et al. utilized a graphene/PLA filament with controllable graphene content, ranging from 1 to 40 wt.% with the optimal load of 15-20% that showed sufficient conductivity as well as mechanical stability. These filaments enabled the creation of 3D printed freestanding anodes with sufficient conductivity and printability which led to the elimination of the need for a copper current collector. The results showed that the initial specific capacity was 500 mAh g^{-1} which reaches to about 100 mAh g^{-1} with the Coulombic efficiency around 99.9% at 40 mA g^{-1} over 200 cycles. Comparing the achieved capacity with the theoretical capacity of graphite (375 mAh g^{-1}) and graphene (744 mAh g^{-1}), it can be concluded that this capacity lies between these two values. It is clear that the 3D printed anode exhibits graphene-like electrochemical performance. One of the key steps in achieving these results was the chemical treatment with NaOH, which improved the amount of porosity in the samples, leading to enhanced electrolyte wetting and improved battery performance [146].

Hu et al. produced TPU-LFP, TPU-LTO (Lithium titanate), TPU-Graphite, and TPU-NCM filaments and printed high-performance cathodes and anodes via FDM (Figure 2-3c). The

easy fabrication of these active filaments, with excellent homogeneity, stability, and mechanical properties, highlight their potential for industrial-scale fabrication for 3D printed lithium-ion batteries. The cells made with TPU-LFP cathode showed the initial capacity of 114.1 mAh g⁻¹ with 99.12% capacity retention (113.1 mAh g⁻¹) with 99.75% Coulombic efficiency after 200 cycles, and 98.9% capacity retention after 400 cycles. Moreover, the cell made by the TPU-LTO anode showed 117.2% capacity retention increasing from 102.4 to 120.0 mAh g⁻¹ with 100.39% Coulombic efficiency over 200 cycles, and 97.94% capacity retention with 99.04% Coulombic efficiency over 270 cycles. Additionally, the full cell assembled by the TPU-LFP cathode and TPU-LTO anode exhibited 97.1% capacity retention at the rate of 0.3 C and a Coulombic efficiency of 97.4% after 50 cycles. The capacity retention in this work is higher compared to the similar ones which is related to the well-integrated mesh structure with pores that facilitate sufficient ionic transport. They also compared the results of the TPU-based electrodes with the PLA-based ones from earlier works which revealed that the PLA-based electrodes exhibited higher internal resistance, and collapsed sooner after cycling due to the weaker mechanical flexibility of this filament which results in irreversible cracks. Consequently, TPU demonstrated more promising results for long-cycling [147].

In another study, Maurel et al. developed a 3D-printable polyethylene oxide/lithium bis(trifluoromethanesulfonyl)imide (PEO/LiTFSI) filament which was designed for use as the electrolyte in lithium-ion batteries. The achieved ionic conductivity was $2.18 \times 10^{-3} \text{ S cm}^{-1}$ at 90°C which shows the capability of FFF in fabricating solid-state electrolytes usable in higher temperature. It is worth mentioning that EIS tests were conducted at three different sample holders; lateral, sandwich and interdigitated-comb. Among them, lateral sample holder exhibited the highest values of conductivity among them which can be attributed to polymer chain orientation along the substrate. Furthermore, the reported conductivity in an interdigitated-comb holder appeared to be lower compared to the commonly employed sandwich holder. The advantage of the interdigitated-comb holder lies in its ability to measure conductivity without requiring precise sample thickness which minimizes potential measurement errors. Due to the poorer mechanical properties of the PEO/LiTFSI filament compared to the pure PEO ones, some modifications should be made, including lowering the printing temperature, replacing the extruder with an open

model for better filament visibility, adding Bondtech Drive Wheels for smoother filament feeding, removing the heatsink to prevent filament buckling, and installing a larger diameter nozzle for improved printing and good homogeneity in the achieved samples (Figure 2-3b) [148].

Reyes et al. 3D printed a hybrid polymer electrolyte using PLA infused with a mixture of EMC, propylene carbonate, and LiClO_4 . They used 3D-printed LTO along with graphene nanoplatelets as the anode, and 3D-printed LMO along with MWCNTs as the cathode. Two sets of experiments were conducted: in the first set, the individual components, electrolyte, anode, and cathode, were printed separately and assembled into a full cell battery. In the second set, the entire full cell was printed in one shot as a fully-printed battery. These cells were then integrated into wearable electronic devices such as LCD sunglasses and LED bangles. Initially, LiPF_6 and LiClO_4 as infused salts in PLA were compared. LiPF_6 showed higher ionic conductivity of 1.7 mS cm^{-1} at 20°C , but it degraded upon exposure to moisture and lost its conductivity. On the other hand, LiClO_4 maintained its mechanical integrity and conductivity of 0.085 mS cm^{-1} at 20°C after exposure to ambient conditions for 24 hours. For the electrodes, graphene was chosen for the LTO anode, while MWCNTs were selected for the LMO cathode to create filaments with desired conductivity and high capacity while maintaining printability. In this regard, the larger LMO particles, as active material in the cathode, can provide more electrical contact points with the MWCNT network. On the other hand, the smaller LTO particles interact better with the graphene network. Moreover, the average discharge capacity of the fully assembled reached 3.91 mAh cm^{-3} at 20 mA g^{-1} with an average Coulombic efficiency of over 88.5% after the first 50 cycles. A single-print battery had a lower capacity (1.16 mAh cm^{-3}) compared to fully assembled batteries (3.91 mAh cm^{-3}), possibly due to an incomplete infusion of components. Despite improvements in Coulombic efficiency, the efficiency remained lower than conventional lithium-ion batteries, possibly due to increased electrical resistivity of the printed electrodes [129].

In their work, Wolf et al. employed indirect 3D printing to fabricate Ti-based electrodes for redox flow batteries with three different ordered unit cells, including the Kenics mixer, the Ross Low-Pressure Drop mixer (RLPD), and the Sulzer mixer (SMX), and compared

these designs to disordered 3D porous electrodes. The fabrication process involved 3D printing of a high impact polystyrene (HIPS) mold, which was then filled with a paste containing 79.4 wt% Ti, 9 wt% epoxy, and 11.6 wt% glycerol. Subsequently, excess materials were removed, and the green body was sintered, and finally coated with graphite to make them electrochemically active. Although the disordered structures had a larger surface area, the results from the ordered 3D structures from this work were either similar or better compared to the disordered structures. The flow rate results showed that the 3D electrodes in this study minimized local concentration depletion which enabled higher current densities by providing clear paths and reducing the formation of gaseous by-products. Moreover, ordered 3D electrodes exhibited similar potentials with stable operation for over 10 hours. Additionally, at an equal flow rate of 100 ml min^{-1} , the pumping power for structured 3D electrodes was two orders of magnitude lower than for the disordered electrode which was attributed to the structured design that creates clear preferential flow paths, reduces pressure losses, and increases mass transport rates [149].

Table 2-3 provides a summary of examples of FFF printed battery components, including anode, cathode, separator, and electrolyte which shows the potential of this method to fabricate all-solid-state batteries. In Table 2-4, the key components for filament preparation along with the printing temperature, fabrication steps, and design considerations are outlined. Notably, the printing temperature is determined by the filament composition and typically requires adjustment to be approximately 15 degrees higher than the melting temperature of the filament composite [130]. Furthermore, 3D printing enables the creation of customized shapes which offers significant benefits for real-world applications. Figure 2-3d illustrates the capacity retention of the FFF printed cells as a function of cycles. As can be seen, the fabricated cells show high-capacity retention.

Table 2-3. Summary and comparison of electrochemical performance for FFF of batteries.

Printed component	Electrochemical system	Discharge Capacity	Coulombic efficiency	Cycle numbers	Application	Ref.
Anode: PLA/Si/graphene	Counter electrode: Metallic lithium Electrolyte: 1 M LPF in DC and EC	327 mA h g ⁻¹ at the current density of 20 mA g ⁻¹	96%	350	Lithium-Ion Battery	[143]
Anode: PLA/Graphite	Counter electrode: Metallic lithium Electrolyte: 1 M LPF in DC and EC	200 mAh g ⁻¹ at the current density of 18.6 mA g ⁻¹ (C/20)	N/A	5	Lithium-Ion Battery	[130]
Cathode: PLA/LFP Separator: PLA/SiO ₂	Counter electrode: Metallic lithium Electrolyte: 1 M LPF in DC and EC	165 mAh ⁻¹ at C/20	N/A	~30	Lithium-Ion Battery	[144]
Cathode: Carbon/ V ₂ O ₅	Electrolyte: 2 M ZnSO ₄ aqueous solution Separator: Glass fiber	183 mAh g ⁻¹ at 3 A g ⁻¹ current density	99.99%	200	Aqueous Zinc-Ion Batteries	[145]
Anode: PLA/Graphene	Counter electrode: Metallic lithium Electrolyte: 1 M LPF in DC and EC	100 mAh g ⁻¹ at 40 mA g ⁻¹	99.9%	200	Lithium-Ion Battery	[146]
Cathode: TPU-LFP	Electrolyte: 1 M LPF in DC and EC Separator: Celgard 3501	113.1 mAh g ⁻¹ at the rate of 0.3 C	99.75%	200	Lithium-Ion Battery	[147]
Anode: TPU-LTO	Electrolyte: 1 M LPF in DC and EC Separator: Celgard 3501	120.0 mAh g ⁻¹ at the rate of 0.3 C	100.39%	200	Lithium-Ion Battery	[147]
Anode: PLA/Graphene/LTO Cathode: PLA/MWCNTs/LMO Electrolyte: PLA/PC:EMC:LiClO ₄	Separator: Polypropylene disk	3.91 mAh cm ⁻³ for assembled-cell and 1.16 mAh cm ⁻³ for the single print cell at 20 mA g ⁻¹	88.5%	50	Lithium-Ion Battery	[129]
Cathode: Ti-based electrode	Anode: zinc plate Separator: Nafion 117 membrane	N/A	N/A	N/A	Redox Flow Battery	[149]

Table 2-4. Key Parameters for FFF Process

Filament formulation	Printing Parameters	Fabrication steps	Design	Ref.
Active material: Carbon black, Silicon, Graphite-based powder Filament substrate: PLA	Filament diameter: 1.75 mm Nozzle diameter: 0.4 mm Nozzle temperature: 210°C Bed temperature: 60°C Printing speed: 40 mm s ⁻¹ Infill density: 100%	Filament preparation using twin-screw extruder, 3D printing	Circular disc	[143]
Active material: Graphite Plasticizer: PC, and poly(ethylene glycol) dimethyl ether Solvent: Dichloromethane (DCM) Filament substrate: PLA	Z-Direction resolution: 0.25 mm Filament diameter: 1.75 mm Nozzle diameter: 0.4 mm Nozzle temperature: 150°C Bed temperature: 60°C	Filament preparation, 3D printing	Circular disc	[130]
Active material Filament 1 (negative electrode): Graphite Active material Filament 2 (positive electrode): LFP Active material Filament 3 (Separator): SiO ₂ Solvent: Dichloromethane (DCM) Filament substrate: PLA	Z-Direction resolution (first layer): 0.20 mm Z-Direction resolution (following layers): 0.05 mm Filament diameter: 1.75 mm Nozzle diameter: 0.4 mm Nozzle temperature: 195°C Bed temperature: 60°C	Filament preparation, 3D printing	Random customized shapes	[144]
Filament substrate: Commercially available conductive carbon filament	Nozzle temperature: 230°C Bed temperature: 60°C	3D printing of carbon filament, Oven drying at 50°C for 6 hours, Atomic layer deposition of V ₂ O ₅	Circular disc	[145]
Active material: Graphene Filament substrate: PLA	Filament diameter: 1.75 mm Nozzle temperature: 190°C	Filament preparation, 3D printing, Chemical pretreatment	Circular disc	[146]

Active material: LFP, conductive additive Ketjen Black (KB) Solvent: Dimethylformamide (DMF) Filament substrate: TPU	Layer Height: 100 μm Nozzle temperature: 260-350°C Bed temperature: 50°C	Filament preparation, 3D printing	Random customized shapes	[147]
Active material: LTO, KB Solvent: Dimethylformamide (DMF) Filament substrate: TPU	Nozzle temperature: 260-300°C Bed temperature: 50°C	Filament preparation, 3D printing	Random customized shapes	[147]
Active material filament 1: LTO, graphene Active material filament 2: LMO, MWCNTs Active material filament 3: PLA/PC:EMC:LiClO ₄ Filament substrate: PLA	Layer Height: 100 μm Filament diameter: 1.75 mm Nozzle temperature: 210°C Bed temperature: 50°C Printing speed: 20-40 mm s ⁻¹	Filament preparation, 3D printing	customized designed LCD sunglasses and bangles	[129]
Filament substrate: HIPS	N/A	3D printing of mold, Electrode filling, curing at 40 for 3 h, sintering at 1000°C for 90 min	Kenics mixer unit cell, RLPD, SMX	[149]

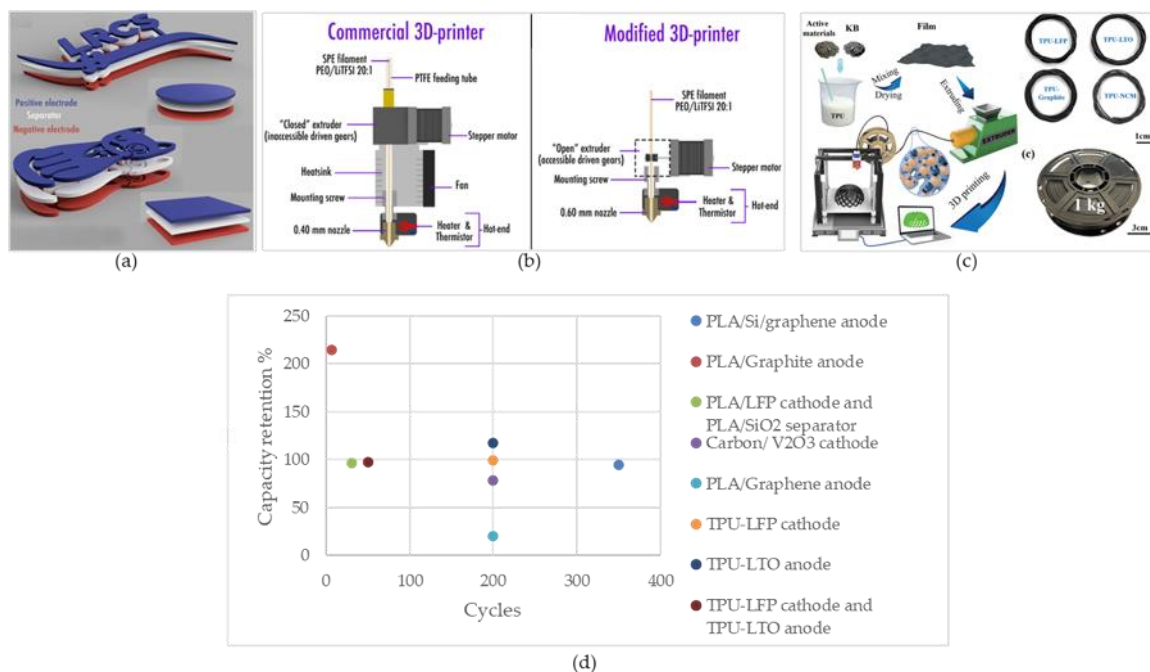


Figure 2-3. (a) “one shot” FFF of battery [144], (b) required modifications for printing customized PEO/LiTFSI filament [148], (c) illustration of FFF of TPU-based electrodes. Reproduced from Hu et al. (2023) with permission from Wiley [147], (d) Capacity retention of the cells fabricated by FFF.

2.3.3 Hybrid energy storage system design for mobile

This method operates by selectively depositing small droplets of specialized inks onto a substrate in a layer-by-layer process. The ink contains essential materials for battery components, such as electrodes, electrolytes, and current collectors, finely dispersed within a liquid carrier. After each layer is printed, it may undergo processes like drying or curing before the printer proceeds to deposit the subsequent layer [32,150].

IJP offers numerous advantages in battery fabrication. By depositing precise amounts of the ink only where needed to eliminate waste, IJP ensures that the materials are utilized efficiently which results in minimizing environmental impact and cost [151,152]. Another advantage is its lower viscosity requirement compared to DIW. This characteristic simplifies the formulation and handling of printable inks which makes the IJP practical and adaptable for a wide range of materials and applications [150]. This method is also capable of multi-material deposition which provides the controlled deposition of active materials of battery components [153]. Moreover, the affordability of IJP equipment along with the

ease of use make this technique an accessible choice for the battery manufacturing process [138].

Despite the advantages, a uniform printed structure through IJP can be challenging and to maintain both battery performance and structural integrity, fine features and adhesion layers precisely is required [150]. Furthermore, while IJP requires lower ink viscosity than DIW, the properties of the ink, such as viscosity and density, need to be optimized to meet the standards. This optimization is essential to avoid issues including the ink agglomeration and the nozzle clogging [151].

2.3.3.1 Some examples of IJP of batteries

Lawes et al. utilized IJP for efficient and cost-effective fabrication of silicon anodes using Si nanoparticles and PEDOT:PSS as a conductive binder. Their work demonstrated the significance of selecting a binder for inkjet printing, as it revealed that binders such as PVP and CMC exhibit rapid capacity decay or low initial capacities due to poor reversibility and electron conduction. On the other hand, anodes made by PEDOT:PSS binder achieved remarkable cycling performance. The SEM results supported this by showing a continuous polymer network maintained during lithiation and delithiation which ensures intimate contact with Si nanoparticles. The initial capacity was measured 3800 mAh g⁻¹ in the first cycle which reduced to 2700 in the following cycles. Moreover, the achieved capacity was more than 1700 mAh g⁻¹ at 0.1 C showing the capacity retention of 63% over 100 cycles. The Coulombic efficiency starts from 31% and 75% in the first two cycles and increases to 98.6% for the remaining cycles. The electrical conductivity of PEDOT:PSS and reversible deformation properties formed a continuous conductive network, ensuring rapid electron transfer and accommodating SiNP volume changes during charge and discharge [155].

Chen et al. utilized IJP to fabricate a dendrite-free Zn anode with Ag nanoparticles for Zn metal batteries. They inkjet-printed Ag nanoparticles-modified carbon cloth (AgNPs@CC) which reduces nucleation overpotential compared to bare CC and promotes uniform Zn nucleation. Notably, the increased surface wettability of AgNPs@CC compared to CC indicated improved Zn-ion migration potential of the printed part. Another finding was that

AgNPs on CC surfaces ensure uniform electric field distribution which controls the Zn deposition morphology and reduces dendrite growth and side reactions during cycling. This result highlights AgNPs crucial role in modulating Zn nucleation and deposition. Furthermore, AgNPs enhance thermal conductivity which ensure uniform temperature distribution and suppress dendrite formation during fast charging and discharging processes. This resulted in the initial discharge capacity of 255 mAh g^{-1} at 5 A g^{-1} reaching 184 mAh g^{-1} after 1200 cycles with only 0.023% capacity fade rate in each cycle with the Coulombic efficiency of about 99.5% within 800 cycles. Nonetheless, as reported in this work, the similar anode fabricated without inkjet-printed Ag nanoparticles exhibited a capacity retention rate of 42.9% after 700 cycles [156].

Kushwaha et al. utilized IJP to deposit graphene inks made from graphene nanosheets in ethanol solvent and ethyl-cellulose stabilizer onto different substrate including Cu foil (Figure 2-4a). The print was followed by annealing to achieve conductivity and porosity. Based on the Raman spectroscopy results, the printed samples after pyrolysis showed increased ordering, which improves electrical conductivity and lithium-ion storage kinetics. Notably, cyclic voltammetry revealed that lithium intercalation and deintercalation which is controlled by diffusion, occur at lower potential scan rates, while at higher potentials both Li-intercalation/deintercalation and surface charge storage occur. This indicates significant contributions from both surface and bulk charge storage processes. This phenomenon is attributed to the well-ordered structure of the annealed graphene film. Moreover, SEM and TEM analysis showed a porous structure with interconnected nanoflakes, which also contribute to enhanced electrical conductivity and faster Li-ion insertion and removal. The reversible capacity was about 520 mAh g^{-1} with capacity retention of about 87% after 100 cycles at 2C which is a high current density. Furthermore, the initial Coulombic efficiency was 95% reaching to more than 99% over 100 cycles. Another important parameter was the dimensions of the graphene, which had a thickness of about 3 nm and lateral dimensions of 2-3 nm. These dimensions make the ink suitable for preventing nozzle clogging during printing due to its small size relative to the nozzle diameter [157].

In their other work, Kushwaha et al. used IJP to deposit a graphene layer onto an Al current collector foil, addressing corrosion issues in cathode current collector. This work significantly suppresses corrosion which leads to better electrical connectivity. Furthermore, they showed that the number of printing layers with subsequent annealing in an Ar atmosphere at 350°C was crucial for achieving uniformity and enhancing the electrical conductivity. The results showed about 180 mAh g⁻¹ initial capacity at C/5 with ~90% capacity retention. The comparable or superior cyclic stability of the inkjet-printing of graphene on Al current collector compared to other coating methods offered practical advantages in terms of cost-effectiveness, scalability, and tunability [158].

Viviani et al. investigated the impact of carbon-based additives, such as carbon black (CB) and multi-walled carbon nanotubes (CNT), on the electrochemical performance of inkjet-printed thin-film LTO electrodes in lithium-ion batteries. Between the carbon-based additives, despite slightly larger particle dimensions of the CNT, the LTO-CNT electrodes showed an optimal compromise between CNT length and conductivity properties. Notably, its impedance increase upon cycling was less compared to LTO-CB which suggests a more stable and homogeneous SEI formation. As the results, LTO-CNT electrodes achieved the highest specific capacity, reaching 128 mAh g⁻¹ at 0.5 C, and exhibited excellent cycle stability with negligible capacity loss (100% capacity retention) and the average Coulombic efficiency of 100% over 100 cycles [159].

Kolchanov et al. utilized inkjet printing to fabricate thin-film Li-ion batteries through the optimization of Li_{1.2}Mn_{0.54}Ni_{0.13}Co_{0.13}O₂ (LMR) cathode. It was found that printing resolution significantly influenced the printing quality and duration which enabled quality enhancement and process time reduction along with drop spacing optimization. Additionally, adjusting the number of deposited layers improved cathode weight and eliminated local printing imperfections. Moreover, the thickness measurements indicated a decrease in the film growth rate with increased layer deposition which was attributed to void filling and ink spreading. Notably, the ordered layered structure of LMR with minimal intrinsic stress facilitated lithium-ion intercalation and deintercalation. The study demonstrated comparable discharge capacities 240 mAh g⁻¹ between inkjet and conventional methods at 0.01 C rate with 68.7% capacity retention over 70 cycles. It is

worth mentioning that the specific energy values of inkjet-printed active layers were comparable to those of high energy density lithium cell cathode layers used in smartphone which suggests their potential suitability for similar applications [160].

Figure 2-4b illustrates the capacity retention of the IJP printed cells. As can be seen, AgNPs@CC anode fabricated by this method shows high capacity retention of 100% over 1200 cycles which is noticeable and indicates the high electrochemical performance of the cell.

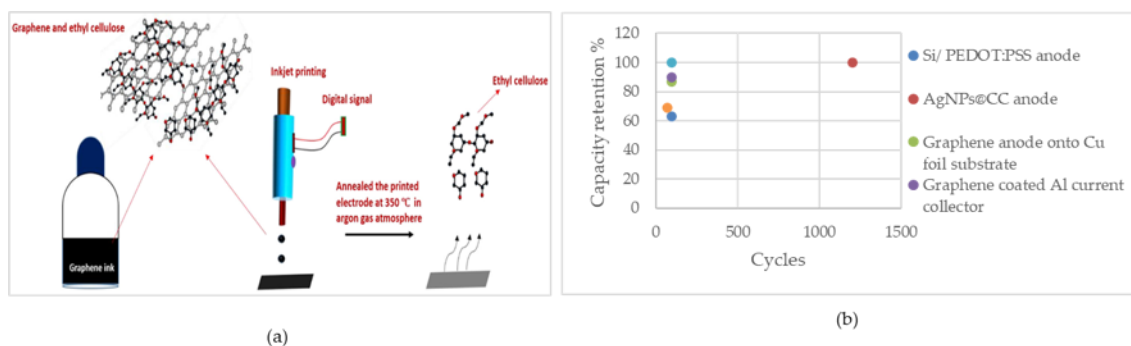


Figure 2-4. (a) Illustration of the IJP process for fabricating a graphene thin-film electrode [157], (b) Capacity retention of the cells fabricated by IJP.

The examples shown Table 2-5 represent the effectiveness of IJP to improve the battery performance through the fabrication of different battery components.

In Table 2-6, the foundational materials utilized in IJP are shown. Notably, similar to DIW, a post-printing drying process is essential to remove any residual solvent, ensuring the integrity of the printed structure and reducing the effect of the non-conductive and non-active components, which have negative effects on battery performance. Moreover, the majority of the samples fabricated through IJP are in thin film designs, which, along with the higher power density in battery performance as mentioned earlier.

Table 2-5. Summary and comparison of electrochemical performance for IJP of batteries.

Printed component	Electrochemical system	Discharge Capacity	Coulombic efficiency	Cycle numbers	Application	Ref.
Anode: Si/PEDOT:PSS	Counter electrode: Metallic lithium Electrolyte: 1 M LPF in DEC and EC, and ethyl methyl carbonate (EC:DEC:EMC)	1700 mA h g ⁻¹ at 0.1 C	98.6%	100	Lithium-Ion Battery	[155]
Anode: AgNPs@CC	Counter electrode: Zn foil Electrolyte: 1m Zn(CF ₃ SO ₃) ₂ aqueous solution Separator: Glass fiber	184 mAh g ⁻¹ at 5 A g ⁻¹	99.5%	1200 & 800	Heat-Resistant Zinc Batteries	[156]
Anode: Graphene onto Cu foil substrate	Counter electrode: Li metal foil Electrolyte: 1 LPF in EC and EMC Separator: Glass microfiber filter paper	520 mAh g ⁻¹ at 2C	99%	100	Lithium-Ion Battery	[157]
Current collector: graphene coated Al	Cathode: LiNi _{1/3} Mn _{1/3} Co _{1/3} O ₂ (Li-NMC111)	180 mAh g ⁻¹ at C/5	N/A	100	Lithium-Ion Battery	[158]
Anode: LTO	Counter electrode: Li metal foil Electrolyte: 50 μl of 1 M LPF in EC:DEC Separator: Celgard 2400	128 mAh g ⁻¹ at 0.5 C	100%	100	Lithium-Ion Battery	[159]
Cathode: LMR	Counter electrode: Li metal foil Electrolyte: 1 M LPF EC/PC/DEC/EMC/PA Separator: Celgard 2325	240 mAh g ⁻¹ at 0.01 C	N/A	70	Lithium-Ion Microbatteries	[160]

Table 2-6. Key Parameters for IJP Process

Ink formulation	Printer parameters	Fabrication steps	Design	Ref.
Active material: SiNPs carbon black Binder: PEDOT:PSS, Polyvinylpyrrolidone (PVP), CMC Solvent: DI-water Ink viscosity: 10 mPa.s	Printing temperature: Ambient Number of printed layers: 25	Ink preparation, 3D printing, Drying at vacuum oven at 60°C overnight	N/A	[155]
Active material: Conductive silver Solvent: Triethylene glycol monethyl ether Ink viscosity: 9~11 cPa.s	Printhead Diameter: 60 μm Droplet Diameter: 45-55 μm	Ink preparation, 3D printing, Annealing at 180°C for 1 h	Layer-by-layer serpentine path	[156]
Active material: Graphene nanosheets Binder: Ethyl-cellulose Solvent and solution: Ethanol and terpineol (anhydrous), NaCl	Printhead Diameter: 80 μm Droplet Diameter: 90-110 μm Printing Speed: 50 mm s^{-1} Printhead temperature: 30°C Substrate temperature: 60°C	Ink preparation, 3D printing, Annealing at 350°C for 1 h and 30 min	Thin film	[157]
Active material: Graphene nanosheets Binder: Ethyl cellulose Solvent: ethanol/terpineol	Droplet volume: 110 pL Droplet Step Size: 100 μm Printhead temperature: 30°C Substrate temperature: 60°C	Ink preparation, 3D printing, Annealing at 350°C for 1 h and 30 min	Thin film	[158]
Active material: $\text{Li}_4\text{Ti}_5\text{O}_{12}$ powder, carbon-based conductive agent (CB and CNT), 1 mM lithium dodecyl sulfate (LDS), lithium polyacrylate (Li-PAA) Binder: PVP Solvent: Ethylene glycol (EG), 2-propanol (IPA) Ink viscosity: 2.5 to 3 cPa.s viscosity at 10 to 10 ⁴ s ⁻¹ shear rates	Printhead Diameter: ~30 μm Printhead Resolution: 600 dpi	Ink preparation, 3D printing, Drying at 80°C for 3 h	Thin film	[159]
Active material: LMR, Carbon Black Binder: PVDF Solvent: NMP Ink viscosity: 3 to 20 cPa.s viscosity at 25 to 34 mN m ⁻¹ surface tension	Droplet volume: 10 pL Substrate temperature: 45°C	Ink preparation, 3D printing, Oven drying at 200°C for 2 h	Thin film	[160]

2.3.4 Stereolithography

SLA, a prominent light-assisted 3D printing technology, operates by employing a light source to solidify a polymer resin selectively layer by layer. The versatility and precision offered by SLA make it a valuable tool in various industries, with notable applications emerging within the energy storage systems [32,161,162].

One of the advantages of SLA is its high resolution, which can reach up to 0.5 micrometers which makes it a well-suited for applications demanding complex geometries [31,73,163,164]. Additionally, SLA is nozzle-free, setting it apart from some other 3D printing methods. This feature eliminates the risk of nozzle clogs or filament feed issues which makes the printing process more reliable and uninterrupted [31,72,165]. Furthermore, objects produced through SLA generally exhibit smooth and highly detailed surface finishes [71,166]. The technique also excels in layer bonding due to its chemical curing process, resulting in strong layer-to-layer adhesion. This attributes to high mechanical strength, structural integrity, and durability of printed objects [167].

The preparation of printable resins containing the right blend of active materials, photoinitiators, and monomers can be a complex process [31]. Flowability of the resin is another crucial consideration. If the flowability is not properly balanced, it can hinder the printing process and result in suboptimal print quality [31]. Additionally, the refractive index of the resin is of great importance. An unsuitable refractive index can cause UV light to scatter within the resin, which can result in defects, incomplete curing, compromised mechanical properties, and a lack of printing accuracy [31,161,168]. An unsuitable refractive index can cause UV light to scatter within the resin, which can result in defects, incomplete curing, compromised mechanical properties, and a lack of printing accuracy [31,161,168]. SLA 3D printing system tends to be relatively expensive high cost for industrial applications too [72]. The price per printed object, especially for simpler designs or smaller projects, might be comparable to those from other 3D printing methods. The overall affordability of SLA technology may vary depending on factors such as the complexity of the printed objects and the specific requirements of the application. Furthermore, post-processing requirements are often necessary for SLA prints. These post-

processing steps, such as excess resin cleaning, can be time-consuming and may influence the final accuracy and surface finish of printed objects [32].

2.3.4.1 Some examples of SLA of batteries

He et al. developed a solid polymer electrolyte (SPE) containing lithium bis(trifluoromethanesulfonyl)imide (LiTFSI) for all-solid-state lithium metal batteries using SLA. The printed structure exhibited high ionic conductivity of $3.7 \times 10^{-4} \text{ S cm}^{-1}$. At various charge rates, the discharge capacity decreased due to polarization; however, the 3D structure consistently outperformed other structures. Notably, the 3D structure exhibited an initial specific capacity of 166 mAh g^{-1} at 0.1 C with higher capacity retention (78%) after 250 cycles compared to other structures (19%), and maintained a Coulombic efficiency of approximately 100%. The obtained 3D-SPE replicated contained spiral walls with dimensions of $100 \mu\text{m}$ width, $150 \mu\text{m}$ height, and $200 \mu\text{m}$ spacing on a planar substrate of $100 \mu\text{m}$ thickness. This design ensured perfect adherence of the cathode to the electrolyte and enabled large-scale printing for practical applications. Further analysis revealed that the addition of succinonitrile (SCN) in the polymer resin weakened the mechanical strength of the electrolyte, resulting in decreased conductivity. The charge-discharge cycle demonstrated stability for at least 600 hours without interruption. Moreover, the 3D structure exhibited lower impedance compared to other structures which leads to improved cycling performance [89].

Chen et al. utilized SLA to fabricate poly (ethylene glycol) (PEG)-base gel polymer electrolyte containing LiClO_4 salt. The cell was made by a 3D printed solid electrolyte flown by LTO and LFP as electrodes. It was shown that the incorporation of solvated lithium salt into the polymer matrix facilitates lithium ion transportation, particularly within the amorphous regions which led to improved mobility of polymer chains and higher ionic conductivity. The results indicated that the electrolyte can deliver high ionic conductivity of $4.8 \times 10^{-3} \text{ S cm}^{-1}$ with delivered the discharge capacity of $1.4 \mu\text{Ah cm}^{-2}$ over 2 cycles at $5 \mu\text{A}$ current which showed the favorable interaction between the active material and the gel polymer electrolyte. It should be considered that cycling with a higher current (C/5) showed gradual capacity decline over cycles which led to failure by the 10th. It is likely due to lithium dendrite growth which causes short circuits. Some optimizations

include adding SiO₂ to the electrolyte to suppress dendrites or applying a PEG-based materials on the separator for enhanced mechanical strength improve the cycling performance [166].

Norjely et al. employed SLA to fabricate a polyurethane acrylate (PUA)-based gel polymer electrolyte containing lithium perchlorate (LiClO₄) for solid-state lithium-ion batteries. The results showed the amorphous phase of the printed parts which enhanced the ionic conductivity by facilitating quicker segmental motion and bond rotations. Additionally, the higher concentration of LiClO₄ can alter the surface morphology from smooth to textured which results to enhancing the Li⁺ transportation and higher ionic conductivity. The ionic conductivity of the printed solid electrolyte with 10 wt% of LiClO₄ was high equal to $1.24 \times 10^{-3} \text{ S cm}^{-1}$ showing the method promising in the fabrication of the solid-state lithium ion batteries. It should be considered that beyond 10 wt.% LiClO₄ recrystallization or agglomeration occur which reduce free ions and diminish ionic conductivity due to possible ion pair formation and Coulomb attraction-induced neutralization [170].

Zekoll et al. used SLA to create 3D templates from structured ceramic-polymer solid electrolytes made by Li_{1.4}Al_{0.4}Ge_{1.6}(PO₄)₃ (LAGP). These electrolytes were composed of a 3D ceramic scaffold with the channels filled by non-conducting polymers including polypropylene or epoxy polymer followed by polymerization which resulted in polymer-filled channels within the ceramic scaffold. The high ionic conductivity of $1.6 \times 10^{-4} \text{ S cm}^{-1}$ along with the high mechanical stability were achieved. The consistent density throughout the structure which is achievable with designs such as the cube and diamond, is crucial for maintaining conductivity while minimizing the impact of non-conductive materials. These designs exhibited preferential fracture paths, which are beneficial for mechanical integrity [90].

Lee et al. employed DLP printing for making high conductivity poly(ethylene oxide) (PEO) SPE. The structure composed of a crosslinked polymer matrix which contained nanochannels filled with ionic liquid which exhibited high mechanical strength and an ionic conductivity of $3 \times 10^{-4} \text{ S cm}^{-1}$. The results showed that increasing the volume fraction of the conductive component improves the ionic conductivity without sacrificing

the mechanical strength. These structures are beneficial to use these SPEs in customized applications with complex shapes [171].

Katsuyama et al. utilized SLA 3D printing and pyrolysis to fabricate hard carbon microlattices with three different unit cell length (x) and beam width (y) as a free-standing anode for sodium ion batteries. They measured the amount of shrinkage about 70% in x and 75% in y (Figure 2-5a). Charge-discharge profiles of samples with different sizes related to the beam width, where smaller samples corresponded to finer beams, revealed that finer structures exhibited higher capacity, reduced overpotential, and improved rate performance. Notably, the smallest sample exhibited the best behavior. Furthermore, areal capacity decreased with increasing charging rate, with degradation proportional to feature size. The galvanostatic intermittent titration technique (GITT) demonstrated that smaller beam widths led to decreased overpotential and variation in voltage. Additionally, XRD results from the samples after the pyrolysis indicated Low crystallinity due to the formation of hard carbon. Moreover, an interlayer distance of 3.79 \AA was observed which was larger than perfect graphite (3.35 \AA) and results in increased ion storage capacity. As the result, the highest specific capacity which was related to the sample with the finer beam was 225 mAh g^{-1} at 5 mA g^{-1} with the Coulombic efficiency of 80% in the initial cycle to 99.4% over the 2nd cycle. The capacity retention was measured about 80% over 100 cycles [172].

Ye et al. employed a DLP printer to fabricate a Si/PEDOT:PSS/PEG electrode with a Si content of 31.7 wt% for lithium-ion batteries to maximize energy storage while minimizing battery weight. PEDOT:PSS served as the conductive component, ensuring structural integrity and flexibility of the printed part. Battery performance demonstrated promise for silicon-based anodes, with an improved Coulombic efficiency of up to 86.3% after 125 cycles and an initial discharge capacity of 1539 mAh g^{-1} . The reversible capacity reached 1105 mAh g^{-1} with 72% retention at 800 mA g^{-1} current density, attributed to tolerance to mechanical stress. Despite conventional Si exhibiting high initial charge/discharge capacity (2560 mAh g^{-1} with 81.3% Coulombic efficiency, 3D printed samples showed enhanced charge/discharge behavior compared to conventional Si electrodes. It is noteworthy that the photograph from the printed parts illustrated the decreased transparency of the PEDOT:PSS/PEG by adding silicon which impacts the printability with

high silicon load. Furthermore, viscosity analysis revealed increased viscosity with Si addition, limiting the amount of loaded silicon. SEM images depicted embedded and encapsulated Si primarily on the surface within a honeycomb design which provides more micropores and channel structures for Li ions diffusion. EIS analysis indicated lower charge transfer resistance for Si/PEDOT:PSS/PEG electrodes compared to the conventional Si electrodes which suggests improved electrochemical performance [173].

Table 2-7 shows that until now, much of the research conducted on SLA printing of batteries focused on gel-based/solid electrolyte. Table 2-8 presents the parameters and processes associated with SLA printing. In this method, the presence of the active material and photoinitiator is important for printing battery components when the goal is to directly fabricate them through 3D printing. Figure 2-5b illustrates the capacity retention of the cells assembled by the SLA printed battery component.

Table 2-7. Summary and comparison of electrochemical performance for SLA of batteries.

Printed component	Electrochemical system	Discharge Capacity	Coulombic efficiency	Cycle numbers	Other properties	Application	Ref.
Electrolyte: LiTFSI	Anode: Li metal foil Cathode: LFP	166 mAh g ⁻¹ at 0.1 C	100%	250	Ionic conductivity: 3.7×10^{-4} S cm ⁻¹	Lithium-Ion Battery	[89]
Electrolyte: PEG-base gel polymer	Anode: LTO Cathode: LFP	1.4 μ Ah cm ⁻² at 5 μ A	N/A	2	Ionic conductivity: 4.8×10^{-3} S cm ⁻¹	Lithium-Ion Battery	[169]
Electrolyte: PUA-base gel polymer	Stainless steel electrodes	N/A	N/A	N/A	Ionic conductivity: 1.24×10^{-3} S cm ⁻¹	Lithium-Ion Battery	[170]
Electrolyte: LAGP solid electrolyte	Lithium electrodes	N/A	N/A	N/A	Ionic conductivity: 1.6×10^{-4} S cm ⁻¹	Lithium-Ion Battery	[90]
Electrolyte: PEO solid electrolyte	Activated carbon-based electrodes coated on stainless steel	N/A	N/A	N/A	Ionic conductivity: 3×10^{-4} S cm ⁻¹	Lithium battery systems, Photovoltaic cells, Supercapacitors, Fuel cells	[171]
Anode: hard carbon microlattices	Counter electrode: sodium metal foil Electrolyte: 1.0 m NaPF ₆ in PC Separator: Glass fiber filter	225 mAh g ⁻¹ at 5 mA g ⁻¹	99.4%	2	N/A	Sodium Ion Batteries	[172]
Anode: Si/PEDOT:PSS/PEG	Counter electrode: Li metal foil Electrolyte: LPF EC/DEC (v/v=1/1) with 5% FEC Separator: Celgard 2400	1105 mAh g ⁻¹ at 800 mA g ⁻¹	86.3%	125	N/A	Lithium-Ion Battery	[173]

Table 2-8. Key Parameters for SLA Process

Resin formulation	Printer parameters	Fabrication steps	Design	Ref.
Active component: Lithium bis(trifluoromethanesulfonyl)imide (LiTFSI) Polymer resin: Poly(ethyleneglycol) diacrylate(PEGDA), SCN Photoinitiator: Phenylbis(2,4,6-trimethylbenzoyl)phosphine oxide	Light wavelength: 355 nm Power density: 10 W cm ⁻²	Resin preparation, 3D printing, Drying in a vacuum oven at 25°C for 2h, Further drying under Ar gas for 48 h	3D-Archimedean spiral structured	[89]
Active material: 1 M LiClO ₄ Polymer resin: PEGDA Photoinitiator: Phenylbis(2,4,6-trimethylbenzoyl)phosphine oxide Photoabsorber: Sudan I	Printer resolution: 10µm Layer Thickness: 30µm Exposure time: 13 s	Resin preparation, 3D printing	Zigzag shape	[169]
Active material: 1 M LiClO ₄ Polymer resin: PUA	Light wavelength: 405 nm	Resin preparation, 3D printing	Circular disk	[170]
Polymer resin: photoresist IP-S	Light wavelength: 780 nm	3D printing the template, LAGP synthesis, Template immersion into LAGP, Heat treatment to 900°C for 5 h, Impregnation of LAGP with polypropylene/ Epoxy polymer	3D cubic bicontinuous microarchitectures	[90]
Polymer resin: Photopolymer Translucent Resin	Printer resolution: 50µm First layer exposure time: 35 s Other layers exposure time: 2 s Light wavelength: 514 nm	3D printing, Pyrolysis at 400°C for 4 h and 1000°C for 4 h	Lattice structure	[172]
Active material: Silicon powder (30 wt%), PEDOT:PSS Polymer resin: PEG hydrogel Solvent: Distilled water (DW) Photoinitiator: Bis(2,4,6-trimethylbenzoyl) phenylphosphineoxide (BAPO)	Printer resolution: 75µm Laser spot diameter: 200µm Light wavelength: 375 nm	Resin preparation, 3D printing, Drying in a vacuum oven at 80°C for 8 hours	Honeycomb micropatterned	[173]

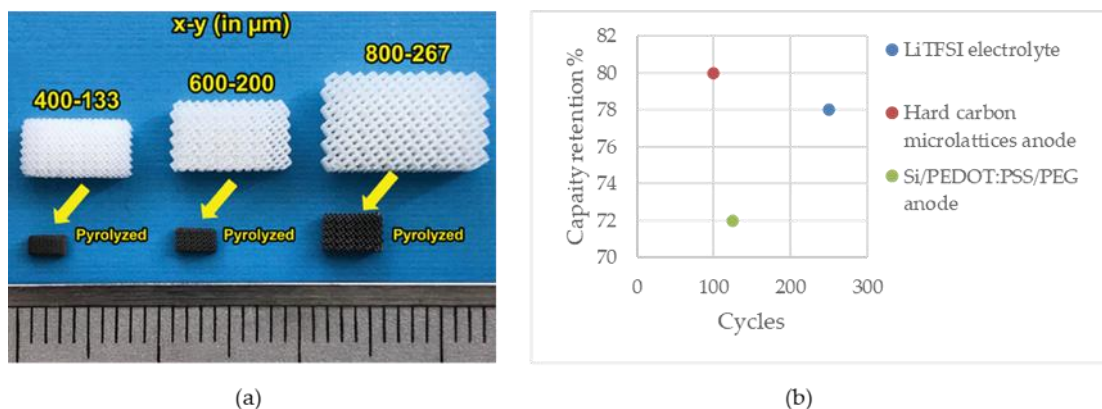


Figure 2-5. (a) SLA printed electrodes before and after pyrolysis. Reproduced from Katsuyama et al. (2022) with permission from Wiley [172], (b) Capacity retention of the cells fabricated by SLA.

Furthermore, Table 2-9 summarizes the advantage and disadvantages of the abovementioned methods.

Table 2-9. Advantages and disadvantages of DIW, FFF, IJP, and SLA

Method	Advantages	Disadvantages
Direct Ink Writing	<ul style="list-style-type: none"> - High resolution - Affordable - Ease of use - Minimal post-production treatment - Flexibility in material selection 	<ul style="list-style-type: none"> - Ink formulation - Material rheological properties optimization - Poor mechanical properties
Fused Filament Fabrication	<ul style="list-style-type: none"> - Multi-material printing - No need for ink preparation - Minimal waste - Economical - High production rates 	<ul style="list-style-type: none"> - Filament formulation - Risk of nozzle clogging - Poor mechanical properties in z-direction - Low surface quality
InkJet Printing	<ul style="list-style-type: none"> - Multi-material printing - Affordable - Ease of use - Lower viscosity requirement - Flexibility in material selection 	<ul style="list-style-type: none"> - Nonuniform printed structure - Ink formulation
Stereolithography	<ul style="list-style-type: none"> - Multi-material printing - High resolution - Nozzle-free printing process - Smooth and highly detailed surface finishes - Strong layer-to-layer adhesion - High mechanical strength - Structural integrity 	<ul style="list-style-type: none"> - Resin formulation - Resin flowability - Resin refractive index for resin - Relatively high cost for industrial applications - Post-processing requirements
	<ul style="list-style-type: none"> - Durability 	

It is clear from this review of experimental results that closely align with theoretical electrochemical performance that 3D printing methods for battery fabrication are

promising. There is potential for 3D printing to be incorporated in manufacturing high-performance batteries, primarily due to its inherent design freedom. One of the other interesting aspects of 3D-printing batteries is the capability to fabricate solid-state electrolytes which opens the path to developing all-solid-state batteries. This innovation not only could enhance battery performance but also enables the creation of fully 3D-printed batteries. Compared to batteries with liquid electrolytes, solid-state batteries often exhibit superior performance, particularly in the areas of safety.

It is also clear from this review that a range of 3D printing methods can be used for various battery components. In this regard, DIW and IJP enable the loading of active and conductive materials into printable ink to facilitate the production of desired components. On the other hand, FFF offers a customizable approach by loading these materials into filaments. Additionally, compared to the other methods, it can be seen that for SLA substantial research has been focused primarily on the fabrication of solid electrolytes. Nevertheless, successful fabrication of other battery components, including free-standing anodes [172], demonstrates the potential of SLA in broadening battery component fabrication.

3D printing has proven its ability to fabricate battery components using high-performance materials. Silicon, for example, as a major byproduct of the solar photovoltaic (PV) industry [174], stands out as a promising anode material due to its high theoretical capacity (around 3,579 mAh g⁻¹) [175]. The primary challenge associated with utilizing silicon as an anode is the substantial volume change experienced by the material during battery cycling, thereby constraining its application. Various 3D printing methods, including DIW [122], FFF [143], IJP [155], and SLA [173], have successfully produced silicon anodes with high electrochemical performance by addressing the volume change issue through special structures achievable via 3D printing, as well as by adding carbon additives that can accommodate the volume change of silicon by covering it. Finally, the high resolution and high fabrication rate of SLA as well as the capability to fabricate solid electrolytes and silicon anodes makes it an exceptionally promising candidate for the production of all-solid-state batteries with superior electrochemical performance, as well as high safety, efficiency, and sustainability. Therefore, among various 3D printing methods, the SLA

method is particularly promising for battery fabrication. Challenges, however, remain related to the non-conductive and non-active polymer resin and cost considerations. In this regard, the adoption of the free and open-source hardware (FOSH) development of scientific tools approach is promising as it has been shown to decrease capital costs on average by about 90% [176]. Specific technologies for battery research can be extremely cost effective. For example, a USD \$20,000 potentiostat and galvanostat used for characterizing thin-film batteries can be replaced with a USD\$100 open-source tool [177]. In addition, open battery management is also available [178] including for in situ monitoring of Li-ion cells [179]. There has also been more application specific FOSH such as a maintenance tool for light-EV batteries [180]. Finally, there has been work to make completely FOSH all-iron batteries [181,182], which provides a model for the FOSH 3D printable batteries discussed here. Integrating an open-source toolchain, spanning from material preparation to battery packaging, emerges as a promising approach to reduce fabrication costs and enhance accessibility to 3D printing technologies for battery research and production.

2.4 Conclusions

The advent of 3D printing marks a potential transformative shift in the fabrication of energy storage devices as it introduces a new potential for rapid innovation and customization for batteries for specific applications. In contrast to traditional manufacturing, the precision of 3D printing coupled to geometrical freedom can be used to improve battery performance and offer more efficient energy storage solutions. Notably, as shown in this review 3D-printing of batteries offers a path to higher energy density, capacity, and overall performance compared to the conventional manufacturing techniques. Overall, the evidence presented through numerous case studies from labs making substantial progress all over the world shows the potential of 3D printing as a promising solution to enhance energy storage capabilities. Furthermore, the design freedom of 3D printing makes the fabrication of complex geometries and structures possible and emerges as another key aspect to improve the energy storage capacities and applications in the future. In addition, 3D printing is a promising method to enable the use of new materials for battery fabrication to improve battery performance. From an environmental protection viewpoint, the waste

reduction associated with 3D printing of batteries is a way toward a more environmentally friendly future directly. Indirectly, the improved performance and flexibility in applications as well as the potential to reduce energy storage costs, could have a substantial positive impact in enabling intermittent renewable energy sources to displace fossil fuels. As 3D printing technologies become more accessible, the prospect of cost-effective production for customized batteries is extremely promising.

Chapter 3

3 Open-Source Hardware for Battery Fabrication

The fabrication of silicon-based anodes for lithium-ion batteries from recycled solar cells requires a series of critical material processing steps. The silicon material recovered from end-of-life photovoltaic panels typically exists in the form of large wafers, which are unsuitable for direct use in battery electrodes. To enable efficient lithiation and integration into 3D-printable resins, the silicon must be reduced to micrometer or even nanometer-scale particles. This size reduction significantly increases the surface area, improves electrode kinetics, and enhances the mechanical stability of the final anode structure.

Achieving the necessary particle size distribution demands a robust and scalable milling process. To address this need, an open-source ball mill was developed. Designed for AC and off-grid photovoltaic powered operation and low-cost construction, this ball mill provides a sustainable solution for converting silicon wafers into fine powders suitable for resin formulations. By building on openly shared designs and accessible components, the ball mill ensures that material preparation remains affordable, customizable, and reproducible across different laboratory environments.

Following size reduction, the powdered silicon must be homogeneously incorporated into a photocurable resin for stereolithography (SLA) 3D printing. Uniform dispersion is essential for maintaining print quality, mechanical integrity, and consistent electrochemical performance. To facilitate this mixing process, an open-source bottle roller was designed and fabricated. The bottle roller provides continuous, gentle agitation of the silicon-resin mixture to have even particle distribution.

Also, a proper enclosed place was required to prepare and process the materials in. To satisfy this, an Open-source inert gas glove box was designed and fabricated.

In this Chapter, the motivation for the development of these open-source hardware tools is discussed, along with the design considerations, fabrication processes, and operational principles behind them. Together, the open-source ball mill and bottle roller form an

integral part of the proposed toolchain, which support the transition from solar cell waste to lithium-ion battery anodes.

3.1 AC/off-grid photovoltaic powered open-source ball mill

Ball milling is used for comminution by rotating a drum to grind materials using balls with specific diameters. Ball milling advantages include the potential for high capacity, predicted fineness in a specific amount of time, reliability, safety, and simplicity, but has disadvantages of high weight, energy consumption and costs, which limit accessibility. To overcome these limitations this work applies the free and Open-source hardware approach coupled to distributed digital manufacturing to fabricate a ball mill with a simple, customizable design that can be used in a wide range of scientific applications and circumstances including those without access to reliable grid electricity. The highly customizable design reduces the cost to <US\$130 for an AC powered version and <US\$315 for a switchable power that enables off-grid operation with a solar module and battery. Using a solar photovoltaic energy source not only improves the power reliability but also makes it easier to move the ball mill for use in field environments. The Open-source ball mill can reduce silicon particle sizes from the millimeter scale down to the nanometer scale.

3.1.1 Hardware in context

Comminution is used to reduce the particle size, change the shape of particles, eliminate agglomeration, provide mechanical alloying, mixing, changing materials properties, and producing powder [183]. There are different grinding techniques such as rod mills, vibrating grinders, medium agitating mills, jet mills, and ball-medium types. The latter one has different methods based on the motion mode of the mill body including tumbling ball mills, vibrating mills, cylindrical ball mills, conical ball mills, and planetary mills. Ball milling is a technology used for grinding, preparing, and modifying materials. The purpose of the ball milling is to rotate a drum with a motor and grind the inside materials using balls with specific diameters. Ball milling has applications in different scientific areas, including chemistry for fabricating microstructures [184], nanostructures [185–187], and chemical

and mechanochemical synthesis [188–191]. The advantage of ball milling compared to other comminution methods are the potential for high capacity, predicted fineness in a specific amount of time, reliability, safety, simplicity, and servicing [183]. Ball milling, however, has disadvantages, including high weight, high energy consumption because of the waste of energy in heat, friction, and sound [183], as well as high cost (Table 3-1). Although commercial ball mills can satisfy these applications, their costs are limiting accessibility in many labs as they range from approximately US\$350 to over US\$5,000 for simple laboratory ball mill.

Table 3-1. Commercial ball mill costs in CAD

Commercial Proprietary Product	Cost (CAD\$)	Specifications
Laboratory Ball Mill [192]	349.00	<ul style="list-style-type: none"> • Capacity: 2 kg • Material: Stainless Steel • Dimensions L x W x H: 46.5 x 26 x 26 Cm • Weight: 5 kg
Ball Mill 2 kg Heavy Duty IN 220 Volt Laboratory Ball Grinder [193]	836.00	<ul style="list-style-type: none"> • Capacity: 2 kg • Material: Stainless Steel • Speed: 80 rpm
One-tier jar high-capacity laboratory jar mill [194]	4,891.65	<ul style="list-style-type: none"> • Capacity: 27 kg • Dimensions H x W x D: 26.9 x 26.7 x 25.4 Cm • Speed: 20 to 300 rpm
Cole-Parmer Jar Mill [195]	6,665.62	<ul style="list-style-type: none"> • Capacity: 13 kg • Dimensions H x W x D: 15.2 x 34.3 x 25.4 Cm • Material: Steel • Speed: 10 to 260 rpm

High costs for scientific equipment like ball mills has been a historic issue as it limits access to scientific tools and drives inequity [196]. Fortunately, there is a proven approach to reducing the cost of scientific equipment is to apply free and Open-source hardware (FOSH) technological development models [197,198,198]. Most recently a review found for a wide range of scientific tools, that Open-source technologies provide economic savings of 87% compared to equivalent or lesser proprietary tools [199]. These economic savings increased slightly to 89% for those that used Open-source electronics like Arduino technology [200], and even more to 92% for those that used RepRap-class 3-D printing [199]. Combining both Open-source electronics and 3-D printing the savings averaged 94% for free and Open-source tools over commercial equivalents (or lesser tools) [199]. At the same time, building their own hardware [200], using parametric FOSH [201,202], allows scientists to build high-quality bespoke research equipment [203–205]. There has been some development of FOSH tools for mixing including a sample rotator mixer and shaker [29], an orbital shaker [206], a nutating mixer [207], stirring [30], and 3-D programmable shaker [208]. Yet despite many low-cost ball mills published in the DIY and maker grey literature [209–217], there are no Open-source ball mills published in the scientific literature, which have been validated. The DIY ball mills available also suffer from several shortcomings. The most important concern about many of these home-made ball mills is that they do not use customized drum in their design, and they use the readily available containers with their own specified lid. As a result, they cannot meet the requirements of having standard diameter to height ratio to get the highest-quality results and it is impossible or difficult to customize them to achieve this ratio [209,211,214,216,217]. Other issues regarding the readily available home-made ball mills include noise making [210,212,217], high weight and large device size [212,216–218], unreliability since the drum is not held in place [211,215,216], design instability [183,184], big drum size, which is not applicable for scientific experiments that use low-weight materials [218], and non-controllable speed, which is in contrary with the requirement of the critical speed [215,216].

To close this gap, this work applies the open-source hardware approach and distributed digital manufacturing to fabricate a ball mill to both reduce costs and provide the user with

a simple, customizable design that can be used in a wide range of circumstances including those without access to reliable grid electricity.

3.1.2 Hardware description

The open-source ball mill developed here is fully customizable and designed to be fabricated with distributed manufacturing. The parametric designs of the main components are 3-D printable on a low-cost readily accessible RepRap-class fused filament 3-D printer, and the electronic parts, bearings, magnets, and balls are provided by a wide-range of off-the-shelf vendors. The design both reduces the mass as well as allows users to customize the volume of the ball mill. Electronic designs are provided to power the device from an AC wall outlet as well as a DC source such as a battery or solar photovoltaic mini-module. Testing and validation are provided to compare the quality of the open-source ball mill with the available commercial ones, and a comparison in price is made to show the economic advantage of the open-source device with commercial peers.

- Reducing the expenses for grinding materials in laboratory experiments including grinding, preparing, mixing, and modifying.
- Customizing the design based on the bespoke needs of the project
- A low weight, which makes the ball mill portable
- The possibility of using both AC and a DC photovoltaic mini-module as the power sources

The design files, bill of materials, and operation principles are outlined in <https://osf.io/xa4ws/>. Also, Figure 3-1 shows the figure of the final product.

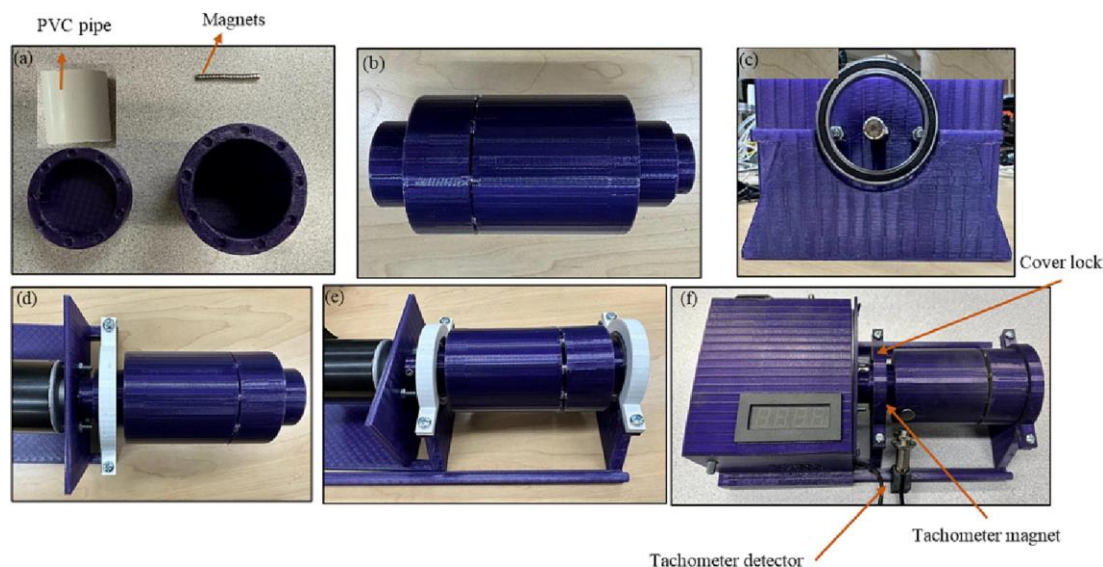


Figure 3-1. Assembly of the open-source ball mill: (a) individual components, including the PVC pipe, 3D-printed drum, and magnets; (b) assembled drum; (c) end view showing insertion of the front bearing; (d) mounting of the drum onto the drive shaft; (e) fully mounted drum secured on the support frame; and (f) complete ball mill system.

3.1.3 Validation and characterization

Many research projects utilize ball mills. To demonstrate the effectiveness of the Open-source ball mill it is validated here by grinding silicon particles from waste solar photovoltaic cells. Other research groups have used ball milling before for this application. For example, Nilssen et al. investigated the properties of silicon after ball milling with a planetary ball mill at different times, ball sizes, and speeds [219]. These parameters affect the phase form, crystalline or amorphous, and the sizes of the silicon particles. Zhu et al. determined the influence of ball milling factors, including milling time and speed, in nano silicon production with zirconia balls. They showed that increasing the speed and milling time increases the rate of breaking particles and results in more evenly particles distribution [220]. In a study by Li et al., the influence of ball size on the particle properties is investigated. They controlled the mass ratio between balls and powder in a 10:1 amount [221]. The results showed that different range of ball sizes from 5 mm to 15 mm diameters could grind the SiC particles from 39.7 and 111 micrometer to 7.51 and 19 micrometers, respectively after 5 hours. For the open-source ball mill, the ability to grind silicon particles from waste solar photovoltaic cells was tested in detail. The consumed energy was

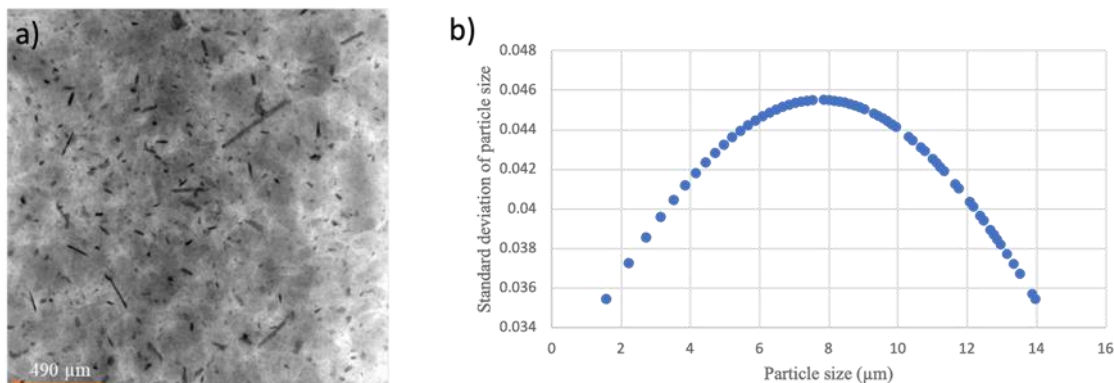


Figure 3-2. a) Micro-CT image of silicon particles after 18 hours ball milling, and b) Particle size distribution after 18 hours ball milling.

monitored with a digital multimeter (± 0.01 kWh) and the final particle sizes for silicon powder are measured using micro-CT. For this purpose, multi-millimeter size silicon wafer shards are added to the drum. It takes about 1 minute to load the ball mill. The ball milling was done in four steps with 190 rpm speed. It takes about 40 seconds for the tachometer to read the speed correctly [222]. For each step, the particles were milled for 6 hours, the particle sizes were determined with the use of the micro-CT and the Open-source imaging processing software Fiji (with ImageJ2). The Open-source ball mill was run in three sets of six hours and the particle size was measured after each run (Figure 3-3 and Figure 3-2a). The unloading video is provided in OSF directory [222]. The results show that the silicon particles size reduced from 0.8 mm down to 7 μm 18 hours (Figure 3-2b). As the results clearly show the ball mill can grind materials down to micrometer size, which is desirable for many scientific applications.

The capabilities of the Open-source ball mill include:

- Reducing the cost of ball milling hardware down to CAD\$170 for an AC powered device. In addition, the device can be made power switchable to enable off-grid operation with a solar module and battery for CAD\$420.
- Using the solar photovoltaic as the energy source not only improves the power reliability but also makes it easier to move the ball mill for use in field environments.

- Low weight resulting from the structure materials which are 3-D printed plastic also make the ball mill readily transportable.
- The Open-source ball mill showed that it could reduce silicon particle sizes from mm down to the micrometer scale.
- Finally, it is highly customizable, which helps the user to change the drum size for specific applications and it can be printed out of various materials including a wide range of plastics, composites, ceramics or metals.

One of the limitations of the Open-source ball mill is that plastic construction might reduce the stability of the ball mill at higher loads (i.e. it is so low weight it might need clamping fixture to secure it to a desktop).

The Open-source ball mill was shown to be effective, but there are several areas of potential improvement. First, the mass of the plastic parts could be further reduced by iterative

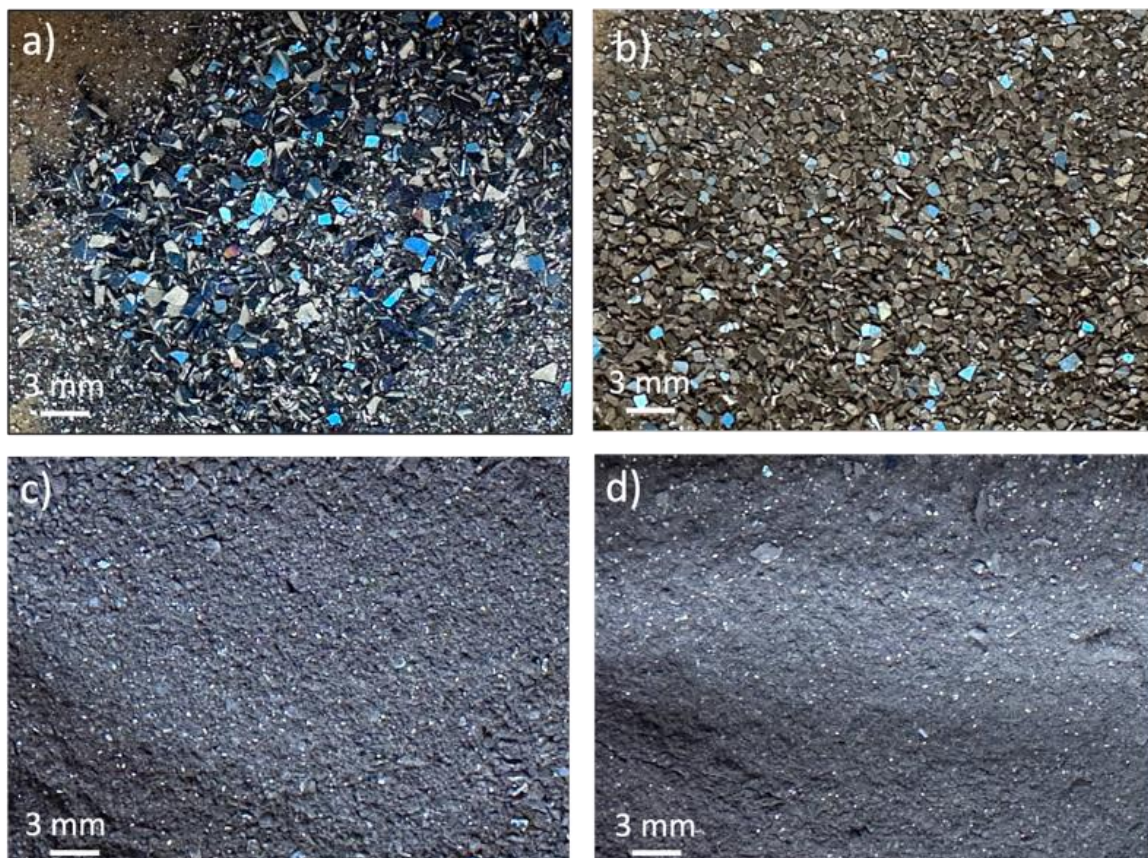


Figure 3-3. Smart phone pictures of silicon particles: a) before ball milling, b) after 6 hours ball milling, c) after 12 hours ball milling, and d) after 18 hours ball milling.

design governed by simulations to calculate the stress-strain in different parts and remove the material that are under less stress, to reduce the materials used in the design and make it even more economical. This design could also be built upon by developing an Open-source planetary ball mill to increase the efficiency. The Open-source ball mill in the AC version is less costly than the conventional proprietary ball mills, however, when adding the ability for switchable power with a solar photovoltaic mini module the costs again have become prohibitive for some users. This is primarily because all the electronic components are off-the-shelf. Future work could focus on making Open-source equivalents of the solar charge controller and the boost converter. An integrated Open-source circuit could be developed that replaces all of the electronics for both systems and be available for synthesis using Open-source circuit mills [138,223–225] or electronics 3-D printing [226]. Lastly, although the levelized cost of electricity from full-scale solar photovoltaic modules is now often the least costly of electrical sources and the IEA believes the lowest cost in history [227], photovoltaic mini-modules can be significantly more expensive. For example, the spot price on large scale purchases of full-size photovoltaic modules made of high-quality monocrystalline silicon passivated emitter and rear (PERC) cells is \$0.235/W on Dec. 10, 2022 [228], while the mini-module used here costs more than \$1.00/W. This indicates there is a potential to fabricate Open-source solar photovoltaic modules that could beat the current costs of even mass-produced mini-modules and there has been some development of Open-source photovoltaic modules [229], that could be leveraged here to make lower-cost field deployable DIY solar powered instruments.

Finally, future work is needed in the area of material compatibility. Earlier the potential for material contamination was discussed concerning the balls, which is a well-known issue with ball mills of all types and is corrected simply by the material selection of the ball. In this case, for some applications there may also be an issue with the walls of the cylinder (e.g. if polymer contamination is an issue for a particular project). In general, this can be fixed by post-processing the powder with solvents to remove contamination the 3-D printing polymers, which can be easily removed through using appropriate solvent [230].

3.1.4 Conclusions

To summarize, the highly customizable, low-weight open-source ball mill is fabricated using low-cost readily accessible RepRap-class fused filament 3-D printers. It can be powered by both an AC power supply as well as a solar PV module and battery with switchable power. The latter enables off-grid operation when proper and reliable grid electricity is not accessible and makes it easier to use the ball mill in the field environment. The final product cost is less than US\$130 when using the AC powered version and less than US\$315 when is powered by the solar photovoltaic system. The open-source ball mill is applicable for use in a wide range of scientific applications. As an example the open-source ball mill is also made with standard dimensions to work effectively and has been demonstrated to grind silicon particles from waste PV modules from 0.8 mm to 7 μm in 18 hours.

3.2 Open-source scientific bottle roller

Proprietary bottle rolling systems automate some laboratory applications, however, their high costs limit accessibility. This work provides designs of an Open-source bottle roller that is compatible with distributed digital manufacturing using 3-D printed parts and readily available commercial components. The experimental results show that the Open-source bottle roller can be fabricated for CAD\$210 (about USD\$150) in materials, which is 86% less expensive than the most affordable proprietary bottle roller on the market. The design, however, is more robust with enhanced capabilities. The design can be adapted to the user's needs but is already compatible with incubators with a low profile (dimensions 50 cm x46 cm x8.8 cm) and capable of being operated at elevated temperatures. The systems can be adjusted to revolves from 1 to 200 RPM, exceeding the rotational speed of most commercial systems. The Open-source bottle roller as tested has a capacity greater than 1.2 kg and can roll twelve 100 mL bottles simultaneously. Validation testing showed that it can operate for days at 80 RPM without human intervention or monitoring for days at both room temperature and elevated temperatures (50 °C). Future work includes adapting the designs for different sizes and for different fabrication techniques to further reduce costs and increase flexibility.

3.2.1 Hardware in context

A scientific bottle roller is used to rotate bottles at a set speed ranging from 1 revolution per minute (RPM) up to 80 RPM [231]. Bottle rollers are used in a range of scientific research areas such as cell cultivation [232,233], sediment leaching [233], gold particulate separation [234], chemical blending [235], drying [236], and many other applications outside of the lab such as mixing essential oils or bituminous mixtures [237]. Although commercial bottle rolling systems automate some of these laboratory applications, their costs limit accessibility as the retail price of a simple single-layer bottle roller costs CAD\$1540 (US\$1136.97) [238] and those that are used in incubators can cost over CAD\$2910 (US\$2148.44) [239]. The large costs of proprietary scientific bottle rollers summarized in Table 3-2 limit accessibility in the scientific community. It should be noted that the CAD\$ to US\$ exchange rate used was about 1.355.

Table 3-2. Proprietary commercial bottle roller costs and specifications.

Commercial Proprietary Product	Cost	Specifications
Thermo Scientific Bottle/Tube Roller [238]	CAD\$1,539.00 (US\$1136.24)	Speed Range: 1 to 80 RPM
		Temperature Range: 4 °C to 60 °C
		Number of rollers: 6
Fisherbrand Digital Bottle Roller [240]	CAD\$1,888.98 (US\$1394.62)	Speed Range: 1 to 80 RPM
		Temperature Range: 4 °C to 60 °C
		Number of rollers: 3
Bottle/Tube Roller [231]	CAD\$2,188.11 (US\$1615.47)	Speed Range: 2 to 38 RPM
		Temperature Range: 4 °C to 60 °C
		Number of rollers: 2
Scientific Low-Profile Bottle Roller [241]	CAD\$3,239.98 (US\$2392.06)	Speed Range: 1 to 80 RPM
		Temperature Range: 0 °C to 60 °C
		Number of rollers: 10
FlexiRoll Digital Tube/Bottle Roller Shaker [242]	CAD\$3,329.86 (US\$2458.42)	Speed Range: 0.5 to 80 RPM
		Temperature Range: 4 °C to 60 °C
		Number of rollers: 15–20

As discussed in Section 3.1.1, free and open-source hardware (FOSH) combined with distributed digital manufacturing offers a proven pathway to reduce the cost of scientific equipment while enabling customization and user control. However, despite the existence of several open-source mixing and agitation devices, there is currently no validated open-source bottle roller design available in the scientific literature that can be readily fabricated using a digital distribution model.

This work aims to overcome this limitation by reducing the cost of bottle rollers using the open hardware approach and distributed digital manufacturing. Specifically, this section provides the designs for an Open-source bottle roller that is a less expensive alternative to commercial bottle rolling systems, while also increasing the capacity of the bottle roller to allow for fewer bottle rolling systems to be used to complete a larger task. The Open-source bottle roller is manufactured using 3-D printed parts for custom mechanical parts and readily available components for the power supply, rollers, bearings, and speed controller.

3.2.2 Hardware description

The open-source bottle roller can be printed on any thermoplastic materials extrusion-based 3-D printer, but to overcome commercial limitations, the main components of the device are fabricated using a RepRap-class fused filament 3-D printer. Furthermore, the electronic parts, rollers, bearings, and speed controller are provided from readily available components in the local markets. The Open-source bottle roller is fully customizable and allows the user to increase the capacity of bottles on a larger scale. Testing and validation are provided to compare the quality of the Open-source bottle roller with the available commercial ones, and a comparison in price is made to show the economic advantage of the open-source one with commercial peers. The features of the Open-source bottle roller include:

- Low-cost chemical mixing for laboratory purposes
- Customizable design based on the user's needs
- Compatible with incubators with a low profile (dimensions 50 cmx46 cmx8.8 cm)
- Revolves 1 to 200 RPM, while the maximum speed of most commercial systems is 80 RPM
- Operational in an incubator at elevated temperatures (50 °C)
- Holds 12 bottles of 100 mL simultaneously. (Capacity greater than 1.2 kgs)

The design files, bill of materials, and operation principles are outlined in <https://osf.io/ps57u/>.

3.2.3 Validation and characterization

In this section, the performance of the Open-source bottle roller design was evaluated by comparing it to commercially available options. For this purpose, the information on the specifications and performance were collected as are provided in Table 1. The variables that will be investigated are: 1) the ability to maintain the appropriate speed that is required for the bottle roller to be effective over the duration of the desired amount of time at room temperature, and 2) the bottle roller ability to maintain constant speed while maintaining structural integrity in an oven at 50 °C.

Validation testing for the open-source bottle roller was designed to test the durability of the design in a heated environment for an extended period and be able to function at the same level as a commercial bottle roller. Validation testing took place for 48 h by placing twelve roller bottles completely filled with water, which had a weight of 100 mL per bottle. The speed controller allows fixing the speed at a precise number, including 80 rpm. With the open-source bottle roller fully loaded it was placed in a 50 °C oven with the rotation speed on the bottle roller set to 80 RPM. The bottle roller design and components were validated by maintaining full functionality after 24 h of continuous operation in the 50 °C oven. The operation of the Open-source bottle roller can be seen in two supplementary videos [52], [53].

The capabilities of the Open-source bottle roller include:

- The capital cost is reduced to CAD\$210, which is 86% less expensive than the most affordable commercial bottle roller shown in Table 1.
- Capability of rolling 12 bottles filled with 100 mL water for at least 48 h without failure in room temperature at 80 RPM speed. Although the motor became slightly warm after several days of operation, it functioned safely without raising any concerns about causing injury during use or failure. Ability to operate for 24h at elevated temperatures (50 °C) without failure.
- The bottles roll smoothly on the PVC pipes. To enhance the friction between the bottles and the pipes for applications with heavier masses, the pipes can be sanded or have rubber added to create a rougher/higher surface friction surface.
- Having a broader range of speeds offers the advantage of utilizing the bottle roller for other scientific applications. For instance, this device can be used to achieve homogeneous dispersion of silicon particles into polymer resin for 3-D printing of silicon-based objects via an SLA printer.
- Since the open-source bottle roller is customizable, it can accommodate different sizes of bottles by using PVC pipes with various dimensions.
- The device includes multiple belts that can be easily removed when the user needs to rotate fewer bottles. By removing belts, the user can reduce the number of pipes that roll, optimizing the device's performance for their specific application.

3.2.4 Future work

The Open-source bottle roller was designed to be manufactured by most desktop 3-D printers. This asset, however, can be a limitation as because of the printer bed size being smaller than the device, the main body of the bottle roller is separated into eight pieces, which significantly impacts the structural strength. The connectors and reinforcement bars are designed to overcome this limitation by connecting these pieces together, but they result in the excess of printed parts, a slight increase in the height of the system and added costs for connectors. There are several Open-source approaches to solving this issue. First, a large format Open-source 3-D printer could be used to print the entire structural frame in a single print. If the large format printer was also a waste plastic fused granular fabrication (FGF)-based 3-D printer (cartesian [243], delta [244], or hang printer [245,246]) the costs of the system could be reduced further by about 10% as recycled PETG particles could be used instead of filament. For example, the bottle roller could be fabricated by waste plastic PET water bottles [247]. Moreover, by selecting a higher melting point 3-D printable polymer like polycarbonate (PC) even higher temperature operation may be possible [248]. Another potential solution to this design limitation is to utilize open-source laser cutting or CNC milling [249] to cut the four sides of the bottle roller on a plastic sheet. Further the plastic sheets could be fabricated in an Open-source hot press from recycled plastic as well [250]. This way, the bottle roller can be held in place, and the connectors and reinforcement bars can be eliminated and ensure overall strength and stability. In addition, to reduce the purchased components the PVC pipes can be replaced by 3-D printed pipes or extrusion molded pipes from an Open-source recyclebot [131,251–254].

Moreover, the bottle roller is customizable to be used in different scale applications. The smaller version can be obtained using PVC pipes with smaller diameter. It should be pointed out that the same percentile cost savings could be had by using either filament from an open-source recyclebot or small-scale FGF [255,256]. In this regard, changing the dimensions of the provided designs can be helpful. Also, the user can make the bigger version through adding outer plates. The other design that can be useful and adapted easily from the current design for some applications is the stacked version that consist of some bottle rollers on top of each other. This would be helpful for scaling bottle rolling

applications to greater production volumes. The bottle roller can also be used for non-cylindrical components or specialty vessels. To do this a 3-D printed component can be fashioned to hold these non-optimal vessels. To illustrate this Figure 3-4 shows a 3-D printable holder for a microcentrifuge tube, which can then be used on the Open-source bottle roller. Similar strategies can be used for many microcentrifuge tubes or other types or shapes of containers.



Figure 3-4. 3D printable adapter for microcentrifuge tube.

3.3 Open-source Inert Gas Glove Box

A glove box is a controlled environment used for a wide range of scientific experiments. While glove boxes provide significant advantages, their high economic costs ranging from over \$1,000 to over \$15,000 limits their accessibility in under-resourced labs. There are lower-cost DIY designs available on the internet, but they have not been well characterized nor validated. To overcome these limitations, in this work, an Open-source glove box design is developed for scientific applications using readily available components and digital distributed manufacturing using open-source RepRap-class 3D printers. The ability of the glove box to hold an inert atmosphere is quantified using an oxygen analyzer. The Open-source glove box can be customized to the dimensions of the user and the volume of the experiment. The design also enables the use of customizable transfer chambers that can be adjusted based on the scientific application. The Open-source glove box is built from a low-cost enclosure while preventing contamination. The highly portable device can reduce oxygen down to 19 ppm using an inert gas. The economic savings of the validated device compared to proprietary systems is over 95%.

3.3.1 Hardware in context

A glove box is a controlled enclosure used to handle air- and moisture-sensitive materials in chemical synthesis, materials processing, biological research, and electrochemical device assembly [257]. Typical glove boxes consist of a sealed chamber equipped with gloves, a transfer port, and an inert gas supply (e.g., nitrogen or argon) to maintain low oxygen and moisture levels [258]. Such controlled environments are essential in materials and battery research, where exposure to oxygen or moisture can degrade reactive components, alter interfacial chemistry, and compromise experimental reproducibility [259]. For example, when working with metal alkyls and aryls, it is necessary to maintain oxygen levels below 15 ppm [260–262]. In the synthesis of tin oxide sheets, glove boxes maintain oxygen levels between 10–100 [263]. In the analysis of the organic solar cells, an environment with 20 ppm oxygen level should be provided [264]. In biochemical laboratories, glove boxes are essential for working with oxygen-sensitive enzymes and compounds to maintain their stability and activity [265]. In biological research, they

provide sterile conditions necessary for applications like cell research [266]. Additionally, in cryo-TEM experiments, glove boxes help prevent sample dehydration and preserve the original state of specimens [4]. In nuclear laboratories, they are used to secure safe handling of radioactive materials [258]. Moreover, in battery assembly, glove boxes prevent environmental contamination and provide the safe handling of reactive materials [266], similar to the function of a fume hood in preventing the release of unsafe particles and chemicals into the environment [267]. While glove boxes provide significant advantages, their high economic costs ranging from CAD\$1,424 to CAD\$15,120 (see Table 3-3), can limit their accessibility in under-resourced labs. To address this issue there are three main approaches. First, some researchers have explored alternative approaches to conduct their targeted research. For instance, Kubota et al. adopted mechanochemistry for C-N cross-linking reactions in the solid-state to avoid the need for a glove box [257,268]. Similarly, Yaghoobi et al. employed a crystal engineering approach and optimized deposition methods to fabricate perovskite solar cells and modules without using a glove box [269]. Although it is possible to engineer experiments to avoid using glove boxes, this is not always possible. Researchers in various fields, such as material sciences, pharmaceuticals, agrochemicals, and sensors, may face challenges in the usability of synthetic methods due to not having access to a glove box [259]. To address the expenses associated with necessary research equipment, a second strategy involves building the equipment. There are several Do It Yourself (DIY) designs available all of which are made from a clear plastic box and elbow-length waterproof gloves. For instance, in a prominent design published by *Make Magazine* [270], PVC pipes are used for the arm holders which are securely attached to the box with sealant to prevent the leakage [271]. To manage the internal atmosphere, a ventilation fan and air hose are used to blow air out of the box which creates a slightly lower pressure inside compared to the outside. This setup helps maintain a controlled environment. This glove box is designed to be easy to use, portable, and low-cost; however, there are limitations including the lack of a transfer chamber, which restricts the ability to safely insert and remove materials without contaminating the internal atmosphere. Additionally, the atmosphere inside the box is not inert, which is critical for many laboratory applications. The method of purging oxygen using a fan is not practical for achieving the low oxygen level that is required in many scientific applications.

Furthermore, the glove box has not been validated which makes it unreliable for precise laboratory research [271]. In another glove box design, PVC pipes were used as arm holders, and argon gas was introduced at 10 cubic feet per minute, which required 6.5 minutes to fill the box and displace the air. While the box slowed lithium metal oxidation, the presence of residual air made it unreliable for precise laboratory experiments [272]. In another found DIY glove box, the Fresno Mycology Society used short piping as arm holds and applied epoxy to secure the pipes. This glove box is also easy to use and portable but it is not designed to have an inert atmosphere [273]. Another approach used plastic water outlets for replacing the air with inert atmosphere, but again this glove box has not been validated [274]. A summary of these DIY glove boxes is shown in Table 3-4.

As discussed in Section 3.1.1, free and open-source hardware (FOSH) and distributed digital manufacturing provide a proven pathway for reducing the cost of scientific equipment while enabling customization and validation [275,276]. Existing DIY glove box designs used in the second approach do not rely on distributed digital manufacturing for parts. This is a missed opportunity as the literature indicates distributed manufacturing with 3D printing reduces costs and increase customization on a wide range of products [283–286]. In addition, all of the designs in Table 2 have not been well characterized and validated. To overcome these limitations, in this section, an Open-source glove box design is developed for scientific applications using readily available components and digital distributed manufacturing using a RepRap-class 3D printer.

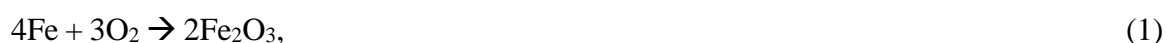
Table 3-3. Representative selection of commercial glove boxes specifications.

Commercial Proprietary Product	Cost (CAD\$)	Dimensions	Material	Applications	Unique specifications
sidENTRY Glove Box [287]	5,429.00	30 x 24 x 24 in	Acrylic	Medical and Laboratory	Portable
Scienceware portable glove box [288]	2,370.00	27 x 13 x 22 in	Acrylic	Isolating materials that need to be processed	Portable
Plas-Labs compact glove box [289]	15,120.00	63 x 31 x 34 in	N/A	Toxic materials and pharmaceuticals	-Determining the dry weight or moisture content of aqueous solutions, adhesives, cereals, toxic chemicals, pharmaceuticals, paper, plastics, and light radioactive materials -Multiple electrical outlet strip
Pasaurina Glove Box [290]	1,423.88	23.6 x 19.7 x 20.5 in	Body framework/Stainless steel, Positive side window portion/PC	N/A	N/A

Table 3-4. DIY glove boxes.

Maker	Materials	Validation	Advantage	Disadvantage	Ref.
Make Magazine	Clear plastic box, PVC pipes, sealant, elbow-length waterproof gloves, ventilation fan, air hose	Not validated	Easy to use, portable, low-cost	Lacks transfer chamber, atmosphere not inert, impractical oxygen purging method, not reliable for precise laboratory work, lacks transfer chamber, not adequate arm holds for many users	[271]
MHS	Clear plastic box, PVC pipes, epoxy, hose barb, barb valve, argon tank	Inaccurately validated	Easy to use, portable, low-cost, uses argon for inert atmosphere	Residual air present, inaccurate validation with match test, unreliable for precise laboratory experiments, lacks transfer chamber, not adequate arm holds for many users	[272]
Fresno Mycology Society	Clear plastic box, short piping sections, epoxy	Not validated	Easy to use, portable, low-cost	Lacks transfer chamber, atmosphere not inert, arm holds may not be adequate for all users, unreliable for precise lab work, lacks transfer chamber, not adequate arm holds for many users	[273]
Patti	Clear plastic box, PVC pipes, PVC glue, silicone, plastic water outlets	Not validated	Easy to use, potentially useful for basic tasks	Atmosphere control uncertain, may not meet requirements for sensitive applications, lacks transfer chamber, not adequate arm holds for many users	[274]

The ability of the glove box to hold an inert atmosphere is quantified using an oxygen analyzer. This open-source glove box design effectively bridges the gap between unvalidated DIY glove box solutions and expensive commercial systems by offering a validated, low-cost, and customizable alternative. Unlike many DIY designs, it includes a transfer chamber and has been quantitatively validated to reach oxygen levels as low as 19 ppm, which shows reliable performance for scientific applications. At the same time, it maintains the adaptability and affordability of DIY approaches through open-source digital manufacturing methods by achieving over 95% cost savings compared to commercial models. To attempt to enhance the inert atmosphere within the glove box, iron powder was also used as an oxygen scavenger [291]. The use of iron as an oxygen scavenger is based on its chemical reactivity with oxygen. When iron is exposed to oxygen, it undergoes an oxidation reaction that forms iron oxide (Fe_2O_3 or Fe_3O_4). This reaction can, in theory, remove oxygen from the environment. The reactions can be described by the following equations:



These exothermic reactions proceed spontaneously in the presence of oxygen which gradually reduce the oxygen content inside the sealed glove box. Also, when moisture is present in the environment, iron powder can also reduce moisture through its reaction with water. This reaction, where iron reacts with both oxygen and water to form iron hydroxide, can be represented as:



This process not only removes oxygen and moisture from the environment, but the presence of moisture accelerates the oxidation process, which makes the iron powder more efficient at scavenging oxygen and maintaining a more inert and stable atmosphere within the glove box [291].

Considering equation (1), 1 mole of Fe reacts with 0.75 moles of O_2 . The molar mass of Fe is 55.85 [292] g/mol, and of O_2 is 32 g/mol [293]. Therefore, 1 g of Fe can scavenge:

$$\text{Moles of Fe} = \frac{1 \text{ g}}{55.85 \text{ g/mol}} \approx 0.0179 \text{ mol}, \quad (4)$$

$$\text{Moles of O}_2 \text{ scavenged} = 0.0179 \times 0.75 \approx 0.0134 \text{ mol}, \quad (5)$$

$$\text{Mass of O}_2 \text{ scavenged} = 0.0134 \times 32 \approx 0.429 \text{ g}. \quad (6)$$

At Standard temperature and pressure (STP), 1 mole of O₂ gas occupies 22.4 L [294].

Therefore, 0.0134 mol O₂ occupies:

$$0.0134 \times 22.4 \approx 0.3 \text{ L}. \quad (7)$$

This suggests that 1 g of Fe can remove about 300 mL of oxygen gas at standard conditions. In the current glove box (with the capacity of 74 Qt equal to 70.2 L), the initial oxygen concentration (~3,520 ppm) represents:

$$3,520 \text{ ppm} = \frac{3,520}{10^6} \times 70.2 \text{ L} \approx 0.247 \text{ L of O}_2. \quad (8)$$

This shows that, in theory, 1 g of Fe powder could scavenge more oxygen than required to reach 0 ppm in the box. However, it should be noted that in the present work, iron powder was observed to reduce oxygen levels only to 19 ppm. This suggests that practical factors limit this capacity. The formation of a passivation layer of iron oxide on the surface of the iron powder reduces the availability of reactive sites, which inhibit further oxygen uptake. Additionally, the lack of sufficient moisture can slow down the reaction kinetics, particularly for reactions that rely on water as a catalyst. Incomplete exposure of the iron particles to the glove box atmosphere also limits their effectiveness, as not all reactive surfaces come into contact with the gas phase.

3.3.2 Hardware description

The Open-source glove box can provide low-cost custom components since the connections are fabricated by a RepRap-class fused filament 3-D printer, and the other parts including the clamps, the gloves and the box are readily available in the market. The arm holds are customizable and can be resized based on the user convenience.

- Low-cost enclosure for preventing contamination while doing scientific experimental
- Economic savings of over 95%
- Customizable arm holds
- Customizable transfer chambers that can be adjusted based on the user's convenience and the scientific application.
- Portability
- Customizable volume based on the user need
- Oxygen reduction down to 19 ppm using an inert gas

3.3.3 Validation and characterization

The validation of the glove box was carried out using an OMD-507 In-line Oxygen Analyzer, which is capable of measuring oxygen concentrations from 0.1 ppm to 100%. This high precision provides an accurate monitoring of oxygen levels within the glove box. During the validation process, 99.999% UHP nitrogen gas (Linde Canada Inc.) was continuously purged into the glove box at a flow rate of about 4.7 liters per minute. For further analysis of the environmental conditions inside the glove box, a battery powered digital pinless moisture meter (Mastercraft) with an accuracy of $\pm 4\%$ was used to monitor moisture levels. This device allows for non-destructive measurement of moisture content. The results of the validation test show that the initial oxygen concentration was reduced from 3,520 ppm to 19 ppm within 20 minutes as shown in Figure 3-5a. Achieving such low oxygen levels is important for maintaining an inert atmosphere in applications that are

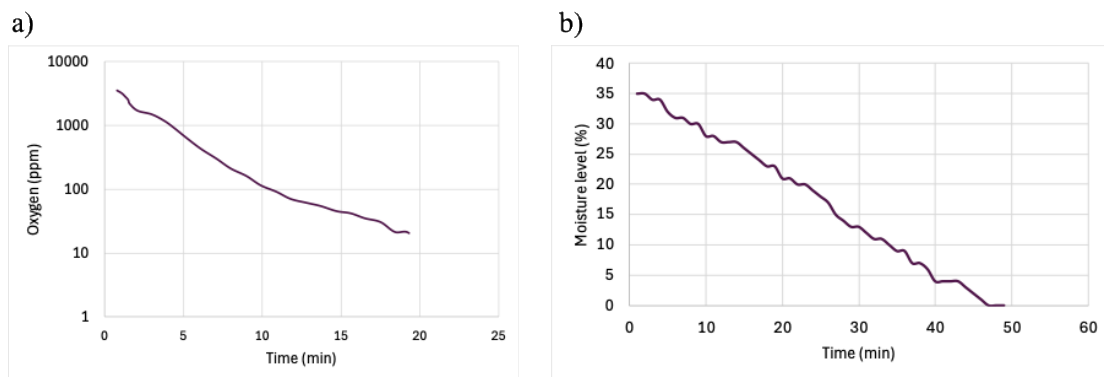


Figure 3-5. a) Oxygen reduction in the glove box vs time, b) Moisture level reduction in the glove box vs time

related to work with air-sensitive and moisture-sensitive substances such as synthesis of tin oxide sheets (10-100 ppm), or analysis of the organic solar cells (<20ppm) [261,263,264]. In addition, the moisture level went down to 0% (Figure 3-5b) [295]. The validation experiment was repeated with the same results.

This comprehensive validation confirms that the glove box can maintain a controlled atmosphere with small oxygen and moisture levels. Such conditions are essential for a wide range of sensitive applications, including material science research and electronics manufacturing. The amount of oxygen inside the box after purging nitrogen was measured using an oxygen analyzer. The oxygen level reduction experiments were repeated two times. For every run It took about 20 minutes to reduce the amount of oxygen from about 3520 ppm to <20ppm (see supplemental data [295]). The oxygen level reduction experiments were repeated two times, and in both trials, the glove box consistently reached oxygen concentrations of 19 ppm within 20 minutes, which confirms reliable performance under standard operating conditions. However, fluctuations in oxygen levels can occur if the glove box is frequently opened or if minor leaks develop over time.

Additionally, while the current system does not include integrated sensors for continuous monitoring, such features are discussed as potential future improvements.

Compared to existing DIY glove box designs, which often lack a transfer chamber and have not been validated for low oxygen levels, the presented open-source glove box offers a validated inert atmosphere (reduction to 19 ppm) and includes a customizable transfer chamber that allows safe loading and unloading of materials without compromising the internal environment. This design also leverages digital distributed manufacturing via 3D printing, which offers customization not found in conventional DIY setups. In contrast to commercial glove boxes, which can cost up to CAD\$15,120, this open-source design achieves over 95% cost savings while retaining essential functionality and flexibility for laboratory applications.

While the glove box achieves a significant reduction in oxygen concentration (from 3,520 ppm to <20 ppm in 20 minutes), the time required for purging will vary depending on the size of the box selected and initial oxygen levels. Additionally, for very sensitive

applications that require ultra-low oxygen levels (<1 ppm), such as battery assembly (<0.1 ppm) [296], and cell culture experiments (<9.1 ppm), the system would need further optimization. Although iron powder was employed as an oxygen scavenger, it did not reduce oxygen levels below 19 ppm, which indicates the need for more efficient scavenging materials or methods. Also, the moisture levels were measured using a moisture meter with an accuracy of $\pm 4\%$. This accuracy may be low for applications that require extremely dry environments. It should be noted that the sensors used in this work for oxygen and moisture validation were third-party devices not integrated directly into the glove box itself. Many commercial glove boxes incorporate integrated sensors for real-time monitoring, which can be essential for ultra-sensitive applications requiring continuous atmosphere control. Although this open-source design does not include built-in sensors, future developments could explore the incorporation of integrated sensors for continuous monitoring, to provide enhanced control over experimental conditions.

A limitation of this work is the inherently porous nature of the untreated printed parts produced using FFF-based 3D printing, which may affect long-term sealing performance. To mitigate this limitation, a high infill density (above 80%) can be employed during the 3D printing process to ensure less porous structures. Although the components performed well in the performed experiments, post-treatment options such as epoxy coatings or chemical sealing are recommended to enhance gas impermeability and maintain low oxygen concentrations during extended use or in more sensitive applications. However, an advantage of this open-source and 3D-printed approach is that any component that becomes unsuitable for use over time can be easily reprinted and replaced, which minimizes operational disruptions and reducing costs.

Future developments could explore more effective oxygen scavengers that are capable of reducing oxygen levels to below 1 ppm and would enable the glove box to be used in more sensitive applications, such as activated carbon [297], molecular sieves [298], and copper-based scavengers [299]. Also, adding automated control systems that adjust purging rates in real-time based on oxygen and moisture sensor feedback could further enhance efficiency. By reducing the reliance on constant purging and improving the overall efficiency of gas use, future versions of the glove box could contribute to sustainability and

reduced operational costs, particularly in research and industrial applications that require long-term use of inert environments.

Chapter 4

4 Recycling Silicon Photovoltaic Cells into Silicon Anodes for Li-ion Batteries Using 3D Printing

With the increasing adoption of solar energy, the disposal of end-of-life photovoltaic modules has become a growing environmental concern. As crystalline silicon has significant potential as an anode material for lithium-ion batteries, this chapter investigates recycling waste solar cell material into batteries using 3D printing. An open-source toolchain is developed to ensure accessible replication including a ball mill for grinding the waste silicon, a bottle roller for synthesizing novel stereolithography (SLA) resins and an SLA 3D printer for geometric control of the deposition of the materials. The materials were characterized at each step using spectrometry analysis, differential thermal analysis and thermogravimetric analysis of the polymer resin, optical microscopy on the printed parts, as well as scanning electron microscopy, energy-dispersive X-ray spectroscopy, and X-ray diffraction on the pyrolyzed parts. Electrochemical characterizations, including cyclic voltammetry, galvanostatic charge-discharge, and electrochemical impedance spectroscopy, were performed on the assembled batteries. A mixture of 12% ground silicon solar cells with SLA resin was used for 3D printing the anodes and the samples were pyrolyzed at 1400°C. The electrochemical tests from the anodes demonstrated a specific capacity of around 400 mAh/g with 89% capacity retention and Coulombic efficiency more than 100% over 200 cycles. This chapter presents a promising sustainable solution by integrating recycled solar cell waste into lithium-ion battery anode production, which can address both waste management and energy storage challenges.

4.1 Introduction

Developing electronic devices such as portable electronics and electric vehicles and the demand for storing the green energy have attracted increasing interest and efforts toward investigating high performance energy storage devices among which electric batteries are designed to store and release electricity through electrochemical reactions [1,2]. Batteries

are classified into primary (non-rechargeable, single-use) and secondary (rechargeable, reusable) types [1]. Rechargeable lithium-ion batteries dominate the secondary battery field due to their high theoretical charge capacity (4200 m Ah g^{-1}), high energy density (300 Wh kg^{-1}), and portability [300–302]. Lithium-ion batteries are made of three main parts: anode, cathode, and electrolyte. Graphite and carbon-based materials have been widely used as anode due to the good electrochemical properties and low cost, but their applications are limited due to low capacity, which results in poor theoretical capacity in lithium ion batteries down to 372 m Ah g^{-1} [303,304]. Silicon is one of the most promising alternatives for graphite due to its multiple advantages, including both abundance and a high specific capacity of about 3579 mAh g^{-1} [304]. Crystalline silicon (c-Si) photovoltaic (PV) modules, which make up over 93% of total production, contain about 0.67 kg of silicon per module which represent a significant source of silicon waste material [305]. Although PV is a well-established renewable energy source that provides a sustainable state [306] it still provides an operational life of 20–30 years under warranty [307]. At the end of 2016, there were around 250,000 metric tons of solar panel waste globally, and this volume is projected to increase to more than 60-78 million metric tons cumulatively by 2050 [307]. Recycling this waste economically is a challenge [308,309] so establishing an upcycled application would have high value. Silicon in this solar waste is a good candidate for use in anodes in lithium-ion batteries because it has already undergone modification and purification [310]. Silicon-based anodes for large-scale applications are limited, however, due to their poor intrinsic conductivity, and huge volume change, more than 300%, during lithiation and delithiation. The volume change creates particle pulverization and repeated formation of solid electrolyte interface (SEI) layer that results in low columbic efficiency (61.7%) [175,304,311,312]. One of the solutions to address these issues is compositing silicon particles with carbon. In this regard, silicon provides the anode with high capacity while carbon increases the conductivity and alleviates the volume change by surrounding the silicon in the structure [312]. The conventional way to fabricate batteries is based on preparing slurries, then tape casting onto the current collector, and subsequently assembling and packaging the cell components [313]. Unfortunately, this fabrication method is difficult to optimize and customize the design and decreases the efficiency. For improving the energy density, a thicker anode is required to accommodate more active

materials for storing Li ions inside the electrode, but through the conventional method, increasing the thickness is equal to decrease the power density since it is more difficult for the Li ions to transport through the entire thickness and reach the active sites inside the structure [314]. To address this, 3D printing, with its ability to precisely control and engineer the design, can help achieve a shorter ion transportation distance while maintaining a high solid load of active materials. This approach allows for the enhancement of both energy density and power density simultaneously [315]. Various geometries have been proposed to enhance battery performance, among which the 3D porous structure is not achievable through conventional methods but can be easily fabricated using 3D printing. Among different 3D printing methods, direct ink writing (DIW), inkjet printing, photopolymerization, fused filament fabrication (FFF) (material extrusion), aerosol jet printing, and selective laser sintering are promising for battery fabrication [31,51,316]. Although the most popular 3D printing methods, the extrusion-based methods require complex material preparation to optimize the material rheological behaviour with high viscosity and suitable density [317,318]. Stereolithography (SLA), however, is not restricted by extrusion and provides the part with more flexibility, and design resolution comparing to other methods including FFF or DIW and can be a promising candidate for fabricating battery components. Thus, SLA printing of the Si based anode can be a solution to enhance the battery performance [319]. To test this hypothesis, in this work, a novel low-cost open-source hardware [275,280] method is proposed to 3D print the anode part of a Li-ion battery using silicon PV solar cell waste. For the first step, the waste is ground using an open-source ball mill to obtain <50 microns particles [27]. This particle size offers several advantages, including higher tapped density, lower specific surface area (which minimizes side reactions), and higher volumetric capacity compared to nanometer-sized particles [320]. Then, the silicon particles along with dispersant and photo-initiator are mixed with UV-curable resin by an open-source bottle roller [28]. The slurry was then used to print an acrylate-silicon composite using an SLA 3D printer. After pyrolysis in an N₂ atmosphere, the anodes were assembled into coin cells in a glove box. The materials were characterized at each step using spectrometry analysis, differential thermal analysis (DTA), and thermogravimetric analysis (TGA) of the polymer resin, optical microscopy on the printed parts, as well as scanning electron microscopy (SEM), energy-dispersive X-ray

spectroscopy (EDS), X-ray diffraction (XRD) on the pyrolyzed parts before and after cycling, and Raman spectra on the pure transparent red resin before and after pyrolysis. Additionally, electrochemical characterizations, including cyclic voltammetry, galvanostatic charge-discharge, and electrochemical impedance spectroscopy (EIS), were performed on the assembled batteries.

4.2 Experimental Section

The schematic of the processing steps is shown in Figure 4-1.

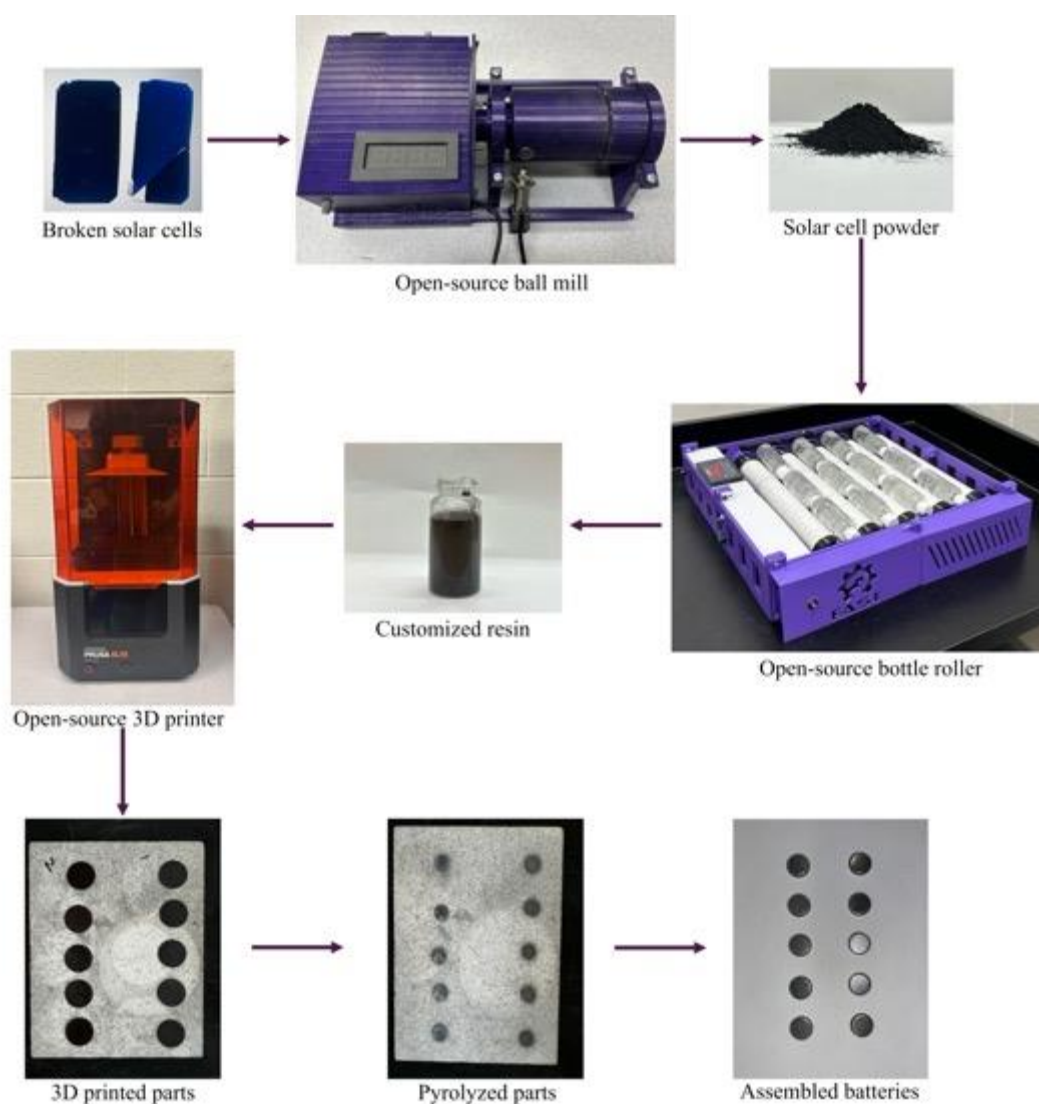


Figure 4-1. Processing steps for recycling silicon solar cells into batteries.

4.2.1 Materials

The broken c-Si-based solar photovoltaic cells were acquired from Heliene Inc. (Sault Ste. Marie, Ontario, Canada). The dispersant used here is cetyltrimethylammonium bromide (CTAB) (Sigma Aldrich, Ontario, Canada). The Prusament resins (transparent red, transparent amber, transparent blue, orange, and flexible) are purchased from the official Prusa Research (Prague, Czech Republic), the Anycubic resins (black and grey) are ordered from amazon.ca, and the 3DRS resins (colorbase, hard grey, white) are obtained from 3D Printing Canada (Ontario, Canada). Bis(2,4,6-Trimethylbenzoyl) phenylphosphine oxide is used as the photoinitiator which is provided from IGM resins (Charlotte, North Carolina). The 32 μ m mesh size sieve from KimLab (Ontario, Canada).

4.2.2 Resin fabrication

The processing steps are illustrated in Figure 4-1. The broken solar cells, they were ground down using the open-source ball mill. The ground solar waste was sieved with 32 micrometer sieves. To remove impurities from the broken solar cell powder, a washing process was carried out, as explained in the literature. Specifically, 9.0 g of broken solar cell powder was mixed with 150 mL of 37 wt% HCl. The mixture was stirred and heated to 80°C for 1 hour. After 1 hour, the mixture was allowed to cool to room temperature, and the solid residue was then filtered to obtain the purified silicon material and was placed in the oven in 60°C overnight. Then the powder was mixed with 2% of the solid load CTAB as the dispersant and 1% of the resin photoinitiator.

After that, the polymer resin was added to the powder. The solid load was 12wt% of the resin. The solution was moved into dark bottles to prevent the resin from curing. Using the open-source bottle roller, the mixture was mixed overnight to make a homogenous customized resin to be used in SLA printer.

4.2.3 3D printing of customized resin

For this step, the coin-shape anodes were designed with Onshape, and sliced in the PrusaSlicer. The design and all data for this article are available on the Open Science Framework. A series of experiments was carried out to determine the most suitable

combination of layer thickness and exposure time to print the sample. Because the silicon resin requires a longer curing period than standard polymer resin without additives, its complete polymerization is the primary consideration in selecting the printing parameters. Different curing times were evaluated through trial and error to identify the shortest time that would cause each resin to adhere properly while minimizing the print time. For the initial layer, curing times under 31 seconds resulted in film breakage and incomplete bonding of the polymer resin to the build plate, which caused print failures. As a result, 31 seconds was used as the minimum time needed to adhere the polymer resin to the build plate. This finding was further validated by the photorheology result shown in Figure 4-2. Similarly, the silicon resin required at least 40 seconds to fully polymerize as curing it for any shorter duration led to insufficient curing and failed prints. Layer thickness values of 0.01 mm, 0.03 mm, and 0.05 mm were also evaluated. A 0.01 mm layer thickness was not suitable due to insufficient curing and long printing times, whereas a 0.05 mm thickness prevented proper light penetration through the resin and led to print failures. Among these options, a 0.03 mm layer thickness was optimal, which resulted in successful print while maintained sufficient resolution and acceptable print speed. After that, the samples were printed using Original Prusa SL1S SPEED 3D printer (Prague, Czech Republic). In this step multi-material printing was done. For this purpose, one vat was poured with the flexible resin, and the other one was poured with the customized resin. Since the customized resin caused contamination in the vat which affects the print quality in the future, an open-source vat was used for this purpose. The vat containing the flexible resin was placed in the printer and the print was started. In this step, when the machine started to print the first layer, pause/ stop was clicked. After the printer finishes printing the first layer, the build platform goes up and the vat is replaced by that for the customized resin. Then, the print is resumed. After the print finishes, the printed parts were separated from the build platform by a scraper. In this step, the layer printed by the flexible resin can be

separated easily. Then, the printed part was put in a curing machine that the excess resin that was uncured gets cured.

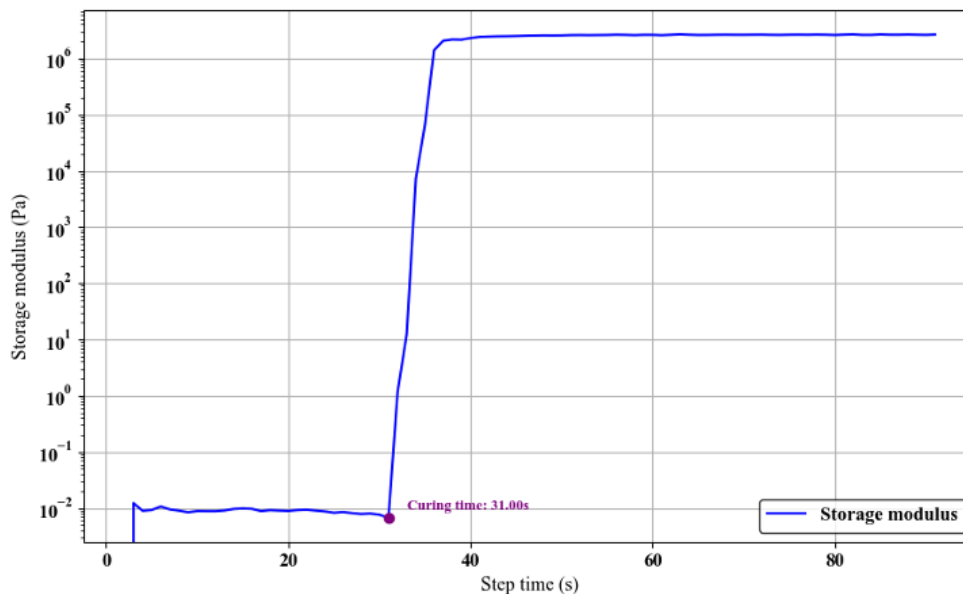


Figure 4-2. Photorheology results of the plain resin, showing the storage modulus as a function of step time.

4.2.4 Pyrolysis

The printed samples were placed in a gas-sealed box furnace, Model 1616 FL (CM Furnaces, USA), for pyrolysis. The samples were heated up to 850°C with 1°C/ min and the temperature was increased to 1400°C with 3°C/ min and they were kept in this temperature for 2h. After that, the furnace was cooled down to the room temperature with 10°C/ min rate.

4.2.5 Material tests

The Ocean Insight FLAME spectrometer was used to measure the absorbance index of different resin types before and after adding the solid load. The samples were scanned over the selected wavelength range of 200-800 nm and the absorbance was recorded. To analysis the amount of carbon in different types of the resins, DTA and TGA tests were conducted using Netzsch STA 409 (Netzsch GmbH, Selb, Germany) at 10 °C min⁻¹ up to 1200 °C in

flowing Air/N₂ (150 cc min⁻¹), to measure the carbon content after pyrolysis in an air atmosphere with a flow rate of 30 ml/min, starting from room temperature and heating to 800°C at a rate of 10°C min⁻¹. OpenFlexure Microscope from IO Rodeo was used to measure the dimensions of the printed parts. A scanning electron microscope (SEM) image was conducted to see the morphology and microstructure. Energy dispersive X-Ray (EDX) was used to identify the type of elements that are present as well as the percentage of each element concentration within the pyrolyzed samples. SEM and EDX were conducted using Hitachi SU3500 scanning electron microscope with an Oxford Instruments X-act EDX detector (Hitachi, Japan, Oxford instruments UK). X-Ray diffraction (XRD) was performed using Bruker D8 advance x ray diffractometer (Bruker GmbH, Germany), to analyze the phase and crystallinity of the samples after the pyrolysis. Raman spectroscopy was performed using a Raman microscope with a 514 nm laser excitation source (Renishaw, UK), to characterize the chemical structure of the pure transparent red resin samples before and after pyrolysis.

4.2.6 Electrochemical tests

The electrochemical performance of the fabricated anodes was evaluated using CR2032 coin cells. The assembly of these cells was conducted in an argon-filled glove box with oxygen and moisture levels maintained below 0.1 ppm. Celgard 2400 was used as the separator, and the electrolyte was composed of 1 M LiPF₆ in a mixture of ethylene carbonate (EC), diethyl carbonate (DEC), and dimethyl carbonate (DMC) in a 1:1:1 volume ratio with a fluoroethylene carbonate (FEC) additive. The chemicals were provided from Gotion, USA. Lithium metal (China) served as both the counter and reference electrode. Electrochemical tests were performed using CS300 model potentiostat from Corrtest, China. Cyclic voltammetry was performed using the potential in the range of 0.01 to 2.5 V (vs. Li⁺/Li) with a scan rate of 0.1 mV/s. Galvanostatic charge-discharge testing was carried out in the voltage range of 0.01 to 1.5 V (vs. Li/Li⁺) at a current rate of 1C.

4.3 Results and discussion

4.3.1 UV-Vis spectrometry

The absorbance results for the silicon-based resins indicate that adding solid content leads to an increase in resin absorbance index which means more energy is required to start the polymerization (Figure 4-3A). Due to the dark color, Si powder is known for its high optical absorbance and refractive index. This high optical absorbance of Si means that sufficient light does not reach deeper parts of the slurry to initiate photopolymerization [321]. This significantly reduces the penetration depth and curing thickness of the printed part [321]. It is also noticeable that adding carbon black to the resin while having the same solid load increases the absorbance of the resin compared to when the resin only contains silicon which is because carbon black is darker in colour. As a result, the amount of solid load in the resin is more limited. Also, to achieve effective curing, a photoinitiator, which

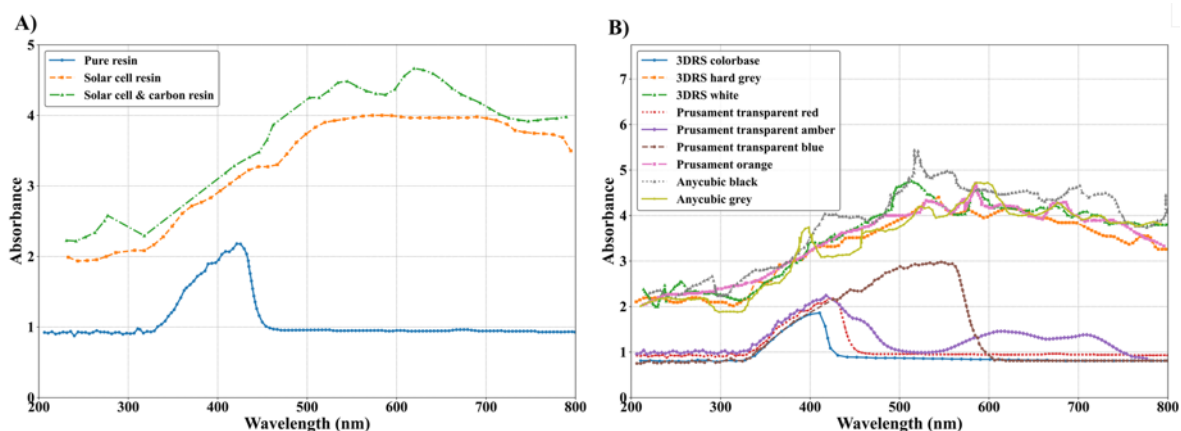


Figure 4-3. UV–Vis spectra of (a) resin formulations containing solid load and (b) pure acrylate resins, showing absorbance as a function of wavelength.

has high initiating activity and a broad absorption wavelength range is required [321]. Also, spectrometry analysis of different polymer resins from various manufacturers reveals that the colorbase resin from 3DRS, which is transparent, exhibits the lowest absorbance index (Figure 4-3B). Following this, the Prusament transparent red resin also shows a relatively low absorbance index. Thus, the colorbase and transparent red resins are identified as the most suitable candidates.

4.3.2 DTA and TGA

The DTA results show the decomposition of various elements at different temperatures (Figure 4-4A). The peaks observed up to 600°C are attributed to the decomposition of organic compounds of H₂O, CO, CO₂, CH₄, and H₂, as well as the polymer burnout. This stage of decomposition results in significant weight loss, which leaves the free carbon residue behind. The TGA curves reveal that the Prusament transparent red resin exhibits less weight loss compared to the other tested resins (Figure 4-4B). This indicates a higher carbon content in this resin which means that after pyrolysis it shows less shrinkage. This characteristic is beneficial for anode fabrication where mechanical integrity and strength are important. Considering the TGA results along with the UV-vis spectrometry, the best candidate for customizing the resin is the transparent red resin, as it offers a low absorbance index and the highest carbon content.

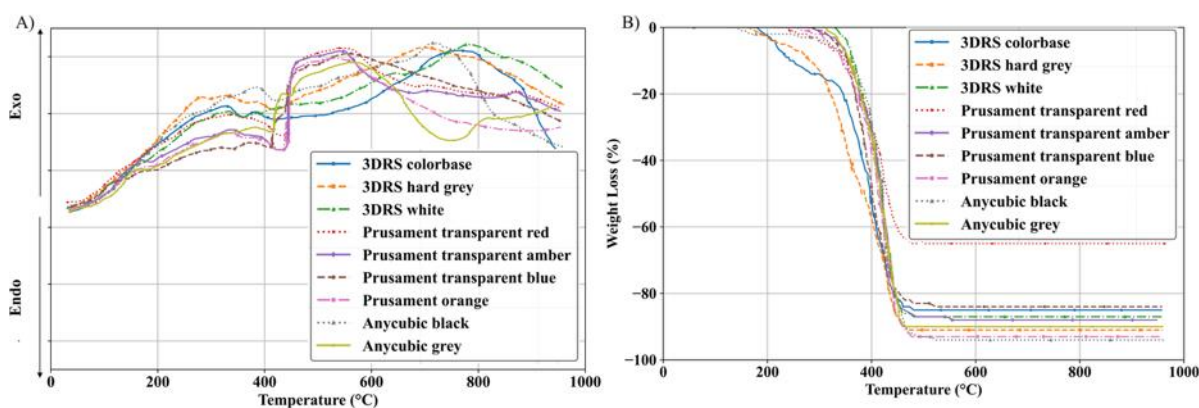


Figure 4-4. A) DTA, and B) TGA results from different acrylate resins.

4.3.3 Raman spectra and XRD

Figure 4-5A shows the Raman spectra of the pure transparent red resin before and after pyrolysis. Before pyrolysis, the spectrum exhibits peaks at 1287, 1414, 1616, 1641, 1700, 1725, 2881, and 2947 cm⁻¹, which are corresponding to various functional groups characteristic of the polymeric structure. The peaks in the 1700-1725 cm⁻¹ range indicate the presence of carbonyl groups. Also, peaks at 2881 and 2947 cm⁻¹ are related to C-H stretching in aliphatic and aromatic structures. The bands at lower wavenumbers suggest C=C and C-O stretching modes, which are consistent with the acrylate-based resin

composition [322–324]. After pyrolysis, the spectrum shows only two dominant peaks at 1607 and 1373 cm^{-1} . These correspond to the G-band and D-band, respectively, which are characteristic of graphitic carbon. The disappearance of peaks associated with oxygen-containing and aliphatic groups confirms the decomposition of the organic matrix, which leaves behind a disordered carbonaceous structure. The presence of the D-band explains the formation of defective or amorphous carbon, while the G-band indicates the development of graphitic domains [325]. These results confirm that pyrolysis effectively removes non-carbon elements and converts the resin into a partially graphitized material with residual disorder. Additionally, a broad peak appears between 2600 and 3000 cm^{-1} , which corresponds to the 2D band of graphitic carbon [326]. In the initial pyrolysis run, the 3D-printed anode samples were heated to 1400°C. In the XRD results shown in Figure 4-5B, the peaks at 36.18°, 60.49°, and 72.24° are attributed to the SiC phase (reference code 01-073-1708). These peaks correspond to the characteristic diffraction angles of SiC, specifically the (111), (220), and (311) crystallographic planes, respectively. This XRD analysis shows that the reaction between silicon and carbon at high temperatures led to SiC formation. In addition to the primary peaks, several minor diffraction peaks are observed in the as-prepared sample, which likely result from interactions among impurities during high-temperature processing. For instance, the small peaks at 27.55°, 66.23°, and 70.58° are attributed to SiO₂ (silicon dioxide) (reference code: 01-086-1564). This finding aligns with the EDS analysis of the acid-washed samples, where residual oxygen was detected. The presence of SiO₂ may arise from partial oxidation of silicon during pyrolysis or from residual silicon oxides that were present in the original material prior to thermal treatment. Additionally, peaks at 34.16° and 65.31° are related to FeO (iron (II) oxide) (reference code: 96-900-9771), which is supported by EDS results showing traces of residual Fe after acid washing. Additionally, post-cycling XRD analysis revealed a change in the silicon crystal size. Initially, using the Scherrer Formula, the average size of silicon crystallite was measured to be 249 Å, but after cycling, it decreased to 163 Å. The reduction in crystal size suggests that the silicon experienced stress-induced fracturing during the lithiation/delithiation process, which is a well-known limitation of silicon-based anodes. Despite this structural degradation, the carbon matrix played a key role in buffering the mechanical strain, accommodating the volume changes, and preventing structural collapse.

This is supported by the battery cycling performance, which demonstrates that the carbon network effectively mitigated cracking and maintained electrode integrity over extended charge-discharge cycles.

Furthermore, post-cycling XRD analysis indicates a noticeable reduction in peak intensities. This decrease can be attributed to the formation of amorphous lithium silicate (Li_xSiO_y) and lithium silicide (Li_xSi) phases [326]. Additionally, the incorporation of lithium into the silicon structure disrupts its original crystalline arrangement, which further contributes to the peak intensity reduction.

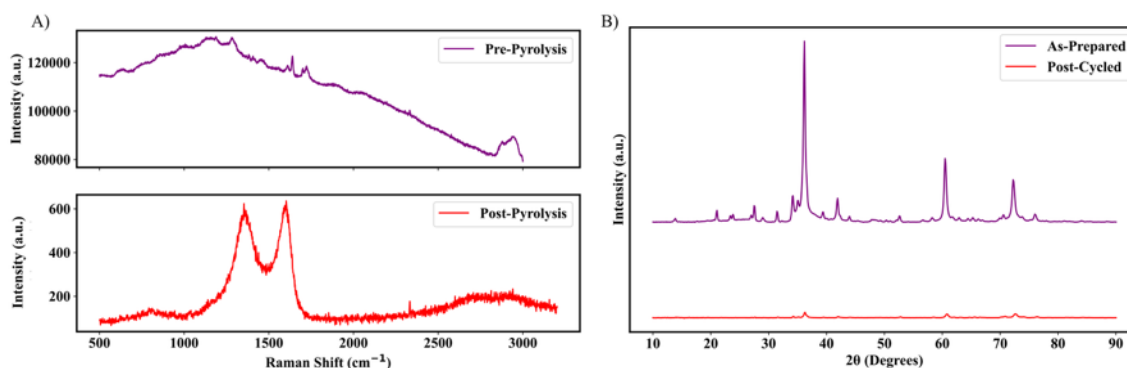


Figure 4-5. A) Raman spectra of transparent red resin before and after pyrolysis, showing Raman intensity as a function of Raman shift, and B) XRD pattern of samples pyrolyzed at 1400 °C, showing diffraction intensity as a function of 2θ .

4.3.4 Optical Microscopy and Visual Inspection

Optical microscope analysis of the printed samples (Figure 4-8A) taken by the Openflexure microscope revealed that the first cured depth, printed with the polymer resin, increased from the 0.03 mm set in the slicer to 0.4 mm. This increase is attributed to the increase in the exposure time for the first layer to ensure the resin was fully cured and adhered to the build platform. Conversely, the cured thickness of the silicon resin reduced from 0.03 mm to 0.016 mm which is due to the absorbance of the light by the powder which was shown by the UV-Vis spectrometry. Also, the CAD model of the designed anode, along with the dimensions of the printed and pyrolyzed parts, are shown in Figure 4-6. The anode was designed with an initial diameter of 18.5 mm and a thickness of 0.9 mm. The printed part retained a diameter of 18.5 mm, which was consistent with the CAD design. The thickness

of the as-printed part was measured at 0.5 mm, which corresponds to the silicon resin layer after the polymer resin was removed. During pyrolysis, the anode experienced dimensional shrinkage due to the removal of organic components and structural densification. The diameter decreased to 9 mm, which corresponds to a shrinkage of 51%, while the thickness reduced to 0.4 mm, which corresponds to a shrinkage of 20%.

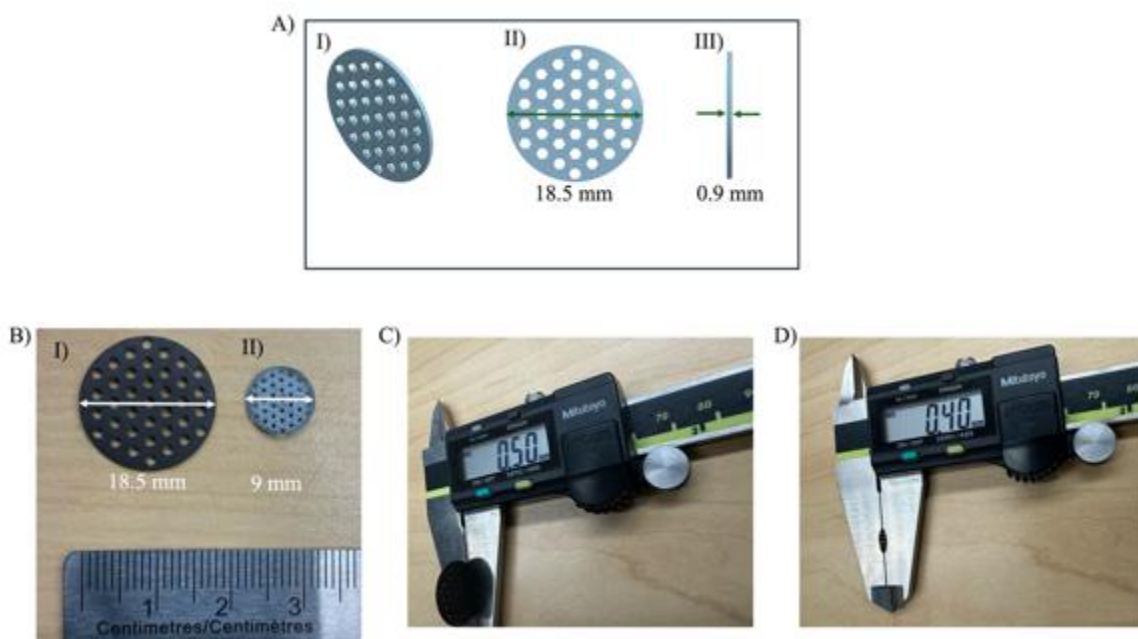


Figure 4-6. A) CAD model of the designed anode (I) Isometric view, (II) front view (diameter), and (III) side view (thickness), B) pictures of the (I) as-printed sample, and (II) pyrolyzed sample, C) the measured thickness of the as-printed sample, and D) the measured thickness of the pyrolyzed sample.

4.3.5 SEM and EDX

The SEM images of the as ball milled and acid washed solar cell powder are shown in Figure 4-7. As can be seen in Figure 4-7A and B, silicon (Si), carbon (C), oxygen (O), silver (Ag), aluminum (Al), tin (Sn), lead (Pb), and iron (Fe) coexist within the powder. Following the acid wash with HCl (Figure 4-7C and Figure 4-7D), the composition is altered, with only Si, C, O, and Fe remaining in the powder. During the acid washing process, Al is converted into soluble aluminum chloride (AlCl_3), Sn into tin chloride (SnCl_2), and Ag into Silver chloride (AgCl). Si remains intact because it reacts with HCl

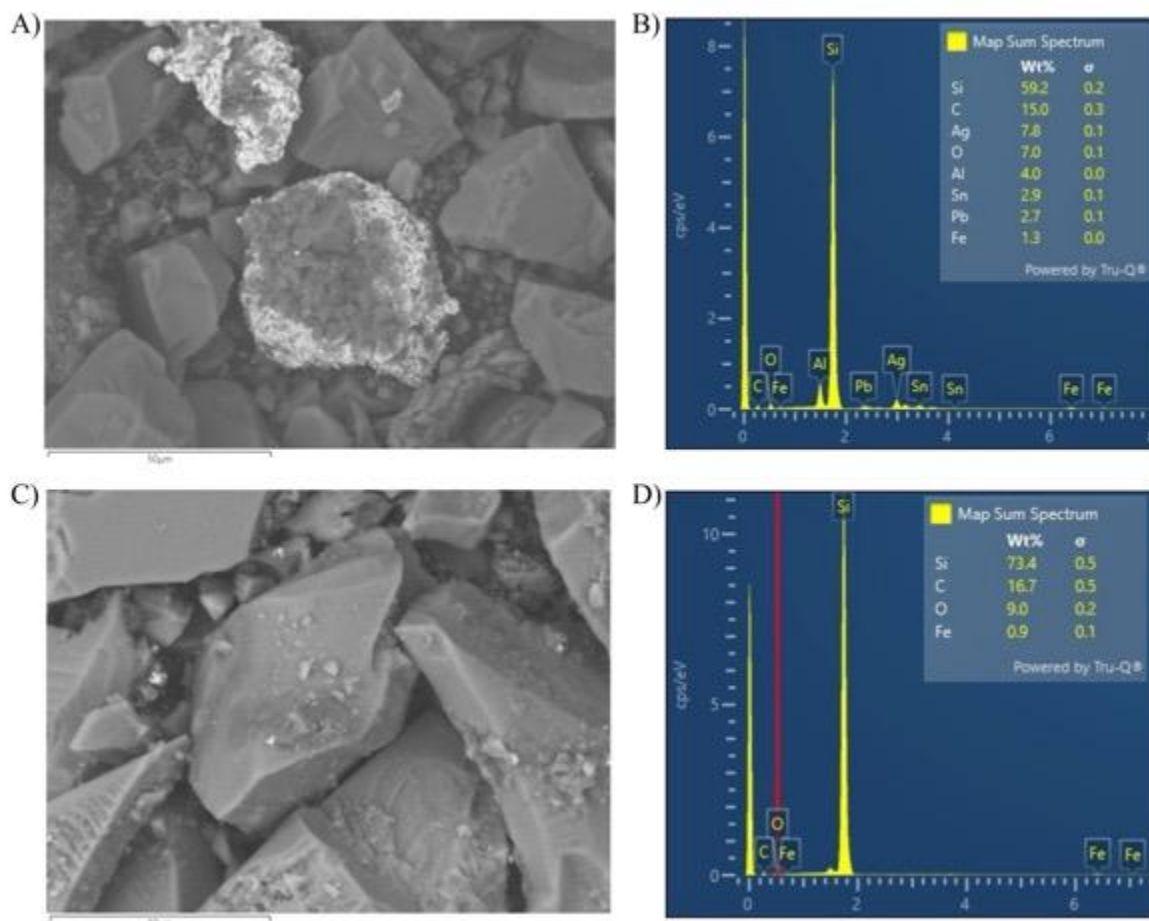


Figure 4-7. SEM images of (A, B) as-ball-milled solar cell powder and (C, D) acid-washed solar cell powder after ball milling.

only at elevated temperatures (above 350°C). SEM images of the 3D printed samples after pyrolysis (Figure 4-8B) revealed the formation of distinct carbon residue and silicon carbide (SiC) domains which support the XRD finding. The EDX analysis shown in Figure 4-8C further confirmed the presence of these phases, which shows clear signals corresponding to carbon and silicon. At this elevated temperature, silicon from the solar cell waste reacted with carbon residue from the acrylate resin and led to the formation of SiC. The generation of SiC is undesirable for lithium-ion battery anodes due to its electrochemical inactivity and non-conductive nature. While silicon has a high capacity for lithium storage, the formation of SiC reduces the amount of active silicon available for the (de)lithiation process. This limits the overall charge storage capacity of the anode and a reduction in the specific capacity observed during electrochemical testing could be attributed to the formation of this component. Moreover, the relatively low electrical

conductivity of SiC, which arises from its wide bandgap and the scarcity of free charge carriers [327], disrupts electron conduction pathways and prevents Li-ion diffusion. In addition, SiC tends to nucleate or accumulate at grain boundaries during high-temperature processing, since these regions have higher defect densities and localized stress that facilitate the reaction between silicon and carbon. As a result, SiC clusters can create localized resistive regions, which makes the charge transport more difficult and adversely affects both rate capability and long-term cycling stability. These factors lead to decreased charge-transfer efficiency and reduced overall battery performance. To achieve better performance, the formation of conductive carbon network surrounding the silicon particles is desirable. This carbon structure would improve electrical conductivity and buffer the expansion of silicon during lithiation which preserves the structural integrity of the anode.

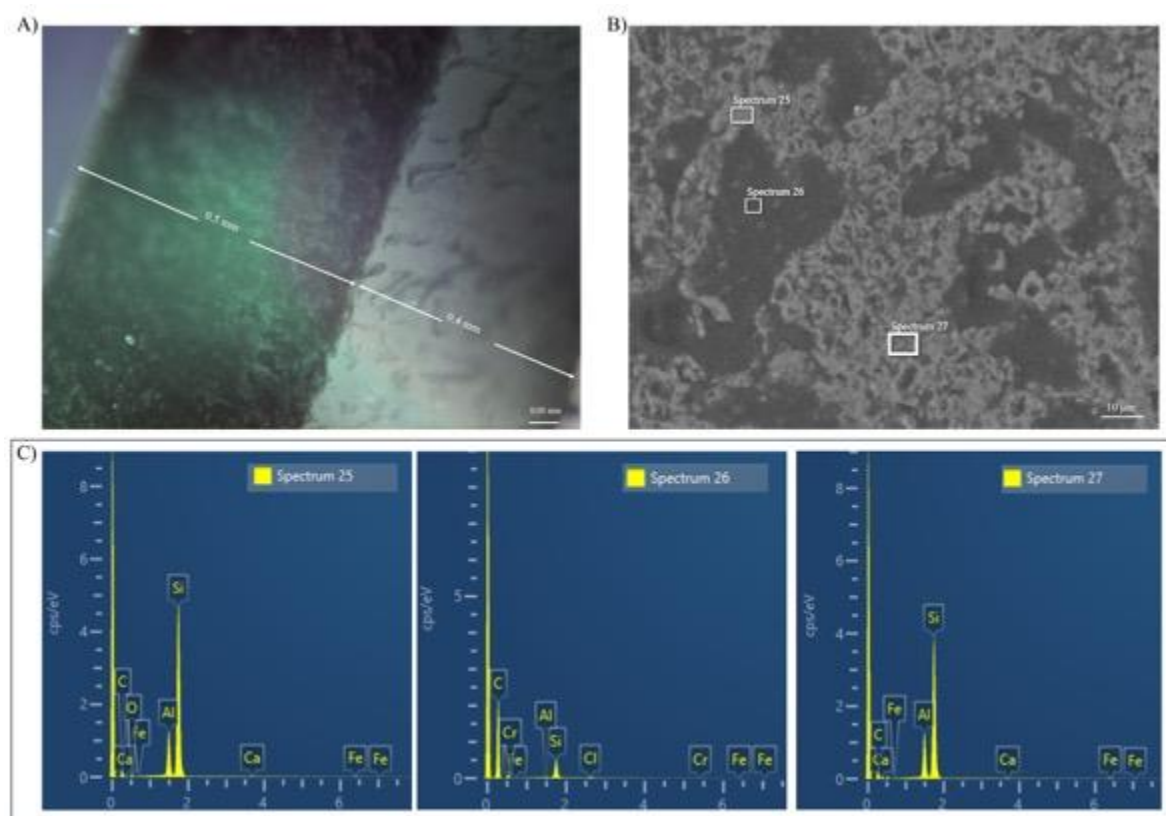


Figure 4-8. A) Optical microscopy image of printed sample using Openflexure microscope, B) SEM, and C) EDS elemental analysis of the pyrolyzed samples at 1400°C.

4.3.6 Cyclic Voltammetry (CV)

Figure 4-9A displays the cyclic voltammetry profile of the anode material. As confirmed by EDS, the structure contains both silicon and oxygen, and as shown by the XRD results, crystalline silicon oxide is present. The reduction peak at 0.9 V is attributed to the irreversible conversion of surface silicon oxide into Li_xSiO_y [328–330], which is a reaction that also contributes to the formation of the SEI. Although this process results in some initial capacity loss, it introduces a buffering matrix that helps accommodate the significant volume expansion during lithiation. Following this, the reduction peak at 0.46 V corresponds to the reversible lithiation of the silicon phase, which leads to the formation of a lithium-silicon alloy. Notably, given the confirmed presence of oxygen in the structure, this reversible reaction involves not only the formation of pure lithium silicide but also oxygen-modified lithiated silicon species, which could further enhance the capacity of the anode. In the delithiation sweep, the peak at 0.25 V indicates Li–Si dealloying, while the peak at 0.86 V likely reflects the evolution or partial decomposition of the SEI, which suggests ongoing changes in the organic and inorganic SEI components over cycles. This behavior suggests a stable and reversible lithiation-delithiation process, with minimal degradation over the observed cycles. Additionally, the overlapping curves and the slight increase in intensity at 0.25 V across cycles imply high reversibility, which shows that the anode material maintains a consistent electrochemical response.

4.3.7 Galvanostatic Cycling

The galvanostatic charge/discharge result is shown in Figure 4-9B. The specific capacity at 1C began at approximately 400 mAh/g, with a Coulombic efficiency exceeding 100% and 89% capacity retention over 200 cycles. These values are comparable to reports in the literature indicating 426.78 mAh/g at a rate of 0.5 A/g, where 10% solar cells and 90% graphite were used as anodes through conventional methods [310]. Additionally, other studies have reported higher capacities, such as 306 mAh/g at a 1C rate (0.55 A/g) when using 5% silicene and 95% graphite [330]. The specific capacity is also higher than the commercial graphite (~325mAh/g) [330] when cycled at 1C with the capacity retention of 66% over 200 cycles. Despite the relatively low percentage of active material (12%) in the

samples, the performance remains comparable to traditional methods which highlights the potential of this approach.

It is expected that increasing the solid load will further enhance efficiency by increasing the availability of active silicon for lithium storage, which would, in turn, raise the specific capacity. Also, as confirmed earlier by SEM and XRD results, the reduced specific capacity observed may be linked to the formation of SiC.

4.3.8 Electrochemical Impedance Spectroscopy (EIS)

The EIS curve of the anode in Figure 4-9C reveals a semi-circle in the high-frequency region with a low charge transfer resistance (R_{ct}) of 35.56 Ω , comparable to the 21.45 Ω reported in the similar work [310] and significantly lower than the 146 Ω observed in another work [331], and commercial graphite (~577 Ω) [331]. Additionally, the slight zero-point offset in the high-frequency region can be attributed to minimal resistance through the electrodes and low contact resistances within the cell components. This performance is likely due to three main factors. First, the conductive carbon network formed during pyrolysis facilitates efficient electron transport and rapid charge transfer at the silicon-electrolyte boundary. This carbon can help maintain a stable interface, which minimizes typical issues in silicon anodes, including high internal resistance and volume expansion. Secondly, the meshed geometry produced by 3D printing creates interconnected pathways that support both electron conduction via the carbon framework and ionic diffusion within the silicon matrix. This design provides an efficient interface for charge transfer, which reduces internal resistance. An additional benefit of the meshed geometry is evident in the flatter Warburg tail, which shows enhanced diffusion properties. Also, one of the notable advantages of the 3D printed anode design is the absence of polymer binders. Traditional anode structures often incorporate polymers like polyvinylidene fluoride (PVDF) [332,333] or carboxymethyl cellulose (CMC) [334] to bind the active materials together and enhance mechanical integrity. These polymers can hinder ionic conductivity and increase internal resistance, however, limiting overall electrochemical performance. In the

binder-free approach, ionic pathways are less obstructed, which may contribute more efficient lithium-ion transport.

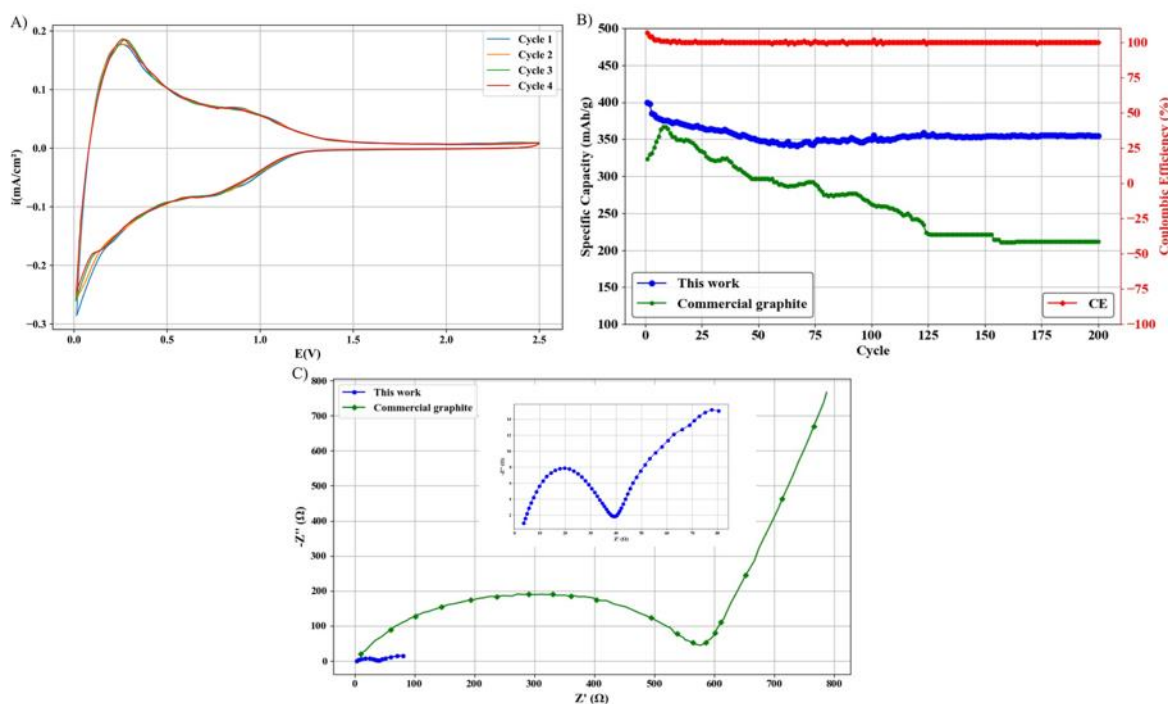


Figure 4-9. A) CV curves of printed silicon–carbon composite anodes, showing current as a function of voltage, B) Specific capacity comparison between printed anodes and a commercial graphite anode, showing specific capacity versus cycle number, and C) EIS Nyquist plots comparing printed anodes and a commercial graphite anode, showing Z' versus $-Z''$.

4.4 Discussion

The results presented earlier show that for 3D printing the anodes with solar cell waste using an SLA printer, the initial step involves selecting the appropriate polymer resin. The absorbance index increases with the addition of solid load to the polymer resin, which subsequently reduces the penetration depth of light and decreases curing thickness. Therefore, resins with minimal absorbance index peaks are preferred. Another critical factor in resin selection is carbon content. In this regard, higher carbon content results in reduced shrinkage in the final part. Based on these considerations, the Prusament transparent red resin with 47% carbon content was chosen. Printing the customized resin posed challenges, as the resin with solar cell waste did not adhere to the build plate.

To address this, multimaterial printing was employed. Initially, a polymer resin without solid load was used for the first layer. Subsequently, printing was paused, and the vat was changed to one containing the customized resin. However, this approach led to a new issue which was the separation of the polymer resin and the customized resin. This separation is critical because during pyrolysis, layers printed with polymer resin experience greater shrinkage which result in warping and non-uniformity in the anode structure. To address this, a flexible resin was used for the initial layer. The flexible resin has lower surface energy compared to the acrylate resin which results in inadequate interfacial contact. Additionally, the elastic nature of the flexible resin contrasts with the rigidity and denser network of the acrylate resin which causes internal stresses that induce delamination. Variations in photoinitiators and cure rates further contribute to incomplete or improper bonding at the interface. All these factors, help in the separation of the layers printed by the customized resin from the layers printed by the polymer resin. This is similar to the substrate release mechanisms used in metal 3D printing [335,336].

After pyrolysis in a nitrogen atmosphere, the anodes were assembled into half cells and the electrochemical results demonstrate that SLA printing using solar cell waste is a promising method for producing lithium-ion battery anodes. These anodes showed 400 mAh/g specific capacity with 89% capacity retention and achieved more than 100% Coulombic efficiency over 200 cycles. This capacity is approximately 94% of that reported in similar literature, where a specific capacity of 426.78 mAh/g, 87.5% capacity retention, and 100% Coulombic efficiency over 200 cycles was achieved using an anode composed of 10% solar cells and 90% graphite via conventional methods [310]. Additionally, the 3D printed anodes showed a 30.7% improvement in specific capacity compared to another study, which reported 306 mAh/g, over 93% capacity retention, and 97% Coulombic efficiency for 500 cycles with an anode made from 5% silicene and 95% graphite [331]. Also, the anode fabricated in this work shows higher specific capacity than the commercial graphite (~325 mAh/g) [331]. The notable advantage of this work, however, lies in the fact that no graphite was used in the fabrication of these anodes. The absence of graphite not only simplifies the process but also reduces dependency on this commonly used carbon source which makes the approach more sustainable and offers flexibility in tailoring the material composition.

Moreover, the choice of acrylate resin as a carbon source, compared to graphite, presents additional sustainability benefits. Unlike graphite, which requires energy-intensive mining and purification processes that have environmental impacts such as deforestation and water consumption [337–340], acrylate resin can be sourced from industrial byproducts or bio-based feedstocks [341–343]. This makes it a more environmentally friendly alternative. Moreover, acrylate resin is highly customizable [344], which allows for chemical modifications, such as introducing functional groups like carboxyl or hydroxyl groups to enhance the binding of the resin with silicon particles [345], that can improve the performance of the anode and structure. The use of acrylate resin, especially in combination with solar cell waste, also aligns with a circular economy approach [346] which repurposes waste materials and potentially lowering the overall carbon footprint of the anode production process.

This battery performance in this work is attributed to the residual carbon effect [347] from the pyrolysis of the polymer resin, which buffers volume changes in silicon atoms during cycling. The carbon also enhances conductivity within the anode and increases accessibility to active sites, contributing to overall battery efficiency and stability [347]. So far in this work, the fabrication of anodes for lithium-ion batteries using solar cell waste through SLA printing has been successfully developed which demonstrated stable battery performance. The observed electrochemical performance metrics, with a specific capacity higher than that of commercial graphite-based batteries (372 mAh/g), suggest that the approach is promising and can be further optimized. This method is an innovative recycling technique and is promising in integrating waste materials from the PV industry into battery production which addresses sustainability and recycling challenges. The vast amounts of generated solar cell waste could be repurposed which leads to substantial material savings and reduced environmental impact. By 2030, it is estimated that approximately 1.7-8 million tons of solar photovoltaic waste will be generated globally [348]. Each standard 250 W solar panel weighs around 19 kg and contains approximately 0.573 kg of silicon [349]. This means that 51 thousand tons of silicon will go to waste as solar panels reach the end of their life cycle by 2030. If the resin used for anode fabrication contained a solid load of 12% solar waste, approximately 0.0015 gr of solar waste would be incorporated into each coin cell, with each anode weighing 0.0125 g. Given the total amount of silicon

waste, it can be calculated that approximately 34 billion batteries could be produced annually. By using the method introduced in this work for anode production, around 403.75 tons of graphite could be saved annually in the production of 34 billion batteries. This estimate is based on the assumption that each anode weighs 0.0125 g, and considering that commercial batteries typically use more than 95% graphite in the anode [350]. Therefore, by replacing graphite with silicon from solar waste, a significant graphite demand could be reduced annually.

The remaining challenge in this work is the low amount of solid load in the resin, which is limited due to the high absorbance index of the silicon powder. In other studies, increasing the Si/C loading has increased SEI resistance, which was primarily due to reduced accessibility of lithium ions to the active material caused by the conventional fabrication method [314]. In contrast, the porous electrode geometry in this work makes the silicon particles exposed to the electrolyte. This unique architecture allows lithium ions to diffuse more easily through the structure, even at higher solid loads. Moving forward, future work is needed to enhance the role of silicon and its high capacity in the battery by increasing the solid load in the polymer resin. This can involve modifying the chemical composition of the customized resin as well as adjusting printer slicer parameters to optimize the ability to print high silicon loaded resins to improve performance and efficiency. It has been shown that increasing the active material loading in the anode leads to thicker electrodes, which allow more lithium ions to penetrate deeper into the structure. This makes it more difficult for the ions to return, however, which results in irreversible capacity loss and lower initial Coulombic efficiency. By leveraging 3D printing, this challenge can be addressed by precisely controlling the electrode architecture, optimizing porosity, and enhancing ion transport pathways to improve electrochemical performance [314]. Also, since the current pyrolysis temperature has been shown to produce silicon carbide, which, as discussed, has reduced the battery performance, lower pyrolysis temperatures can be explored. Additionally, while the printed samples showed promising results, using advanced microstructures could further optimize their performance. The application of 3D printing in battery fabrication extends beyond geometric control. For instance, it enables the fabrication of complex and fine-grained microstructures, such as porous, hierarchical, and graded architectures [351], which can enhance lithium-ion transport, optimize

electrolyte accessibility, and improve mechanical stability. For instance, gyroid lattice structures offer a balance between high porosity and mechanical resilience, which can reduce the risk of cracking and create uniform stress distribution. Additionally, hierarchical designs [352–354], which combine macro-scale porosity for efficient electrolyte flow with micro-scale features to maximize active surface area, have the potential to improve electrochemical performance. Furthermore, graded architectures [355,356], which are characterized by gradual transitions in material density or pore size, can effectively buffer the mechanical stresses caused by the expansion and contraction of silicon during cycling, which enhance cycle life. Another avenue for improvement will be the utilization of pre-ceramic polymers, combined with solar cell waste, in a ratio with acrylate resin to further optimize the material properties and overall performance. Using pre-ceramic polymers presents several advantages, which include high structural stability and volumetric strain suppression [357]. By adding solar cell waste to this composition, an increased Si-Li alloying due to the higher silicon content and improved electrical conductivity is expected. Furthermore, while acid washing was performed to remove impurities from the recycled silicon powder, some residual contaminants remain, as identified in the XRD and EDS analyses. To further purify the material, alternative acid washing practices should be explored to effectively eliminate these impurities and improve the overall quality and consistency of the recycled silicon. Also, while the focus of this work was on demonstrating the feasibility of SLA 3D printing for fabricating anodes using solar cell waste, further electrochemical testing including rate performance is needed to comprehensively evaluate battery performance.

Chapter 5

5 Effect of Pyrolysis Temperature on the Performance of 3D Printed Silicon–Carbon Anodes Derived from Recycled Photovoltaic Silicon

In this Chapter, the effect of pyrolysis temperature on their structural, electrical, and electrochemical properties of 3D printed silicon–carbon composite anodes fabricated from crystalline silicon solar photovoltaic cell waste was investigated. The aim was to suppress the formation of electrochemically inactive SiC observed at 1400 °C in previous work, while maintaining high electrical conductivity and stable structure. Printed anodes were pyrolyzed at 800 °C, 1100 °C, and 1200 °C. The results showed that pyrolysis temperature influences both the microstructure and electrochemical performance of the printed anodes. Pyrolysis at 1200 °C was produced a highly conductive carbon matrix without formation of electrochemically inactive SiC. XRD analysis confirmed that at 1200 °C, no SiC peaks appeared. The enhanced graphitization observed in Raman spectra at this temperature, coupled with the reduced charge-transfer resistance in electrochemical impedance spectroscopy, indicates that the carbon network achieved high electronic conductivity while preserving the active silicon phase. As a result, the anode had an initial specific capacity of approximately 771 mAh g⁻¹, with the initial Coulombic efficiency of 99.9%, and a capacity retention of 61% over 120 cycles. The performance achieved here demonstrates an improvement over the earlier SLA-printed PV-silicon anodes pyrolyzed at 1400 °C, which confirms that tuning pyrolysis temperature is a key strategy to obtain the optimal morphology.

5.1 Experimental Section

Materials preparation, resin formulation, 3D printing of the customized resin, and electrochemical testing followed the same procedures described in Chapter 4. The primary difference in this Chapter is the pyrolysis schedule. After post-curing, the printed anode samples were pyrolyzed in a gas-tight box furnace (Model 1616 FL, CM Furnaces, USA).

The temperature was first increased to 250 °C at a controlled rate of 1 °C min⁻¹, followed by a ramp of 3 °C min⁻¹ to the final pyrolysis temperatures of 800 °C, 1100 °C, or 1200 °C. Each sample was held at its target temperature for 2 hours under continuous nitrogen flow to maintain an inert environment. After the dwell period, the furnace was allowed to cool naturally to room temperature at approximately 10 °C min⁻¹. In this Chapter, electrical conductivity of the pyrolyzed anodes was evaluated using a four-point probe method (Keithley Instruments, Cleveland, OH, USA). Measurements were conducted at room temperature by applying a constant current through the outer probes and recording the voltage drop across the inner probes. It should be noted that this technique measures the in-plane electrical conductivity [358], rather than the through-thickness conductivity, which would more directly reflect electron transport across the electrode during cell operation. Nevertheless, the in-plane measurements are considered representative of the overall electronic conductivity of the material and suitable for comparative analysis [359]. The sheet resistance was calculated, and conductivity values were derived based on the sample thickness. Electrical conductivity ($\sigma = 1/R_s t$) was determined from four-point probe measurements of sheet resistance (R_s) using a Signatone SP4 setup and the average film thickness (t) [360]. Electrochemical tests were performed using a CS300 model potentiostat (Corrtest, China) and CHI660E potentiostat. Galvanostatic charge–discharge testing was carried out within a voltage range of 0.01–1.5 V vs. Li/Li⁺ at room temperature at 0.77 A g⁻¹. Rate performance was assessed by cycling cells at different current densities (0.154 A g⁻¹, 0.231 A g⁻¹, 0.385 A g⁻¹, 0.77 A g⁻¹, and 3.465 A g⁻¹) to evaluate the capacity retention at higher charging and discharging rates, followed by recovery at 0.154 A g⁻¹. Specific capacities were calculated from the discharge/charge capacity of the galvanostatic curves. The mass of the active materials was calculated 3–4 mg. Cyclic voltammetry measurements were performed between 0.01 and 1.5 V vs. Li⁺/Li at a scan rate of 0.15 mV s⁻¹ to analyze the lithiation/delithiation behaviour and redox reactions. EIS was conducted at open-circuit voltage with a perturbation amplitude of 10 mV over a frequency range of 100 kHz to 0.01 Hz.

5.2 Results

5.2.1 Pre-cycling

5.2.1.1 XRD

One of the limitations identified in previous work was the presence of SiC in the pyrolyzed samples at 1400 °C, which was found to be electrochemically inactive and contributed to a reduction in battery capacity [361]. In this work, efforts have been made to address this issue by having the samples pyrolyzed at lower temperatures, where the formation of SiC is intended to be prevented. The XRD patterns of the pyrolyzed samples, shown in Figure 5-1, at 800 °C, 1100 °C, and 1200 °C indicate a dominant presence of crystalline silicon across all temperatures, with the 28.7° (111), 47.76° (022), 56.69° (131), 69.86° (040), 77.2° (133), and 89.06° (242), which aligned with Reference pattern COD-9013102 for silicon [362], using Open-source Profex program [363]. The peaks of COD-9013102 for silicon were extracted using Pymatgen (Python Materials Genomics) library [364]. No additional features are observed, which suggest carbon remains chemically stable and does

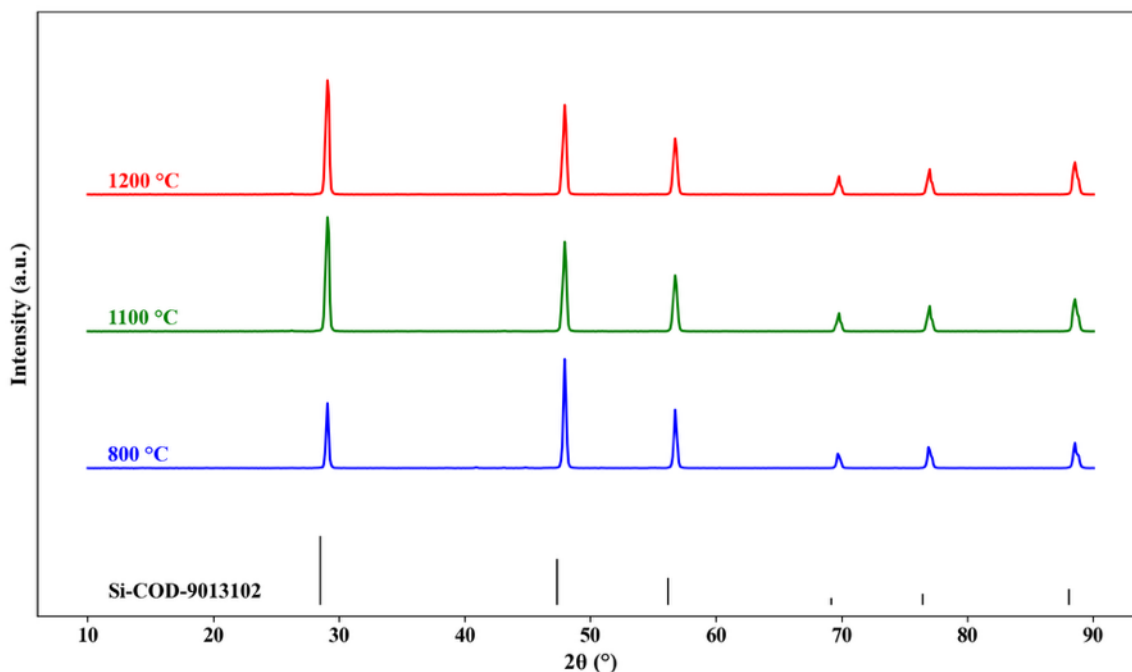


Figure 5-1. XRD patterns of silicon–carbon composite anodes pyrolyzed at 800 °C, 1100 °C, and 1200 °C, showing diffraction intensity as a function of 2θ.

not react with silicon to form new phases such as SiC. A notable difference from the XRD results reported in the previous work is the absence of several minor diffraction peaks, which were likely associated with impurity-related interactions [361]. This improvement is attributed to the use of nitric acid in the purification process in the present chapter, rather than the hydrochloric acid that was used previously. This leads to reduced impurity levels in the recycled solar cell material and improved reproducibility of the results.

5.2.1.2 Raman spectroscopy

Figure 5-2 shows the Raman spectra of the samples after pyrolysis. All samples exhibit the characteristic D ($\sim 1340\text{ cm}^{-1}$) and G ($\sim 1600\text{ cm}^{-1}$) bands associated with disordered and graphitic carbon structures, respectively [310]. At $800\text{ }^{\circ}\text{C}$, the carbon framework is largely amorphous, reflected by a high $I_{\text{D}}/I_{\text{G}}$ ratio of 1.01. This indicates incomplete conversion of the resin to carbon and the presence of many defects and randomly oriented sp^2 layers that limit electrical conductivity. As the pyrolysis temperature increases, the $I_{\text{D}}/I_{\text{G}}$ ratio decreases and reaches to 0.88 at $1200\text{ }^{\circ}\text{C}$. This signifies the reduction of disordered carbon structure and the growth of more ordered graphitic domains [365]. At the same time, the G band becomes sharper and narrower at elevated temperatures, which confirms the enhancement of graphitic order and enlargement of sp^2 domains [366]. Also, narrowing D band by increasing the temperature up to 1100 indicates an increase in the size and/or number of the ordered graphitic domains [367]. At lower temperature ($800\text{ }^{\circ}\text{C}$), the 2D band at $\sim 2670\text{ cm}^{-1}$ and the D+G band at $\sim 2900\text{ cm}^{-1}$ appear as weak peaks. The 2D band is known to change in intensity and shape with the number of graphene layers [368]. These weak features are typical of disordered carbon with small, isolated sp^2 regions [369]. As the temperature increases, both bands become stronger. This change might happen because the carbon layers begin to align and stack on top of each other, which creates stronger interactions between the graphene-like sheets. This stacking is imperfect, and the layers are not still fully ordered like in crystalline graphite. This partial ordering shows that the material is moving from an amorphous to a more graphitic structure [370]. As a result, the

carbon network becomes more continuous, which helps electrons move more easily. This is an important factor for improving the performance of the anode in lithium-ion batteries.

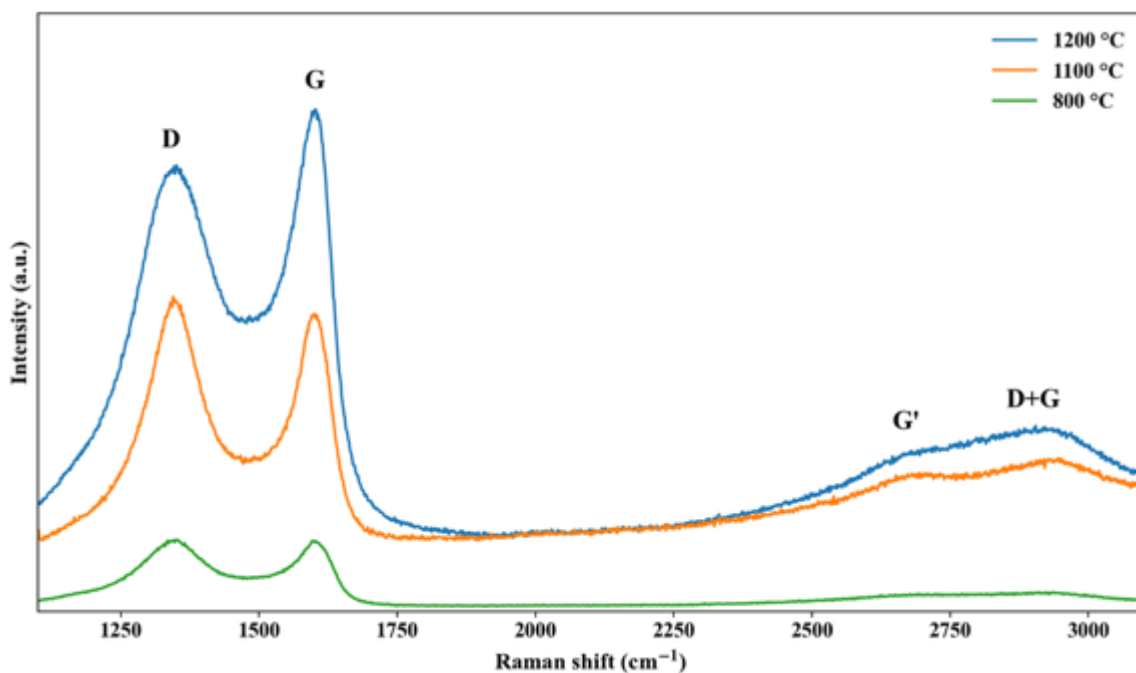


Figure 5-2. Raman spectra of silicon–carbon composite anodes pyrolyzed at 800 °C, 1100 °C, and 1200 °C, showing Raman intensity as a function of Raman shift.

5.2.1.3 Four-Point Probe Measurement

The electrical conductivity of the samples was measured using a four-point probe technique after pyrolysis at 800 °C, 1100 °C, and 1200 °C (Figure 5-3). Conductivity increased significantly from 413 S m⁻¹ at 800 °C to 1158 S m⁻¹ at 1100 °C and 1342 S m⁻¹ at 1200 °C. The sharp rise between 800 °C and 1100 °C reflects the major structural transformation of the ceramic matrix. At this temperature the ceramic restructures into a continuous carbonaceous framework, while disorder in the carbon phase decreases. These results demonstrate that higher temperatures create better carbon structure which facilitate electron transportation in batteries.

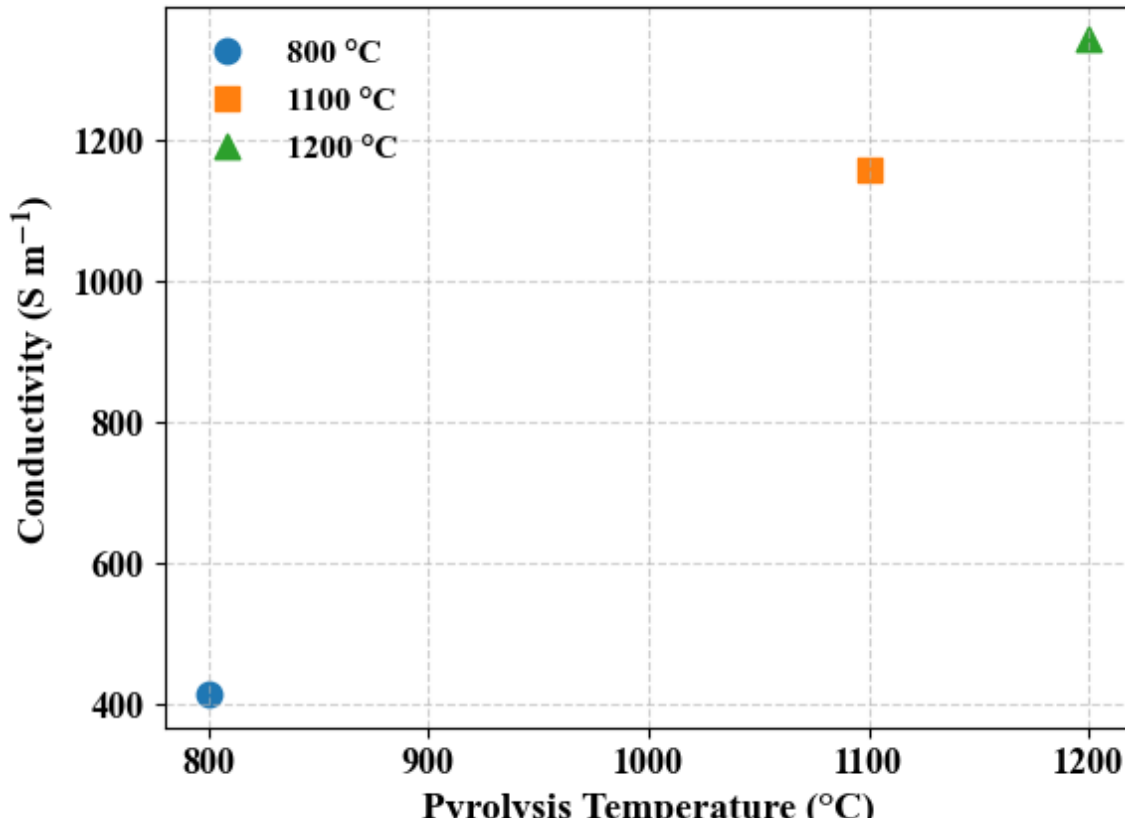
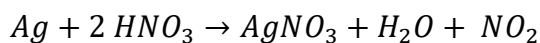


Figure 5-3. Electrical conductivity of silicon-carbon composite anodes pyrolyzed at 800 °C, 1100 °C, and 1200 °C, measured by four-point probe, showing conductivity as a function of pyrolysis temperature.

5.2.1.4 SEM and EDS

Figure 5-4 shows the EDS mapping of the acid-washed solar-cell powder. It shows that the Al and Ag are removed after the acid wash. The treatment equation is as the following [371]:



Traces of fluorine (F) remain which originates from fluorinated backsheet materials or manufacturing-related fluoride residues [372]. Figure 5-5 shows a printed sample containing solar cell powder. The layer-by-layer morphology of the SLA process is clearly visible. EDS mappings of the samples pyrolyzed at 800 °C, 1100 °C, and 1200 °C are presented in Figure 5-6. For each temperature, this figure includes four panels: (a, e, i) are

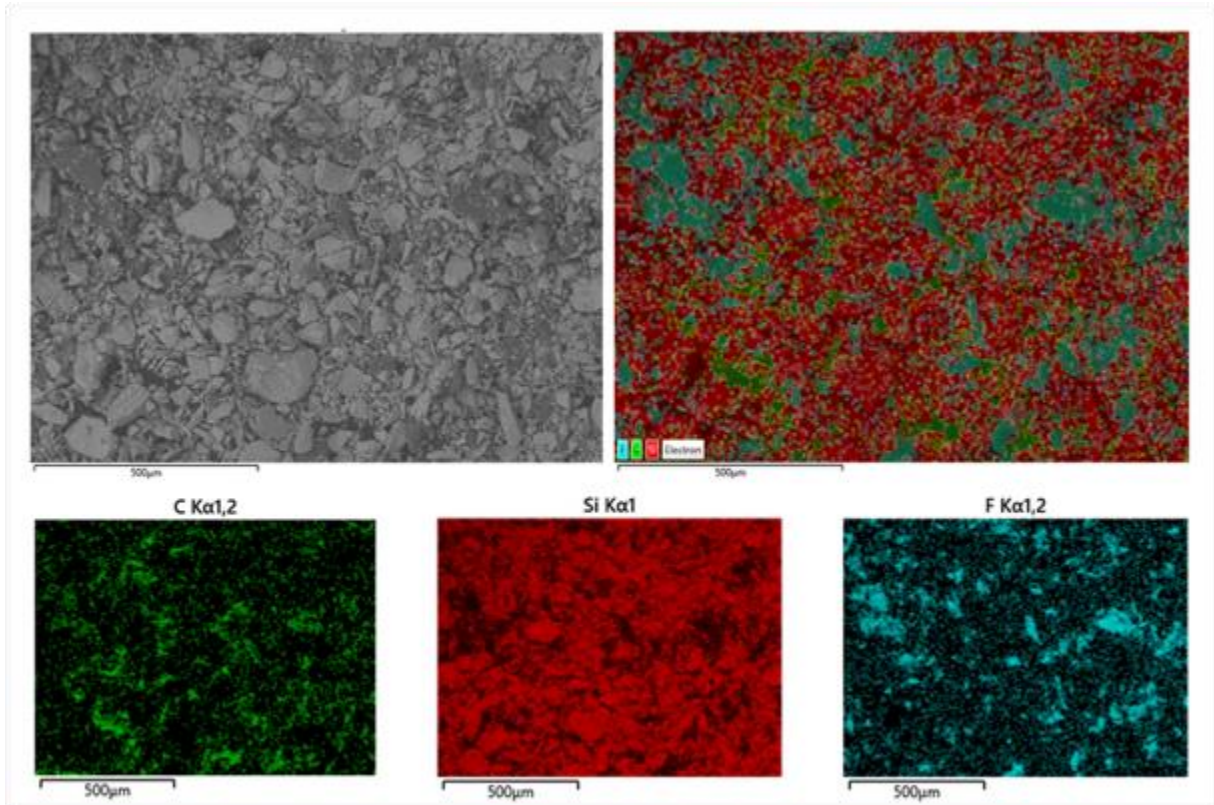


Figure 5-4. EDS elemental mapping of acid-washed solar cell powder showing the spatial distribution of constituent elements.

the SEM micrograph of the selected region; (b, f, j) the carbon (C) elemental map; (c, g, k) the silicon (Si) elemental map; and (d, h, l) the oxygen (O) elemental map. The results confirm a uniform distribution of silicon and oxygen within the carbon matrix.

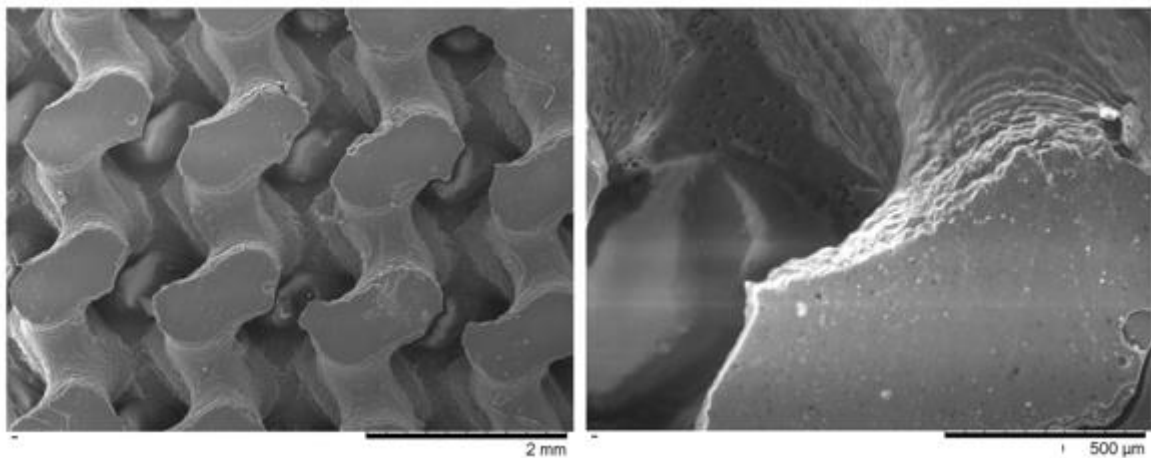


Figure 5-5. SEM images of an SLA-printed solar-cell-derived silicon sample showing surface morphology and microstructural features.

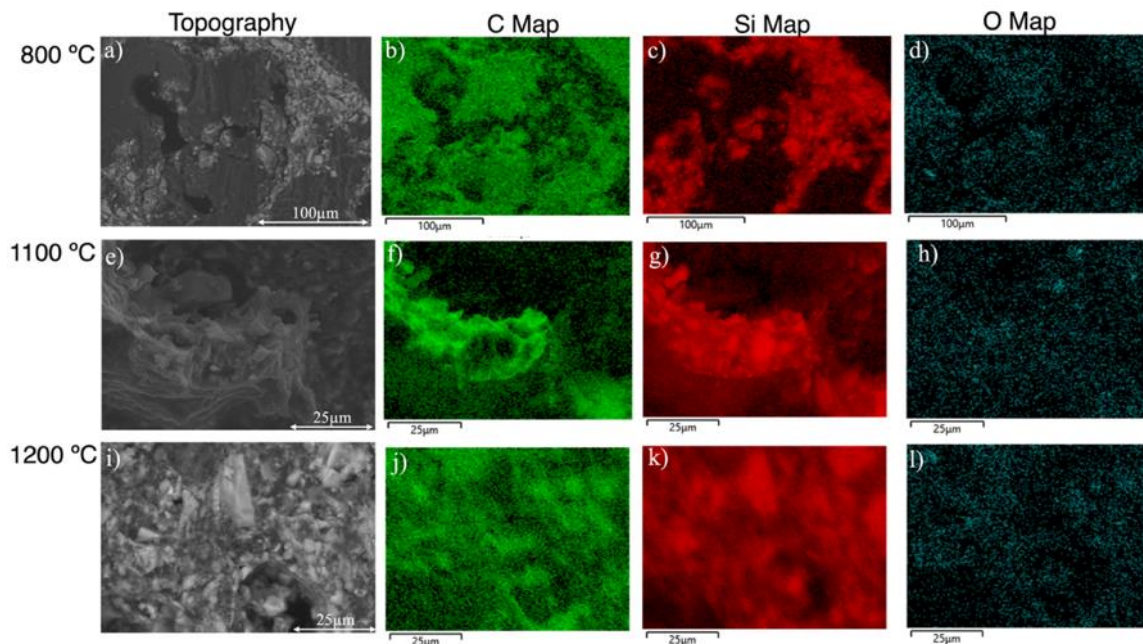


Figure 5-6. EDS elemental mapping of silicon–carbon composite anodes pyrolyzed at (a–d) 800 °C, (e–h) 1100 °C, and (i–l) 1200 °C.

5.2.2 Electrochemical results

5.2.2.1 Galvanostatic Cycling

To evaluate and compare the electrochemical performance of the anodes fabricated at different pyrolysis temperatures, galvanostatic charge–discharge measurements were conducted at a current of 0.77 A g^{-1} for 40 cycles. The purpose of this test was to identify the sample that shows the best specific capacity and cycling stability. The most promising sample was then subjected to rate performance, extended cycling for 120 cycles, and cyclic voltammetry to further assess its electrochemical performance. As shown in Figure 5-7a, the sample pyrolyzed at 800 °C showed an initial specific capacity of 359 mAh g^{-1} , with 37 % capacity retention after 40 cycles. The lower specific capacity and poor capacity retention compared to the previous work with the sample pyrolyzed at 1400 °C [361] is likely due to incomplete conversion of the resin to carbon, which reduces electrical conductivity and weakens the structural integrity of the carbon framework. These limitations lead to severe volume expansion during lithiation, causing electrode pulverization and ultimately the loss of electrical contact during cycling [373]. The samples

pyrolyzed at 1100 °C showed improved electrochemical performance, by delivering initial specific capacities of 719 mAh g⁻¹, with capacity retentions of 78 %. This improvement is likely due to the increased graphitization of the carbon matrix, better electrical conductivity, and enhanced structural stability, which together facilitate more efficient lithium-ion transport and accommodate the volume changes during cycling [374]. The sample pyrolyzed at 1200 °C exhibited the best performance among all and achieved an initial specific capacity of 771 mAh g⁻¹ with ~99.9 % initial Coulombic efficiency in the first measured cycle after formation, and 88 % capacity retention over 40 cycles. The superior electrochemical behavior at this temperature is supported by the structural and compositional improvements, the higher electrical conductivity, lower oxygen content, and more ordered carbon structure that discussed earlier. The optimized balance between graphitization and residual amorphous carbon provides both efficient electronic pathways and mechanical buffering for silicon particles during lithiation and delithiation. Additionally, the improved interfacial contact between silicon and the conductive carbon matrix facilitates faster charge transfer and mitigates irreversible capacity losses. As a result, this sample was selected for extended cycling for 120 cycles. As shown in Figure 5-7b, the sample showed the >98% Coulombic efficiency and capacity retention of 61% throughout the long cycling, which reveals its structural stability and electrochemical durability. The voltage versus capacity profiles of the anode pyrolyzed at 1200 °C shown in Figure 5-7c, demonstrate a stable lithiation/delithiation process with gradual capacity fading and preserved curve shapes over 120 cycles.

5.2.2.2 Rate Capability

For the electrode pyrolyzed at 1200 °C, the rate profile shown in Figure 5-7d demonstrates high capacity at low current densities. At 0.154 A g⁻¹, the electrode delivers a specific capacity of 1126-1292 mAh g⁻¹. This indicates efficient lithiation and good activation behavior. As the current rate increases, the capacity gradually declines due to kinetic limitations and reaches 236-202 mAh g⁻¹ at 3.465 A g⁻¹. When the current density returns to 0.154 A g⁻¹, the capacity recovers to 905-1111 mAh g⁻¹, which is corresponding to approximately 80–85 % of the initial value. This high recovery confirms strong rate capability and minimal structural degradation. The reversible behavior suggests the

formation of a stable SEI layer and a mechanically robust microstructure capable of sustaining repeated high rate cycling without significant loss of active material or electrical contact.

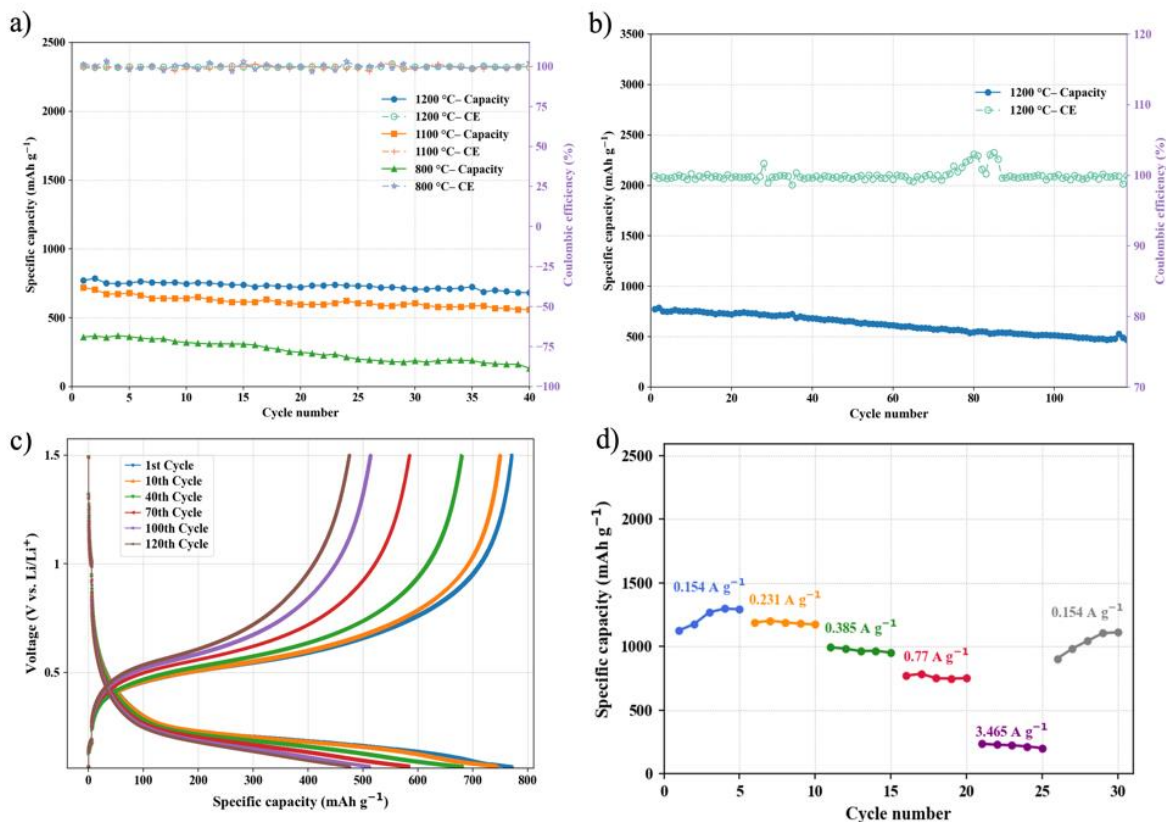


Figure 5-7. a) Galvanostatic charge–discharge voltage profiles of anodes pyrolyzed at 800–1200 °C, showing voltage versus specific capacity, b) Long-term cycling performance of the anode pyrolyzed at 1200 °C, showing specific capacity versus cycle number, c) Voltage versus specific capacity profiles of the anode pyrolyzed at 1200 °C, d) Rate performance showing specific capacity as a function of current density.

5.2.2.3 Cyclic Voltammetry (CV)

The cyclic voltammetry of the sample pyrolyzed at 1200 °C shown in Figure 5-8 exhibits well-defined and reversible redox peaks, which indicate a stable lithium insertion and extraction behavior. During the cathodic sweep, a reduction peak appears around 0.2 V. This peak corresponds to the lithiation of silicon and the formation of amorphous Li–Si alloys (Li_xSi_y) [375]. In the subsequent anodic sweep, two oxidation peaks are observed at approximately 0.35 V and 0.52 V, which can be attributed to the dealloying of Li_xSi_y and

the extraction of Li^+ ions from silicon [374]. The relatively high current (≈ 2 mA) indicates enhanced electrical conductivity of the electrode, which is likely the result of improved carbonization and conductive network formation during pyrolysis. Furthermore, the gradual increase in peak current over the first three cycles suggests a progressive electrode activation process, where the active material becomes more accessible to Li^+ ions upon repeated cycling [305,376].

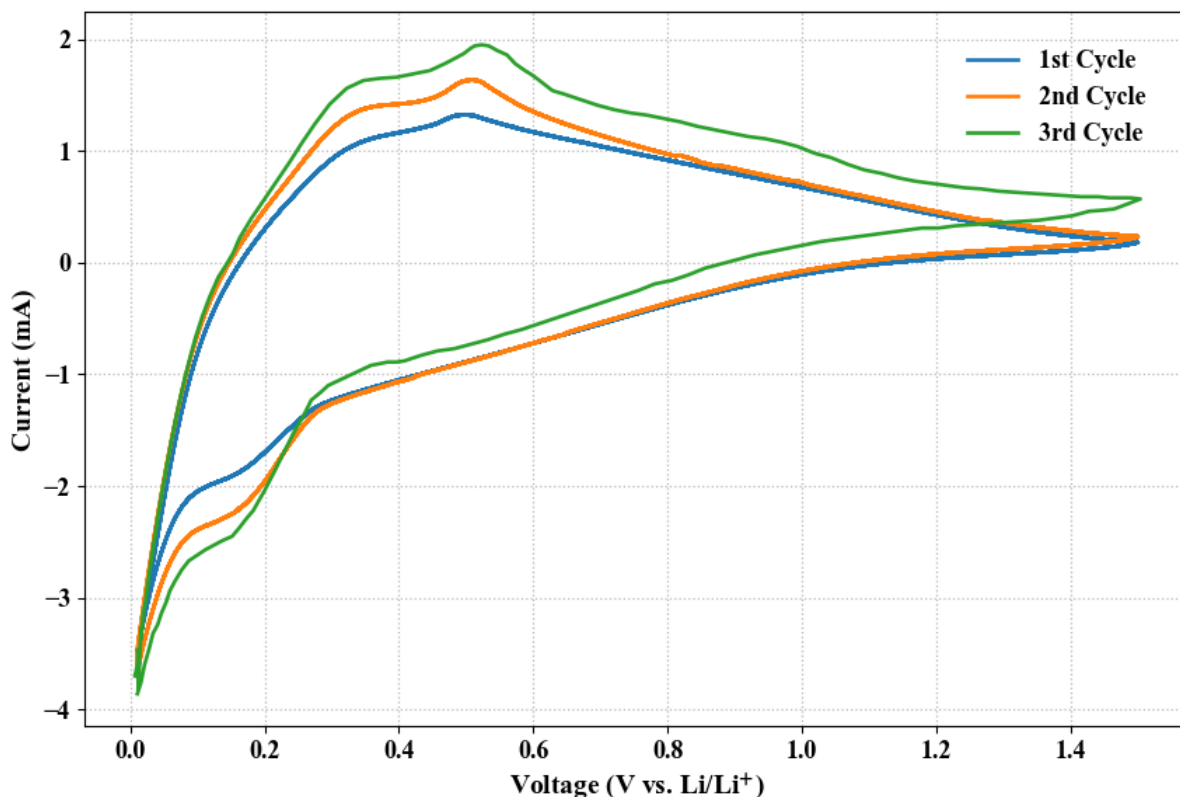


Figure 5-8. CV curves of the silicon-carbon composite anode pyrolyzed at 1200 °C, showing current as a function of voltage.

5.2.2.4 Electrochemical Impedance Spectroscopy (EIS)

Figure 5-9 shows the Nyquist plots of anodes pyrolyzed at 800, 1100, and 1200 °C. The 800 °C sample exhibits the poorest kinetics which are often associated with high charge transfer resistance ($R_{ct} \approx 140 \Omega$), which can be attributed to incomplete carbonization and high interfacial resistance. Increasing the pyrolysis temperature to 1100 °C significantly improves performance ($R_{ct} \approx 62.5 \Omega$), which reflects better graphitization, enhanced

electronic percolation, and more effective electrolyte penetration. The 1200 °C anode outperforms all other samples, by delivering the lowest impedance values ($R_{ct} \approx 25 \Omega$). This superior behavior arises from a favorable microstructural balance achieved at 1200 °C, including the formation of a continuous conductive carbon network that promotes electrolyte wetting and reduces ion transport distances, and a fine dispersion of Si that maintains abundant active interfacial sites and supports a stable, thin SEI.

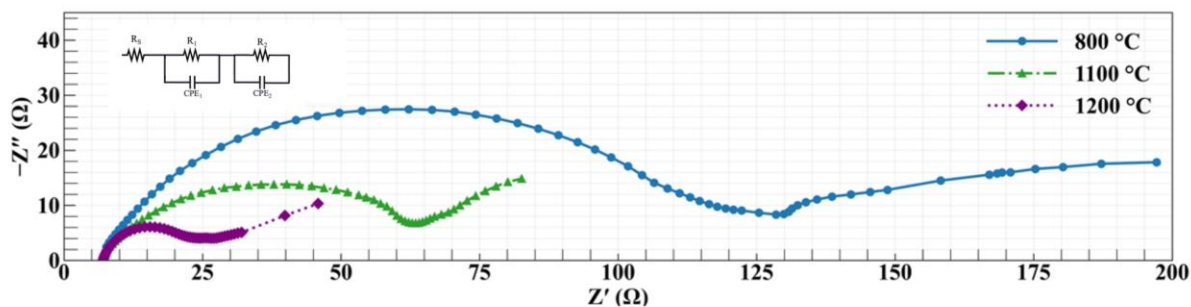


Figure 5-9. EIS Nyquist plots of silicon-carbon composite anodes pyrolyzed at 800 °C, 1100 °C, and 1200 °C, showing Z' versus $-Z''$.

5.2.3 Post cycling

5.2.3.1 XPS

To investigate the composition of the SEI film, XPS full spectrum of the electrode before and after cycling is conducted. Figure 5-10 illustrates the XPS of the pyrolyzed electrode at 1200 before cycling. The pyrolyzed electrode surface shows mainly C, O and Si elements. Elemental Si has Si 2p around 96.95 and 97.55 eV, and oxidized states shift to higher binding energy up to 99.21 and 101.42 eV for Si^{4+} in SiO_2 . C 1s spectrum shows peaks at 281.80, 282.20, 283.70, 285.70, 286.70, 281.05 corresponding to C=C, C-C and CH, C-O, C=O, COOH, and M-C respectively. M-C is a carbide bond and can be attributed to Si-C which makes up 2.8% of the curve area. After 40 cycles, Li 1s, F 1s and P 2p appear along with C, O, and Si, which show the formation of SEI. SEI is a mixture of inorganic (Li_2O , Li_2CO_3 , LiF, $\text{Li}_2\text{C}_2\text{O}_4$) and organic (lithium alkyl carbonates (ROCO_2Li) and other polymeric carbonates) components formed from LiPF_6 and carbonate solvent decomposition [377]. The Li 1s peak around 53–55 eV corresponds to Li^+ in SEI compounds such as Li_2O , Li_2CO_3 and LiF [378]. C 1s peaks at 282.68, 284.57, 286.38,

287.75, 281.09 correspond to C–C, C–O, C=O, CO₃, and M–C. CO₃ can be attributed to Li₂CO₃ and lithium alkyl carbonates (ROCO₂Li) from electrolyte decomposition [378,379]. F 1s at 682.66 and 684.93 eV correspond to Li–F and C–F₂ respectively. These species arise from LiPF₆ degradation [379]. These changes confirm that cycling generates a mixed inorganic and organic SEI layer on top of the silicon anode which can act as a protective layer for the anode.

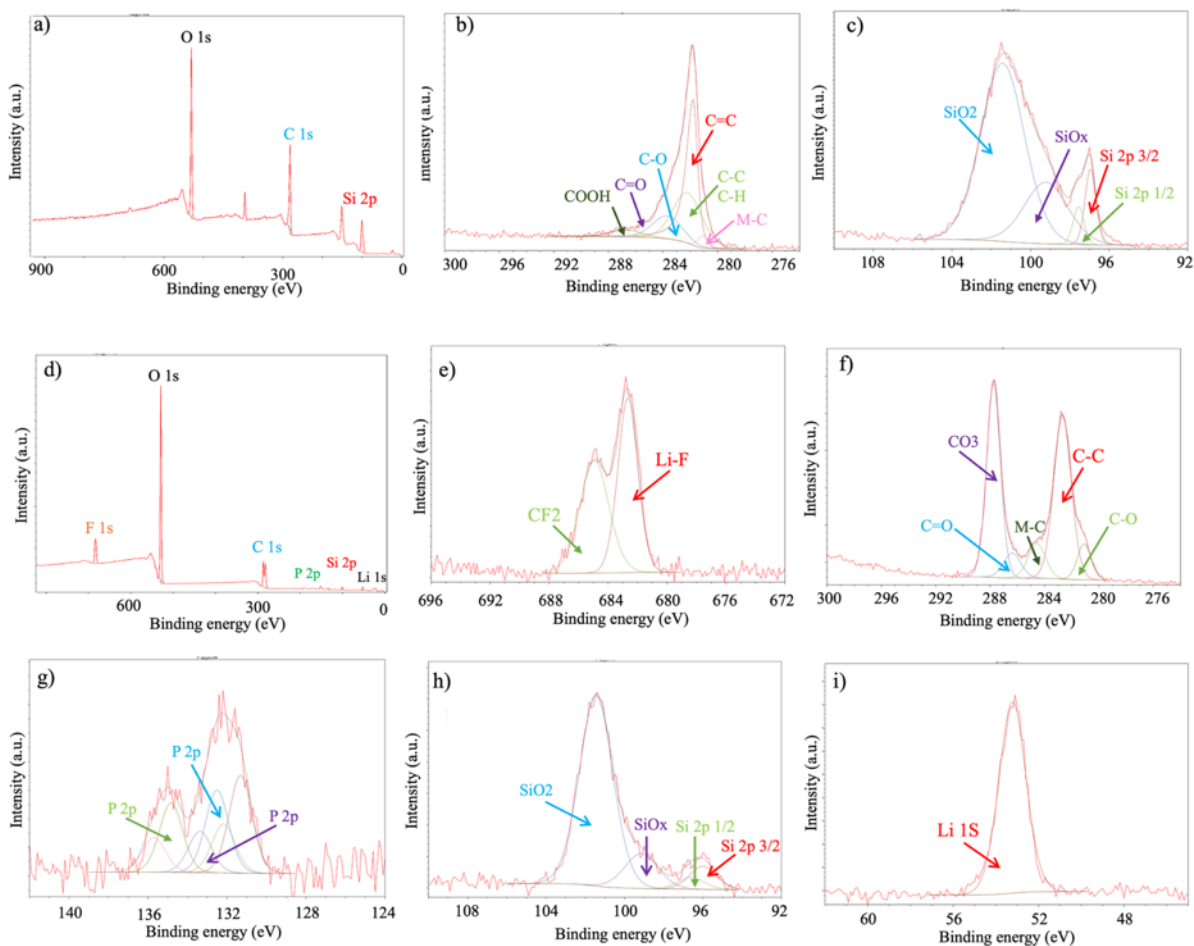


Figure 5-10. XPS spectra of the silicon-carbon composite anode showing (a-c) the sample pyrolyzed at 1200 °C and (d-i) the post-cycled sample.

5.2.3.2 Raman

Figure 5-11 compares the Raman spectra of the sample pyrolyzed at 1200 °C before and after electrochemical cycling. Prior to cycling, the Raman spectrum is dominated by the first-order Si–Si vibrational mode at $\sim 520\text{ cm}^{-1}$, which is characteristic of crystalline silicon, together with the D and G bands of carbon and an ID/IG ratio of 0.88, as discussed

in the Raman analysis of the pyrolyzed samples. In addition, a broad, low-intensity feature observed near $\sim 932\text{ cm}^{-1}$ is attributed to the second-order Raman response of silicon, which is commonly observed in Si-rich materials. In addition, the Raman spectra exhibit higher-wavenumber features in the $2500\text{--}3200\text{ cm}^{-1}$ range, which are attributed to second-order carbon bands, including the 2D (G') band and combination modes (D+G). After 40 electrochemical cycles, the Si–Si Raman modes are strongly suppressed, indicating significant amorphization of near-surface crystalline silicon. This behaviour is consistent with the electrochemical response, where repeated lithiation and delithiation lead to the formation of amorphous Li_xSi_y phases. In contrast, the D and G band intensities and the ID/IG ratio remain essentially unchanged, indicating that the overall degree of disorder and graphitization of the resin-derived carbon framework is preserved during cycling, despite surface and electronic changes induced by repeated electrochemical cycling. Also, A slight elevation of the baseline in the post-cycled spectrum is attributed to fluorescence contributions.

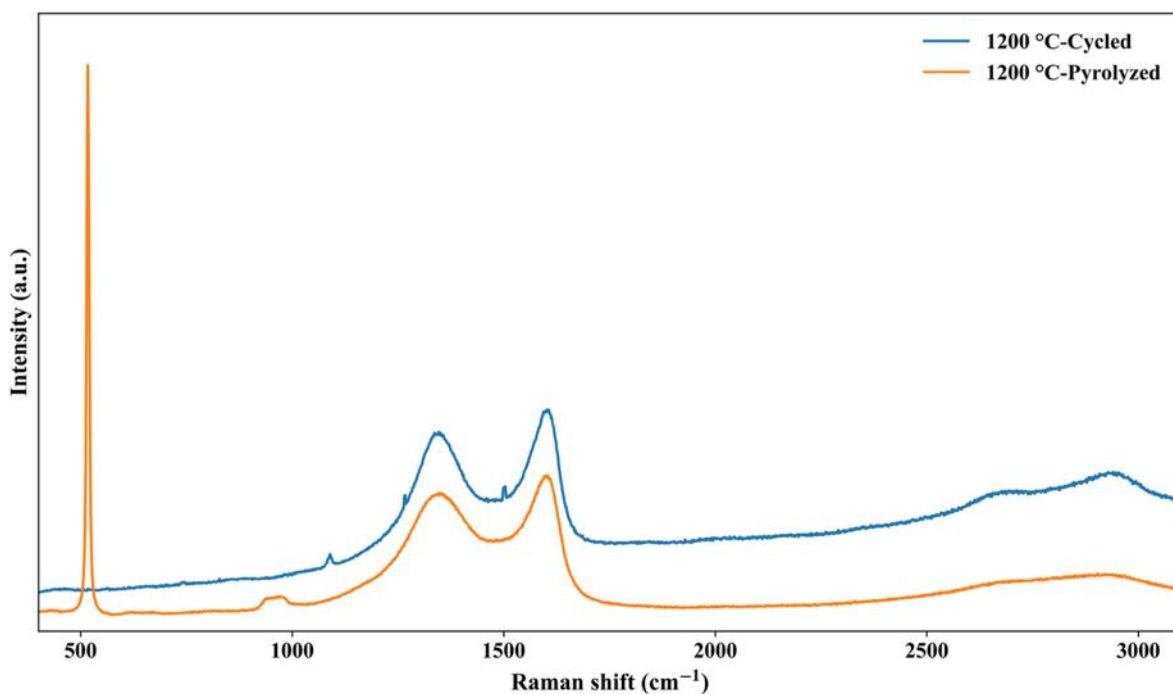


Figure 5-11. Raman spectra of the silicon–carbon composite anode pyrolyzed at 1200 °C before and after electrochemical cycling, showing Raman intensity as a function of Raman shift.

5.3 Discussion

In this chapter, 3D printed silicon–carbon composite anodes were fabricated from solar cell waste to investigate the effect of pyrolysis temperature on their structural, electrical, and electrochemical properties. The aim was to suppress the formation of electrochemically inactive SiC observed at 1400 °C in previous work [361], while maintaining high electrical conductivity and stable structure. Printed anodes were pyrolyzed at 800 °C, 1100 °C, and 1200 °C. The results confirm that controlled pyrolysis temperature strongly influences both the phase composition and functional behavior of the composites. Lower temperatures effectively suppressed the formation of SiC, which led to preserving the active crystalline silicon phase. The degree of carbonization and graphitization, however varied with temperature. At 800 °C, Raman and conductivity analyses indicate that the transformation of polymer to carbon was incomplete, which leaves an amorphous, oxygen-rich matrix with limited electronic pathways. This incomplete conversion results in low electrical conductivity and weak structural cohesion, which leads to reduced specific capacity and poor cycle stability. The low capacity retention at lower temperatures can also be attributed to insufficient mechanical strength of the carbon network, which is unable to accommodate the large volumetric expansion of silicon during lithiation and delithiation. As the pyrolysis temperature increases, the carbon network becomes more ordered. This improves its ability to buffer silicon expansion, maintain electrical contact, and stabilize the SEI. The progressive improvement in carbon ordering and conductivity from 800 °C to 1200 °C led to an increase in both specific capacity and capacity retention. The anode pyrolyzed at 1200 °C exhibited the highest initial specific capacity of 771 mAh g⁻¹, with a Coulombic efficiency of ~99.9%, and capacity retention of 61% over 120 cycles. The enhanced conductivity and partial graphitization at 1200 °C enabled efficient charge transport and mechanical resilience, with no SiC formation. Electrochemical impedance spectroscopy corroborated this trend by showing a significant reduction in charge-transfer resistance with temperature. In contrast, at 1400 °C, the excessive conversion of Si to SiC, reduced the available active material, which resulted in lower overall capacity [361]. Therefore, of the pyrolysis temperature tested 1200 °C represents a practical compromise, that achieves sufficient electrical performance without the high energy cost or silicon loss associated with more aggressive thermal treatments. It is important to note that the electrochemical

behavior of the printed sample observed at 1200 °C should be interpreted as a promising step toward upcycling silicon solar cells, rather than as a direct comparison to high-performance Si–C anodes. The moderate capacity retention achieved here reflects the constraints of a sustainable, upcycled-material system. The processing conditions must remain replicable and compatible with realistic cost and energy limitations. In addition, the silicon particles used in this work remained in the micrometer size range, because they were prepared using a low-cost Open-source ball mill [27] rather than a high-energy commercial milling system capable of producing nanoscale powders. This choice was made to align with the sustainability goals of the work, by using accessible, low-energy, and replicable processing methods over resource-intensive techniques. This work demonstrates a sustainable way for recycling solar cells into high-performance energy-storage materials. The optimized 1200 °C treatment yields a composite that balances carbon conductivity, structural stability, and silicon preservation. Because the focus of this chapter was on identifying an energy-conscious temperature range using accessible tools, temperatures above 1200 °C were not pursued. The process, which has been mostly carried out with open hardware to increase replicability [380–382] can enhance the economic and environmental feasibility of PV-silicon recycling by upcycling electronic waste into functional components for high-value lithium-ion batteries. To make a fully-Open-source tool chain, future work is needed to use Open-source electronics to drive an Open-source pyrolysis system [383], test Open-source glove boxes [384] for assembly, and develop an Open-source battery press. A limitation of this work was that the infrastructure required for through-thickness conductivity measurements was not available, and only in-plane conductivity could be obtained. Although through-thickness transport is directly relevant to battery operation, in-plane conductivity is a widely used to assess carbon network in polymer-derived ceramic systems [385]. Also, the consistent trends observed among in-plane conductivity, Raman I_D/I_G ratios, and the decrease in R_{ct} indicate that the structural evolution captured by in-plane measurements meaningfully reflects improvements in electronic pathways. Despite these encouraging results, further improvements are needed to bridge the gap between the achieved and theoretical capacity of the sample. Future work can focus on improving percolation pathways through the incorporation of either carbon nanotubes (CNTs) [386] or carbon black [387] into the resin formulation. Introducing one

of these additives is expected to increase the proportion of active silicon which contributes to charge storage. Also, full-cell validation against commercial cathodes is essential to assess practical performance and efficiency under application-relevant conditions. Finally, extended cycling (≥ 500 –1000 cycles) should be considered to verify durability and long-term stability.

5.4 Conclusions

Through this investigation, the pyrolysis temperature was identified as a critical factor that influences both the microstructure and electrochemical performance of the printed anodes. Among the studied temperatures, 1200 °C was found to be the optimal condition that produced a highly conductive carbon matrix without formation of electrochemically inactive SiC. XRD analysis confirmed that at 1200 °C, no SiC peaks appeared. The enhanced graphitization observed in Raman spectra at this temperature, coupled with the reduced charge-transfer resistance in EIS measurements, indicates that the carbon framework achieved high electronic conductivity while preserving the active silicon phase. As a result, the anode pyrolyzed at 1200 °C exhibited an initial specific capacity of approximately 771 mAh g⁻¹, with the initial Coulombic efficiency of 99.9%, and a capacity retention of 61% over 120 cycles. The achieved performance demonstrates a substantial improvement over the earlier SLA-printed PV-silicon anodes pyrolyzed at 1400 °C (~400 mAh g⁻¹, 89% retention, >100% CE over 200 cycles) which confirms that tuning pyrolysis temperature is a key strategy for enhancing reversible capacity in these silicon anodes.

Chapter 6

6 Upcycling Post-Consumer Plastic and Waste Silicon Photovoltaic Cells into Carbon-Enhanced Silicon Anodes for Li-ion Batteries Using 3D Printing

This chapter demonstrates a scalable, environmentally friendly pathway to a circular economy of lithium-ion battery anode fabrication. Specifically, carbon nanotubes (CNT) upcycled from waste plastic and silicon derived from waste photovoltaic cells are incorporated into a novel resin for SLA-based additive manufacturing and then pyrolyzed at 1200 °C. The resulting materials were analyzed using scanning electron microscopy, X-ray diffraction, energy-dispersive X-ray and Raman spectroscopy. Electrochemical performance was evaluated through galvanostatic charge–discharge, cyclic voltammetry, and electrochemical impedance spectroscopy analyses. The resulting CNT-Si–resin composite improves the electrochemical performance of battery anodes as they had an initial discharge capacity of 862 mAh/g with an initial Coulombic efficiency of 98.88%, which increased to 1,044 mAh/g upon cycling, compared with 771 mAh/g for the CNT-free anode under the same testing conditions. The upcycled electrode retained 100% of its capacity after 40 cycles and 73% after 120 cycles. This along with the materials characterization confirms the better structural robustness of the CNT-supported carbon framework as a continuous, conductive, and mechanically resilient network that enhances charge transport, that can buffer silicon volume expansion and stabilize the Si–C interface during cycling. These results show sustainable fabrication can match performance of more complex, chemically engineered systems.

6.1 Experimental section

6.1.1 Materials and Method

The experimental procedure for silicon preparation, resin formulation, stereolithographic printing, pyrolysis, and cell assembly builds upon the previously reported works [361] with modifications to incorporate carbon additives. End-of-life crystalline silicon (c-Si) photovoltaic cells were obtained from Heliene Inc. (Sault Ste. Marie, Ontario, Canada), mechanically fragmented, and ground using an open-source ball mill [27]. All silicon

materials were handled in an Open-source glove box [388]. The resulting powder was passed through a 32 μm stainless-steel mesh (KimLab, Ontario, Canada) and purified through a modified nitric-acid leaching process. In this step, 100 mL of deionized water was combined with 127 mL of HNO_3 (70 wt%, ~ 15.8 M, Sigma-Aldrich, Ontario, Canada), and the silicon powder was gradually introduced under magnetic stirring at 80 $^\circ\text{C}$ for 15 min. The solids were collected by vacuum filtration, rinsed with deionized water, and dried overnight at 60 $^\circ\text{C}$.

The purified silicon was then incorporated into a customized photopolymer resin. The carbon-containing formulation was investigated, in which CNTs were blended with the recycled silicon. To ensure sustainability in the supply of material, the CNTs used in this chapter were produced from a catalytic chemical vapor deposition (CVD) process that used waste plastics as the carbon source. This process was developed to transform hydrocarbon gases produced by the pyrolysis of household polyolefin wastes, making hydrogen and high-quality multiwalled CNTs. In this sustainable approach, plastic waste products such as Ziploc bags, garbage bags, and medical masks were first subjected to pyrolysis. The pyrolysis shaker reactor (PSR) developed at the Institute for Chemicals and Fuels from Alternative Resources (ICFAR) was used [389].

The PSR simulates industrial rotary kilns when used for cold-start pyrolysis, in which the plastic feedstock is gradually heated to 500 $^\circ\text{C}$ without pre-processing [390]. This process achieved liquid hydrocarbon yields of 70–80 wt% across all feedstocks, with a gaseous by-product rich in light hydrocarbons such as methane, ethylene, and propane. Raw municipal film wastes can also be pyrolyzed for similar liquids and gas products [391]. These gaseous by-products were then repurposed as feedstock for CNT synthesis to enhance process sustainability [392]. For this purpose, the hydrocarbon gases were passed through a horizontal quartz tube furnace (Fisher Scientific, 800 W, 25 mm diameter, maximum 1100 $^\circ\text{C}$; tube: Technical Glass Products, 25 mm outer diameter, wall thickness 1.5 mm, 600 mm length) containing a catalyst bed of 40-50 g porous iron particles (97.3% pure sponge iron, Iron Powders of North America) and alumina particles (containing $\sim 85\%$ Al_2O_3 and $\sim 10\%$ SiO_2) and operated at 800 $^\circ\text{C}$. Further details on the CVD reactor are available in Ref. [393]. The hydrocarbons were catalytically decomposed, generating a

hydrogen-rich gas phase (92–95% H₂ by recycling the outlet gas) and solid carbon products in the form of a mixture of multiwalled carbon nanotubes (diameter 70-100 nm, 50-120 layers) and carbon nanofibers (diameter 100-160 nm), referred to collectively as CNTs in this chapter for brevity. Raman spectroscopy of the CNTs revealed an I_D/I_G ratio of 1.21 ± 0.29 and 1.10 ± 0.05 for polypropylene and polyethylene pyrolysis gas feeds, respectively [394].

In this case, the CNTs accounted for 20 wt% of the solid fraction, while silicon contributed the remaining 80 wt%. The powders were dispersed into Prusament transparent red resin (Prusa Research, Prague, Czech Republic), together with cetyltrimethylammonium bromide (CTAB, Sigma Aldrich) as a dispersant and bis(2,4,6-trimethylbenzoyl)phenylphosphine oxide (IGM Resins, North Carolina, USA) as the photoinitiator. Resin mixing was performed in the dark using an open-source bottle roller [28] to ensure homogeneous dispersion of the conductive phase throughout the polymer matrix. Coin-cell anode geometries were designed in Onshape [395], sliced using PrusaSlicer [396], and fabricated with an ELEGOO Mars 4 Ultra 9K Resin 3D Printer (ELEGOO Technology Co., China). The printed samples were converted into anodes via pyrolysis in a gas-tight box furnace (Model 1616 FL, CM Furnaces, USA). The temperature was increased to 850 °C at 1 °C min⁻¹, followed by a second ramp to the target pyrolysis temperature of 1200 °C at 3 °C min⁻¹. Samples were held at the final temperature for 2 h under flowing nitrogen to prevent oxidation and were then cooled to room temperature at 10 °C min⁻¹.

6.1.2 Material tests

Microstructural features and elemental composition were studied using scanning electron microscopy (SEM, Hitachi SU3500, Hitachi, Japan) equipped with an Oxford Instruments X-act EDS detector (Oxford Instruments, UK). Phase analysis and crystallographic information were obtained through X-ray diffraction (XRD, Bruker D8 Advance, Bruker GmbH, Germany) using Cu K α radiation ($\lambda = 1.5406 \text{ \AA}$) over a 2θ range of 10°–90° with a scanning speed of 2° min⁻¹. Raman spectroscopy (Renishaw Raman microscope, Renishaw, UK) with a 514 nm excitation laser was used to analyze structural ordering within the carbon and silicon phases.

6.1.3 Electrochemical tests

The electrochemical behavior of the prepared anodes was examined using CR2032 half cells. Cell assembly was performed in an argon-filled glove box, where O₂ and H₂O levels were kept below 0.1 ppm to prevent contamination. Lithium metal (Primet Lab, China) was used as both the counter and reference electrode, while Celgard 2400 served as the separator. The electrolyte (Primet Lab, China) consisted of 1 M LiPF₆ dissolved in a mixture of ethylene carbonate (EC), diethyl carbonate (DEC), and dimethyl carbonate (DMC) in a 1:1:1 volume ratio, with fluoroethylene carbonate (FEC) added as an electrolyte additive. Electrochemical measurements were conducted using a CS300 potentiostat (Corrtest, China). Galvanostatic charge–discharge cycling was performed between 0.01 and 1.5 V vs. Li/Li⁺ at room temperature to evaluate cycling stability. The mass of active materials was calculated as 3 mg. Cyclic voltammetry (CV) was carried out in the voltage window of 0.01–1.5 V vs. Li/Li⁺ at a scan rate of 0.15 mV s⁻¹ to investigate lithiation/delithiation mechanisms and associated redox processes. Electrochemical impedance spectroscopy (EIS) was performed over the frequency range of 100 kHz to 0.01 Hz with a 10 mV AC perturbation to assess charge-transfer resistance and interfacial properties.

6.2 Results

6.2.1 XRD

Figure 6-1 shows the XRD pattern of the sample containing CNT pyrolyzed at 1200 °C. XRD analysis confirmed the presence of crystalline silicon at all pyrolysis temperatures, with characteristic diffraction peaks appearing at 28.7° (111), 47.76° (022), 56.69° (131), 69.86° (040), 77.2° (133), and 89.06° (242). These peaks align with the reference silicon pattern COD-9013102 [362], identified using the open-source Profex software [363] and further validated by extracting the peak positions from the COD database through the Pymatgen (Python Materials Genomics) library [364]. The crystallite sizes calculated from peak broadening were 289 Å, 306 Å, 254 Å, 266 Å, and 391 Å. No visible signal of SiC is

observed, which indicates that pyrolysis at 1200 °C did not result in the formation of a SiC interphase.

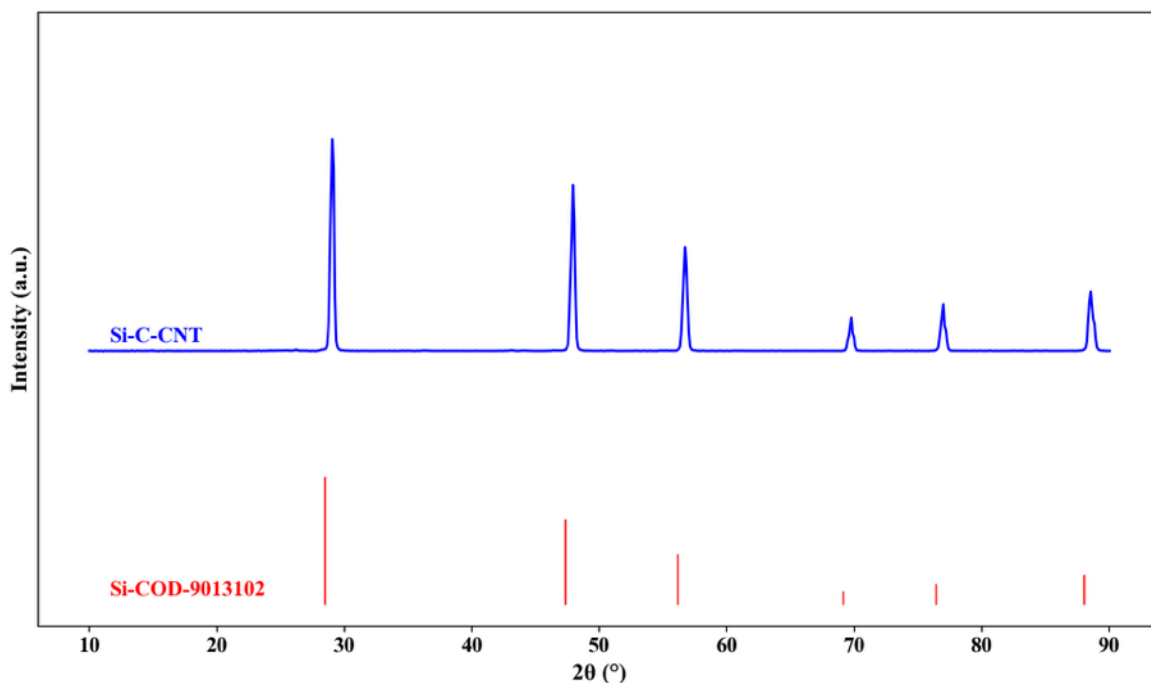


Figure 6-1. XRD patterns of silicon–carbon composite anodes containing carbon nanotubes, showing diffraction intensity as a function of 2θ .

6.2.2 Raman

Figure 6-2 illustrates the Raman spectrum of the sample containing CNT pyrolyzed at 1200 °C. The result exhibits the characteristic bands of multi-walled carbon nanotubes including the D ($\sim 1350\text{ cm}^{-1}$), G ($\sim 1580\text{ cm}^{-1}$), and 2D ($\sim 2700\text{ cm}^{-1}$) bands [397]. The D band corresponds to disorder-induced vibrations from defects or amorphous regions in the carbon lattice, and the G band arises from the in-plane stretching of sp^2 -bonded carbon atoms in graphitic domains [397]. Also, the 2D band, which is the first overtone of the D band, is present in graphitic materials and is commonly used to assess long-range ordering [397,398]. The intensity ratio of I_D/I_G is ~ 1.03 , which suggests a partially ordered carbon network with moderate structural defects. This is consistent with the polymer-to-carbon conversion at 1200 °C on previous work [399].

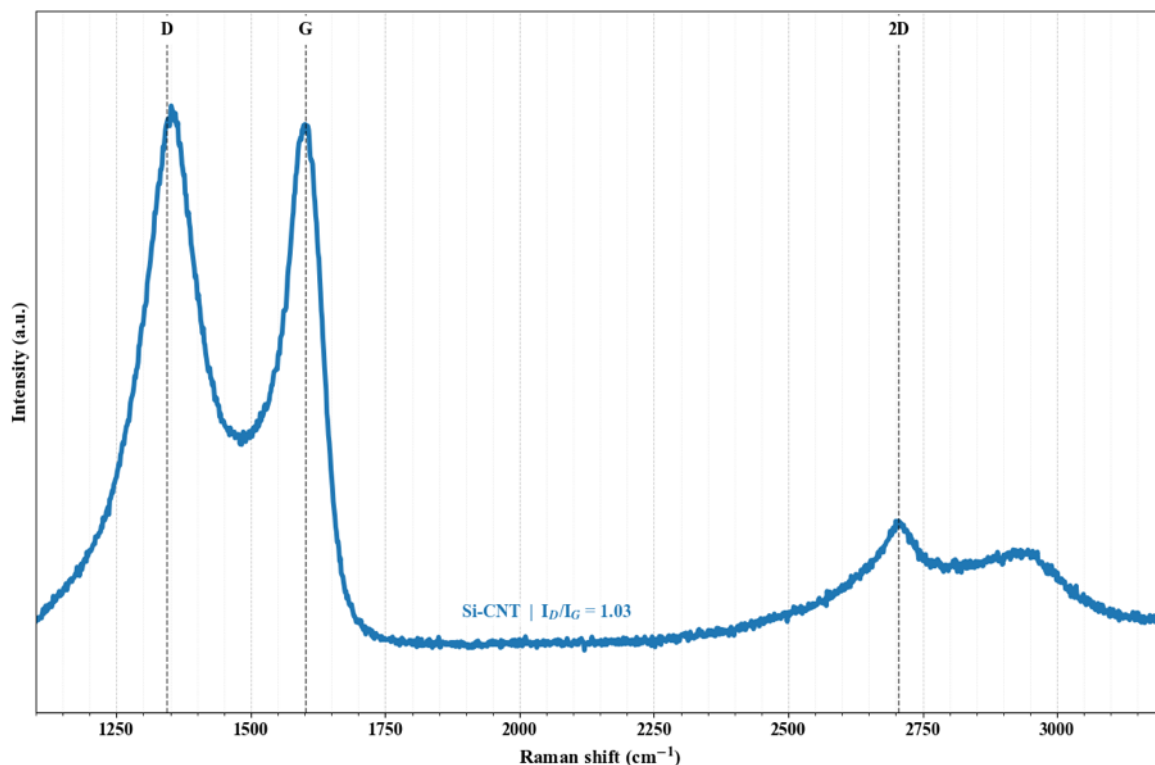


Figure 6-2. Raman spectra of silicon–carbon composite anodes containing carbon nanotubes, showing Raman intensity as a function of Raman shift.

6.2.3 SEM and EDS

The SEM–EDS of the composite pyrolyzed at 1200 °C is shown in Figure 6-3. The SEM image shows a compact surface with finely distributed particles embedded within the carbon matrix. This indicates successful distribution of the particles into the resin before printing. The elemental maps confirm that carbon, which originates from the resin and CNTs, forms a continuous and well-connected network across the surface, while silicon is evenly dispersed and does not form large agglomerates. Oxygen appears only in small amounts, which suggests partial reduction of surface oxides. The overlap of Si and C supports strong interfacial contact between silicon and the carbon matrix, which enhances electronic connectivity and structural stability.

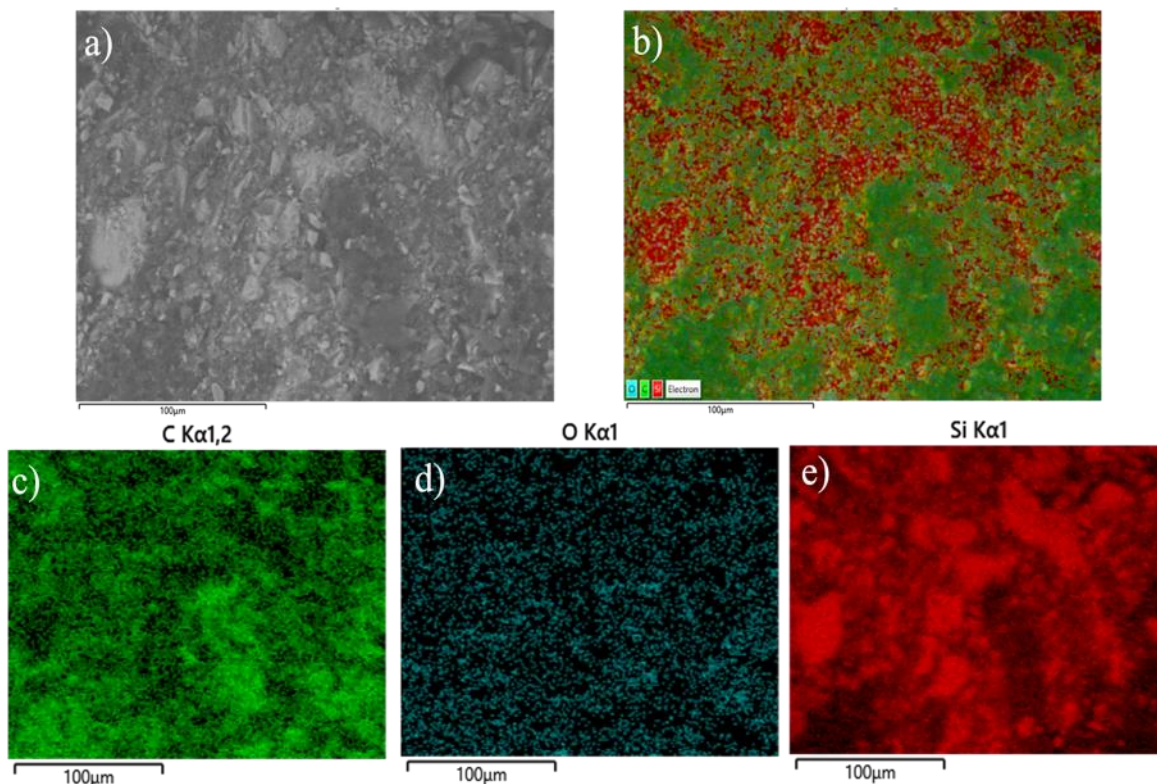


Figure 6-3. EDS analysis of the silicon–carbon composite anode containing carbon nanotubes: (a) SEM micrograph of the selected region, (b) overlaid EDS elemental map, (c) carbon elemental map, (d) oxygen elemental map, and (e) silicon elemental map.

6.2.4 Galvanostatic Cycling

Figure 6-4 shows the galvanostatic charge–discharge profiles of the composite anode pyrolyzed at 1200 °C at 0.88 mA g⁻¹ current rate. The initial discharge capacity is 862 mAh g⁻¹ with the initial Coulombic efficiency of 98.88% and capacity retention of 73% after 120 cycles. Compared to the previous Si–resin composite without CNTs [400], which delivered an initial discharge capacity of 771 mAh g⁻¹ under the same conditions, the current composite exhibits an improvement in electrochemical performance. CNT additives in the composite act as one-dimensional conductive bridges and form a continuous network that enhances electron transport and reduces internal resistance [401] which is supported by the EIS result. CNTs provide line contact rather than point contact, which results in more efficient electronic pathways through the electrode. Additionally, the CNTs can serve as

elastic scaffolds that buffer the high volume expansion of Si during lithiation through maintaining structural integrity and electrical connectivity [402]. The connected CNT–carbon network formed during pyrolysis encapsulates silicon particles and minimizes

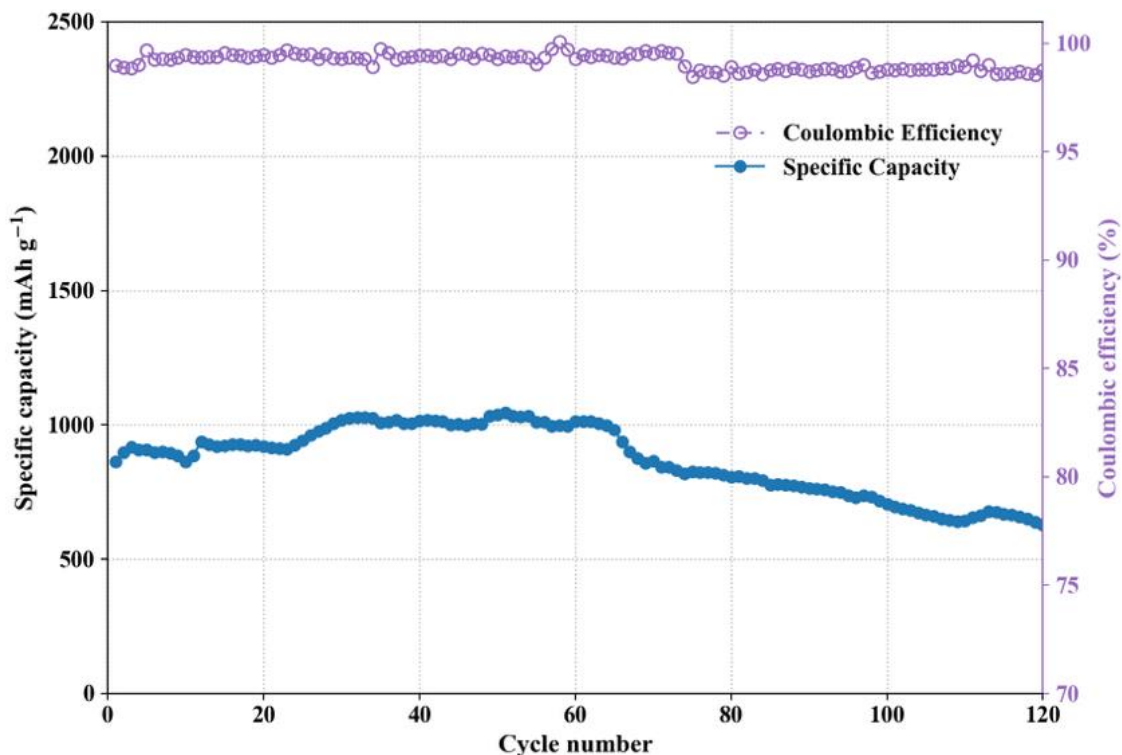


Figure 6-4. Galvanostatic charge–discharge voltage profiles of the silicon–carbon composite anode containing carbon nanotubes, showing voltage as a function of specific capacity.

particle pulverization [403]. It is noteworthy that the discharge capacity increases to 1044 mAh g⁻¹ in the subsequent cycles. This behavior can be attributed to the gradual activation of previously isolated silicon domains, a phenomenon consistent with previous reports [404].

6.2.5 Cyclic Voltammetry (CV)

The cyclic voltammetry curve of the composite pyrolyzed at 1200 °C shown in Figure 6-5 reveals the typical lithiation and delithiation features of a silicon-based anode. During the cathodic scan, a broad reduction peak is observed which is around 0.2 V vs. Li/Li⁺ and extends toward 0 V. This peak corresponds to the lithiation of crystalline silicon to form amorphous Li_xSi_y [375]. In the anodic sweep, two broad oxidation peaks appear at approximately 0.35 V and 0.52 V, which are associated with the delithiation of the

amorphous Li_xSi_y phase [374]. The curves overlap closely, which indicates that the amorphization process has completed and the SEI is stable. Also, the relatively high current response (≈ 2 mA) reflects efficient charge transport within the electrode [376].

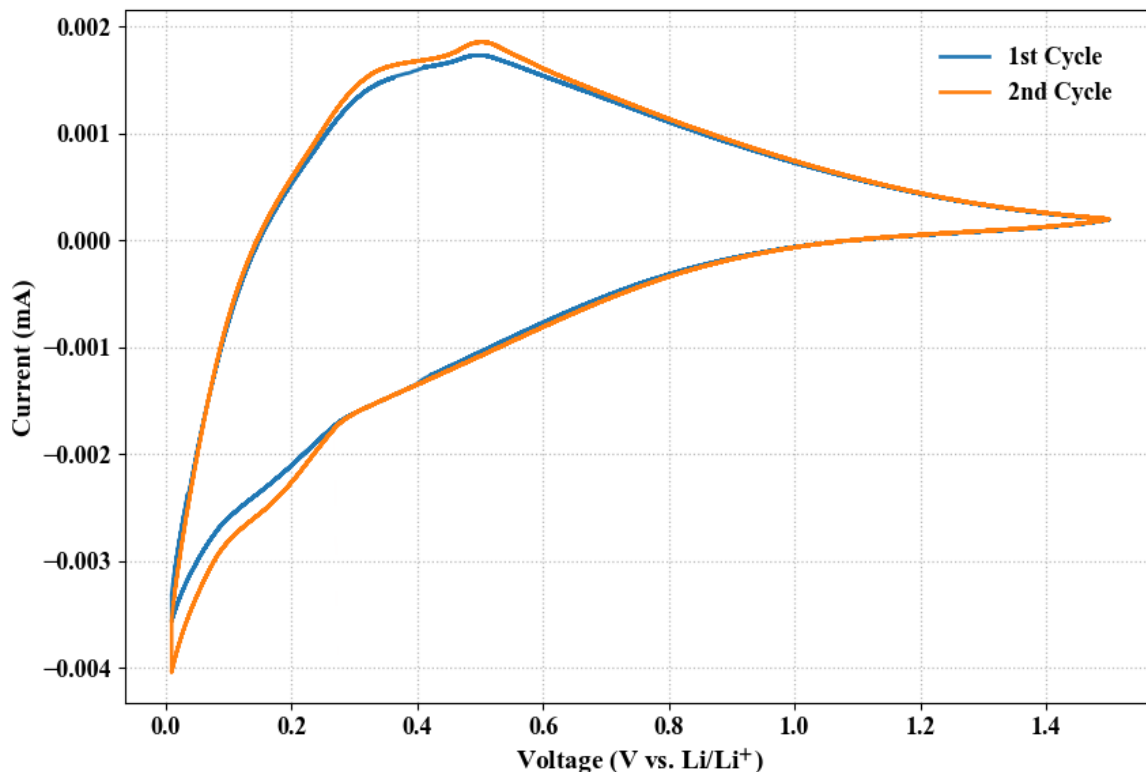


Figure 6-5. CV curves of the silicon-carbon composite anode containing carbon nanotubes, showing current as a function of voltage.

6.2.6 Electrochemical Impedance Spectroscopy (EIS)

Figure 6-6 shows the Nyquist plot of the composite. The spectrum consists of a semicircle in the high-to-medium frequency region, followed by a sloped line in the low-frequency region, corresponding to the charge-transfer process and lithium-ion diffusion, respectively. The small semicircle diameter ($R_{CT} \approx 12 \Omega$), indicates rapid charge-transfer kinetics and high electrical conductivity. This low impedance is primarily attributed to the highly conductive framework created by the carbon from the resin matrix achieved during pyrolysis and the added CNTs, which together form a continuous network and facilitate electron transport. Also, interfacial contact between silicon and the carbonaceous matrix minimizes interfacial resistance, while the porous structure enhances electrolyte

accessibility and Li^+ diffusion. Compared to the previous composite without CNTs, which exhibited higher impedance values at $1200\text{ }^\circ\text{C}$ ($R_{\text{CT}} \approx 25\ \Omega$), the present composite reveals

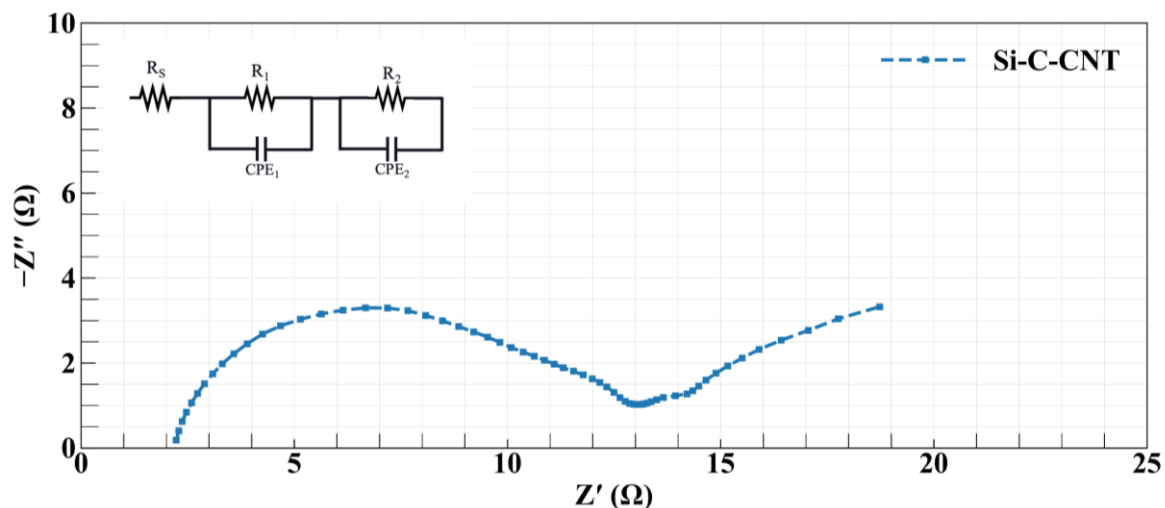


Figure 6-6. EIS Nyquist plot of the silicon-carbon composite anode containing carbon nanotubes, showing Z' versus $-Z''$. enhanced conductivity and faster electrochemical kinetics. This improvement confirms the crucial role of CNTs in reinforcing the conductive framework and stabilizing the silicon-carbon interface, which results in better electrochemical performance [400].

6.3 Discussion

The integration of CNTs into the Si-resin composite substantially enhances the electrochemical performance compared with the CNT-free system in the previous work. In that earlier configuration, a discharge capacity of $771\ \text{mAh g}^{-1}$ was achieved under identical testing conditions. By incorporating CNTs, the initial capacity was $862\ \text{mAh g}^{-1}$ and increased to $1044\ \text{mAh g}^{-1}$ upon cycling, which is an improvement in both utilization and activation of the silicon phase. This enhancement confirms that the conductive and elastic characteristics of CNTs further address poor electronic conductivity and mechanical instability of the silicon anodes.

Table 6-1 compares the results to CNT-reinforced Si/C anodes in the literature. Although some CNT-Si films report higher gravimetric capacities, these systems rely on specialized deposition techniques that may limit practical scalability. In contrast, the SLA-printed composite in this work was prepared by a simple, scalable, and sustainable fabrication

route. Compared with chemically bonded CNT–Si systems, the performance obtained here is within a similar range but achieved with recycled silicon, pyrolytic CNTs, and a fully open, low-cost toolchain.

Table 6-1. Comparison of CNT-reinforced Si/C anodes in the literature and this work

Study (Ref.)	Architecture	Capacity	Notes
This work	SLA-printed Si + CNT + resin-derived carbon	862 → 1044 mAh g ⁻¹	Recycled PV Si; CNTs from waste plastic; printed electrode
Previous work [400]	SLA-printed Si + resin-derived carbon	771 mAh g ⁻¹	Recycled PV Si; No CNT; printed electrode
Zhao et al [405]	Si/CNFs + in-situ CNTs	639.9 mAh g ⁻¹	Strong dual-network CNT support
Ikonen et al [406]	TCPSi chemically bonded to CNTs	1150 mAh g ⁻¹	Strong Si–CNT bonding improves cycling stability
Zhang et al [407]	CNT/(Fe@Si@SiO ₂)	968 mAh g ⁻¹	CNT scaffold supports core–shell Si composites

The enhanced capacity and reduced impedance confirm that the resin-derived carbon matrix contributes to three-dimensional conductivity and structural support, which is further improved by CNTs that create a continuous electron pathway and act as elastic bridges between silicon particles, reduce the interfacial resistance, and buffer volume expansion. Relative to commercial graphite (372 mAh g⁻¹), the CNT-reinforced anode still provides nearly three times higher capacity.

In addition to improved performance, the sustainability aspect of this work represents a key advancement. The CNTs used here were sustainably synthesized from hydrocarbon gases generated during the pyrolysis of household plastic waste, which eliminates the need for high-cost purified carbon precursors. With the upcycling of end-of-life photovoltaic silicon, this chapter shows a circular-economy approach in which two waste streams, plastic and solar cells, are transformed into components for lithium-ion battery anodes. This chain reduces environmental burden and provides a low-cost, additive-manufacturing-based route to advanced anode materials.

The main limitation of this work is that the electrochemical evaluation was limited to half-cell configuration against lithium metal. To assess real-world applicability, future testing in full-cell systems paired with commercial cathodes is essential to determine the practical energy density, Coulombic efficiency, and compatibility with industrial electrolytes. Future work should therefore focus on testing the anode in full-cell configurations.

6.4 Conclusions

This work introduces a scalable and green pathway toward silicon anodes for energy-storage applications by demonstrating that incorporating CNTs into a Si–resin composite improves the electrochemical performance of recycled silicon anodes. The CNT-reinforced composite delivered an initial discharge capacity of 862 mAh g⁻¹ with an initial Coulombic efficiency of 98.88%, which increased to 1044 mAh g⁻¹ upon cycling, compared with 771 mAh g⁻¹ for the CNT-free anode under the same testing conditions. The electrode exhibited stability and retained 100% of its capacity after 40 cycles and 73% after 120 cycles. This confirms the better structural robustness of the CNT-supported carbon framework. The improvement arises from the formation of a continuous, conductive, and mechanically resilient network that enhances charge transport, that can buffer silicon volume expansion and stabilize the Si–C interface during cycling. The CNTs used in this work were sustainably synthesized from hydrocarbon gases obtained through the pyrolysis of household plastic waste. Beyond electrochemical results, this approach advances the circular economy for lithium-ion batteries by upcycling two waste streams. This strategy is a proof of concept of fabricating anode materials through a simple, additive-manufacturing-based, and environmentally friendly process. Achieving the capacity without the use of aggressive chemical treatments demonstrates that sustainable fabrication routes can match the performance of more complex, chemically engineered systems.

Chapter 7

7 Conclusions, Limitations, and Future Works

This work shows that open-source hardware, additive manufacturing and recycled materials can combine to produce practical, high-performance lithium-ion battery anodes. Through the open-source ball mill, bottle roller, and inert-gas glove box, waste photovoltaic silicon was ground, dispersed in custom SLA resins, and printed into anode geometries. Pyrolysis was used to convert the non-conductive and non-active resin to carbon. The first generation of 3D-printed, PV-derived anodes containing ground solar cell silicon and pyrolyzed at 1 400 °C delivered specific capacities of about 400 mAh g⁻¹, with 89 % capacity retention and Coulombic efficiencies of 100 % over 200 cycles. These results proved that end-of-life solar cells can be upcycled into functional battery materials and set a performance baseline for subsequent optimization. In this work, the presence of electrochemically inactive SiC in the material structure indicated the need to optimize the pyrolysis temperature. This motivated the next stage of the study, which focused on adjusting the thermal treatment to suppress SiC formation and preserve the active silicon phase.

Exploration of pyrolysis temperature revealed that this step critically influences both microstructure and electrochemical behaviour. Reducing the pyrolysis temperature to 1 200 °C prevented formation of electrochemically inactive SiC, improved graphitization and conductivity in the carbon matrix, and raised the initial specific capacity to ≈771 mAh g⁻¹.

A final step in performance came from reinforcing the Si–resin composite with CNTs synthesized from pyrolysis of household plastic waste. The CNT-supported anodes delivered initial discharge capacities of ≈862 mAh g⁻¹ with 98.9 % initial Coulombic efficiency and continued to increase upon cycling, reaching ≈1 044 mAh g⁻¹. The electrodes retained 100 % of their capacity after 40 cycles and ≈73 % after 120 cycles. This shows that the CNT network enhances charge transport, buffers silicon volume changes, and stabilizes the Si–C interface. This not only demonstrates the power of composite design

but also shows a circular-economy approach, as both silicon and CNTs were sourced from waste streams.

These performance results prove the feasibility and potential of combining recycled materials, open-source hardware, and additive manufacturing to produce sustainable lithium-ion battery anodes.

Despite these successes, several limitations remain that create opportunities for further improvement. The current glove box prototype reduced oxygen levels to 19 ppm, but it should be noted that lithium-ion battery assembly requires oxygen and moisture concentrations below 1 ppm. Achieving and maintaining such strict conditions will demand more efficient purification methods, such as high-capacity scavengers (activated carbon, molecular sieves, copper-based materials) and multi-stage cartridges. Also, integrating automated control systems that adjust purge rates based on real-time oxygen and humidity readings would minimize gas consumption, enhance reproducibility, and lower operating costs.

The need for strict environmental control is rooted in the reactivity of lithium metal and the electrolyte components. Even trace amounts of water can decompose into hydrogen and oxygen, while LiPF_6 can degrade to form PF_5 and HF which are species that can corrode or dissolve active materials and current collectors. Similarly, oxygen can react with lithium to form Li_2O and Li_2O_2 , which consume active lithium and alter the SEI. Strengthening the moisture and oxygen removal mechanisms in the glove box is therefore essential for having safe handling of lithium and for achieving reliable and reproducible electrochemical cell assembly in future studies.

A further opportunity for future work is the deliberate control of electrode porosity. In this study, porosity arises indirectly from resin formulation, solid loading, printing parameters, and pyrolysis-induced mass loss, rather than being independently tuned. In industrial additive manufacturing of battery electrodes, powder-based printing approaches have demonstrated that porosity can be explicitly controlled to optimize ionic transport, electrolyte accessibility, and electrode utilization. Future work could adapt porosity-control strategies such as sacrificial pore formers, graded architectures, or modified

pyrolysis protocols within the SLA and polymer-derived carbon framework developed here.

Another important direction for future work is a life cycle assessment (LCA) and net energy analysis. Although the maximum pyrolysis temperature used in this work is lower than that typically required for industrial graphite graphitization, a comprehensive LCA is still needed to confirm that the overall process results in net energy savings. Such an analysis should consider all processing steps, including silicon recovery, powder processing, additive manufacturing, pyrolysis, and cell assembly, to verify that this approach offers energy and sustainability advantages over conventional anode production routes.

Future work should also explore the use of different electrolyte formulations to evaluate their influence on SEI formation, interfacial stability, and long-term cycling performance of the silicon–carbon composite anodes. In addition, future studies could investigate alternative lattice and architected electrode structures to optimize ion transport, mechanical stability, and areal capacity.

In parallel, developing and validating an open-source battery press is an important next step in the hardware toolchain. A practical future direction is to design a low-cost, 3D-printable press frame with interchangeable die sets, which is preferably instrumented with a load cell to quantify applied pressure. This extension would complete the open-source workflow from powder processing to electrode printing and cell assembly.

Another limitation is that the electrochemical evaluation in this work was limited to half-cell configurations using lithium metal as both the counter and reference electrodes. While this configuration is standard for fundamental research, it does not represent the performance of the anodes under realistic conditions.

A practical starting point is to pair the recycled-Si and recycled-Si-CNT anodes with LiFePO_4 (LFP) cathodes in full cells. LFP is attractive due to its excellent cycling stability and safer voltage window. Experimental design could follow established full-cell protocols used for silicon-based and 3D-printed anodes, including formation cycles at low current

(e.g., C/10 or C/20) within an appropriate voltage window (e.g., 2.5–3.8 V for Si||LFP), and rate-capability and long-term cycling tests at higher C-rates (C/2, 1C, and beyond). Building on these templates for full cells will allow direct comparison of the recycled-Si anodes with Si-C-based and 3D-printed electrodes.

Although full-cell testing was outside the scope of this work due to budget constraints and the exploratory nature of the project, the foundation established here, including materials, processing conditions, and open-source tooling, makes such studies in the future both feasible and well-defined.

While this project achieved its main objective of the proof of the concept of a viable open-source approach for producing lithium-ion battery anodes from recycled silicon, the outlined improvements offer a clear pathway toward higher performance, greater reliability, and future large-scale implementation.

8 References

- [1] Tarascon J-M, Armand M. Issues and challenges facing rechargeable lithium batteries. *Nature* 2001;414:359–67. <https://doi.org/10.1038/35104644>.
- [2] Dunn B, Kamath H, Tarascon J-M. Electrical Energy Storage for the Grid: A Battery of Choices. *Science* 2011;334:928–35. <https://doi.org/10.1126/science.1212741>.
- [3] Cao F, Barsukov IV, Bang HJ, Zaleski P, Prakash J. Evaluation of Graphite Materials as Anodes for Lithium-Ion Batteries. *J Electrochem Soc* 2000;147:3579. <https://doi.org/10.1149/1.1393942>.
- [4] Li Z, Zhang Y, Liu T, Gao X, Li S, Ling M, et al. Silicon Anode with High Initial Coulombic Efficiency by Modulated Trifunctional Binder for High-Areal-Capacity Lithium-Ion Batteries. *Advanced Energy Materials* 2020;10:1903110. <https://doi.org/10.1002/aenm.201903110>.
- [5] Electricity in the U.S. - U.S. Energy Information Administration (EIA) n.d. <https://www.eia.gov/energyexplained/electricity/electricity-in-the-us.php> (accessed January 19, 2024).
- [6] Pearce JM, Parncutt R. Quantifying Global Greenhouse Gas Emissions in Human Deaths to Guide Energy Policy. *Energies* 2023;16:6074. <https://doi.org/10.3390/en16166074>.
- [7] D'Amato G, Cecchi L. Effects of climate change on environmental factors in respiratory allergic diseases. *Clinical & Experimental Allergy* 2008;38:1264–74. <https://doi.org/10.1111/j.1365-2222.2008.03033.x>.
- [8] Haines A, Kovats R, Campbell-Lendrum D, Corvalan C. Climate change and human health: impacts, vulnerability, and mitigation. *The Lancet* 2006;367:2101–9. [https://doi.org/10.1016/S0140-6736\(06\)68933-2](https://doi.org/10.1016/S0140-6736(06)68933-2).
- [9] Denkenberger DC, Pearce JM. Feeding everyone: Solving the food crisis in event of global catastrophes that kill crops or obscure the sun. *Futures* 2015;72:57–68. <https://doi.org/10.1016/j.futures.2014.11.008>.
- [10] Barnes DF, Floor WM. RURAL ENERGY IN DEVELOPING COUNTRIES: A Challenge for Economic Development. *Annu Rev Energy Environ* 1996;21:497–530. <https://doi.org/10.1146/annurev.energy.21.1.497>.
- [11] Peters GP, Hertwich EG. CO₂ Embodied in International Trade with Implications for Global Climate Policy. *Environ Sci Technol* 2008;42:1401–7. <https://doi.org/10.1021/es072023k>.

- [12] Stern N. The Economics of Climate Change. *American Economic Review* 2008;98:1–37. <https://doi.org/10.1257/aer.98.2.1>.
- [13] Heidari N, Pearce JM. A review of greenhouse gas emission liabilities as the value of renewable energy for mitigating lawsuits for climate change related damages. *Renewable and Sustainable Energy Reviews* 2016;55:899–908. <https://doi.org/10.1016/j.rser.2015.11.025>.
- [14] Pryor SC, Barthelmie RJ. Climate change impacts on wind energy: A review. *Renewable and Sustainable Energy Reviews* 2010;14:430–7. <https://doi.org/10.1016/j.rser.2009.07.028>.
- [15] Global wind and solar energy share in electricity mix 2022. Statista n.d. <https://www.statista.com/statistics/1302047/global-wind-and-solar-energy-share-electricity-mix/> (accessed September 26, 2023).
- [16] Hub ISK. Wind and Solar Will Provide 50% of Electricity in 2050, BNEF Report Finds | News | SDG Knowledge Hub | IISD n.d. <http://sdg.iisd.org/news/wind-and-solar-will-provide-50-of-electricity-in-2050-bnef-report-finds/> (accessed January 19, 2024).
- [17] Yu H, Helland H, Yu X, Gundersen T, Sin G. Optimal design and operation of an Organic Rankine Cycle (ORC) system driven by solar energy with sensible thermal energy storage. *Energy Conversion and Management* 2021;244:114494. <https://doi.org/10.1016/j.enconman.2021.114494>.
- [18] Ali U. Bloomberg New Energy Outlook 2019: The future of the energy sector. *Power Technology* 2019. <https://www.power-technology.com/news/bloomberg-new-energy-outlook-2019-2/> (accessed September 26, 2023).
- [19] Adeh EH, Good SP, Calaf M, Higgins CW. Solar PV Power Potential is Greatest Over Croplands. *Sci Rep* 2019;9:11442. <https://doi.org/10.1038/s41598-019-47803-3>.
- [20] Garg P, Orosz MS, Kumar P. Thermo-economic evaluation of ORCs for various working fluids. *Applied Thermal Engineering* 2016;109:841–53. <https://doi.org/10.1016/j.applthermaleng.2016.06.083>.
- [21] Zhu Z, Jiang T, Ali M, Meng Y, Jin Y, Cui Y, et al. Rechargeable Batteries for Grid Scale Energy Storage. *Chem Rev* 2022;122:16610–751. <https://doi.org/10.1021/acs.chemrev.2c00289>.
- [22] Kebede AA, Kalogiannis T, Van Mierlo J, Berecibar M. A comprehensive review of stationary energy storage devices for large scale renewable energy sources grid integration. *Renewable and Sustainable Energy Reviews* 2022;159:112213. <https://doi.org/10.1016/j.rser.2022.112213>.

- [23] Harper G, Sommerville R, Kendrick E, Driscoll L, Slater P, Stolkin R, et al. Recycling lithium-ion batteries from electric vehicles. *Nature* 2019;575:75–86. <https://doi.org/10.1038/s41586-019-1682-5>.
- [24] Nair N-KC, Garimella N. Battery energy storage systems: Assessment for small-scale renewable energy integration. *Energy and Buildings* 2010;42:2124–30. <https://doi.org/10.1016/j.enbuild.2010.07.002>.
- [25] Joseph PK, Devaraj E. Design of hybrid forward boost converter for renewable energy powered electric vehicle charging applications. *IET Power Electronics* 2019;12:2015–21. <https://doi.org/10.1049/iet-pel.2019.0151>.
- [26] Ransome T. Lithium Ion Battery. *Renewables4U* 2023. <https://www.renewables4u.com.au/lithium-ion-battery/> (accessed January 19, 2024).
- [27] Mottaghi M, Rahman M, Kulkarni A, Pearce JM. AC/off-grid photovoltaic powered open-source ball mill. *HardwareX* 2023;14:e00423. <https://doi.org/10.1016/j.ohx.2023.e00423>.
- [28] Mottaghi M, Bai Y, Kulkarni A, Pearce JM. Open-source scientific bottle roller. *HardwareX* 2023;15:e00445. <https://doi.org/10.1016/j.ohx.2023.e00445>.
- [29] Dhankani KC, Pearce JM. Open-source laboratory sample rotator mixer and shaker. *HardwareX* 2017;1:1–12. <https://doi.org/10.1016/j.ohx.2016.07.001>.
- [30] Vadivel D, Branciforti DS, Kerroumi O, Dondi M, Dondi D. Mostly 3D printed chemical synthesis robot. *HardwareX* 2022;11:e00310. <https://doi.org/10.1016/j.ohx.2022.e00310>.
- [31] Lyu Z, Lim GJH, Koh JJ, Li Y, Ma Y, Ding J, et al. Design and Manufacture of 3D-Printed Batteries. *Joule* 2021;5:89–114. <https://doi.org/10.1016/j.joule.2020.11.010>.
- [32] Pang Y, Cao Y, Chu Y, Liu M, Snyder K, MacKenzie D, et al. Additive Manufacturing of Batteries. *Advanced Functional Materials* 2020;30:1906244. <https://doi.org/10.1002/adfm.201906244>.
- [33] Tagawa K, Brodd RJ. Production Processes for Fabrication of Lithium-Ion Batteries. In: Yoshio M, Brodd RJ, Kozawa A, editors. *Lithium-Ion Batteries: Science and Technologies*, New York, NY: Springer; 2009, p. 181–94. https://doi.org/10.1007/978-0-387-34445-4_8.
- [34] Bommineedi LK, Upadhyay N, Minnes R. Screen Printing: An Ease Thin Film Technique. In: Sankapal BR, Ennaoui A, Gupta RB, Lokhande CD, editors. *Simple Chemical Methods for Thin Film Deposition: Synthesis and Applications*, Singapore: Springer Nature; 2023, p. 449–507. https://doi.org/10.1007/978-981-99-0961-2_11.

- [35] Wei T-S, Ahn BY, Grotto J, Lewis JA. 3D Printing of Customized Li-ion Batteries with Thick Electrodes. *Advanced Materials* 2018;30:1703027. <https://doi.org/10.1002/adma.201703027>.
- [36] Shi H, Cao J, Sun Z, Ghazi ZA, Zhu X, Han S, et al. 3D Printing Enables Customizable Batteries. *Batteries & Supercaps* 2023;6:e202300161. <https://doi.org/10.1002/batt.202300161>.
- [37] Idrees M, Batool S, Din MAU, Javed MS, Ahmed S, Chen Z. Material-structure-property integrated additive manufacturing of batteries. *Nano Energy* 2023;109:108247. <https://doi.org/10.1016/j.nanoen.2023.108247>.
- [38] Gonçalves R, Lanceros-Méndez S, Costa CM. Electrode fabrication process and its influence in lithium-ion battery performance: State of the art and future trends. *Electrochemistry Communications* 2022;135:107210. <https://doi.org/10.1016/j.elecom.2022.107210>.
- [39] Fonseca N, Thummalapalli SV, Jambhulkar S, Ravichandran D, Zhu Y, Patil D, et al. 3D Printing-Enabled Design and Manufacturing Strategies for Batteries: A Review. *Small* 2023;2302718. <https://doi.org/10.1002/smll.202302718>.
- [40] Ben-Barak I, Schneier D, Kamir Y, Goor M, Golodnitsky D, Peled E. Drop-on-demand 3D-printed silicon-based anodes for lithium-ion batteries. *J Solid State Electrochem* 2022;26:183–93. <https://doi.org/10.1007/s10008-021-05056-z>.
- [41] Ben-Barak I, Kamir Y, Menkin S, Goor M, Shekhtman I, Ripenbein T, et al. Drop-on-Demand 3D Printing of Lithium Iron Phosphate Cathodes. *J Electrochem Soc* 2018;166:A5059. <https://doi.org/10.1149/2.0091903jes>.
- [42] Gao X, Liu K, Su C, Zhang W, Dai Y, Parkin IP, et al. From bibliometric analysis: 3D printing design strategies and battery applications with a focus on zinc-ion batteries. *SmartMat* 2024;5:e1197. <https://doi.org/10.1002/smm2.1197>.
- [43] Torabi F, Ahmadi P. Battery technologies. *Simulation of Battery Systems*, Elsevier; 2020, p. 1–54. <https://doi.org/10.1016/B978-0-12-816212-5.00005-2>.
- [44] Bates JB, Dudney NJ, Neudecker B, Ueda A, Evans CD. Thin-film lithium and lithium-ion batteries. *Solid State Ionics* 2000;135:33–45. [https://doi.org/10.1016/S0167-2738\(00\)00327-1](https://doi.org/10.1016/S0167-2738(00)00327-1).
- [45] Zhou L, Ning W, Wu C, Zhang D, Wei W, Ma J, et al. 3D-Printed Microelectrodes with a Developed Conductive Network and Hierarchical Pores toward High Areal Capacity for Microbatteries. *Advanced Materials Technologies* 2019;4. <https://doi.org/10.1002/admt.201800402>.
- [46] Wang Y, Chen C, Xie H, Gao T, Yao Y, Pastel G, et al. 3D-Printed All-Fiber Li-ion Battery toward Wearable Energy Storage. *Advanced Functional Materials* 2017;27:1703140. <https://doi.org/10.1002/adfm.201703140>.

- [47] Huang J, Yang J, Li W, Cai W, Jiang Z. Electrochemical properties of LiCoO₂ thin film electrode prepared by ink-jet printing technique. *Thin Solid Films* 2008;516:3314–9. <https://doi.org/10.1016/j.tsf.2007.09.039>.
- [48] Dudney NJ, Neudecker BJ. Solid state thin-film lithium battery systems. *Current Opinion in Solid State and Materials Science* 1999;4:479–82. [https://doi.org/10.1016/S1359-0286\(99\)00052-2](https://doi.org/10.1016/S1359-0286(99)00052-2).
- [49] Schwenzel J, Thangadurai V, Weppner W. Developments of high-voltage all-solid-state thin-film lithium ion batteries. *Journal of Power Sources* 2006;154:232–8. <https://doi.org/10.1016/j.jpowsour.2005.03.223>.
- [50] Clement B, Lyu M, Sandeep Kulkarni E, Lin T, Hu Y, Lockett V, et al. Recent Advances in Printed Thin-Film Batteries. *Engineering* 2022;13:238–61. <https://doi.org/10.1016/j.eng.2022.04.002>.
- [51] Ding J, Shen K, Du Z, Li B, Yang S. 3D-Printed Hierarchical Porous Frameworks for Sodium Storage. *ACS Appl Mater Interfaces* 2017;9:41871–7. <https://doi.org/10.1021/acsami.7b12892>.
- [52] Saleh MS, Li J, Park J, Panat R. 3D printed hierarchically-porous microlattice electrode materials for exceptionally high specific capacity and areal capacity lithium ion batteries. *Additive Manufacturing* 2018;23:70–8. <https://doi.org/10.1016/j.addma.2018.07.006>.
- [53] Liu C, Qiu Y, Liu Y, Xu K, Zhao N, Lao C, et al. Novel 3D grid porous Li₄Ti₅O₁₂ thick electrodes fabricated by 3D printing for high performance lithium-ion batteries. *J Adv Ceram* 2022;11:295–307. <https://doi.org/10.1007/s40145-021-0533-7>.
- [54] Liu C, Cheng X, Li B, Chen Z, Mi S, Lao C. Fabrication and Characterization of 3D-Printed Highly-Porous 3D LiFePO₄ Electrodes by Low Temperature Direct Writing Process. *Materials* 2017;10:934. <https://doi.org/10.3390/ma10080934>.
- [55] Martinez AC, Maurel A, Aranzola AP, Grugeon S, Panier S, Dupont L, et al. Additive manufacturing of LiNi_{1/3}Mn_{1/3}Co_{1/3}O₂ battery electrode material via vat photopolymerization precursor approach. *Sci Rep* 2022;12:1–13. <https://doi.org/10.1038/s41598-022-22444-1>.
- [56] Yang Q, Liu Q, Ling W, Dai H, Chen H, Liu J, et al. Porous Electrode Materials for Zn-Ion Batteries: From Fabrication and Electrochemical Application. *Batteries* 2022;8:223. <https://doi.org/10.3390/batteries8110223>.
- [57] Yang Y, Ai L, Yu S, He J, Xu T, Chen D, et al. 3D-Printed Porous GO Framework Enabling Dendrite-Free Lithium-Metal Anodes. *ACS Applied Energy Materials* 2022. <https://doi.org/10.1021/acsaem.2c03267>.

- [58] Chen C, Li S, Notten PHL, Zhang Y, Hao Q, Zhang X, et al. 3D Printed Lithium-Metal Full Batteries Based on a High-Performance Three-Dimensional Anode Current Collector. *ACS Appl Mater Interfaces* 2021;13:24785–94. <https://doi.org/10.1021/acsami.1c03997>.
- [59] Zhang M, Li L, Lin Q, Tang M, Wu Y, Ke C. Hierarchical-Coassembly-Enabled 3D-Printing of Homogeneous and Heterogeneous Covalent Organic Frameworks. *Journal of the American Chemical Society* 2019. <https://doi.org/10.1021/jacs.9b01561>.
- [60] Gupta V, Alam F, Verma P, Kannan AM, Kumar S. Additive manufacturing enabled, microarchitected, hierarchically porous polylactic-acid/lithium iron phosphate/carbon nanotube nanocomposite electrodes for high performance Li-ion batteries. *Journal of Power Sources* 2021;494:229625. <https://doi.org/10.1016/j.jpowsour.2021.229625>.
- [61] Mu Y, Chu Y, Pan L, Wu B, Zou L, He J, et al. 3D printing critical materials for rechargeable batteries: from materials, design and optimization strategies to applications. *Int J Extrem Manuf* 2023;5:042008. <https://doi.org/10.1088/2631-7990/acf172>.
- [62] Menon A, Khan A, Balakrishnan NTM, Raghavan P, Leon Y Leon CA, Khan HA, et al. Advances in 3D Printing for Electrochemical Energy Storage Systems. *J Mater Sci Technol Res* 2021;8:50–69. <https://doi.org/10.31875/2410-4701.2021.08.7>.
- [63] Thakur AR, Dong X. Experimental and numerical studies of slurry-based coextrusion deposition of continuous carbon fiber micro-batteries to additively manufacture 3D structural battery composites. *Composites Part B: Engineering* 2023;255:110632. <https://doi.org/10.1016/j.compositesb.2023.110632>.
- [64] Cheng M. Direct Ink Writing of Polymer Batteries. Ph.D. University of Illinois at Chicago, 2020.
- [65] Ragonese H, Menkin S, Kamir Y, Gladkikh A, Mukra T, Kosa G, et al. Towards smart free form-factor 3D printable batteries. *Sustainable Energy & Fuels* 2018;2:1542–9. <https://doi.org/10.1039/C8SE00122G>.
- [66] Ponnada S, Babu Gorle D, Chandra Bose RS, Sadat Kiai M, Devi M, Venkateswara Raju C, et al. Current Insight into 3D Printing in Solid-State Lithium-Ion Batteries: A Perspective. *Batteries & Supercaps* 2022;5:e202200223. <https://doi.org/10.1002/batt.202200223>.
- [67] Nyika J, Mwema FM, Mahamood RM, Akinlabi ET, Jen T. Advances in 3D printing materials processing-environmental impacts and alleviation measures. *Advances in Materials and Processing Technologies* 2022;8:1275–85. <https://doi.org/10.1080/2374068X.2021.1945311>.

- [68] Mao M, He J, Li X, Zhang B, Lei Q, Liu Y, et al. The Emerging Frontiers and Applications of High-Resolution 3D Printing. *Micromachines* 2017;8:113. <https://doi.org/10.3390/mi8040113>.
- [69] Park Y-G, Yun I, Chung WG, Park W, Lee DH, Park J-U. High-Resolution 3D Printing for Electronics. *Advanced Science* 2022;9:2104623. <https://doi.org/10.1002/advs.202104623>.
- [70] Ahn D, Stevens LM, Zhou K, Page ZA. Rapid High-Resolution Visible Light 3D Printing. *ACS Central Science* 2020. <https://doi.org/10.1021/acscentsci.0c00929>.
- [71] Maurel A, Martinez AC, Grugeon S, Panier S, Dupont L, Cortes P, et al. Toward High Resolution 3D Printing of Shape-Conformable Batteries via Vat Photopolymerization: Review and Perspective. *IEEE Access* 2021;9:140654–66. <https://doi.org/10.1109/ACCESS.2021.3119533>.
- [72] Gao X, Zheng M, Yang X, Sun R, Zhang J, Sun X. Emerging application of 3D-printing techniques in lithium batteries: From liquid to solid. *Materials Today* 2022;59:161–81. <https://doi.org/10.1016/j.mattod.2022.07.016>.
- [73] Zhou S, Usman I, Wang Y, Pan A. 3D printing for rechargeable lithium metal batteries. *Energy Storage Materials* 2021;38:141–56. <https://doi.org/10.1016/j.ensm.2021.02.041>.
- [74] Mu T, Xiang L, Wan X, Lou S, Du C, Zuo P, et al. Ultrahigh areal capacity silicon anodes realized via manipulating electrode structure. *Energy Storage Materials* 2022;53:958–68. <https://doi.org/10.1016/j.ensm.2022.10.021>.
- [75] Zhang M, Mei H, Chang P, Cheng L. 3D printing of structured electrodes for rechargeable batteries. *J Mater Chem A* 2020;8:10670–94. <https://doi.org/10.1039/D0TA02099K>.
- [76] Gao X, Yang X, Wang S, Sun Q, Zhao C, Li X, et al. A 3D-printed ultra-high Se loading cathode for high energy density quasi-solid-state Li–Se batteries. *Journal of Materials Chemistry A* 2020;8:278–86. <https://doi.org/10.1039/C9TA10623E>.
- [77] Ma J, Zheng S, Zhou F, Zhu Y, Das P, Huang R, et al. All 3D printing lithium metal batteries with hierarchically and conductively porous skeleton for ultrahigh areal energy density. *Energy Storage Materials* 2023;54:304–12. <https://doi.org/10.1016/j.ensm.2022.10.036>.
- [78] He H, Luo D, Zeng L, He J, Li X, Yu H, et al. 3D printing of fast kinetics reconciled ultra-thick cathodes for high areal energy density aqueous Li–Zn hybrid battery. *Science Bulletin* 2022;67:1253–63. <https://doi.org/10.1016/j.scib.2022.04.015>.
- [79] Wang J, Sun Q, Gao X, Wang C, Li W, Holness FB, et al. Toward High Areal Energy and Power Density Electrode for Li-ion Batteries via Optimized 3D Printing

- Approach. *ACS Appl Mater Interfaces* 2018;10:39794–801.
<https://doi.org/10.1021/acsami.8b14797>.
- [80] Marschewski J, Brenner L, Ebejer N, Ruch P, Michel B, Poulikakos D. 3D-printed fluidic networks for high-power-density heat-managing miniaturized redox flow batteries. *Energy & Environmental Science* 2017;10:780–7.
<https://doi.org/10.1039/C6EE03192G>.
- [81] Li J, Du Z, Ruther RE, An SJ, David LA, Hays K, et al. Toward Low-Cost, High-Energy Density, and High-Power Density Lithium-Ion Batteries. *JOM* 2017;69:1484–96. <https://doi.org/10.1007/s11837-017-2404-9>.
- [82] Roberts M, Johns P, Owen J, Brandell D, Edstrom K, Enany GE, et al. 3D lithium ion batteries—from fundamentals to fabrication. *Journal of Materials Chemistry* 2011;21:9876–90. <https://doi.org/10.1039/C0JM04396F>.
- [83] Hao F, Han F, Liang Y, Wang C, Yao Y. Architectural design and fabrication approaches for solid-state batteries. *MRS Bulletin* 2018;43:775–81.
<https://doi.org/10.1557/mrs.2018.211>.
- [84] Park Y, Park G, Park J, Lee J. Robust Free-standing Electrodes for Flexible Lithium-ion Batteries Prepared by a Conventional Electrode Fabrication Process. *Electrochimica Acta* 2017;247:371–80.
<https://doi.org/10.1016/j.electacta.2017.07.032>.
- [85] Liu P, Sherman E, Jacobsen A. Design and fabrication of multifunctional structural batteries. *Journal of Power Sources* 2009;189:646–50.
<https://doi.org/10.1016/j.jpowsour.2008.09.082>.
- [86] Bhosale VS, Gaikwad PM, Maladkar NP, Desai KV. A Review on use of 3D Printing for Battery Manufacturing. 2022.
- [87] Divakaran N, Das JP, P v AK, Mohanty S, Ramadoss A, Nayak SK. Comprehensive review on various additive manufacturing techniques and its implementation in electronic devices. *Journal of Manufacturing Systems* 2022;62:477–502.
<https://doi.org/10.1016/j.jmsy.2022.01.002>.
- [88] Bates AM, Preger Y, Torres-Castro L, Harrison KL, Harris SJ, Hewson J. Are solid-state batteries safer than lithium-ion batteries? *Joule* 2022;6:742–55.
<https://doi.org/10.1016/j.joule.2022.02.007>.
- [89] He Y, Chen S, Nie L, Sun Z, Wu X, Liu W. Stereolithography Three-Dimensional Printing Solid Polymer Electrolytes for All-Solid-State Lithium Metal Batteries. *Nano Lett* 2020;20:7136–43. <https://doi.org/10.1021/acs.nanolett.0c02457>.
- [90] Zekoll S, Marriner-Edwards C, Hekselman AKO, Kasemchainan J, Kuss C, Armstrong DEJ, et al. Hybrid electrolytes with 3D bicontinuous ordered ceramic

- and polymer microchannels for all-solid-state batteries. *Energy Environ Sci* 2018;11:185–201. <https://doi.org/10.1039/C7EE02723K>.
- [91] Schnell J, Tietz F, Singer C, Hofer A, Billot N, Reinhart G. Prospects of production technologies and manufacturing costs of oxide-based all-solid-state lithium batteries. *Energy & Environmental Science* 2019;12:1818–33. <https://doi.org/10.1039/C8EE02692K>.
- [92] Zaman W, Hatzell KB. Processing and manufacturing of next generation lithium-based all solid-state batteries. *Current Opinion in Solid State and Materials Science* 2022;26:101003. <https://doi.org/10.1016/j.cossms.2022.101003>.
- [93] Rogers JA, DeSimone JM. Novel materials. *Proceedings of the National Academy of Sciences* 2016;113:11667–9. <https://doi.org/10.1073/pnas.1614927113>.
- [94] Ding L, Jiang M, Li J, Wen J, Zeng M. Kill two birds with one stone: MOFs with carboxyl functionalized channels are used in lithium battery negative terminals and zinc-ion batteries. *Journal of Energy Storage* 2024;85:111169. <https://doi.org/10.1016/j.est.2024.111169>.
- [95] Budinoff HD, McMains S. Will it print: a manufacturability toolbox for 3D printing. *Int J Interact Des Manuf* 2021;15:613–30. <https://doi.org/10.1007/s12008-021-00786-w>.
- [96] Li H, Liang J. Recent Development of Printed Micro-Supercapacitors: Printable Materials, Printing Technologies, and Perspectives. *Adv Mater* 2020;32:1805864. <https://doi.org/10.1002/adma.201805864>.
- [97] Lin Y, Gao Y, Fang F, Fan Z. Recent progress on printable power supply devices and systems with nanomaterials. *Nano Res* 2018;11:3065–87. <https://doi.org/10.1007/s12274-018-2068-y>.
- [98] Ma J, Zheng S, Chi L, Liu Y, Zhang Y, Wang K, et al. 3D Printing Flexible Sodium-Ion Microbatteries with Ultrahigh Areal Capacity and Robust Rate Capability. *Advanced Materials* 2022;34:2205569. <https://doi.org/10.1002/adma.202205569>.
- [99] Nofal M, Al-Hallaj S, Pan Y. Thermal management of lithium-ion battery cells using 3D printed phase change composites. *Applied Thermal Engineering* 2020;171:115126. <https://doi.org/10.1016/j.applthermaleng.2020.115126>.
- [100] Liu Y, Qiao Y, Zhang Y, Yang Z, Gao T, Kirsch D, et al. 3D printed separator for the thermal management of high-performance Li metal anodes. *Energy Storage Materials* 2018;12:197–203. <https://doi.org/10.1016/j.ensm.2017.12.019>.
- [101] Lewis JA. Direct Ink Writing of 3D Functional Materials. *Adv Funct Mater* 2006;16:2193–204. <https://doi.org/10.1002/adfm.200600434>.

- [102] Tagliaferri S, Panagiotopoulos A, Mattevi C. Direct ink writing of energy materials. *Materials Advances* 2021;2:540–63. <https://doi.org/10.1039/D0MA00753F>.
- [103] Saadi M a. SR, Maguire A, Pottackal NT, Thakur MSH, Ikram MM, Hart AJ, et al. Direct Ink Writing: A 3D Printing Technology for Diverse Materials. *Advanced Materials* 2022;34:2108855. <https://doi.org/10.1002/adma.202108855>.
- [104] Chen B, Willenbacher N. High-precision direct ink writing of $\text{Li}_6.4\text{La}_3\text{Zr}_{1.4}\text{Ta}_{0.6}\text{O}_{12}$. *Journal of the European Ceramic Society* 2022;42:7491–500. <https://doi.org/10.1016/j.jeurceramsoc.2022.09.018>.
- [105] Guo Z, Yu P, Liu Y, Zhao J. High-precision resistance strain sensors of multilayer composite structure via direct ink writing: Optimized layer flatness and interfacial strength. *Composites Science and Technology* 2021;201:108530. <https://doi.org/10.1016/j.compscitech.2020.108530>.
- [106] Loaldi D, Piccolo L, Brown E, Tosello G, Shemelya C, Masato D. Hybrid Process Chain for the Integration of Direct Ink Writing and Polymer Injection Molding. *Micromachines* 2020;11. <https://doi.org/10.3390/mi11050509>.
- [107] Yuk H, Zhao X. A New 3D Printing Strategy by Harnessing Deformation, Instability, and Fracture of Viscoelastic Inks. *Advanced Materials* 2017;30. <https://doi.org/10.1002/adma.201704028>.
- [108] Rocha VG, Saiz E, Tirichenko IS, García-Tuñón E. Direct ink writing advances in multi-material structures for a sustainable future. *J Mater Chem A* 2020;8:15646–57. <https://doi.org/10.1039/D0TA04181E>.
- [109] Yirmibesoglu OD, Simonsen LE, Manson R, Davidson J, Healy K, Menguc Y, et al. Multi-material direct ink writing of photocurable elastomeric foams. *Commun Mater* 2021;2:1–14. <https://doi.org/10.1038/s43246-021-00186-3>.
- [110] Xu C, Quinn B, Lebel LL, Therriault D, L'Espérance G. Multi-Material Direct Ink Writing (DIW) for Complex 3D Metallic Structures with Removable Supports. *ACS Appl Mater Interfaces* 2019;11:8499–506. <https://doi.org/10.1021/acsami.8b19986>.
- [111] Renteria A, Balcorta VH, Marquez C, Rodriguez AA, Renteria-Marquez I, Regis J, et al. Direct ink write multi-material printing of PDMS-BTO composites with MWCNT electrodes for flexible force sensors. *Flex Print Electron* 2022;7:015001. <https://doi.org/10.1088/2058-8585/ac442e>.
- [112] Cadiou T, Demoly F, Gomes S. A hybrid additive manufacturing platform based on fused filament fabrication and direct ink writing techniques for multi-material 3D printing. *Int J Adv Manuf Technol* 2021;114:3551–62. <https://doi.org/10.1007/s00170-021-06891-0>.

- [113] Mantelli A, Romani A, Suriano R, Levi M, Turri S. Direct Ink Writing of Recycled Composites with Complex Shapes: Process Parameters and Ink Optimization. *Advanced Engineering Materials* 2021;23. <https://doi.org/10.1002/adem.202100116>.
- [114] Wei M, Zhang F, Wang W, Alexandridis P, Zhou C, Wu G. 3D direct writing fabrication of electrodes for electrochemical storage devices. *Journal of Power Sources* 2017;354. <https://doi.org/10.1016/j.jpowsour.2017.04.042>.
- [115] He W, Chen C, Jiang J, Chen Z, Liao H, Dou H, et al. 3D Printed Multilayer Graphite@SiO Structural Anode for High-Loading Lithium-Ion Battery. *Batteries & Supercaps* 2022;5. <https://doi.org/10.1002/batt.202100258>.
- [116] Li Q, Dong Q, Wang J, Xue Z, Li J, Yu M, et al. Direct ink writing (DIW) of graphene aerogel composite electrode for vanadium redox flow battery. *Journal of Power Sources* 2022;542:231810. <https://doi.org/10.1016/j.jpowsour.2022.231810>.
- [117] Zhu C, Schorr NB, Qi Z, Wygant BR, Turney DE, Yadav GG, et al. Direct Ink Writing of 3D Zn Structures as High-Capacity Anodes for Rechargeable Alkaline Batteries. *Small Structures* 2023;4:2200323. <https://doi.org/10.1002/ssstr.202200323>.
- [118] Liu Z, Tian X, Liu M, Duan S, Ren Y, Ma H, et al. Direct Ink Writing of $\text{Li}_{1.3}\text{Al}_{0.3}\text{Ti}_{1.7}(\text{PO}_4)_3$ -Based Solid-State Electrolytes with Customized Shapes and Remarkable Electrochemical Behaviors. *Small* 2021;17:2002866. <https://doi.org/10.1002/smll.202002866>.
- [119] Tao R, Gu Y, Sharma J, Hong K, Li J. A conformal heat-drying direct ink writing 3D printing for high-performance lithium-ion batteries. *Materials Today Chemistry* 2023;32:101672. <https://doi.org/10.1016/j.mtchem.2023.101672>.
- [120] Li L, Tan H, Yuan X, Ma H, Ma Z, Zhao Y, et al. Direct ink writing preparation of $\text{LiFePO}_4/\text{MWCNTs}$ electrodes with high-areal Li-ion capacity. *Ceramics International* 2021;47:21161–6. <https://doi.org/10.1016/j.ceramint.2021.04.119>.
- [121] Rasul MG, Cheng M, Jiang Y, Pan Y, Shahbazian-Yassar R. Direct Ink Printing of PVdF Composite Polymer Electrolytes with Aligned BN Nanosheets for Lithium-Metal Batteries. *ACS Nanosci Au* 2022:acsnanoscienceau.1c00056. <https://doi.org/10.1021/acsnanoscienceau.1c00056>.
- [122] Liu C, Zhao N, Xu K, Li Y, Mwizerwa JP, Shen J, et al. High-performance LiFePO_4 and $\text{SiO}_2/\text{C}/\text{graphite}$ interdigitated full lithium-ion battery fabricated via low temperature direct write 3D printing. *Materials Today Energy* 2022;29:101098. <https://doi.org/10.1016/j.mtener.2022.101098>.
- [123] Rocha VG, García-Tuñón E, Botas C, Markoulidis F, Feilden E, D'Elia E, et al. Multimaterial 3D Printing of Graphene-Based Electrodes for Electrochemical Energy Storage Using Thermoresponsive Inks. *ACS Appl Mater Interfaces* 2017;9:37136–45. <https://doi.org/10.1021/acsami.7b10285>.

- [124] FDM vs. FFF: Differences and Comparison 2022. <https://www.xometry.com/resources/3d-printing/fdm-vs-fff-3d-printing/> (accessed March 23, 2025).
- [125] Jones R, Haufe P, Sells E, Iravani P, Olliver V, Palmer C, et al. RepRap – the replicating rapid prototyper. *Robotica* 2011;29:177–91. <https://doi.org/10.1017/S026357471000069X>.
- [126] Sells E, Bailard S, Smith Z, Bowyer A, Olliver V. RepRap: The Replicating Rapid Prototyper: Maximizing Customizability by Breeding the Means of Production. *Handbook of Research in Mass Customization and Personalization*, World Scientific Publishing Company; 2009, p. 568–80. https://doi.org/10.1142/9789814280280_0028.
- [127] Bowyer A. 3D Printing and Humanity’s First Imperfect Replicator. *3D Printing and Additive Manufacturing* 2014;1:4–5. <https://doi.org/10.1089/3dp.2013.0003>.
- [128] Sola A. Materials Requirements in Fused Filament Fabrication: A Framework for the Design of Next-Generation 3D Printable Thermoplastics and Composites. *Macromolecular Materials and Engineering* 2022;307:2200197. <https://doi.org/10.1002/mame.202200197>.
- [129] Reyes C, Somogyi R, Niu S, Cruz MA, Yang F, Catenacci MJ, et al. Three-Dimensional Printing of a Complete Lithium Ion Battery with Fused Filament Fabrication. *ACS Appl Energy Mater* 2018;1:5268–79. <https://doi.org/10.1021/acsaem.8b00885>.
- [130] Maurel A, Courty M, Fleutot B, Tortajada H, Prashantha K, Armand M, et al. Highly Loaded Graphite–Polylactic Acid Composite-Based Filaments for Lithium-Ion Battery Three-Dimensional Printing. *Chem Mater* 2018;30:7484–93. <https://doi.org/10.1021/acs.chemmater.8b02062>.
- [131] Baechler C, DeVuono M, Pearce JM. Distributed recycling of waste polymer into RepRap feedstock. *Rapid Prototyping Journal* 2013;19:118–25. <https://doi.org/10.1108/13552541311302978>.
- [132] Cruz Sanchez FA, Boudaoud H, Hoppe S, Camargo M. Polymer recycling in an open-source additive manufacturing context: Mechanical issues. *Additive Manufacturing* 2017;17:87–105. <https://doi.org/10.1016/j.addma.2017.05.013>.
- [133] Cruz Sanchez FA, Boudaoud H, Camargo M, Pearce JM. Plastic recycling in additive manufacturing: A systematic literature review and opportunities for the circular economy. *Journal of Cleaner Production* 2020;264:121602. <https://doi.org/10.1016/j.jclepro.2020.121602>.
- [134] Dertinger SC, Gallup N, Tanikella NG, Grasso M, Vahid S, Foot PJS, et al. Technical pathways for distributed recycling of polymer composites for distributed

- manufacturing: Windshield wiper blades. *Resources, Conservation and Recycling* 2020;157:104810. <https://doi.org/10.1016/j.resconrec.2020.104810>.
- [135] Redondo E, Pumera M. Fully metallic copper 3D-printed electrodes via sintering for electrocatalytic biosensing. *Applied Materials Today* 2021;25:101253. <https://doi.org/10.1016/j.apmt.2021.101253>.
- [136] Mo F, Guo B, Liu Q, Ling W, Liang G, Chen L, et al. Additive manufacturing for advanced rechargeable lithium batteries: A mini review. *Front Energy Res* 2022;10:986985. <https://doi.org/10.3389/fenrg.2022.986985>.
- [137] Chen Y, Liu Y, Chen J, Wang Z, Tang B. Hybrid energy storage system design for mobile multi-material fused deposition modeling. *AIP Advances* 2020;10:075322. <https://doi.org/10.1063/5.0014097>.
- [138] Anzalone GC, Wijnen B, Pearce JM. Multi-material additive and subtractive prosumer digital fabrication with a free and open-source convertible delta RepRap 3-D printer. *Rapid Prototyping Journal* 2015;21:506–19. <https://doi.org/10.1108/RPJ-09-2014-0113>.
- [139] Sujithra R, Dhatreyi B, Saritha D. Nanomaterials-Based Additive Manufacturing for Mass Production of Energy Storage Systems: 3D Printed Batteries and Supercapacitors. *Nanotechnology-Based Additive Manufacturing*, John Wiley & Sons, Ltd; 2023, p. 369–98. <https://doi.org/10.1002/9783527835478.ch13>.
- [140] Anzalone GC, Wijnen B, Pearce JM. Multi-material additive and subtractive prosumer digital fabrication with a free and open-source convertible delta RepRap 3-D printer. *Rapid Prototyping Journal* 2015;21:506–19. <https://doi.org/10.1108/RPJ-09-2014-0113>.
- [141] Laureto JJ, Pearce JM. Anisotropic mechanical property variance between ASTM D638-14 type i and type iv fused filament fabricated specimens. *Polymer Testing* 2018;68:294–301. <https://doi.org/10.1016/j.polymertesting.2018.04.029>.
- [142] Gao X, Qi S, Kuang X, Su Y, Li J, Wang D. Fused filament fabrication of polymer materials: A review of interlayer bond. *Additive Manufacturing* 2021;37:101658. <https://doi.org/10.1016/j.addma.2020.101658>.
- [143] Beydaghi H, Abouali S, Thorat SB, Del Rio Castillo AE, Bellani S, Lauciello S, et al. 3D printed silicon-few layer graphene anode for advanced Li-ion batteries. *RSC Adv* 2021;11:35051–60. <https://doi.org/10.1039/D1RA06643A>.
- [144] Maurel A, Grugeon S, Fleutot B, Courty M, Prashantha K, Tortajada H, et al. Three-Dimensional Printing of a LiFePO₄/Graphite Battery Cell via Fused Deposition Modeling. *Sci Rep* 2019;9:18031. <https://doi.org/10.1038/s41598-019-54518-y>.

- [145] Gao W, Michalička J, Pumera M. Hierarchical Atomic Layer Deposited V_2O_5 on 3D Printed Nanocarbon Electrodes for High-Performance Aqueous Zinc-Ion Batteries. *Small* 2022;18:2105572. <https://doi.org/10.1002/sml.202105572>.
- [146] Foster CW, Zou G, Jiang Y, Down MP, Liauw CM, Garcia-Miranda Ferrari A, et al. Next-Generation Additive Manufacturing: Tailorable Graphene/Polylactic(acid) Filaments Allow the Fabrication of 3D Printable Porous Anodes for Utilisation within Lithium-Ion Batteries. *Batteries & Supercaps* 2019;2:448–53. <https://doi.org/10.1002/batt.201800148>.
- [147] Hu X, Chen Y, Xu W, Zhu Y, Kim D, Fan Y, et al. 3D-Printed Thermoplastic Polyurethane Electrodes for Customizable, Flexible Lithium-Ion Batteries with an Ultra-Long Lifetime. *Small* 2023;19:2301604. <https://doi.org/10.1002/sml.202301604>.
- [148] Maurel A, Armand M, Grugeon S, Fleutot B, Davoisne C, Tortajada H, et al. Poly(Ethylene Oxide)–LiTFSI Solid Polymer Electrolyte Filaments for Fused Deposition Modeling Three-Dimensional Printing. *J Electrochem Soc* 2020;167:070536. <https://doi.org/10.1149/1945-7111/ab7c38>.
- [149] De Wolf R, De Rop M, Hereijgers J. Effects of Structured 3D Electrodes on the Performance of Redox Flow Batteries. *ChemElectroChem* 2022;9:e202200640. <https://doi.org/10.1002/celec.202200640>.
- [150] Yang P, Fan HJ. Inkjet and Extrusion Printing for Electrochemical Energy Storage: A Minireview. *Advanced Materials Technologies* 2020;5:2000217. <https://doi.org/10.1002/admt.202000217>.
- [151] Sousa RE, Costa CM, Lanceros-Méndez S. Advances and Future Challenges in Printed Batteries. *ChemSusChem* 2015;8:3539–55. <https://doi.org/10.1002/cssc.201500657>.
- [152] Sztymela K, Bienia M, Rossignol F, Mailley S, Ziesche S, Varghese J, et al. Fabrication of modern lithium ion batteries by 3D inkjet printing: opportunities and challenges. *Heliyon* 2022;8:e12623. <https://doi.org/10.1016/j.heliyon.2022.e12623>.
- [153] Sowade E, Polomoshnov M, Willert A, Baumann RR. Toward 3D-Printed Electronics: Inkjet-Printed Vertical Metal Wire Interconnects and Screen-Printed Batteries. *Advanced Engineering Materials* 2019;21:1900568. <https://doi.org/10.1002/adem.201900568>.
- [154] Zhao Y, Zhou Q, Liu L, Xu J, Yan M, Jiang Z. A novel and facile route of ink-jet printing to thin film SnO_2 anode for rechargeable lithium ion batteries. *Electrochimica Acta* 2006;51:2639–45. <https://doi.org/10.1016/j.electacta.2005.07.050>.

- [155] Lawes S, Sun Q, Lushington A, Xiao B, Liu Y, Sun X. Inkjet-printed silicon as high performance anodes for Li-ion batteries. *Nano Energy* 2017;36:313–21. <https://doi.org/10.1016/j.nanoen.2017.04.041>.
- [156] Chen T, Wang Y, Yang Y, Huang F, Zhu M, Ang BTW, et al. Heterometallic Seed-Mediated Zinc Deposition on Inkjet Printed Silver Nanoparticles Toward Foldable and Heat-Resistant Zinc Batteries. *Advanced Functional Materials* 2021;31:2101607. <https://doi.org/10.1002/adfm.202101607>.
- [157] Kushwaha A, Jangid MK, Bhatt BB, Mukhopadhyay A, Gupta D. Inkjet-Printed Environmentally Friendly Graphene Film for Application as a High-Performance Anode in Li-ion Batteries. *ACS Appl Energy Mater* 2021;4:7911–21. <https://doi.org/10.1021/acsaem.1c01249>.
- [158] Kushwaha A, Sharma A, Bhatt BB, Mukhopadhyay A, Gupta D. Inkjet-Printed Graphene-Modified Aluminum Current Collector for High-Voltage Lithium-Ion Battery. *ACS Appl Energy Mater* 2023;6:4168–78. <https://doi.org/10.1021/acsaem.2c03870>.
- [159] Viviani P, Gibertini E, Iervolino F, Levi M, Magagnin L. Carbon additive effect on the electrochemical performances of inkjet printed thin-film Li₄Ti₅O₁₂ electrodes. *Journal of Manufacturing Processes* 2021;72:411–8. <https://doi.org/10.1016/j.jmapro.2021.10.039>.
- [160] Kolchanov DS, Mitrofanov I, Kim A, Koshtyal Y, Romyantsev A, Sergeeva E, et al. Inkjet Printing of Li-Rich Cathode Material for Thin-Film Lithium-Ion Microbatteries. *Energy Technology* 2020;8:1901086. <https://doi.org/10.1002/ente.201901086>.
- [161] Pei M, Shi H, Yao F, Liang S, Xu Z, Pei X, et al. 3D printing of advanced lithium batteries: a designing strategy of electrode/electrolyte architectures. *J Mater Chem A* 2021;9:25237–57. <https://doi.org/10.1039/D1TA06683H>.
- [162] Yang Y, Yuan W, Zhang X, Yuan Y, Wang C, Ye Y, et al. Overview on the applications of three-dimensional printing for rechargeable lithium-ion batteries. *Applied Energy* 2020;257:114002. <https://doi.org/10.1016/j.apenergy.2019.114002>.
- [163] Tian X, Zhou K. 3D printing of cellular materials for advanced electrochemical energy storage and conversion. *Nanoscale* 2020;12:7416–32. <https://doi.org/10.1039/D0NR00291G>.
- [164] Narita K, Saccone MA, Sun Y, Greer JR. Additive manufacturing of 3D batteries: a perspective. *Journal of Materials Research* 2022;37:1535–46. <https://doi.org/10.1557/s43578-022-00562-w>.
- [165] Mubarak S, Dhamodharan D, Byun H-S. Recent advances in 3D printed electrode materials for electrochemical energy storage devices. *Journal of Energy Chemistry* 2023;81:272–312. <https://doi.org/10.1016/j.jechem.2023.01.037>.

- [166] Cheng M, Deivanayagam R, Shahbazian-Yassar R. 3D Printing of Electrochemical Energy Storage Devices: A Review of Printing Techniques and Electrode/Electrolyte Architectures. *Batteries & Supercaps* 2020;3:130–46. <https://doi.org/10.1002/batt.201900130>.
- [167] Zakeri S, Vippola M, Levänen E. A comprehensive review of the photopolymerization of ceramic resins used in stereolithography. *Additive Manufacturing* 2020;35:101177. <https://doi.org/10.1016/j.addma.2020.101177>.
- [168] Brinckmann SA, Patra N, Yao J, Ware TH, Frick CP, Fertig RS. Stereolithography of SiOC Polymer-Derived Ceramics Filled with SiC Micronwhiskers. *Advanced Engineering Materials* 2018;20:1800593. <https://doi.org/10.1002/adem.201800593>.
- [169] Chen Q, Xu R, He Z, Zhao K, Pan L. Printing 3D Gel Polymer Electrolyte in Lithium-Ion Microbattery Using Stereolithography. *J Electrochem Soc* 2017;164:A1852–7. <https://doi.org/10.1149/2.0651709jes>.
- [170] Norjeli MF, Tamchek N, Osman Z, Mohd Noor IS, Kufian MZ, Ghazali MIBM. Additive Manufacturing Polyurethane Acrylate via Stereolithography for 3D Structure Polymer Electrolyte Application. *Gels* 2022;8:589. <https://doi.org/10.3390/gels8090589>.
- [171] Lee K, Shang Y, Bobrin VA, Kuchel R, Kundu D, Corrigan N, et al. 3D Printing Nanostructured Solid Polymer Electrolytes with High Modulus and Conductivity. *Advanced Materials* 2022;34:2204816. <https://doi.org/10.1002/adma.202204816>.
- [172] Katsuyama Y, Kudo A, Kobayashi H, Han J, Chen M, Honma I, et al. A 3D-Printed, Freestanding Carbon Lattice for Sodium Ion Batteries. *Small* 2022;18:2202277. <https://doi.org/10.1002/sml.202202277>.
- [173] Ye X, Wang C, Wang L, Lu B, Gao F, Shao D. DLP printing of a flexible micropattern Si/PEDOT:PSS/PEG electrode for lithium-ion batteries. *Chem Commun* 2022;58:7642–5. <https://doi.org/10.1039/D2CC01626E>.
- [174] Yoko A, Oshima Y. Recovery of silicon from silicon sludge using supercritical water. *The Journal of Supercritical Fluids* 2013;75:1–5. <https://doi.org/10.1016/j.supflu.2012.12.019>.
- [175] Sun L, Liu Y, Wu J, Shao R, Jiang R, Tie Z, et al. A Review on Recent Advances for Boosting Initial Coulombic Efficiency of Silicon Anodic Lithium Ion batteries. *Small* 2022;18:2102894. <https://doi.org/10.1002/sml.202102894>.
- [176] Pearce JM. Economic savings for scientific free and Open-source technology: A review. *HardwareX* 2020;8:e00139. <https://doi.org/10.1016/j.ohx.2020.e00139>.

- [177] Dobbelaere T, Vereecken PM, Detavernier C. A USB-controlled potentiostat/galvanostat for thin-film battery characterization. *HardwareX* 2017;2:34–49. <https://doi.org/10.1016/j.ohx.2017.08.001>.
- [178] Sylvestrin GR, Scherer HF, Hideo Ando Junior O. Hardware and Software Development of an Open-source Battery Management System. *IEEE Latin America Transactions* 2021;19:1153–63. <https://doi.org/10.1109/TLA.2021.9461844>.
- [179] Fleming J, Amietszajew T, McTurk E, Towers DP, Greenwood D, Bhagat R. Development and evaluation of in-situ instrumentation for cylindrical Li-ion cells using fibre optic sensors. *HardwareX* 2018;3:100–9. <https://doi.org/10.1016/j.ohx.2018.04.001>.
- [180] Carloni A, Baronti F, Di Rienzo R, Roncella R, Saletti R. An Open-Hardware and Low-Cost Maintenance Tool for Light-Electric-Vehicle Batteries. *Energies* 2021;14:4962. <https://doi.org/10.3390/en14164962>.
- [181] Yensen N, Allen PB. Open-source all-iron battery for renewable energy storage. *HardwareX* 2019;6:e00072. <https://doi.org/10.1016/j.ohx.2019.e00072>.
- [182] Koirala D, Yensen N, Allen PB. Open-source all-iron battery 2.0. *HardwareX* 2021;9:e00171. <https://doi.org/10.1016/j.ohx.2020.e00171>.
- [183] Neikov OD, Yefimov NA. *Handbook of non-ferrous metal powders: technologies and applications*. Elsevier; 2009.
- [184] Gao M, Forssberg E. Prediction of product size distributions for a stirred ball mill. *Powder Technology* 1995;84:101–6. [https://doi.org/10.1016/0032-5910\(95\)02990-J](https://doi.org/10.1016/0032-5910(95)02990-J).
- [185] Zali A, Kashani-Bozorg SF, Lalegani Z, Hamawandi B. Fabrication of TiFe-Based Electrodes Using High-Energy Ball Mill with Mn Additive for NiMH Batteries. *Batteries* 2022;8:182. <https://doi.org/10.3390/batteries8100182>.
- [186] C. Piras C, Fernández-Prieto S, Borggraeve WMD. Ball milling: a green technology for the preparation and functionalisation of nanocellulose derivatives. *Nanoscale Advances* 2019;1:937–47. <https://doi.org/10.1039/C8NA00238J>.
- [187] Uranchimeg K, Jargalsaikhan B, Bor A, Yoon K, Choi H. Comparative Study of the Morphology of Cellulose Nanofiber Fabricated Using Two Kinds of Grinding Method. *Materials* 2022;15:7048. <https://doi.org/10.3390/ma15207048>.
- [188] Basset D, Matteazzi P, Miani F. Designing a high energy ball-mill for synthesis of nanophase materials in large quantities. *Materials Science and Engineering: A* 1993;168:149–52. [https://doi.org/10.1016/0921-5093\(93\)90718-T](https://doi.org/10.1016/0921-5093(93)90718-T).
- [189] Paramanantham SS, Brigljević B, Aleksey N, Nagulapati VM, Han G-F, Baek J-B, et al. Numerical simulation of ball milling reactor for novel ammonia synthesis

under ambient conditions. *Energy* 2022:125754.
<https://doi.org/10.1016/j.energy.2022.125754>.

- [190] Chattopadhyay S. Green Synthetic Approaches for Medium Ring-Sized Heterocycles of Biological Interest. *Green Synthetic Approaches for Biologically Relevant Heterocycles*, 2015, p. 291–315. <https://doi.org/10.1016/B978-0-12-800070-0.00011-6>.
- [191] Rodríguez B, Rantanen T, Bolm C. Solvent-Free Asymmetric Organocatalysis in a Ball Mill. *Angewandte Chemie International Edition* 2006;45:6924–6. <https://doi.org/10.1002/anie.200602820>.
- [192] Laboratory Ball Mill 2 kg Motor Driven Heavy Duty with 5 Big Stainless Steel Balls (15 mm) and 15 Small Stainless Steel Balls (8 mm) : Amazon.ca: Industrial & Scientific n.d. <https://www.amazon.ca/Crabby-Laboratory-Driven-Stainless-2KG-SS/dp/B0988BF4BL> (accessed November 17, 2022).
- [193] Ball Mill 2 kg Heavy Duty IN 220 Volt Laboratory Ball Grinder. Scimedstore n.d. <https://scimedstore.com/products/ball-mill-2-kg-heavy-duty-in-220-volt> (accessed November 17, 2022).
- [194] One-tier jar high-capacity laboratory jar mill; 13" roller, 115 VAC/60 Hz from Cole-Parmer Canada n.d. <https://www.coleparmer.ca/i/one-tier-jar-high-capacity-laboratory-jar-mill-13-roller-115-vac-60-hz/0414900> (accessed November 17, 2022).
- [195] Cole-Parmer Jar Mill without Jars; 115/230 VAC, 50/60 Hz from Cole-Parmer Canada n.d. <https://www.coleparmer.ca/i/cole-parmer-jar-mill-without-jars-115-230-vac-50-60-hz/0417250> (accessed November 17, 2022).
- [196] Chagas AM. Haves and have nots must find a better way: The case for open scientific hardware. *PLOS Biology* 2018;16:e3000014. <https://doi.org/10.1371/journal.pbio.3000014>.
- [197] Coakley M, Hurt DE. 3D Printing in the Laboratory: Maximize Time and Funds with Customized and Open-Source Labware. *SLAS Technology* 2016;21:489–95. <https://doi.org/10.1177/2211068216649578>.
- [198] Pearce JM. Quantifying the Value of Open-source Hardware Development. *Modern Economy* 2015;6:1–11. <https://doi.org/10.4236/me.2015.61001>.
- [199] Pearce JM. Economic savings for scientific free and Open-source technology: A review. *HardwareX* 2020;8:e00139. <https://doi.org/10.1016/j.ohx.2020.e00139>.
- [200] Banzi M, Shiloh M. *Getting Started With Arduino: The Open-source Electronics Prototyping Platform*. Maker Media, Inc.; 2022.

- [201] Machado F, Malpica N, Borromeo S. Parametric CAD modeling for Open-source scientific hardware: Comparing OpenSCAD and FreeCAD Python scripts. *PLOS ONE* 2019;14:e0225795. <https://doi.org/10.1371/journal.pone.0225795>.
- [202] Oberloier S, Pearce JM. General Design Procedure for Free and Open-Source Hardware for Scientific Equipment. *Designs* 2018;2:2. <https://doi.org/10.3390/designs2010002>.
- [203] Dryden MDM, Fobel R, Fobel C, Wheeler AR. Upon the Shoulders of Giants: Open-Source Hardware and Software in Analytical Chemistry. *Anal Chem* 2017;89:4330–8. <https://doi.org/10.1021/acs.analchem.7b00485>.
- [204] Damase TR, Stephens D, Spencer A, Allen PB. Open-source and DIY hardware for DNA nanotechnology labs. *J Biol Methods* 2015;2:e24. <https://doi.org/10.14440/jbm.2015.72>.
- [205] Harnett C. Open-source hardware for instrumentation and measurement. *IEEE Instrumentation & Measurement Magazine* 2011;14:34–8. <https://doi.org/10.1109/MIM.2011.5773535>.
- [206] Nedbal J, Gao L, Suhling K. Bottom-illuminated orbital shaker for microalgae cultivation. *HardwareX* 2020;8:e00143. <https://doi.org/10.1016/j.ohx.2020.e00143>.
- [207] Trivedi DK, Pearce JM. Open-source 3-D Printed Nutating Mixer. *Applied Sciences* 2017;7:942. <https://doi.org/10.3390/app7090942>.
- [208] Zhang C, Wijnen B, Pearce JM. Open-Source 3-D Platform for Low-Cost Scientific Instrument Ecosystem. *SLAS Technology* 2016;21:517–25. <https://doi.org/10.1177/2211068215624406>.
- [209] How I built a quick and easy home-made ball mill 2019. <https://mdpub.com/ballmill/index.html> (accessed February 25, 2023).
- [210] Ball mill - home made - YouTube n.d. <https://www.youtube.com/watch> (accessed February 25, 2023).
- [211] DIY | Homemade ball mill 2020. <https://www.youtube.com/watch> (accessed February 25, 2023).
- [212] Mad Scientist Hut. Simple Home Made Ball Mill (DIY) 2015. <https://www.youtube.com/watch> (accessed February 25, 2023).
- [213] Biotele. Make a Ball Mill in 5 Minutes. *Instructables* n.d. <https://www.instructables.com/Make-a-Ball-Mill-in-5-Minutes/> (accessed February 25, 2023).
- [214] How to Make a Ball Mill: 12 Steps (with Pictures). *wikiHow* 2020. <https://www.wikihow.com/Make-a-Ball-Mill> (accessed February 25, 2023).

- [215] How to make a Rock Tumbler Ball Mill n.d. <https://www.youtube.com/watch> (accessed February 25, 2023).
- [216] How to make a Ball mill 2022. <https://www.youtube.com/watch> (accessed February 25, 2023).
- [217] My Latest Ball Mill Design - YouTube n.d. <https://www.youtube.com/watch> (accessed February 25, 2023).
- [218] Michaud LD. DIY Ball Mill Plans - Homemade Rod Mill Drawing. *Mineral Processing & Metallurgy* 2016. <https://www.911metallurgist.com/blog/homemade-diy-ball-mill> (accessed February 25, 2023).
- [219] Nilssen BE, Kleiv RA. Silicon Powder Properties Produced in a Planetary Ball Mill as a Function of Grinding Time, Grinding Bead Size and Rotational Speed. *Silicon* 2020;12:2413–23. <https://doi.org/10.1007/s12633-019-00340-0>.
- [220] Mayville PJ, Petsiuk AL, Pearce JM. Thermal Post-Processing of 3D Printed Polypropylene Parts for Vacuum Systems. *JMMP* 2022;6:98. <https://doi.org/10.3390/jmmp6050098>.
- [221] Zhu X, Cai X, Zhang S, Wang L, Cui X. The Impact of Ball Milling Process Parameters on the Preparation of Nano Silicon Powder. *Integrated Ferroelectrics* 2021;217:255–64. <https://doi.org/10.1080/10584587.2021.1911318>.
- [222] Pearce J, Kulkarni A, Mottaghi M. Open-source ball mill 2022. <https://doi.org/10.17605/OSF.IO/XA4WS>.
- [223] Gutierrez RSG, Vasquez JJG. Experiences in automated construction of PC boards using an Open-source cnc machine. 2015 IEEE Thirty Fifth Central American and Panama Convention (CONCAPAN XXXV), Tegucigalpa: IEEE; 2015, p. 1–4. <https://doi.org/10.1109/CONCAPAN.2015.7428463>.
- [224] Oberloier S, Pearce J. Belt-Driven Open-source Circuit Mill Using Low-Cost 3-D Printer Components. *Inventions* 2018;3:64. <https://doi.org/10.3390/inventions3030064>.
- [225] Sathyakumar N, Prasath Balaji K, Ganapathi R, Pandian SR. A Build-Your-Own Three Axis CNC PCB Milling Machine. *Materials Today: Proceedings* 2018;5:24404–13. <https://doi.org/10.1016/j.matpr.2018.10.236>.
- [226] Goh GL, Zhang H, Chong TH, Yeong WY. 3D Printing of Multilayered and Multimaterial Electronics: A Review. *Adv Electron Mater* 2021;7:2100445. <https://doi.org/10.1002/aelm.202100445>.
- [227] Staff CB. Solar is now ‘cheapest electricity in history’, confirms IEA. *Carbon Brief* 2020. <https://www.carbonbrief.org/solar-is-now-cheapest-electricity-in-history-confirms-iea/> (accessed December 11, 2022).

- [228] Polysilicon Solar Price - PVinsights 2020. <http://pvinsights.com/> (accessed December 11, 2022).
- [229] Biosphere Solar - V.0.4 - How To.pdf - biosphere-solar-v04. Wikifactory n.d. <https://wikifactory.com/@biosphere-solar/biosphere-solar-v04/file/Biosphere%20Solar%20-%20V.0.4%20-%20How%20To.pdf> (accessed April 25, 2025).
- [230] Heikkinen ITS, Kauppinen C, Liu Z, Asikainen SM, Spoljaric S, Seppälä JV, et al. Chemical compatibility of fused filament fabrication-based 3-D printed components with solutions commonly used in semiconductor wet processing. *Additive Manufacturing* 2018;23:99–107. <https://doi.org/10.1016/j.addma.2018.07.015>.
- [231] Bottle/Tube Roller. Thermo Fisher 2022. <https://www.thermofisher.com/order/catalog/product/88881003> (accessed December 13, 2022).
- [232] Berson RE, Friederichs G. A Self-Feeding Roller Bottle for Continuous Cell Culture. *Biotechnol Prog* 2008;24:154–7. <https://doi.org/10.1021/bp070122w>.
- [233] Duan D, Ji Y, Zhou M, Gao J. Pilot-scale preparation of clinical-grade third generation lentivirus. *Sheng Wu Gong Cheng Xue Bao* 2019;35:1307–16. <https://doi.org/10.13345/j.cjb.190127>.
- [234] Mguni NG, Bhebhe S, Danha G, Tshuma J, Hlabangana N. Determining Optimum Wet Milling and Leaching Parameters for Maximum Recovery of Gold. *International Journal of Engineering Research* 2017.
- [235] Boudreau MD, Taylor HW, Baker DG, Means JC. Dietary Exposure to 2-Aminoanthracene Induces Morphological and Immunocytochemical Changes in Pancreatic Tissues of Fisher-344 Rats. *Toxicological Sciences* 2006;93:50–61. <https://doi.org/10.1093/toxsci/kfl033>.
- [236] Guajardo MC, Scott ML, Noel L, Boze B, McAllister JC. Insecticide Resistance Evaluation of *Culex quinquefasciatus*, 2017. *Arthropod Management Tests* 2019;44. <https://doi.org/10.1093/amt/tsz012>.
- [237] Lantieri C, Lamperti R, Simone A, Vignali V, Sangiorgi C, Dondi G, et al. Use of image analysis for the evaluation of rolling bottle tests results. *International Journal of Pavement Research and Technology* 2017;10:45–53. <https://doi.org/10.1016/j.ijprt.2016.11.003>.
- [238] Thermo Scientific Bottle/Tube Roller - Digital Bottle/Tube Roller, 80 rpm | TEquipment 2020. <https://www.tequipment.net/Thermo-Scientific/Bottle/Tube-Roller/Tube-Roller-Mixers/> (accessed December 13, 2022).

- [239] Rolling Apparatus 2022. <https://www.fishersci.ca/ca/en/products/I9C8L35Q/rolling-apparatus.html> (accessed December 16, 2022).
- [240] Rocker, rotator, mixer, rockers, shake, shaker, rotators, mixers, compact, digital, tube, flasks, incubator, incubating, incubate 2022. <https://www.fishersci.ca/shop/products/fisher-scientific-digital-bottle-roller/11676250> (accessed December 15, 2022).
- [241] Ibi Scientific Low-Profile Bottle Roller; 90-240 VAC, 50/60 Hz from Cole-Parmer 2022. <https://www.coleparmer.com/i/ibi-scientific-low-profile-bottle-roller-90-240-vac-50-60-hz/3620203> (accessed December 13, 2022).
- [242] Argos Technologies FlexiRoll Digital Tube/Bottle Roller Shaker - Cole-Parmer 2022. <https://www.coleparmer.com/p/argos-technologies-flexiroll-digital-tube-bottle-roller-shaker/67028> (accessed December 13, 2022).
- [243] Woern A, Byard D, Oakley R, Fiedler M, Snabes S, Pearce J. Fused Particle Fabrication 3-D Printing: Recycled Materials' Optimization and Mechanical Properties. *Materials* 2018;11:1413. <https://doi.org/10.3390/ma11081413>.
- [244] Shaik YP, Schuster J, Shaik A. A Scientific Review on Various Pellet Extruders Used in 3D Printing FDM Processes. *OALib* 2021;08:1–19. <https://doi.org/10.4236/oalib.1107698>.
- [245] Rattan RS, Nauta N, Romani A, Pearce JM. Hangprinter for large scale additive manufacturing using fused particle fabrication with recycled plastic and continuous feeding. *HardwareX* 2023;13:e00401. <https://doi.org/10.1016/j.ohx.2023.e00401>.
- [246] Petsiuk A, Lavu B, Dick R, Pearce JM. Waste Plastic Direct Extrusion Hangprinter. *Inventions* 2022;7:70. <https://doi.org/10.3390/inventions7030070>.
- [247] Little HA, Tanikella NG, J. Reich M, Fiedler MJ, Snabes SL, Pearce JM. Towards Distributed Recycling with Additive Manufacturing of PET Flake Feedstocks. *Materials* 2020;13:4273. <https://doi.org/10.3390/ma13194273>.
- [248] Reich MJ, Woern AL, Tanikella NG, Pearce JM. Mechanical Properties and Applications of Recycled Polycarbonate Particle Material Extrusion-Based Additive Manufacturing. *Materials* 2019;12:1642. <https://doi.org/10.3390/ma12101642>.
- [249] Pearce JM. *Create, Share, and Save Money Using Open-Source Projects*. McGraw-Hill Education; 2021.
- [250] Andrews H. Small-scale plastic recycling. *Renew: Technology for a Sustainable Future* 2020:40–2. <https://search.informit.org/doi/10.3316/informit.541902721728683>.

- [251] Mohammed MI, Mohan M, Das A, D. Johnson M, Singh Badwal P, McLean D, et al. A low carbon footprint approach to the reconstitution of plastics into 3D-printer filament for enhanced waste reduction. *KEG* 2017;2:234. <https://doi.org/10.18502/keg.v2i2.621>.
- [252] Zhong S, Pearce JM. Tightening the loop on the circular economy: Coupled distributed recycling and manufacturing with recyclebot and RepRap 3-D printing. *Resources, Conservation and Recycling* 2018;128:48–58. <https://doi.org/10.1016/j.resconrec.2017.09.023>.
- [253] Mohammed MI, Wilson D, Gomez-Kervin E, Vidler C, Rosson L, Long J. The Recycling of E-Waste ABS Plastics by Melt Extrusion and 3D Printing Using Solar Powered Devices as a Transformative Tool for Humanitarian Aid 2018. <https://doi.org/10.26153/TSW/17001>.
- [254] Woern AL, McCaslin JR, Pringle AM, Pearce JM. RepRapable Recyclebot: Open-source 3-D printable extruder for converting plastic to 3-D printing filament. *HardwareX* 2018;4:e00026. <https://doi.org/10.1016/j.ohx.2018.e00026>.
- [255] Alexandre A, Cruz Sanchez FA, Boudaoud H, Camargo M, Pearce JM. Mechanical Properties of Direct Waste Printing of Polylactic Acid with Universal Pellets Extruder: Comparison to Fused Filament Fabrication on Open-Source Desktop Three-Dimensional Printers. *3D Printing and Additive Manufacturing* 2020;7:237–47. <https://doi.org/10.1089/3dp.2019.0195>.
- [256] Fontana L, Giubilini A, Arrigo R, Malucelli G, Minetola P. Characterization of 3D Printed Polylactic Acid by Fused Granular Fabrication through Printing Accuracy, Porosity, Thermal and Mechanical Analyses. *Polymers* 2022;14:3530. <https://doi.org/10.3390/polym14173530>.
- [257] Kubota K, Takahashi R, Uesugi M, Ito H. A Glove-Box- and Schlenk-Line-Free Protocol for Solid-State C–N Cross-Coupling Reactions Using Mechanochemistry. *ACS Sustainable Chem Eng* 2020;8:16577–82. <https://doi.org/10.1021/acssuschemeng.0c05834>.
- [258] Rentetzi M. Determining Nuclear Fingerprints: Glove Boxes, Radiation Protection, and the International Atomic Energy Agency. *Endeavour* 2017;41:39–50. <https://doi.org/10.1016/j.endeavour.2017.02.001>.
- [259] Sather AC, Lee HG, Colombe JR, Zhang A, Buchwald SL. Dosage delivery of sensitive reagents enables glove-box-free synthesis. *Nature* 2015;524:208–11. <https://doi.org/10.1038/nature14654>.
- [260] Hazardous Substance Fact Sheet 2024. <https://www.nj.gov/health/eoh/rtkweb/documents/fs/0015.pdf> (accessed 2024).
- [261] Air Sensitive Compounds. Ossila 2024. <https://www.ossila.com/pages/air-sensitive-compounds> (accessed 2024).

- [262] metal alkyls and aryls oxygen ppm tolerance - Google Search 2024.
<https://www.google.com/search> (accessed 2024).
- [263] Daeneke T, Atkin P, Orrell-Trigg R, Zavabeti A, Ahmed T, Walia S, et al. Wafer-Scale Synthesis of Semiconducting SnO Monolayers from Interfacial Oxide Layers of Metallic Liquid Tin. *ACS Nano* 2017;11:10974–83.
<https://doi.org/10.1021/acsnano.7b04856>.
- [264] Szolga LA, Stan CA. Plexiglass glove box for organic solar cells. *IOP Conf Ser: Mater Sci Eng* 2021;1032:012048. <https://doi.org/10.1088/1757-899X/1032/1/012048>.
- [265] Marengo M, Puglisi R, Oliaro-Bosso S, Pastore A, Adinolfi S. Enzymatic and Chemical In Vitro Reconstitution of Iron-Sulfur Cluster Proteins. *Methods Mol Biol* 2021;2353:79–95. https://doi.org/10.1007/978-1-0716-1605-5_5.
- [266] Barton CJ. A Review of Glove Box Construction and Experimentation 1961.
<https://doi.org/10.2172/4043015>.
- [267] First MW. Laboratory Chemical Hoods: A Historical Perspective. *AIHA Journal* 2003;64:251–9. <https://doi.org/10.1080/15428110308984815>.
- [268] Kubota K, Takahashi R, Ito H. Mechanochemistry allows carrying out sensitive organometallic reactions in air: glove-box-and-Schlenk-line-free synthesis of oxidative addition complexes from aryl halides and palladium(0). *Chem Sci* 2019;10:5837–42. <https://doi.org/10.1039/C9SC01711A>.
- [269] Yaghoobi Nia N, Zendehtel M, Cinà L, Matteocci F, Di Carlo A. A crystal engineering approach for scalable perovskite solar cells and module fabrication: a full out of glove box procedure. *J Mater Chem A* 2018;6:659–71.
<https://doi.org/10.1039/C7TA08038G>.
- [270] Make: DIY Projects and Ideas for Makers | 2024. <https://makezine.com/> (accessed 2024).
- [271] DIY Hacks & How To's: DIY Glove Box. 2013.
<https://www.youtube.com/watch?v=oGDUNB3w1aU>. 2024.
- [272] Very Simple DIY Glove Box. 2016.
<https://www.youtube.com/watch?v=4nJ1FKZNQVA/> (accessed 2024). 2024.
- [273] Making a Glove Box. 2016. <https://www.youtube.com/watch?v=lSwJosoNbZY/> (accessed 2024). 2024.
- [274] How to make simple Glove Box (DIY Glove Box). 2018.
<https://www.youtube.com/watch?v=MLVIFqolblQ>. 2024.

- [275] Pearce JM. Building Research Equipment with Free, Open-Source Hardware. *Science* 2012;337:1303–4. <https://doi.org/10.1126/science.1228183>.
- [276] Pearce JM. Open-Source Lab. Elsevier; 2014. <https://doi.org/10.1016/C2012-0-07249-3>.
- [277] Pearce JM. Cut costs with open-source hardware. *Nature* 2014;505:618–618. <https://doi.org/10.1038/505618d>.
- [278] Bowyer A. 3D Printing and Humanity’s First Imperfect Replicator. *3D Printing and Additive Manufacturing* 2014;1:4–5. <https://doi.org/10.1089/3dp.2013.0003>.
- [279] Oberloier S, Pearce JM. General Design Procedure for Free and Open-Source Hardware for Scientific Equipment. *Designs* 2018;2:2.
- [280] Gibb A. Building Open-source Hardware: DIY Manufacturing for Hackers and Makers. Addison-Wesley Professional; 2014.
- [281] Banzi M, Michael S. Getting Started with Arduino. 2014.
- [282] Baden T, Chagas AM, Gage G, Marzullo T, Prieto-Godino LL, Euler T. Open Labware: 3-D Printing Your Own Lab Equipment. *PLOS Biology* 2015;13:e1002086. <https://doi.org/10.1371/journal.pbio.1002086>.
- [283] Wittbrodt BT, Glover AG, Laureto J, Anzalone GC, Oppliger D, Irwin JL, et al. Life-cycle economic analysis of distributed manufacturing with open-source 3-D printers. *Mechatronics* 2013;23:713–26. <https://doi.org/10.1016/j.mechatronics.2013.06.002>.
- [284] Srari JS, Kumar M, Graham G, Phillips W, Tooze J, Ford S, et al. Distributed manufacturing: scope, challenges and opportunities. *International Journal of Production Research* 2016.
- [285] Petersen EE, Pearce J. Emergence of Home Manufacturing in the Developed World: Return on Investment for Open-Source 3-D Printers. *Technologies* 2017;5:7. <https://doi.org/10.3390/technologies5010007>.
- [286] Pearce J, Qian J-Y. Economic Impact of DIY Home Manufacturing of Consumer Products with Low-cost 3D Printing from Free and Open-source Designs. *European Journal of Social Impact and Circular Economy* 2022;3:1–24. <https://doi.org/10.13135/2704-9906/6508>.
- [287] Bel-Art H50026-0000 sidENTRY™ Glove Box, Acrylic, 30"L x 24"W x 24"H 2024. <https://www.globalindustrial.ca/p/h50026-0000-glove-box-acrylic-30l-x-24w-x-24h/> (accessed 2024).
- [288] Scienceware portable glove box system port I.D. 6 in. isolation chambers 2024. <http://www.sigmaldrich.com/> (accessed 2024).

- [289] Plas-Labs compact glove box AC/DC input 120 V AC, Plas-Labs, 830-ABD isolation chambers 2024. <http://www.sigmaldrich.com/> (accessed 2024).
- [290] Products QT-T of B. AS ONE 3-4041-01 AS-600S Pasaurina Glove Box 2024. <https://qtetech.com/en/en/as-one-3-4041-01-as-600s-pasaurina-glove-box-pr46949/> (accessed 2024).
- [291] Foltynowicz Z, Bardenshtein A, Sangerlaub S, Antvorskov H, Kozak W. Nanoscale, zero valent iron particles for application as oxygen scavenger in food packaging. *Food Packaging and Shelf Life* 2017;11:74–83. <https://doi.org/10.1016/j.fpsl.2017.01.003>.
- [292] PubChem. Iron 2025. <https://pubchem.ncbi.nlm.nih.gov/compound/23925> (accessed June 2, 2025).
- [293] PubChem. Oxygen 2025. <https://pubchem.ncbi.nlm.nih.gov/compound/977> (accessed June 2, 2025).
- [294] When we say that a mole of any gas occupies 22.4L at STP, do we mean a mole of molecules of the gas or of the atoms? If oxygen occupies 2... Quora 2025. <https://www.quora.com/When-we-say-that-a-mole-of-any-gas-occupies-22-4L-at-STP-do-we-mean-a-mole-of-molecules-of-the-gas-or-of-the-atoms-If-oxygen-occupies-22-4-L-at-STP-does-this-volme-contain-1-mole-of-diatomic-oxygen-and-2-moles-of> (accessed June 2, 2025).
- [295] Mottaghi M, Pearce JM. Open-source glove box 2024. <https://doi.org/10.17605/OSF.IO/XNQK3> (accessed 2024).
- [296] Hou Y, Hou C, Zhai Y, Li H, Chen T, Fan Y, et al. Enhancing the electrocatalytic activity of 2D micro-assembly Co₃O₄ nanosheets for Li–O₂ batteries by tuning oxygen vacancies and Co³⁺/Co²⁺ ratio. *Electrochimica Acta* 2019;324:134884. <https://doi.org/10.1016/j.electacta.2019.134884>.
- [297] Phillips J, Xia B, Menendez JA. Calorimetric study of oxygen adsorption on activated carbon. *Thermochimica Acta* 1998;312:87–93. [https://doi.org/10.1016/S0040-6031\(97\)00442-5](https://doi.org/10.1016/S0040-6031(97)00442-5).
- [298] Robards K, Haddad PR, Jackson PE. Gas Chromatography. In: Robards K, Haddad PR, Jackson PE, editors. *Principles and Practice of Modern Chromatographic Methods*, Boston: Academic Press; 2004, p. 75–177. <https://doi.org/10.1016/B978-0-08-057178-2.50006-6>.
- [299] Dey A, Neogi S. Oxygen scavengers for food packaging applications: A review. *Trends in Food Science & Technology* 2019;90:26–34. <https://doi.org/10.1016/j.tifs.2019.05.013>.

- [300] Zhang H, Wang L, Li H, He X. Criterion for Identifying Anodes for Practically Accessible High-Energy-Density Lithium-Ion Batteries. *ACS Energy Lett* 2021;6:3719–24. <https://doi.org/10.1021/acseenergylett.1c01713>.
- [301] Liu K, Liu Y, Lin D, Pei A, Cui Y. Materials for lithium-ion battery safety. *Sci Adv* 2018;4:eaas9820. <https://doi.org/10.1126/sciadv.aas9820>.
- [302] Boukamp BA, Lesh GC, Huggins RA. All-Solid Lithium Electrodes with Mixed-Conductor Matrix. *J Electrochem Soc* 1981;128:725. <https://doi.org/10.1149/1.2127495>.
- [303] Zamfir MR, Nguyen HT, Moyon E, Lee YH, Pribat D. Silicon nanowires for Li-based battery anodes: a review. *J Mater Chem A* 2013;1:9566. <https://doi.org/10.1039/c3ta11714f>.
- [304] Casimir A, Zhang H, Ogoke O, Amine JC, Lu J, Wu G. Silicon-based anodes for lithium-ion batteries: Effectiveness of materials synthesis and electrode preparation. *Nano Energy* 2016;27:359–76. <https://doi.org/10.1016/j.nanoen.2016.07.023>.
- [305] Rahman MM, Mateti S, Sultana I, Hou C, Falin A, Cizek P, et al. End-of-Life Photovoltaic Recycled Silicon: A Sustainable Circular Materials Source for Electronic Industries. *Adv Energy Sustain Res* 2021;2:2100081. <https://doi.org/10.1002/aesr.202100081>.
- [306] Pearce JM. Photovoltaics — a path to sustainable futures. *Futures* 2002;34:663–74. [https://doi.org/10.1016/S0016-3287\(02\)00008-3](https://doi.org/10.1016/S0016-3287(02)00008-3).
- [307] Chowdhury MdS, Rahman KS, Chowdhury T, Nuthammachot N, Techato K, Akhtaruzzaman Md, et al. An overview of solar photovoltaic panels' end-of-life material recycling. *Energy Strategy Reviews* 2020;27:100431. <https://doi.org/10.1016/j.esr.2019.100431>.
- [308] McDonald NC, Pearce JM. Producer responsibility and recycling solar photovoltaic modules. *Energy Policy* 2010;38:7041–7. <https://doi.org/10.1016/j.enpol.2010.07.023>.
- [309] Yu HF, Hasanuzzaman M, Rahim NA, Amin N, Nor Adzman N. Global Challenges and Prospects of Photovoltaic Materials Disposal and Recycling: A Comprehensive Review. *Sustainability* 2022;14:8567. <https://doi.org/10.3390/su14148567>.
- [310] Boon Tay Y, Sim Y, Ang Koon Keong J, Iszaki Bin Patdillah M, Min Chua H, Tang Jun Jie E, et al. Upcycling End of Life Solar Panels to Lithium-Ion Batteries Via a Low Temperature Approach. *ChemSusChem* 2022;15:e202200978. <https://doi.org/10.1002/cssc.202200978>.

- [311] Zhou J, Lin N. Synthetic Methodologies for Si-Containing Li-Storage Electrode Materials. *Adv Energy and Sustain Res* 2022;3:2100198. <https://doi.org/10.1002/aesr.202100198>.
- [312] Huang X, Guo R, Lin Y, Cao Y, Wu J. Si/SiC/C in-situ composite microspindles as anode materials for lithium-ion batteries. *Electrochimica Acta* 2022;422:140546. <https://doi.org/10.1016/j.electacta.2022.140546>.
- [313] Smekens J, Gopalakrishnan R, Steen N, Omar N, Hegazy O, Hubin A, et al. Influence of Electrode Density on the Performance of Li-ion Batteries: Experimental and Simulation Results. *Energies* 2016;9:104. <https://doi.org/10.3390/en9020104>.
- [314] Liu Y, Shu Z, Wang Q, Wu J, Lu W, Wang Q, et al. Understanding the effects of different loadings on properties of a silicon/carbon anode for lithium batteries. *RSC Adv* 2024;14:38085–93. <https://doi.org/10.1039/D4RA06867J>.
- [315] Wang J, Sun Q, Gao X, Wang C, Li W, Holness FB, et al. Toward High Areal Energy and Power Density Electrode for Li-ion Batteries via Optimized 3D Printing Approach. *ACS Appl Mater Interfaces* 2018;10:39794–801. <https://doi.org/10.1021/acsami.8b14797>.
- [316] Shen K, Mei H, Li B, Ding J, Yang S. 3D Printing Sulfur Copolymer-Graphene Architectures for Li-S Batteries. *Adv Energy Mater* 2018;8:1701527. <https://doi.org/10.1002/aenm.201701527>.
- [317] Li B, Liang X, Li G, Shao F, Xia T, Xu S, et al. Inkjet-Printed Ultrathin MoS₂-Based Electrodes for Flexible In-Plane Microsupercapacitors. *ACS Appl Mater Interfaces* 2020;12:39444–54. <https://doi.org/10.1021/acsami.0c11788>.
- [318] Zong W, Ouyang Y, Miao Y-E, Liu T, Lai F. Recent advances and perspectives of 3D printed micro-supercapacitors: from design to smart integrated devices. *Chem Commun* 2022;58:2075–95. <https://doi.org/10.1039/D1CC05544E>.
- [319] Mottaghi M, Pearce JM. A Review of 3D Printing Batteries. *Batteries* 2024;10:110. <https://doi.org/10.3390/batteries10030110>.
- [320] Sun L, Liu Y, Wang L, Chen Z, Jin Z. Stabilizing porous micro-sized silicon anodes via construction of tough composite interface networks for high-energy-density lithium-ion batteries. *Nano Research* 2024;17:1–9. <https://doi.org/10.1007/s12274-024-6937-2>.
- [321] Tang J, Guo X, Chang H, Hu K, Shen Z, Wang W, et al. The preparation of SiC ceramic photosensitive slurry for rapid stereolithography. *Journal of the European Ceramic Society* 2021;41:7516–24. <https://doi.org/10.1016/j.jeurceramsoc.2021.08.029>.

- [322] Miliani C, Ombelli M, Morresi A, Romani A. Spectroscopic study of acrylic resins in solid matrices. *Surface and Coatings Technology* 2002;151–152:276–80. [https://doi.org/10.1016/S0257-8972\(01\)01606-1](https://doi.org/10.1016/S0257-8972(01)01606-1).
- [323] Murli C, Song Y. Pressure-Induced Polymerization of Acrylic Acid: A Raman Spectroscopic Study. *J Phys Chem B* 2010;114:9744–50. <https://doi.org/10.1021/jp1034757>.
- [324] E. Eijsink L, S. Sardjan A, G. Sinnema E, Besten H den, Berg KJ van den, Flapper J, et al. In situ EPR and Raman spectroscopy in the curing of bis-methacrylate–styrene resins. *RSC Advances* 2022;12:2537–48. <https://doi.org/10.1039/D1RA09386J>.
- [325] Blyweert P, Nicolas V, Macutkevic J, Fierro V, Celzard A. Tannin-Based Resins for 3D printing of Porous Carbon Architectures. *ACS Sustainable Chem Eng* 2022;10:7702–11. <https://doi.org/10.1021/acssuschemeng.2c01686>.
- [326] Schuepfer DB, Badaczewski F, Guerra-Castro JM, Hofmann DM, Heiliger C, Smarsly B, et al. Assessing the structural properties of graphitic and non-graphitic carbons by Raman spectroscopy. *Carbon* 2020;161:359–72. <https://doi.org/10.1016/j.carbon.2019.12.094>.
- [327] Garrido-Diez D, Baraia I. Review of wide bandgap materials and their impact in new power devices. 2017 IEEE International Workshop of Electronics, Control, Measurement, Signals and their Application to Mechatronics (ECMSM), 2017, p. 1–6. <https://doi.org/10.1109/ECMSM.2017.7945876>.
- [328] Sun L, Wang X, Liu Y, Xu H, Wang H, Lu Y, et al. Facile Redox Synthesis and Surface Engineering of Porous Silicon from Zintl Compound for High-Performance Lithium Ion Battery Anodes. *ACS Applied Materials & Interfaces* 2024;16. <https://doi.org/10.1021/acsaami.4c10691>.
- [329] Li J, Yang S, Zhou H, Wang L, Yang Z, Meng P, et al. Facile synthesis of SiO₂/C anode using PVC as carbon source for lithium-ion batteries. *J Mater Sci: Mater Electron* 2019;30:69–78. <https://doi.org/10.1007/s10854-018-0256-x>.
- [330] Sun L, Liu Y, Wang L, Jin Z. Advances and Future Prospects of Micro-Silicon Anodes for High-Energy-Density Lithium-Ion Batteries: A Comprehensive Review. *Advanced Functional Materials* 2024;34:2403032. <https://doi.org/10.1002/adfm.202403032>.
- [331] Kanaphan Y, Klamchuen A, Piyavarakorn V, Harnchana V, Srilomsak S, Nash J, et al. Multilayer Silicene Nanosheets Derived from a Recycling Process Using End-of-Life Solar Cells Producing a Silicene/Graphite Composite for Anodes in Lithium-Ion Batteries. *ACS Sustainable Chem Eng* 2023;11:13545–53. <https://doi.org/10.1021/acssuschemeng.3c02027>.

- [332] Li H, Huang X, Chen L, Wu Z, Liang Y. ChemInform Abstract: A High Capacity Nano-Si Composite Anode Material for Lithium Rechargeable Batteries. ChemInform 2000;31. <https://doi.org/10.1002/chin.200001017>.
- [333] Fransson L, Eriksson T, Edström K, Gustafsson T, Thomas JO. Influence of carbon black and binder on Li-ion batteries. Journal of Power Sources 2001;101:1–9. [https://doi.org/10.1016/S0378-7753\(01\)00481-5](https://doi.org/10.1016/S0378-7753(01)00481-5).
- [334] Eshraghi N, Berardo L, Schrijnemakers A, Delaval V, Shaibani M, Majumder M, et al. Recovery of nano-structured silicon from end-of-life photovoltaic wafers with value-added applications in lithium-ion battery. ACS Sustainable Chemistry and Engineering 2020;8:5868–79. <https://doi.org/10.1021/acssuschemeng.9b07434>.
- [335] Haselhuhn AS, Gooding EJ, Glover AG, Anzalone GC, Wijnen B, Sanders PG, et al. Substrate Release Mechanisms for Gas Metal Arc Weld 3D Aluminum Metal Printing. 3D Printing and Additive Manufacturing 2014;1:204–9. <https://doi.org/10.1089/3dp.2014.0015>.
- [336] Haselhuhn AS, Wijnen B, Anzalone GC, Sanders PG, Pearce JM. In situ formation of substrate release mechanisms for gas metal arc weld metal 3-D printing. Journal of Materials Processing Technology 2015;226:50–9. <https://doi.org/10.1016/j.jmatprotec.2015.06.038>.
- [337] Climate-change impacts of graphite production higher than reported — study. MININGCOM 2021. <https://www.mining.com/climate-change-impacts-of-graphite-production-higher-than-previously-reported-study/> (accessed November 1, 2024).
- [338] Engels P, Cerdas F, Dettmer T, Frey C, Hentschel J, Herrmann C, et al. Life cycle assessment of natural graphite production for lithium-ion battery anodes based on industrial primary data. Journal of Cleaner Production 2022;336:130474. <https://doi.org/10.1016/j.jclepro.2022.130474>.
- [339] Jara AD, Betemariam A, Woldetinsae G, Kim JY. Purification, application and current market trend of natural graphite: A review. International Journal of Mining Science and Technology 2019;29:671–89. <https://doi.org/10.1016/j.ijmst.2019.04.003>.
- [340] Jacob Robin R. Viability and Eco-Consequences of Synthetic and Natural Graphite for Lithium-Ion Battery Anodes in the USA. IEEE Engineering Management Review 2024;52:131–47. <https://doi.org/10.1109/EMR.2024.3372697>.
- [341] Andreska J, Hanel L. Historical occurrence and extinction of Atlantic salmon in the River Elbe from the fourteenth to the twentieth centuries. Archives of Polish Fisheries 2015;23. <https://doi.org/10.1515/aopf-2015-0001>.
- [342] Pomilovskis R, Kaulina E, Mierina I, Abolins A, Kockova O, Fridrihsone A, et al. Wood pulp industry by-product valorization for acrylate synthesis and bio-based

- polymer development via Michael addition reaction. *Journal of Bioresources and Bioproducts* 2023;8:265–79. <https://doi.org/10.1016/j.jobab.2023.06.001>.
- [343] Veith C, Diot-Néant F, Miller SA, Allais F. Synthesis and polymerization of bio-based acrylates: a review. *Polym Chem* 2020;11:7452–70. <https://doi.org/10.1039/D0PY01222J>.
- [344] Borrello J, Nasser P, Iatridis JC, Costa KD. 3D printing a mechanically-tunable acrylate resin on a commercial DLP-SLA printer. *Additive Manufacturing* 2018;23:374–80. <https://doi.org/10.1016/j.addma.2018.08.019>.
- [345] Jiang W, Jin X, Li H, Zhang S, Zhou T, Xie H. Modification of nano-hybrid silicon acrylic resin with anticorrosion and hydrophobic properties. *Polymer Testing* 2020;82:106287. <https://doi.org/10.1016/j.polymertesting.2019.106287>.
- [346] Korhonen J, Honkasalo A, Seppälä J. Circular Economy: The Concept and its Limitations. *Ecological Economics* 2018;143:37–46. <https://doi.org/10.1016/j.ecolecon.2017.06.041>.
- [347] Martinez AC, Schiaffino EM, Aranzola AP, Fernandez CA, Seol M-L, Sherrard CG, et al. Multiprocess 3D printing of sodium-ion batteries via vat photopolymerization and direct ink writing. *J Phys Energy* 2023;5:045010. <https://doi.org/10.1088/2515-7655/acf958>.
- [348] Komoto K, Lee J-S, Heath G, Wade A. End-of-Life Management of Photovoltaic Panels: Trends in PV Module Recycling Technologies. International Energy Agency Photovoltaic Power Systems Program (IEA PVPS); 2018.
- [349] Sah D, Chitra, Kumar S. Recovery and analysis of valuable materials from a discarded crystalline silicon solar module. *Solar Energy Materials and Solar Cells* 2022;246:111908. <https://doi.org/10.1016/j.solmat.2022.111908>.
- [350] European Carbon and Graphite Association (ECGA). Graphite in batteries 2023. https://ecga.net/wp-content/uploads/2023/02/Graphite-in-batteries_Infosheet_final.pdf.
- [351] Fonseca N, Thummalapalli SV, Jambhulkar S, Ravichandran D, Zhu Y, Patil D, et al. 3D Printing-Enabled Design and Manufacturing Strategies for Batteries: A Review. *Small* 2023;19:2302718. <https://doi.org/10.1002/sml.202302718>.
- [352] Guo Z, Zhou C. Recent advances in ink-based additive manufacturing for porous structures. *Additive Manufacturing* 2021;48:102405. <https://doi.org/10.1016/j.addma.2021.102405>.
- [353] Wang R, Zhang Y, Xi W, Zhang J, Gong Y, He B, et al. 3D printing of hierarchically micro/nanostructured electrodes for high-performance rechargeable batteries. *Nanoscale* 2023;15:13932–51. <https://doi.org/10.1039/D3NR03098A>.

- [354] Du J, Cao Q, Tang X, Xu X, Long X, Ding J, et al. 3D printing-assisted gyroidal graphite foam for advanced supercapacitors. *Chemical Engineering Journal* 2021;416:127885. <https://doi.org/10.1016/j.cej.2020.127885>.
- [355] Hyun G, Ham Y, Harding J, Jeon S. Towards optimal 3D battery electrode architecture: Integrating structural engineering with AI-driven optimization. *Energy Storage Materials* 2024;69:103395. <https://doi.org/10.1016/j.ensm.2024.103395>.
- [356] Ji W, Qu H, Zhang X, Zheng D, Qu D. Electrode Architecture Design to Promote Charge-Transport Kinetics in High-Loading and High-Energy Lithium-Based Batteries. *Small Methods* 2021;5:2100518. <https://doi.org/10.1002/smt.202100518>.
- [357] Bishoyi SS, Mohanta TR, Behera SK. Preceramic polymer derived carbon encapsulated Si-C hybrids for lithium-ion battery anodes. *Journal of Alloys and Compounds* 2024;1002:175267. <https://doi.org/10.1016/j.jallcom.2024.175267>.
- [358] Chandra H, Allen SW, Oberloier SW, Bihari N, Gwamuri J, Pearce JM. Open-Source Automated Mapping Four-Point Probe. *Materials* 2017;10:110. <https://doi.org/10.3390/ma10020110>.
- [359] Entwistle J, Ge R, Pardikar K, Smith R, Cumming D. Carbon binder domain networks and electrical conductivity in lithium-ion battery electrodes: A critical review. *Renewable and Sustainable Energy Reviews* 2022;166:112624. <https://doi.org/10.1016/j.rser.2022.112624>.
- [360] Smits FM. Measurement of sheet resistivities with the four-point probe. *The Bell System Technical Journal* 1958;37:711–8. <https://doi.org/10.1002/j.1538-7305.1958.tb03883.x>.
- [361] Mottaghi M, Kulkarni A, Pearce JM. Recycling silicon photovoltaic cells into silicon anodes for Li-ion batteries using 3D printing. *RSC Sustain* 2025. <https://doi.org/10.1039/D4SU00808A>.
- [362] Dutta BN. Lattice constants and thermal expansion of silicon up to 900 °C by X-ray method. *Physica Status Solidi (b)* 1962;2:984–7. <https://doi.org/10.1002/pssb.19620020803>.
- [363] Doebelin N, Kleeberg R. Profex: a graphical user interface for the Rietveld refinement program BGMN. *J Appl Cryst* 2015;48:1573–80. <https://doi.org/10.1107/S1600576715014685>.
- [364] Ong SP, Richards WD, Jain A, Hautier G, Kocher M, Cholia S, et al. Python Materials Genomics (pymatgen): A robust, open-source python library for materials analysis. *Computational Materials Science* 2013;68:314–9. <https://doi.org/10.1016/j.commatsci.2012.10.028>.
- [365] Wu P, Guo X, Su Z, Liu C, Chen S, Zheng Z, et al. Preparation of silicon oxycarbide (SiOC) anodes for high performance Li-ion batteries using competitive

- relationship between crosslinking and polymerization. *Chemical Engineering Journal* 2022;446:137354. <https://doi.org/10.1016/j.cej.2022.137354>.
- [366] Dibandjo P, Graczyk-Zajac M, Riedel R, Pradeep VS, Soraru GD. Lithium insertion into dense and porous carbon-rich polymer-derived SiOC ceramics. *Journal of the European Ceramic Society* 2012;32:2495–503. <https://doi.org/10.1016/j.jeurceramsoc.2012.03.010>.
- [367] Greenough M, Zhao Z, Jacobsohn LG, Tong J, Bordia RK. Low/intermediate temperature pyrolyzed polysiloxane derived ceramics with increased carbon for electrical applications. *Journal of the European Ceramic Society* 2021;41:5882–9. <https://doi.org/10.1016/j.jeurceramsoc.2021.04.007>.
- [368] Wall M. Raman Spectroscopy Optimizes Graphene Characterization. *Advanced Materials and Processes* 2012;170:35–8. <https://doi.org/10.31399/asm.amp.2012-04.p035>.
- [369] Liu Y, Fang Y, Qian J, Liu Z, Yang B, Wang X. Bio-inspired polydopamine functionalization of carbon fiber for improving the interfacial adhesion of polypropylene composites. *RSC Adv* 2015;5. <https://doi.org/10.1039/C5RA20045H>.
- [370] Xia A, Yin J, Chen X, Liu X, Huang Z. Polymer-Derived Si-Based Ceramics: Recent Developments and Perspectives. *Crystals* 2020;10:824. <https://doi.org/10.3390/cryst10090824>.
- [371] Eshraghi N, Berardo L, Schrijnemakers A, Delaval V, Shaibani M, Majumder M, et al. Recovery of Nano-Structured Silicon from End-of-Life Photovoltaic Wafers with Value-Added Applications in Lithium-Ion Battery. *ACS Sustainable Chem Eng* 2020;8:5868–79. <https://doi.org/10.1021/acssuschemeng.9b07434>.
- [372] Danz P, Aryan V, Möhle E, Nowara N. Experimental Study on Fluorine Release from Photovoltaic Backsheet Materials Containing PVF and PVDF during Pyrolysis and Incineration in a Technical Lab-Scale Reactor at Various Temperatures. *Toxics* 2019;7:47. <https://doi.org/10.3390/toxics7030047>.
- [373] Sujith R, Gangadhar J, Greenough M, Bordia RK, Panda DK. A review of silicon oxycarbide ceramics as next generation anode materials for lithium-ion batteries and other electrochemical applications. *J Mater Chem A* 2023;11:20324–48. <https://doi.org/10.1039/D3TA01366A>.
- [374] Yi Z, Lin N, Zhao Y, Wang W, Qian Y, Zhu Y, et al. A flexible micro/nanostructured Si microsphere cross-linked by highly-elastic carbon nanotubes toward enhanced lithium ion battery anodes. *Energy Storage Materials* 2019;17:93–100. <https://doi.org/10.1016/j.ensm.2018.07.025>.
- [375] Sun L, Wang X, Liu Y, Xu H, Wang H, Lu Y, et al. Facile Redox Synthesis and Surface Engineering of Porous Silicon from Zintl Compound for High-Performance

- Lithium Ion Battery Anodes. *ACS Appl Mater Interfaces* 2024;16:52349–57. <https://doi.org/10.1021/acsami.4c10691>.
- [376] He W, Chen C, Jiangmin J, Chen Z, Liao H, Dou H, et al. 3D Printed Multilayer Graphite@SiO Structural Anode for High-Loading Lithium-Ion Battery. *Batteries & Supercaps* 2022;5. <https://doi.org/10.1002/batt.202100258>.
- [377] Kim M, Yang Z, Son S-B, Trask SE, Jansen A, Bloom I. Effect of cathode on crosstalk in Si-based lithium-ion cells. *J Mater Chem A* 2021;9:26904–16. <https://doi.org/10.1039/D1TA06304A>.
- [378] Huey Z, Ha Y, Frisco S, Norman A, Teeter G, Jiang C-S, et al. Multi-modal characterization methods of solid-electrolyte interphase in silicon-graphite composite electrodes. *Journal of Power Sources* 2023;564:232804. <https://doi.org/10.1016/j.jpowsour.2023.232804>.
- [379] An SJ, Li J, Daniel C, Mohanty D, Nagpure S, Wood DL. The state of understanding of the lithium-ion-battery graphite solid electrolyte interphase (SEI) and its relationship to formation cycling. *Carbon* 2016;105:52–76. <https://doi.org/10.1016/j.carbon.2016.04.008>.
- [380] Chagas AM. Haves and have nots must find a better way: The case for open scientific hardware. *PLOS Biology* n.d.;16:p.e3000014.
- [381] Daniel K. F, Peter J. G. Open-Source Hardware Is a Low-Cost Alternative for Scientific Instrumentation and Research. *Modern Instrumentation* 2012;2012. <https://doi.org/10.4236/mi.2012.12002>.
- [382] Arancio J, Morales Tirado M, Pearce J. Equitable Research Capacity Towards the Sustainable Development Goals: The Case for Open Science Hardware. *JSPG* 2022;21. <https://doi.org/10.38126/JSPG210202>.
- [383] Hafting FK, Kulas D, Michels E, Chipkar S, Wisniewski S, Shonnard D, et al. Modular Open-Source Design of Pyrolysis Reactor Monitoring and Control Electronics. *Electronics* 2023;12:4893. <https://doi.org/10.3390/electronics12244893>.
- [384] Maryam M, Joshua MP. Open-source inert gas glove box. *HardwareX* 2025:e00702. <https://doi.org/10.1016/j.ohx.2025.e00702>.
- [385] Wu Z, Cheng X, Tian D, Gao T, He W, Yang C. SiOC nanolayers directly-embedded in graphite as stable anode for high-rate lithium ion batteries. *Chemical Engineering Journal* 2019;375:121997. <https://doi.org/10.1016/j.cej.2019.121997>.
- [386] Cho Y, Piao Y. Shortly Cut Carbon Nanotube as a Conductive Additive for High-Performance Silicon Anodes in Lithium-Ion Batteries. *ACS Omega* n.d.;10:19614–24. <https://doi.org/10.1021/acsomega.5c00295>.

- [387] Araño KG, Armstrong BL, Yang G, Kumara C, Ward TZ, Meyer HMI, et al. Elucidating the Role of Carbon Conductive Additive in the Processing and Electrochemical Behavior of Surface-Modified Si Anodes. *Energy Fuels* 2024;38:6446–58. <https://doi.org/10.1021/acs.energyfuels.4c00039>.
- [388] Mottaghi M, Pearce JM. Open-source Inert Gas Glove Box 2024. <https://doi.org/10.2139/ssrn.5015252>.
- [389] Sanchez Careaga FJ, Porat A, Briens L, Briens C. Pyrolysis shaker reactor for the production of biochar. *The Canadian Journal of Chemical Engineering* 2020;98:2417–24. <https://doi.org/10.1002/cjce.23771>.
- [390] Cao RZ, Saad F, Briens C. Thermochemical Recycling of Household Polyolefin Waste. *Energy Fuels* 2025;39:699–712. <https://doi.org/10.1021/acs.energyfuels.4c04782>.
- [391] Cao RZ, Fazari J, Briens CL, Charpentier PA. Pyrolysis of Typical Ontario Raw Plastic Film Wastes. *Energy Fuels* 2025;39:713–25. <https://doi.org/10.1021/acs.energyfuels.4c04784>.
- [392] Cao RZ, Saad F, Briens C. Thermochemical Recycling of Household Polyolefin Waste. *Energy Fuels* 2025;39:699–712. <https://doi.org/10.1021/acs.energyfuels.4c04782>.
- [393] Julien BN, Holmes N, Ghode RGS, Boutilier MSH. Wall Shear Stress Sensors Based on Carbon Nanotube Pillars. *ACS Appl Nano Mater* 2023;6:20769–81. <https://doi.org/10.1021/acsanm.3c03728>.
- [394] Ghode, Rohit G. S., Cao RZ, Briens CL, Boutilier MSH. Conversion of Bitumen and Waste Plastics Pyrolysis Gases into Hydrogen and Carbon Nanotubes (To be published) 2025.
- [395] Onshape - Cloud-Native Product Development n.d. <https://www.onshape.com> (accessed August 9, 2024).
- [396] PrusaSlicer - Free 3D Printing Software. Prusa3D by Josef Prusa n.d. <https://www.prusa3d.com/prusaslicer/> (accessed July 17, 2024).
- [397] White CM, Banks R, Hamerton I, Watts JF. Characterisation of commercially CVD grown multi-walled carbon nanotubes for paint applications. *Progress in Organic Coatings* 2016;90:44–53. <https://doi.org/10.1016/j.porgcoat.2015.09.020>.
- [398] DiLeo RA, Landi BJ, Raffaele RP. Purity assessment of multiwalled carbon nanotubes by Raman spectroscopy. *J Appl Phys* 2007;101:064307. <https://doi.org/10.1063/1.2712152>.

- [399] Mottaghi M, Kulkarni A, Pearce JM. Effect of Pyrolysis Temperature on the Performance of 3D-Printed Silicon–Carbon Anodes Derived from Recycled Photovoltaic Silicon 2025.
- [400] Mottaghi M, Kulkarni A, Pearce JM. Effect of Pyrolysis Temperature on the Performance of 3D-Printed Silicon–Carbon Anodes Derived from Recycled Photovoltaic Silicon n.d.
https://papers.ssrn.com/sol3/papers.cfm?abstract_id=5812933 (accessed November 27, 2025).
- [401] Mo T, Li Y, Zhao H, Mo T, Li Y, Zhao H. The Utilization of Carbon Nanotubes in Advanced Silicon – Carbon Anode Materials for Lithium-Ion Batteries. *Carbon Nanotubes - Recent Advances, Perspectives and Applications*, IntechOpen; 2024.
<https://doi.org/10.5772/intechopen.114867>.
- [402] Cui L-F, Hu L, Choi JW, Cui Y. Light-Weight Free-Standing Carbon Nanotube-Silicon Films for Anodes of Lithium Ion Batteries. *ACS Nano* 2010;4:3671–8.
<https://doi.org/10.1021/nn100619m>.
- [403] You S, Tan H, Wei L, Tan W, Chao Li C. Design Strategies of Si/C Composite Anode for Lithium-Ion Batteries. *Chemistry – A European Journal* 2021;27:12237–56. <https://doi.org/10.1002/chem.202100842>.
- [404] Ezzedine M, Jardali F, Florea I, Zamfir M-R, Cojocaru C-S. Nanostructuring Strategies for Silicon-based Anodes in Lithium-ion Batteries: Tuning Areal Silicon Loading, SEI Formation/Irreversible Capacity Loss, Rate Capability Retention and Electrode Durability. *Batteries & Supercaps* 2023;6:e202200451.
<https://doi.org/10.1002/batt.202200451>.
- [405] Zhao Y, Pan X, Liu M, Chen X, Zhang R, Zhiyong X. The fabrication of silicon/dual-network carbon nanofibers/carbon nanotubes as free-standing anodes for lithium-ion batteries. *RSC Adv* 2023;13:35026–39.
<https://doi.org/10.1039/D3RA05755K>.
- [406] Ikonen T, Kalidas N, Lahtinen K, Isoniemi T, Toppari JJ, Vázquez E, et al. Conjugation with carbon nanotubes improves the performance of mesoporous silicon as Li-ion battery anode. *Sci Rep* 2020;10:5589.
<https://doi.org/10.1038/s41598-020-62564-0>.
- [407] Zhang M, Li L, Jian X, Zhang S, Shang Y, Xu T, et al. Free-standing and flexible CNT/(Fe@Si@SiO₂) composite anodes with kernel-pulp-skin nanostructure for high-performance lithium-ion batteries. *Journal of Alloys and Compounds* 2021;878:160396. <https://doi.org/10.1016/j.jallcom.2021.160396>.
- [408] Kordesch K, Taucher-Mautner W. HISTORY | Primary Batteries. In: Garcke J, editor. *Encyclopedia of Electrochemical Power Sources*, Amsterdam: Elsevier; 2009, p. 555–64. <https://doi.org/10.1016/B978-044452745-5.00003-4>.

- [409] Owens BB, Reale P, Scrosati B. PRIMARY BATTERIES | Overview. In: Garche J, editor. *Encyclopedia of Electrochemical Power Sources*, Amsterdam: Elsevier; 2009, p. 22–7. <https://doi.org/10.1016/B978-044452745-5.00096-4>.
- [410] Viswanathan B. Chapter 12 - Batteries. In: Viswanathan B, editor. *Energy Sources*, Amsterdam: Elsevier; 2017, p. 263–313. <https://doi.org/10.1016/B978-0-444-56353-8.00012-5>.
- [411] Burheim OS. Secondary Batteries. *Engineering Energy Storage*, Elsevier; 2017, p. 111–45. <https://doi.org/10.1016/B978-0-12-814100-7.00007-9>.
- [412] Lopes PP, Stamenkovic VR. Past, present, and future of lead–acid batteries. *Science* 2020;369:923–4. <https://doi.org/10.1126/science.abd3352>.
- [413] Doughty DH, Roth EP. A General Discussion of Li Ion Battery Safety. *Electrochem Soc Interface* 2012;21:37. <https://doi.org/10.1149/2.F03122if>.
- [414] Flora G, Gupta D, Tiwari A. Toxicity of lead: a review with recent updates. *Interdisciplinary Toxicology* 2012;5:47–58. <https://doi.org/10.2478/v10102-012-0009-2>.
- [415] Posada JOG, Rennie AJR, Villar SP, Martins VL, Marinaccio J, Barnes A, et al. Aqueous batteries as grid scale energy storage solutions. *Renewable and Sustainable Energy Reviews* 2017;68:1174–82. <https://doi.org/10.1016/j.rser.2016.02.024>.
- [416] Quansah DA. Comparative study of electricity storage batteries for Solar Photovoltaic home systems. Doctoral dissertation. 2008.
- [417] Marin-Garcia G, Vazquez-Guzman G, Sosa JM, Lopez AR, Martinez-Rodriguez PR, Langarica D. Battery Types and Electrical Models: A Review. 2020 IEEE International Autumn Meeting on Power, Electronics and Computing (ROPEC), Ixtapa, Mexico: IEEE; 2020, p. 1–6. <https://doi.org/10.1109/ROPEC50909.2020.9258711>.
- [418] Poullikkas A. A comparative overview of large-scale battery systems for electricity storage. *Renewable and Sustainable Energy Reviews* 2013;27:778–88. <https://doi.org/10.1016/j.rser.2013.07.017>.
- [419] Ramachandra Rao S. Resource Recovery from Process Wastes. *Waste Management Series*, vol. 7, Elsevier; 2006, p. 375–457. [https://doi.org/10.1016/S0713-2743\(06\)80095-4](https://doi.org/10.1016/S0713-2743(06)80095-4).
- [420] May GJ, Davidson A, Monahov B. Lead batteries for utility energy storage: A review. *Journal of Energy Storage* 2018;15:145–57. <https://doi.org/10.1016/j.est.2017.11.008>.
- [421] Beaudin M, Zareipour H, Schellenberg A, Rosehart W. Energy Storage for Mitigating the Variability of Renewable Electricity Sources. *Energy Storage for*

- Smart Grids, Elsevier; 2015, p. 1–33. <https://doi.org/10.1016/B978-0-12-410491-4.00001-4>.
- [422] Avril S, Arnaud G, Florentin A, Vinard M. Multi-objective optimization of batteries and hydrogen storage technologies for remote photovoltaic systems. *Energy* 2010;35:5300–8. <https://doi.org/10.1016/j.energy.2010.07.033>.
- [423] Divya KC, Østergaard J. Battery energy storage technology for power systems—An overview. *Electric Power Systems Research* 2009;79:511–20. <https://doi.org/10.1016/j.epsr.2008.09.017>.
- [424] Parker CD. APPLICATIONS – STATIONARY | Energy Storage Systems: Batteries. *Encyclopedia of Electrochemical Power Sources*, Elsevier; 2009, p. 53–64. <https://doi.org/10.1016/B978-044452745-5.00382-8>.
- [425] Lemaire-Potteau E, Perrin M, Genies S. BATTERIES | Charging Methods. *Encyclopedia of Electrochemical Power Sources*, Elsevier; 2009, p. 413–23. <https://doi.org/10.1016/B978-044452745-5.00885-6>.
- [426] Zhu WH, Zhu Y, Davis Z, Tatarchuk BJ. Energy efficiency and capacity retention of Ni–MH batteries for storage applications. *Applied Energy* 2013;106:307–13. <https://doi.org/10.1016/j.apenergy.2012.12.025>.
- [427] Abdin Z, Khalilpour KR. Single and Polystorage Technologies for Renewable-Based Hybrid Energy Systems. *Polygeneration with Polystorage for Chemical and Energy Hubs*, Elsevier; 2019, p. 77–131. <https://doi.org/10.1016/B978-0-12-813306-4.00004-5>.
- [428] Iclodean C, Varga B, Burnete N, Cimerdean D, Jurchiș B. Comparison of Different Battery Types for Electric Vehicles. *IOP Conf Ser: Mater Sci Eng* 2017;252:012058. <https://doi.org/10.1088/1757-899X/252/1/012058>.
- [429] Bernard P, Lippert M. 2015- Nickel–Cadmium and Nickel–Metal Hydride Battery Energy Storage. *Electrochemical Energy Storage for Renewable Sources and Grid Balancing*, Elsevier; 2015, p. 223–51. <https://doi.org/10.1016/B978-0-444-62616-5.00014-0>.
- [430] German JM. Hybrid Electric Vehicles. *Encyclopedia of Energy*, Elsevier; 2004, p. 197–213. <https://doi.org/10.1016/B0-12-176480-X/00180-7>.
- [431] Tsais P-J, Chan LI. 2013- Nickel-based batteries: materials and chemistry. *Electricity Transmission, Distribution and Storage Systems*, Elsevier; 2013, p. 309–97. <https://doi.org/10.1533/9780857097378.3.309>.
- [432] Aktaş A, Kirçiçek Y. Solar Hybrid Systems and Energy Storage Systems. *Solar Hybrid Systems*, Elsevier; 2021, p. 87–125. <https://doi.org/10.1016/B978-0-323-88499-0.00005-7>.

- [433] Cao C, Steinrück H-G. 2023- Molecular-scale synchrotron X-ray investigations of solid-liquid interfaces in lithium-ion batteries. *Encyclopedia of Solid-Liquid Interfaces*, Elsevier; 2024, p. 391–416. <https://doi.org/10.1016/B978-0-323-85669-0.00105-7>.
- [434] Soto A, Berrueta A, Mateos M, Sanchis P, Ursúa A. 2022- Impact of micro-cycles on the lifetime of lithium-ion batteries: An experimental study. *Journal of Energy Storage* 2022;55:105343. <https://doi.org/10.1016/j.est.2022.105343>.
- [435] Keçili R, Arli G, Hussain CM. 2020- Future of analytical chemistry with graphene. *Comprehensive Analytical Chemistry*, vol. 91, Elsevier; 2020, p. 355–89. <https://doi.org/10.1016/bs.coac.2020.09.003>.
- [436] Lei H, Han YY. 2019- The measurement and analysis for Open Circuit Voltage of Lithium-ion Battery. *J Phys: Conf Ser* 2019;1325:012173. <https://doi.org/10.1088/1742-6596/1325/1/012173>.

9 Appendices

Appendix A: Fundamental Concepts and Definitions in Literature

A.1. Battery basics

The following basic definitions for battery terms are provided from established references in the field.

A.1.1. Energy

Energy density is the amount of energy stored in a given volume or mass which defines the battery capacity. The specific energy density or the gravimetric energy density is the energy in the specific weight measured in Wh/kg and the volumetric energy density is the energy stored in the specific volume measured in Wh/m³.

A.1.2. Power

Power density is the rate that the energy is transferred within the battery structure that is particularly crucial in applications such as electric vehicles, where rapid energy delivery is required. Specific power density refers to the rate at which a battery can deliver electrical power relative to its weight and quantifies how quickly a battery can discharge its stored energy, typically measured in watts per unit of weight (W/kg). Volumetric power density signifies the rate at which a battery can deliver electrical power relative to its volume and is measured in watts per unit of volume (W/m³).

A.1.3. Voltage

Nominal voltage indicates the average voltage value assigned to a particular type or model of battery for design and specification purposes. It is often used as a reference point and does not reflect the actual voltage of the battery at any specific moment during its operation. Open circuit voltage (OCV or V_{OC}) is the voltage across the battery terminals when no current is flowing. It represents the potential difference between the positive and negative terminals in the absence of a load and is an indicator of the SOC.

A.1.4. State of the charge (SOC)

SOC is the amount of energy stored in a battery at a given moment and is expressed as a percentage (%) of the total capacity. It indicates how much charge is available for use.

A.1.5. Capacity

Total capacity represents the maximum number of ampere-hours that can be extracted from a fully charged battery cell before it is fully discharged. This limit is determined by the SOC and involves discharging from 100% to 0%. Discharge capacity is the quantity of ampere-hours that can be drawn from a fully charged cell at a constant current rate, stopping before encountering a minimum voltage limit. Unlike total capacity, it does not indicate the complete charge a cell can hold, as it discharges from 100% to a minimum voltage. Reversible charge capacity refers to the amount of charge that can be cyclically stored and released in a reversible electrochemical reaction and indicates the stability of the electrochemical process.

A.1.6. Voltage drops

There are several potential mechanisms that result in voltage drops. First, activation loss happens due to the slow nature of the reactions that occur on the electrode surface. Fuel crossover and internal currents result from electrons passing through the electrolyte which leads to the charge loss in this way. Ohmic loss, or internal resistance, is the energy loss resulting from resistance to the flow of electrons through electrode materials and interconnections, as well as resistance to the flow of ions through the electrolyte. Mass transport (concentration) loss occurs when the electrode surface is depleted from charges over time, and reactants require time to diffuse from the inner bulk to the surface for the reaction to keep on.

A.1.7. Self-discharge

Self-discharge is the result of unwanted chemical reactions that occur internally, leading to various issues such as current leakage, dendrite formation, electrolyte decomposition,

and electrode decomposition. These processes contribute to the gradual discharge of a battery even when it is not in use.

A.1.8. Electrical double layer

During battery operation, the charged electrodes interface with the electrolyte results in the formation of a layer of charges. This occurs due to the attractive forces between the charged electrode surface and the ions present in the electrolyte, and it is referred to as the electrical double layer.

A.1.9. Lithiation/ Delithiation

Lithiation describes the insertion of lithium ions into anode and delithiation refers to the removal from the anode during the charging and discharging of a lithium-ion battery, respectively.

A.1.10. Particle pulverization

Particle pulverization in lithium-ion batteries refers to the mechanical fragmentation or disintegration of electrode materials, especially in the anode, as a result of repeated cycles of lithium-ion intercalation and deintercalation during charging and discharging.

A.1.11. Lithium plating

When the battery voltage exceeds a certain threshold during charging, the excess voltage drives the reduction of lithium ions at the anode surface, leading to the deposition of metallic lithium which is more likely to occur at low temperatures; lower temperatures reduce the lithium-ion mobility and make it easier for lithium ions to deposit as solid lithium on the anode surface which is called lithium plating.

A.1.12. Solid electrolyte interface (SEI)

During the initial cycle, the electrolyte containing lithium salt decomposes to create reactive species. These reactive species, along with the lithium ions, precipitate on the anode surface. This ongoing process results in the formation of multiple layers with

different chemical compositions and properties. Maintaining an optimum thickness in this layer is crucial as it can provide mechanical stability and prevent further decomposition. It is essential, however, for this layer to be thin enough not to reduce ionic conductivity.

A.1.13. Charge/discharge test

The charge/discharge test involves applying a constant current while considering the cut-off voltage and scan rate. During charging, the constant current leads to an increase in potential until the cut-off voltage is reached. Then, the current is reversed, and the potential starts to decrease to the minimum cut-off voltage. This test is a fundamental method for evaluating the capacity, reversibility, stability, and rate capability of the battery.

A.1.14. Cyclic voltammetry test

This test involves tracking the current by linearly sweeping the voltage over time with a specified scan rate, which is higher than that used in charge/discharge cycles. The reason for this is that the test is employed to study the redox reactions, reaction kinetics, and electrochemical behavior of the materials within the battery.

A.1.15. Electrochemical Impedance Spectroscopy (EIS)

EIS is a test that measures various impedance elements in a battery system by applying a small alternating current across a wide range of frequencies and measuring the corresponding response. The output of the test is a plot called Nyquist plot which is made of the real part the impedance on the x axis and the imaginary part of the impedance on the y axis. An equivalent circuit is constructed from a Nyquist plot in order to model and analyze the electrochemical behavior of a system. Different parts of the curve can be explained as the following:

- Ohmic resistance (R_s) is related to the ionic and electronic conductivity of various components in the battery, including the electrolyte, electrodes, and current collector. This is measured at low frequencies, and on the Nyquist plot, it is represented by the real part of the impedance (Figure A - 1a).

- Charge transfer resistance (R_{ct}) is the resistance related to the electrochemical reactions occurring at the interface layer of the electrode-electrolyte. Information about the kinetics of the charge transfer process, such as lithium intercalation at the electrode surface, is provided by this resistance. On the Nyquist plot, this resistance is observed as a semicircle, with the radius of the semicircle representing the charge transfer resistance. This region corresponds to the high-frequency range. An improvement in battery performance is indicated by a reduction in the radius/diameter of this semicircle, suggesting that the charge transfer processes at the electrode-electrolyte interface are more efficient and faster. This layer also serves as a capacitance that stores charges transferring slowly to the electrode. In the equivalent circuit, it is represented as a capacitance in parallel to the charge transfer resistance (Figure A - 1b).
- Warburg impedance (W) is related to the diffusion (mass transport) of lithium ions into the solid electrode and electrolyte. On the Nyquist plot, it is represented by a sloped line. This region corresponds to the medium frequency range on the plot. The slope of the line reflects the diffusion coefficient of the species. A steeper slope indicates more difficult ion diffusion, while a shallower slope suggests easier mass transport and diffusion. The tail of this impedance is also significant. Tail extensions or deviations from the line indicate additional electrochemical processes occurring in the battery (Figure A - 1c).

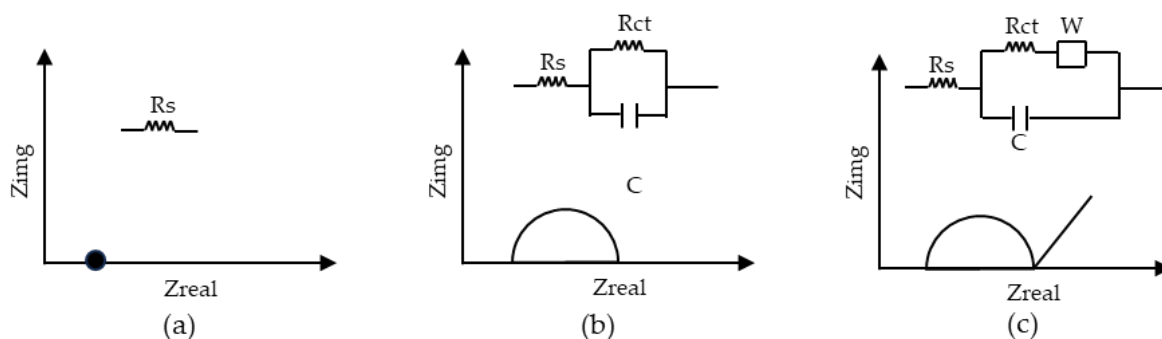


Figure A - 1. Nyquist plot, (a) Ohmic resistance, (b) Charge transfer resistance, and (c) Warburg resistance

A.2. Basic types of batteries

In general, batteries are divided into two categories; primary and secondary batteries. Primary batteries, also known as disposable or non-rechargeable batteries, are designed for single-use applications. They provide a reliable source of power by converting chemical energy into electrical energy. Common examples include zinc-carbon, alkaline zinc-manganese dioxide, and metal-air- batteries [408]. Primary batteries are used for low and intermittent power needs, such as remote controls and smoke detectors [409]. They are however, one of the most expensive sources of electric energy and in general should be replaced by secondary batteries. Secondary batteries are rechargeable batteries that can be reused multiple times by reversing the chemical reactions through an external power source, like a charger. Popular secondary battery types include lead acid, nickel-cadmium (NiCd), nickel-metal hydride (Ni-MH), and lithium-ion (Li-ion) batteries. They are widely used in portable electronics like smartphones, laptops, and electric vehicles, offering cost-effective and eco-friendly alternatives to disposable batteries while reducing long-term waste [410,411].

A.2.1. Lead-acid

A lead-acid battery consists of lead dioxide (PbO_2) anode and a cathode composed of sponge-like lead (Pb), while its electrolyte is made of cost-effective, non-flammable sulfuric acid [412]. During the discharge of lead acid batteries, the lead ions (Pb^{2+}) within the battery engage in a chemical reaction with the electrolyte, leading to the formation of lead sulfate (PbSO_4) crystals. During the charging process, these crystals undergo a transformation, reverting to their elemental states as Pb and PbO_2 [412].

The lead-acid battery has benefits including a long cycle life of up to 1500-5000 cycles [32]. These batteries are also known for their recyclability and cost-effectiveness which holds the largest market share among rechargeable batteries in the automotive industry, primarily due to the abundance of raw materials [412,413]. Nevertheless, one the major concerns about these batteries is toxicity [414]. Moreover, these batteries tend to be relatively heavy and have an energy density within the range of 30 to 50 Wh/kg which is not high compared to the other rechargeable batteries [415]. The open circuit voltage of

lead-acid batteries remains stable at 2.1 volts [412]. It is also worth mentioning that they lack fast-charging capabilities and do not offer a high depth of discharge [412]. Additionally, the Coulombic efficiency of these batteries are 90-95% [416].

A.2.2. NiCd

NiCd batteries consist of a metallic Cd anode, a nickel hydroxide (Ni(OH)_2) cathode, and an aqueous potassium hydroxide (KOH) electrolyte [417,418]. During the discharge OH^{+2} and Ni(OH)_2 on the cathode side and Cd(OH)_2 on the anode side are produced. This reaction reverses during the charging process [419].

NiCd batteries have several advantages. Notably, the NiCd battery offers an energy density ranging from 50 to 75 Wh/kg [420], and a long cycle life that spans from 3,500 to 50,000 cycles [421], with the Coulombic efficiency of 70-80% [416]. It has resilience under mechanical and electrical stress [420], does not release gas [418], has a high depth of discharge, and is suitable for a wide range of industrial applications, including remote controls, aircraft, and diesel engine starters[422]. The main drawbacks of these batteries are the cost [420], and the toxic and heavy materials [423]. Additionally, NiCd batteries suffer from a relatively high self-discharge rate. The open circuit voltage of the nickel-cadmium battery is 1.2 Volts [424].

A.2.3. Ni-MH

Ni-MH batteries are made of a nickel hydroxide anode, a metal hydride cathode, and an electrolyte based on aqueous potassium hydroxide [425]. Hydroxide ions are generated at the negative electrode through the decomposition of water within the electrolyte, while the positive electrode experiences oxidation of the nickel hydroxide [426].

The Ni-MH battery has a high energy density of more than 70 Wh/kg, a power density of more than 200 W/kg, and a broad operational temperature range [427]. It is often considered a safe and environmentally friendly option [428]. Furthermore, its lifespan is high, typically reaching up to 3000 cycles [429], and the Coulombic efficiency is 70-80% [416]. The Ni-MH battery has a notable self-discharge rate, and a limited DOD [430,431]. The open circuit voltage of the Ni-MH battery is between 1.25 and 1.35 V [432].

A.2.4. Li-ion

Lithium-ion batteries typically consist of a graphitic carbon anode with a layer structure. The cathode in these batteries are made of a lithiated metal oxide compounds, including lithium cobaltite (LCO), mixed oxides of nickel, cobalt, and aluminum (NCA), nickel, cobalt, and manganese (NCM), lithium manganese dioxide spinel (LMO), and lithium iron phosphate (LFP) [433]. The electrolyte is also a solution of lithium salts dissolved in organic carbonates [433]. During the charging process, lithium atoms within the cathode transform into lithium ions and migrate towards the carbon-based anode, depositing on the anode surface as lithium atoms [423]. Additionally, these batteries perform with a high Coulombic efficiency of more than 95% [416].

The lithium-ion battery have benefits including a long cycle life of up to 3000 cycles, high energy density ranging from 75 to 125 Wh/kg [434], and minimal self-discharge [435]. Lithium-ion batteries are, however, sensitive to overvoltage [417]. Their open circuit voltage typically falls within the range of 3 to 4.2 volts [436].

Curriculum Vitae

Name: Maryam Mottaghi

Post-secondary Education and Degrees: University of Tehran
Tehran, Iran
2013-2017 B.Sc. in Metallurgy and Materials Science and Eng.

University of Tehran
Tehran, Iran
2017-2020 M.Sc. in Materials Science and Eng.

The University of Western Ontario
London, Ontario, Canada
2022-2026 Ph.D.

Honours and Awards: Corrosion Research and Training Experience (CRTE) Award from Collaborative Research and Training Experience (CREATE) program
2025

Related Work Experience: Graduate Research Assistant
The University of Western Ontario
London, Ontario, Canada
2022-2026

Executive Manager, Electrochemical Society (ECS)

The University of Western Ontario

London, Ontario, Canada

2024-2025

Volunteer Employee

National Research Council (NRC)

Ottawa, Canada

2025

Publications:

- 1- M. Mottaghi and J. M. Pearce, "A Review of 3D Printing Batteries," *Batteries*, vol. 10, no. 3, Art. no. 3, Mar. 2024, doi: [10.3390/batteries10030110](https://doi.org/10.3390/batteries10030110).
- 2- M. Mottaghi, M. Rahman, A. Kulkarni, and J. M. Pearce, "AC/off-grid photovoltaic powered open-source ball mill," *HardwareX*, vol. 14, p. e00423, June 2023, doi: [10.1016/j.ohx.2023.e00423](https://doi.org/10.1016/j.ohx.2023.e00423).
- 3- M. Mottaghi, Y. Bai, A. Kulkarni, and J. M. Pearce, "Open-source scientific bottle roller," *HardwareX*, vol. 15, p. e00445, Sept. 2023, doi: [10.1016/j.ohx.2023.e00445](https://doi.org/10.1016/j.ohx.2023.e00445).
- 4- M. Maryam and M. P. Joshua, "Open-source inert gas glove box," *HardwareX*, p. e00702, Sept. 2025, doi: [10.1016/j.ohx.2025.e00702](https://doi.org/10.1016/j.ohx.2025.e00702).
- 5- M. Mottaghi, A. Kulkarni, and J. M. Pearce, "Recycling silicon photovoltaic cells into silicon anodes for Li-ion batteries using 3D printing," *RSC Sustain.*, Feb. 2025, doi: [10.1039/D4SU00808A](https://doi.org/10.1039/D4SU00808A).
- 6- M. Mottaghi, T. K. Meyer, R. J. Tieman, D. Denkenberger, and J. M. Pearce, "Yield and Toxin Analysis of Leaf Protein Concentrate from Common North American Coniferous Trees," *Biomass*, vol. 3, no. 2, Art. no. 2, June 2023, doi: [10.3390/biomass3020011](https://doi.org/10.3390/biomass3020011).
- 7- M. Mottaghi, M. Woods, L. Danier, A. So, J. M. Reeves, and J. M. Pearce, "Open-source 3D printable forearm crutch," *PLOS ONE*, vol. 20, no. 2, p. e0318987, Feb. 2025, doi: [10.1371/journal.pone.0318987](https://doi.org/10.1371/journal.pone.0318987).

- 8- R. Roy, M. Mottaghi, M. Woods, and J. M. Pearce, “Life Cycle Carbon Emissions Savings of Replacing Concrete with Recycled Polycarbonate and Sand Composite,” *Sustainability*, vol. 17, no. 3, p. 839, Jan. 2025, doi: [10.3390/su17030839](https://doi.org/10.3390/su17030839).
- 9- F. Khodabakhshi et al., “Hydrogen storage behavior of Mg/Ni layered nanostructured composite materials produced by accumulative fold-forging,” *International Journal of Hydrogen Energy*, vol. 47, no. 2, pp. 1048–1062, Jan. 2022, doi: [10.1016/j.ijhydene.2021.10.096](https://doi.org/10.1016/j.ijhydene.2021.10.096)
- 10- M. Mottaghi and J. M. Pearce, “3D Printing of Batteries,” in *Next-Generation Energy Storage Systems. From Advanced Lithium to Beyond-Lithium Batteries*, Wiley-VCH GmbH (in press)
- 11- M. Mottaghi, Asgari, Nima, R. Roy, and J. M. Pearce, “Open-source manufacturing of polypropylene replacements for peat cups in vertical farming: improvements in life cycle embodied energy, greenhouse gas emissions, labor and operational costs” (submitted-revised)
- 12- M. Mottaghi, A. Kulkarni, J. M. Pearce, “Effect of Pyrolysis Temperature on the Performance of 3D-Printed Silicon–Carbon Anodes Derived from Recycled Photovoltaic Silicon”: SSRN.” Accessed: Nov. 27, 2025. [Online]. Available: https://papers.ssrn.com/sol3/papers.cfm?abstract_id=5812933 (submitted)
- 13- M. Mottaghi, A. Kulkarni, R. Ghode, R. Z. Cao, M. S. H. Boutilier, C. Louis Briens, and J. M. Pearce, “Upcycling Post-Consumer Plastic and Waste Silicon Photovoltaic Cells into Carbon-Enhanced Silicon Anodes for Li-ion Batteries Using 3D Printing” (submitted)